Universität Bremen

Fachbereich 1

(Physik und Elektrotechnik)

Natural and artificial radionuclides as tracers in fluvial systems

Dissertation zur Erlangung der Doktorwürde durch den Promotionsausschuss Dr. rer. nat. der Universität Bremen

Vorgelegt von

Maria-Evangelia Souti

March 22, 2018

Datum des Promotionskolloquiums: 20. Juni 2018

Erster Gutachter: Dr. H.W. Fischer

Zweiter Gutachter: Dr. R. Gellermann

To Ioannis and Amelie

Acknowledgements

Foremost, I would like to express my sincere **G**ratitude (with a capital and bold g) to my supervisor Dr. H.Fischer, who supported and encouraged me in any way possible. Thank you, Helmut for trusting my skills and abilities and believing in me even in times when I didn't.

I would like to express my appreciation to all the member of the Radioactivity Group, every single one was there for me all these years, helping me with sampling, assisting me in the lab and making my time in the office fun. Especially to Bernd Hettwig for always helping me find my way around the lab and answering all my questions on gamma spectroscopy. I wouldn't be half as good a spectrometrist as I am now without him. And of course my deepest thanks to Dr. Volker Hormann, for devoting his time reading most of this thesis and guiding me through chemistry and modeling.

But most of all, I would like to thank my family for their love and support all my life. I want to thank my husband for everything, I am sure I would never be able to finish this PhD without him by my side. Special thanks to my German family, Tina and Bernd, for showing me love and being next to me all these years. Last but not least I want to thank my crazy friends for accompanying me in drinking and relieving stress after work!

Special thanks to the staff of the Seehausen wastewater treatment plant, Bremen for their helpful attitude and assistance.

The study is part of the network project TransAqua funded by the German Federal Ministry of Education and Research (BMBF, 15NUK030).

Abstract

The environmental pathways of medical ^{131}I have been the subject of several studies presenting its ability as a tracer in lakes, rivers and estuarine systems. In this study ^{131}I, originating from the local wastewater treatment plant (WWTP), is used as a readily available tracer with the aim of obtaining a better understanding on the distribution of radioisotopes in the tidal influenced Weser River.

In order to detect low concentration of ^{131}I on Weser River water, a well-defined chemical extraction method needs to be applied. Focused on this aspect, upon investigating 12 different methods, a procedure with a high extraction yield (86 ± 15)% which targets inorganic and organically bound iodine at the same time was developed, tested and used for bulk water samples.

Large amount of water and sediment samples were collected and measured by gamma spectroscopy, for the period autumn 2014 – autumn 2015, during 17 different sampling campaigns. The ^{131}I activity concentration in the river water is strongly dependent on the tidal cycle. Its profile is similar to the one in bank sediments with maximum values directly in the WWTP outflow and lowest in the opposite river bank and upstream direction.

A model which computes the ^{131}I behavior in Weser River for routine releases was developed. For assessing the model, water and sediment samples taken from the river are required as well as information on hydrological and morphological data of the river. The model provides realistic radionuclide distributions in water and bank sediments. The simulated currents and ^{131}I activity concentration in the system are, in general, in agreement with observations. Despite the simplifications considered, the assessment of the model indicates its capability of predicting the dispersion of medically derived iodine, originating from the WWTP, in the water body and banks of Weser River. With minor adjustments, one could possibly use the model for the prediction of dispersion for different radionuclides, in different area and in emergency situations.

^{131}I, chemical extraction, river water, bank sediments, model

Contents

Introduction and Overview 1

Chapter 1 – Radionuclide ^{131}I
1.1 Production and decay of ^{131}I 5
1.1.1 ^{131}I production for medical use 5
1.1.2 ^{131}I decay scheme 6
1.2 Medical use of ^{131}I 8
1.3 Environmental pathways of medical ^{131}I 9
1.4 General comment on Chapter 1 11
1.5 References for Chapter 1 12

Chapter 2 – Weser River area
2.1 The Weser River 15
2.2 Tidal influence on Weser River 18
2.3 The Waste Water Treatment Plant in Seehausen 23
2.4 Previous measurements of ^{131}I in Weser River 24
2.5 General comment on Chapter 2 26
2.6 References for Chapter 2 27

Chapter 3 – Modeling in rivers
3.1 Existing models 31
3.2 Model description and governing equations 34
3.2.1 Model description 34
3.2.2 Governing equations 35
3.2.2.1 Hydrodynamics 35
3.2.2.2 Radionuclide transport 39
3.3 Numerical methods 44
3.3.1 The Finite element method 45
3.3.2 The Incompressible Flow & Iterative Solver Software (IFISS) 48
3.4 Errors in Modeling 50
3.5 General comment on Chapter 3 53
3.6 References for Chapter 3 54

Chapter 4 – Gamma Spectroscopy
4.1 Radioactive decay 57
4.2 Modes of radioactive decay 58
4.2.1 Alpha decay 58
4.2.2 Beta decay 59

4.2.3 Spontaneous fission 60
4.2.4 Gamma decay 61
4.2.5 Other sources of photons 61
4.3 Interaction of gamma radiation with matter 62
4.3.1 Photoelectric absorption 62
4.3.2 Compton scattering 63
4.3.3 Pair production 63
4.4 Detection of gamma radiation 64
4.4.1 Scintillation detectors 64
4.4.2 Semiconductor detectors 65
4.4.2.1 Detectors in the laboratory 66
4.4.2.2 Photon interactions within the detector 67
4.4.2.3 Electronics for gamma spectrometry 68
4.5 Gamma spectrum analysis 70
4.5.1 Calculation of calibration curves 70
4.5.2 Peak location and area 75
4.5.3 Background subtraction 76
4.5.4 Efficiency correction 78
4.5.5 Nuclide Identification 78
4.5.6. Minimum Detectable Activity (MDA) determination 79
4.6 Quality Assurance of Gamma Detectors 80
4.7 General Comment on Chapter 4 81
4.8 References for Chapter 4 82

Chapter 5 – Chemical Extraction of ^{131}I
5.1 Iodine Chemistry 83
5.2 Iodine separation methods 84
5.3 ^{131}I extraction methods tested in this work 86
5.3.1 Method I: MM followed by Fe induced precipitation 88
5.3.2 Method II: Fe induced precipitation followed by MM 89
5.3.3 Method III: MM (use of specially manipulated Bentonite) followed by Fe induced precipitation 89
5.3.4 Method IV: Fe induced precipitation followed by MM (formation of 1 precipitate) 89
5.3.5 Method V: MM (use of 10 times higher quantity of $AgNO_3$) followed by Fe induced precipitation 90
5.3.6 Method VI: MM (use of AgOH instead of AgNO3) followed by Fe induced precipitation 90
5.3.7 Method VII: MM (use of AgOH additional to AgNO3) followed by Fe induced precipitation 90

5.3.8 Method VIII: ^{131}I extraction with use of Dowex 1x8 resin followed by Fe Induced precipitation 91
5.3.9 Method IX: ^{131}I extraction with use of mixed bed silver loaded Cl resin and XAD-4resin followed by Fe induced precipitation 91
5.3.10 Method X: MM (excluding the addition of $Na_2HPO_4 \cdot H_2O$) followed by Fe induced precipitation 92
5.3.11 Method XI: MM followed by Ca induced precipitation 92
5.3.12 Method XII: MM followed by Ca induced precipitation (formation of 1 precipitate) 93
5.4 Statistical analysis of chemical yield 95
5.5 Influence of physical and chemical properties of effluent on the chemical yield 97
5.6 Repeatability and Reproducibility 99
5.7 General Comment on Chapter 5 101
5.8 References for chapter 5 102

Chapter 6 – ^{131}I activity concentration in Weser River
6.1 Sampling methods 105
6.2 Selection of sampling locations on Weser River 106
6.3 Sample collection and treatment 108
6.3.1 River water samples 109
6.3.2 Sediment samples 109
6.3.3 Suspended matter samples 110
6.4 1st and 2nd sampling campaigns 111
6.5 CORMIX simulations 113
6.6 ^{131}I activity concentration in Weser River water 118
6.6.1 Tidal influence 118
6.6.2 ^{131}I activity concentration in Weser water 120
6.7 ^{131}I activity concentration in Weser River sediments 123
6.7.1 Bottom sediments 123
6.7.2 Bank sediments 124
6.8 ^{131}I bound to suspended matter in Weser River 128
6.9 General comment on Chapter 6 130
6.10 References for Chapter 6 131

Chapter 7 – Modeling ^{131}I in Weser River
7.1 ^{131}I dispersion sedimentation model in Weser River 135
7.2 Grid approximation 136
7.3 Hydrodynamic sub-model 138
7.4 Radionuclide submodel 144
7.4.1 Radionuclide submodel for river water 144

7.4.2 Radionuclide submodel for bank sediments 154
7.5 General comment on Chapter 7 167
7.6 References for chapter 7 168

Chapter 8 – Summary and Outlook
8.1 Summary 171
8.2 Study in numbers 172
8.3 Outlook 173

Publications 175

Appendix
Appendix 1 – Chemical extraction methods A1
Appendix 2 – Sampling location coordinates A12
Appendix 3 – Water measurement results A18
Appendix 4 – ^{131}I in WWTP effluent A27
Appendix 5 – River discharge A28
Appendix 6 – Sediment measurement results A29
Appendix 7 – Suspended matter results A31
Appendix 8 – Water level data A32
Appendix 9 – Poiseulle flow A34
Appendix 10 – Past sediment measurement results A36
Appendix 11 – Comparison experimental and simulated data A39
Appendix 12 – Analytical solution of 1D advection dispersion equation A47
Appendix 13 – ^{131}I in WWTP effluent-IMIS values A51
Appendix 14 – Corrections in the activity using interactive peak fit function A52
Appendix 15 – MatLab m-files A53
Appendix 16 – Simplification of the 2D advection dispersion equation A80

List of figures

I1	Overview of the main topics covered under the scope of this thesis	2
1.1	^{131}I oral capsule in packaging material	6
1.2	^{131}I decay scheme	7
1.3	Environmental pathway of medical ^{131}I	9
2.1	The river Weser	16
2.2	Weser River in the vicinity of the local WWTP	16
2.3	Successive deepening and widening of the Lower Weser	17
2.4	High and low tide in station Oslebshausen on 25.8.2015	18
2.5	The configuration of Earth, moon and sun responsible for spring and neap tides	19
2.6	HAMELS fitting for observed data in the station Oslebshausen	21
2.7	Simulated tidal cycle for 2 days as a standing wave	22
2.8	The WWTP Bremer Kläranlage Seehausen	23
3.1	Scheme of the model	34
3.2	The FEM description for a range of common physical phenomena	45
3.3	Examples of finite elements in 1-D, 2-D and 3-D	46
3.4	Isoparametric mapping of a P1 and a Q1 element	47
3.5	Proposed phases for computational modeling and simulation	50
4.1	Chart of nuclides	57
4.2	Gamma interaction by Photoelectric effect	62
4.3	Gamma interaction by Compton effect	63
4.4	Gamma interaction by pair production	63
4.5	Configurations of detector generally available	66
4.6	Additional possibilities for interaction within a detector	67
4.7	^{28}Al spectrum illustrating the various spectral features expected	68
4.8	Water sample spectrum	69
4.9	Sediment spectrum	69
4.10	Shape calibration curve in Genie 2000	71
4.11	Efficiency calibration curves for different Marinelli geometries	73
4.12	Efficiency calibration curves for different filling heights on a 0.5 L plastic bottle with constant density	74
4.13	Efficiency calibration curves for different filling densities on a 0.5 L plastic bottle with constant filling height	75
4.14	An example of interactive peak fit use	76
4.15	Background spectrum	77

5.1	The major chemical forms of inorganic iodine in aqueous solutions	84
5.2	^{131}I precipitate	87
5.3	Homogenized sample in gamma spectrometer	87
5.4	Fe precipitate after the Mundschenk method	88
5.5	Fe precipitate before the Mundschenk method	89
5.6	Resin precipitate	91
5.7	Collection of resin precipitate	91
5.8	Fe precipitate after ^{131}I resin extraction	91
5.9	Bentonite precipitate formed with method X	92
5.10	Fe precipitate formed with method X	92
5.11	Normal and empirical cumulative distribution functions	97
5.12	Scatter plots of time span, conductivity, salinity and pH values over the corresponding chemical yield values	99
6.1	^{131}I activity concentration in the sediments and calculated values for river water in different locations on both banks	108
6.2	River water sampling	109
6.3	Petite Ponar grab	109
6.4	Sampling of sediments on the river bank	109
6.5	Filtering device	110
6.6	Suspended matter samples	110
6.7	Suspended matter precipitate. Container diameter 34.6 cm	110
6.8	Sampling points for the 1st and 2nd sampling campaigns	111
6.9	Sampling locations during the first two sampling campaigns and the revised ones	112
6.10	Tide curve and current velocity for the station Bremerhaven Alter Leuchtturm	115
6.11	Simulation results for CORMIX simulations	116
6.12	Sampling locations; 0, 1.1, 2.1, 3.1, 4.1	119
6.13	WWTP outlet with visible height of the high water reach	119
6.14	Normalized ^{131}I concentration different times in the tidal cycle	119
6.15	Sampling locations on sections with 5 equidistant sampling points across the river	120
6.16	Normalized ^{131}I activity 3 to 4 hours after high and low water	122
6.17	Normalized ^{131}I activity on 5 equidistance points across the river	122
6.18	Locations where bottom sediment samples were collected	123
6.19	Bottom sediment samples	123
6.20	Sampled rock and mussels from the bottom of the river	124
6.21	Industrialized area of the Weser River	124

6.22 ^{131}I activity concentration in bank sediments and normalized activity concentrations in river water 125
6.23 ^{131}I bank sediment activity concentration of 2015 and 2008 sampling campaigns 126
6.24 Sampling locations on the outflow of the WWTP of 2008 and 2015 sampling campaigns 126
6.25 Natural and manmade radioisotopes in Weser bank sediments 127
6.26 Sampling locations for suspended matter measurements 128

7.1 Simplified scheme of the model 135
7.2 Weser River in the vicinity of the WWTP 136
7.3 Weser domain discretization 136
7.4 Grid approximation as sum of rectangles 137
7.5 Dirichlet and Neumann boundaries 138
7.6 Simulations for the longitudinal component of the velocity 141
7.7 Simulations for the lateral component of the velocity 142
7.8 Tidally influenced longitudinal velocities 143
7.9 Simulated normalized ^{131}I activity concentration for different values of eddy diffusivity in the range 0.001-0.01 m^2/s (3 hours after HW) 146
7.10 Simulated normalized ^{131}I activity concentration for different values of eddy diffusivity in the range 0.025-0.25 m^2/s (3 hours after HW) 147
7.11 Simulated normalized ^{131}I activity concentration in different times during the tidal cycle 148
7.12 Comparison of simulations with experimental data 3 hours after high/low water 149
7.13 Experimental and Simulation data for different times during the tidal cycle 150
7.14 Scatter plot of simulated vs. experimental normalized ^{131}I activity concentrations 151
7.15 Residuals vs. simulated values plot for assessing the goodness of our model 153
7.16 Variation of the normalized ^{131}I activity concentration 0.5 km downstream the WWTP during the sedimentation period 156
7.17 Simulated activity concentration in sediment using as input the simulated or the measured ^{131}I activity concentration in river water 159
7.18 Simulated activity concentration in sediment, taking into account a background concentration of 1.2 mBq/kg 159
7.19 Comparison of simulated activity concentration in sediment with experimental data in the selected locations, collected at 2008 and 2015 campaigns 160
7.20 Regression and residual plots for OP regression analysis of simulated ^{131}I activity concentration in the bank sediments and experimental data 161
7.21 Comparison of simulated activity concentration in sediment (with dotted lines representing minimum and maximum output of the model for selected parameters) with experimental data 163

7.22 Sensitivity plot for different parameters of our model 165

A1 Figure 6.7 y axis in linear scale A24
A2 Figure 6.8 y axis in linear scale A25
A3 ^{131}I activity concentration of effluent before and after each sampling A27
A4 Overview of the sampling locations A36
A5 Water sampling locations at 2012 A38

List of tables

1.1	Gamma and X-ray radiation of ^{131}I	7
2.1	Most dominant tidal constituents	19
2.2	Harmonics for Weser River – Station Oslebshausen	19
4.1	Performance characteristics of detectors 3 - 6 in the laboratory	66
4.2	Physical characteristics of detectors 3 - 6 in the laboratory	67
5.1	Values of ^{131}I activity concentration in original WWTP water	94
5.2	Kolmogrov-Smirnov calculations	96
5.3	Repeatability of the chemical extraction method	100
5.4	OSPAR II measurements on the chemical yield	100
6.1	^{131}I activity concentration in the sediments and calculated values for river water in different locations on both banks	107
6.2	^{131}I activity concentration on bottom sediments	124
6.3	^{131}I bound to suspended matter results	128
7.1	Grid dimensions	137
7.2	Percentage distribution of sediment classes	157
7.3	Model parameter values given in literature	158
7.4	Regression analysis for OP regression of simulated and measured data in Weser sediments	161
7.5	Range of model parameter values	164
7.6	Sensitivity index of model parameter values	165
A1	^{131}I activity concentration in the WWTP effluent before and after sampling	A27
A2	^{131}I activity concentration in sediment during 2008 sampling campaigns	A36
A3	^{131}I activity concentration in river water during 2012 sampling campaigns	A38

Introduction

This introductory chapter presents the motivation and the goal of this study as well as the overview of this thesis.

Motivation and goal of this work

Nuclear medicine plays an important role within man made radioactive environmental impacts. ^{131}I is the most abundant therapeutic radiopharmaceutical representing close to 90% of all radiotherapies (Barquero et al., 2008). Due to its radioactive (8 days) and biological (100 days) half-lives and its tendency to collect in the thyroid gland, ^{131}I is established as the most efficacious method for the treatment of hyperthyroidism and thyroid cancer. After the patient undergoes an iodine treatment, the activity which is not retained by the thyroid is mainly excreted through the urinary system to the sewage as radioactive effluent. The environmental pathways of medical ^{131}I have been the subject of several studies presenting its ability as a tracer in lakes, rivers and estuarine systems, however so far ^{131}I has not been used as a tracer for studying the complex hydrological and physiochemical processes which influence the distribution of the radioisotope in the water-sediment system.

The goal of this project is the development of a model describing the dispersion of ^{131}I, originating from medical application, in Weser water. For assessing the model, water and sediment samples taken from the river are required as well as information on hydrological and morphological data of the river. In addition, due to low activity concentrations in the Weser River water, a well-defined and tested chemical extraction method needs to be applied for which knowledge of iodine chemistry as well as of existing chemical extraction methods is required.

This model will be a valuable tool in understanding and predicting the dispersion of radionuclides in a complex hydrological system. It could be further applied in different river systems and with the interest of additional radionuclides, leading to a better understanding of the environmental behavior of natural and man-made radioactivity.

Overview of the Thesis

This thesis consists of 8 major chapters (figure I1).

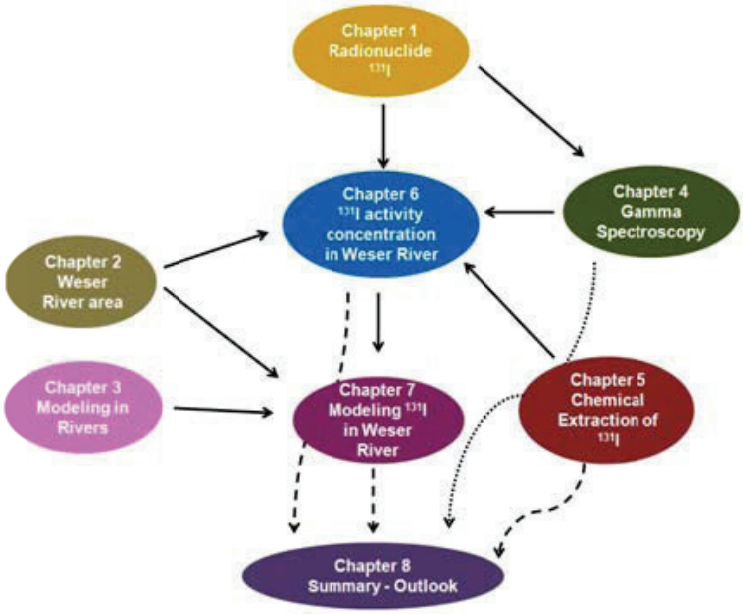

Figure I1: Overview of the main topics covered under the scope of this thesis.

Chapter 1 is devoted to ^{131}I. As the main radioisotope used in this study it is important to provide basic information on is production, decay and its medical use as well as describing the pathways it follows after its release in the urban environment.

In **chapter 2** one can find a description of the investigated area along with information on past studies and measurements of ^{131}I in different media in the selected area.

Chapter 3 presents the main principles of river modeling along with their corresponding mathematical formulations. This chapter is directly related to chapter 7.

Chapter 4 presents the theoretical background on the physics of radiation, the gamma spectroscopic system, its electronic and the analysis of gamma spectra.

Chapter 5 contains description of iodine chemistry and extraction methods present in literature but mostly the results of the methods tested and selected for the quantification of ^{131}I from bulk water samples.

Chapter 6 focuses on presenting the results of the sampling campaigns performed on Weser River during the course of this study. These results are further used on chapter 7 for model assessment.

Chapter 7 describes the model used to compute the ^{131}I behavior in Weser River including comparison of simulated data with experimental values.

Chapter 8 summarizes the results from the previous chapters and provides suggestions on improvements on the methods presented during this study.

All additional data not presented in the main texts, as well as programming code are attached in the Appendix section.

Chapter 1

Radioactive Iodine

Iodine (atomic number 53) is the heaviest of the stable halogens with 37 known isotopes (from ^{108}I to ^{144}I[1]). All but ^{127}I are radioactive with half-lives (see §4.1) spanning from 93.5 μs (^{109}I) to 1.57×10^{7} y (^{129}I) (National Nuclear Data Center, 2017).
^{131}I (half-life 8.02 d) is a major uranium, plutonium fission product and significant contributor to health hazards caused from the open air atomic bomb testing in the '50s and nuclear accidents of Chernobyl and Fukushima (Pravalie, 2014). It is also known as an important radiopharmaceutical due to its useful beta emission (see §4.2.2), its biological half-life (120-138 days in the thyroid , (NCHPS, 2017)) and its tendency to collect in the thyroid gland.
In this chapter information on the production, decay and medical use of ^{131}I is given as well as the pathways it follows after its release in the urban environment.

1.1 Production and decay of ^{131}I

^{131}I was discovered at the University of California-Berkeley by Glenn T. Seaborg and John J. Livingood in 1939. Saul Hertz discovered the use of radioactive iodine in medicine; for the treatment of thyroid disease (Fahey et al., 2017).

1.1.1 ^{131}Iodine production for medical use

^{131}I is mainly produced by irradiating a target material of tellurium dioxide (TeO_2) powder or pellets, enriched with ^{130}Te, where ^{131}Te is produced and decays into ^{131}I with a half life of 25 mins following:

$$^{130}_{52}Te + ^{1}_{0}n \rightarrow ^{131}_{52}Te\,(+\gamma) \xrightarrow{t_{1/2}=25\,\mathrm{min}\,s} ^{131}_{53}I + ^{0}_{-1}e + \gamma$$

The most common procedure for separating the ^{131}I from the radioactive tellurium dioxide is dry distillation. IAEA (2003) in the manual for reactor produced radioisotopes describe both wet and dry distillation methods (along with 3 alternate procedures) as well as production of ^{131}I as a ^{235}U fission product. In Isotope Technologies Dresden GmbH, ^{131}I is separated according to a defined temperature (volatilization) and transferred into the iodine traps by carrier air. As it passes

[1] In National Nuclear Data Center (2017) also ^{145}I with half-life >407 ns is given.

through the separator, which retains reliably the tellurium dioxide impurities and dust particles, is gets absorbed in the iodine traps by weakly alkaline buffer solution producing a sodium iodide stock solution which is further distributed in portions and dispensed in vials.
Other separation procedures include solvent extraction and ion-exchange methods (El-Azony and Qaim, 2008), activated charcoal column (Chattopadhyay and Saha, 2009) and using a tiny Dowex-1 column (Chattopadhyay and Saha, 2010).
The ^{131}I produced can be used directly in the form of Na^{131}I or can be attached to a pharmaceutical to form meta-iodobenzylguanidine (MIBG) (Ansto, 2018).

*Figure 1.1: ^{131}I oral capsule in packaging material (**Global Technologies, 2017**)*

1.1.2 ^{131}I decay scheme

^{131}I with a half-life of 8.02 days (slightly different half-lives are given from different sources: 8.0252 days (National Nuclear Data Center, 2017) and 8.0228 days (Nucleonica, 2017)), decays through a β^- decay process leaving the daughter nuclide ^{131}Xe in an excited state (see §4.2.2). The emission of β^- particles with endpoint energy of 606 keV, have the highest emission probability of 89.6%, followed by the emission of gamma rays with energies of 364 keV and 284 keV with emission probabilities 89.6% and 6.12% respectively. One other way of decay is accomplished by the emission of β^- particles with endpoint energy of 334 keV accompanied by gamma rays with energy of 637 keV with emission probability of 7.16%. While a direct transition to a ground state of ^{131}Xe has not been observed, a transition through a metastable ^{131m}Xe with a half-life of 11.9 days is possible with rather small probability (0.39%) by the emission of β^- particles with endpoint energy of 807 keV. ^{131m}Xe has been measured in our lab in

the styrofoam packing material of ^{131}I capsules (Fischer et al., 2014). An illustration of a ^{131}I decay process is given in figure 1.2.

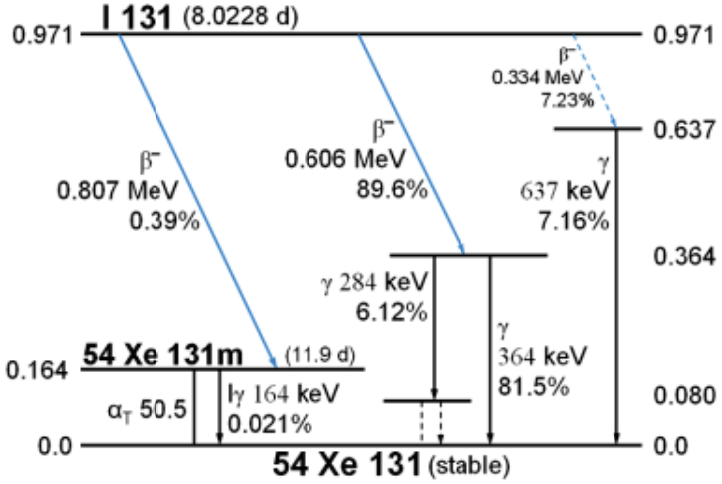

Figure 1.2: ^{131}I decay scheme (Nucleonica, 2017)

Further weaker emissions of gamma rays and X-rays from ^{131}I with their energies (in keV) and corresponding abundance are given in table 1.1. The gamma rays energies are isotope specific and are used for the identification of the radionuclide and the determination of its activity in a sample as explained in §4.4.

Table 1.1: Gamma and X-ray radiation of ^{131}I (National Nuclear Data Center, 2017)

Energy (keV)		Intensity (%)
XR l	4.11	0.63 % *3*
XR kα2	29.461	1.53 % *4*
XR kα1	29.782	2.82 % *8*
XR kβ3	33.562	0.263 % *7*
XR kβ1	33.624	0.509 % *13*
XR kβ2	34.419	0.154 % *4*
	80.185 *2*	2.62 % *4*
	85.9 *2*	9E-5 % *5*
	163.930 *8*	0.0211 % *4*
	177.214 *2*	0.269 % *4*
	232.18 *15*	0.0032 % *4*
	272.498 *17*	0.0576 % *11*

Energy (keV)	Intensity (%)
284.305 *5*	6.12 % *6*
295.8 *2*	0.0018 % *8*
302.4 *2*	0.0047 % *6*
318.088 *16*	0.0774 % *17*
324.651 *25*	0.0212 % *24*
325.789 *4*	0.273 % *21*
358.4 *2*	0.016 % *6*
364.489 *5*	81.5 % *8*
404.814 *4*	0.0546 % *17*
503.004 *4*	0.359 % *4*
636.989 *4*	7.16 % *10*
642.719 *5*	0.217 % *4*
722.911 *5*	1.77 % *3*

1.2 Medical use of ^{131}I

Iodine is needed for the production of thyroid hormone and upon intake it gets concentrated in the thyroid tissue. ^{131}I behaves in the same way, meaning a large part of the intake will be concentrated in the thyroid within 24 to 48 hours. The part which is not retained by the thyroid is excreted from the body within some days mostly in the urine, feaces, sweat, saliva and breath. The absorbed dose to the patient depends on the activity administrated together with the pathology of patient (which determines the distribution and retention of the ^{131}I in the body). Due to its ability of concentrating in the thyroid tissue ^{131}I is used for both diagnostic (in limited cases) and treatment purposes.

A. Diagnostics
Small amount 74 MBq (Yin et al., 2015, Lassmann et al., 2004) of ^{131}I swallowed (as a pill) indicated for use in performance of the radioactive iodide (RAI) uptake test to evaluate thyroid function. Diagnostic doses may also be employed in localizing metastases associated with thyroid malignancies. In recent years, ^{131}I has been abandoned in favor of ^{123}I, a gamma emitter with half-life of 13 h (Radioactivity EU, 2017).

B. Treatment
^{131}I is used for the treatment of hyperthyroidism and thyroid cancer and in some cases also euthyroid goiter and thyroid adenoma.

Hyperthyroidism: Hyperthyroidism is the condition when a thyroid is overactive (caused by Grave's disease) and produces too much of the hormone thyroxine. Usually 3-8 MBq per gram of thyroid tissue is administrated (Silberstein et al., 2012) to slow down the overproduction of thyroxine by damaging and destroying the hyperactive thyroid cells leading to normal thyroid function. The uptake of iodine by a hyperactive thyroid is 50-70% depending on the level of hyperfunction and the normal daily intake of iodine with foodstuffs (Radiation Protection 97, 1998).

Thyroid cancer: In thyroid cancer treatment ^{131}I is used to destroy any remaining thyroid tissue not removed by surgery or to treat some types of thyroid cancer that have spread to lymph nodes and other parts of the body. Due to the fact that the uptake of iodine in thyroid cancer cells is higher than in normal tissue, high activities are administrated of about 2.75-5.5 GBq to kill the remaining cancer cells, 5.57-7.4 GBq for treatment of any metastases and more than 7.4 GBq for distant metastases (Silberstein et al., 2012). Most of the administered iodine (close to 80%) is excreted within 48 h due to the fact that only a small portion of the thyroid issue remains after surgery to uptake the iodine (Radiation Protection 97, 1998).

Euthyroid goiter: Euthyroid goiter is the condition when a thyroid is enlarged however its function is normal. High levels of activity up to 3 GBq (Radiation Protection 97, 1998) may be administrated, due to the large volume of the thyroid, with the aim of reducing the thyroid tissue volume and avoiding surgery.

Thyroid adenoma: The thyroid adenomas (nodules) are monoclonal "new growths" that are formed in response to the same sort of stimuli as are carcinomas. They can be treated with surgery, ethanol injection and ^{131}I treatment, which is the most effective. The administered activity depends on the size of the nodule and usually ranges between 185-740 MBq (Pacini and De Groot, 2016).

1.3 Environmental pathways of ^{131}I

Grünwald and Derwahl (2015) report about 50.000 therapies to be conducted annually in around 120 nuclear medicine facilities in Germany. Following their release, patients with maximal ^{131}I body activity of 250 MBq (SSK,2004) excrete the activity which is not retained from the thyroid, mostly through the urinary system, to the sewage as a radioactive effluent (see also figure 1.3). After entering the sewage system, iodine is diluted and transferred to the inflow of the waste water treatment plant (WWTP), where it circulates through different compartments and is released in the environment as sludge and/or effluent. Once introduced in the aquatic environment, the ^{131}I gets diluted and mixed, attaches to particles and sediments. It can also get incorporated into biota and make its way into the food chain. In one study (Mulas et al., 2017) medical ^{131}I was also present in drinking water treatment plant. Due to its short half live ^{131}I does not transport further in the ecosystem and cannot be found in media where long time scales are needed for migration (eg. groundwater, oceanic sediments etc).

Figure 1.3: Environmental pathway of medical ^{131}I.

Few studies on the sewage system (Chang et al., 2011, Ulbrich and Fischer, 2014) following patients after their release definitely proved the medical origin of the isotope in the urban system. In WWTPs ^{131}I was successfully measured already since 1975 (Prichard et al., 1981). The majority of the literature on the medical ^{131}I in the urban environment deals with measurements and subsequent calculations on radiation exposure and dose assessment of WWTP workers and public (Jimenez et al., 2010, Sundell-Bergman et al., 2008, Rose and Swanson, 2013, Martin and Fenner, 1997, Camacho et al., 2013), concluding to a negligible human exposure. Measurements in different environmental media in regions close to WWTPs, along with measurements of effluent indicated ^{131}Is ability as a tracer (Fischer et al. (2009), Smith et al. (2008), Rose et al. (2013), Montenero et al. (2017), Punt et al. (2007)).

More specifically, Fischer et al. (2009) measured ^{131}I activity concentrations in the Weser River sediments up to 100 Bq/kg (dry mass ; d.m.) and identified the local WWTP as the source (more details in §2.4). Smith et al. (2008) carried out measurements in the New York Harbor area where ^{131}I was successfully measured in surficial sediment samples with activities up to 6.0 ± 1.1 mBq/g, 22 ± 4 mBq/g in filtered suspended mater samples and 254 ± 50 mBq/l in WWTP effluent samples. Despite the limited amount of data, they concluded that ^{131}I can be used as a potentially valuable source-specific, short-lived biogeochemical tracer for particles, sediments and wastewater-sourced contaminants in urbanized aquatic systems. Rose et al. (2013) performed ^{131}I activity concentration measurements in the tidal Potomac River for both river water (range: 0.076 ± 0.006 – 6.09 ± 0.07 Bq/l) and sediments (range: 1.3 ± 0.8 – 117 ± 2 Bq/kg (dry weight)) in 4 sampling points located in a region with 3 different WWTPs. The data collected, along with chlorophyll, total suspended solids and dissolved organic carbon measurements were used for better understanding of iodine biochemistry. Montenero et al. (2017)[2] concluded that the use of ^{131}I as a tracer of sewage effluent from coastal municipalities to the Laurentian Great Lakes appears feasible after measuring ^{131}I in water (up to 8.2 mBq/l), sediments (up to 68Bq/m^2) and biota (algae concentrations up to 91 Bq/kg(dry weight) and mussel concentrations up to 3.7 Bq/kg (dry weight)), following discharge rates of 34 to 1807 MBq per day from both WWTPs of the area. Punt et al. (2007) followed the ^{131}I pathway based on a total administration of 15.1 GBq between three patients over 3 consecutive days and measured ^{131}I in crude sewage (average 26 Bq/l), treated effluent (average 11 Bq/l), sludge (up to 1800 Bq/kg (dry weight) in dewatered sludge), river water (up to 20 Bq/l) and river sediment (up to 67 Bq/kg (dry weight)) of Hogsmill River (tributary of Thames). They also reported dose assessment based on their measurements and their study showed that even with pessimistic exposure scenario, the external exposure would likely be no more than a few percent of the annual dose.

[2] Paper based on Montenero's PhD Thesis (2015): Iodine-131: Measurement and Application of a Novel Tracer in Lake Michigan

1.4 General comment on Chapter 1

In this Chapter a basic introduction on ^{131}I was given, on its production, decay and medical uses as well as on the path it follows in the environment after its excretion from the patients. Although the path is well understood and several studies have focused on its measurement in different environmental media in both WWTPs and river/lake water, sediments and biota and indicated its ability as a tracer, none of the aforementioned studies did use iodine as a tracer (with the exception of Rose et al. (2003) who focused on the iodine biogeochemistry).
Under the scope of this work, the routine releases of ^{131}I as WWTP effluent in the Weser River allowed its successful measurement in both river water and sediments under different hydrological conditions. This study uses medical ^{131}I as a readily available tracer and manages to obtain a better understanding on complex hydrological processes and the underlying physical and chemical processes influencing the distribution of radioisotopes in the water-sediment system.

1.5 References for Chapter 1

Ansto, 2018. Australian Nuclear Science and Technology Organization. Retrieved from: http://www.ansto.gov.au/BusinessServices/ANSTOHealth/Radiopharmaceuticals/MIBG/index.htm

Baquero R., Basurto F., Nunez C., Esteban R., 2008. *Liquid discharges from patients undergoing I-131 treatments.* Journal of Environmental Radioactivity, 99, 10, 1530-1534.

Camacho A., Montana M., Valles I., Devesa R., Cespedes-Sanchez R., Serrano I., 2013. *Temporal evolution of radionuclides in sludge from wastewater treatment plants.* Journal of Radioanalytical and Nuclear Chemistry, 295, 1, 297-306.

Chang B.U., Choi S.W., Song M.H., Lee J.S., Kim Y., 2011. *Medically used radionuclides (^{131}I, ^{99m}Tc) in the urban sewage system: the case of the Daejeon metropolitan city, Korea.* Radiation Protection Dosimetry, 146 (1-3), 318-321.

Chattopadhyay S. and Saha Das S., 2009. *A simple and rapid technique for radiochemical separation of iodine radionuclides from irradiated tellurium using an activated charcoal column.* Applied Radiation and Isotopes, 67, 10, 1748-1750.

Chattopadhyay S. and Saha Das S., 2010. *Recovery of ^{131}I from alkaline solution of n-irradiated tellurium target using a tiny Dowex-1 column.* Applied Radiation and Isotopes, 68,10, 1967-1969.

El-Azony K. M. and Qaim S.M., 2008. *Anion-exchange and solvent extraction studies on the separation of radioiodine with particular reference to the production of ^{123}I via proton irradiation of ^{123}Te metal target.* Journal of Radioanalytical and Nuclear Chemistry, 275:275.

Fahey F.H., Grant F.D., Thrall J.H., 2017. *Saul Hertz, MD, and the birth of radionuclide therapy*. EJNMMI Physics, DOI 10.1186/s40658-017-0182-7

Fischer H.W., Ulbrich S., Pittauerová D., Hettwig B., 2009. *Medical radioisotopes in the environment-following the pathway from patient to river sediment.* Journal of Environmental Radioactivity 200**,** 1079-1085.

Fischer H.W., Souti M.E., Hormann V., Borowski M., 2014. *Xe-131m in medical application of I-131: Importance, Detection and Dosimetry.* Conference Paper from 4th European IRPA Conference 23-27 June 2014, Geneva, Switzerland. Retrieved from: https://www.researchgate.net/publication/311308263_Xe-131m_in_Medical_Application_of_I-131_Importance_Detection_and_Dosimetry

Global Technologies, 2017. Retrieved from: http://www.globaltechbd.net/eczacibasi-monrol/?&SingleProduct=11

Grünwald F. And Derwahl K.M., 2015. *Diagnostik und Therapie von Schilddrüsenerkrankungen*. Lemanns Media.

IAEA, 2003. *Manual for reactor produced radioisotopes.* Retrieved from: http://www-pub.iaea.org/MTCD/publications/PDF/te_1340_web.pdf

Isotope Technologies Dresden GmbH, 2017. Retrieved from: http://www.itd-dresden.de/index.php?article_id=136&clang=1

Jimenez F., Deban L., Pardo R., Lopez R., Garcia-Talavera M., 2011. *Levels of 131I and Six Natural Radionuclides in Sludge from the Sewage Treatment Plant of Valladolid, Spain.* Water Air Soil Pollution, 217: 515-521.

Lassmann M., Luster M., Hänscheid H., Reiners C., 2004, *Impact of ^{131}I Diagnostic Activities on the Biokinetics of Thyroid Remnants*. Journal of Nuclear Medicine, 45, 4, 619-625.

Martin J.E. and Fenner F.D., 1997. *Radioactivity in municipal sewage and sludge*. Public Health Reports, 112 (4), 308-318.

Montenero M.P., Dilbone E.K., Waples J.T., 2017. *Using medically-derived iodine-131 to track sewage effluent in the Laurentian Great Lakes.* Water Research, 123, 773-782.

Mulas D., Camacho A., Serrano I., Garbayo A., Agullo J.M., Devesa R., Duch M.A., 2017. *Presence of medically-derived radionuclides in the urban water cycle*. Poster session presented at the 4th International Conference on Radioecology and Environmental Radioactivity, Berlin, Germany.

National Nuclear Data Center, 2017. Retrieved from: https://www.nndc.bnl.gov/chart/decaysearchdirect.jsp?nuc=131I&unc=nds

NCHPS, 2017. *Nuclide Safety Data Sheet Iodine-131.* Retrieved from: http://www.hpschapters.org/northcarolina/NSDS/131IPDF.pdf

Nucleonica, 2017. Retrieved from: https://www.nucleonica.com/wiki/index.php?title=Decay_Schemes#53_I_131_.28Z.3D53.2C_N.3D78.29

Pacini F. and de Groot L.J., 2016. *The Thyroid and its Diseases. Chapter 18, Thyroid Nodules.* Published in http://www.thyroidmanager.org.

Pravalie R., 2014. *Nuclear Weapons Tests and Environmental Consequences: A Global Perspective.* Ambio, 43 (6), 729-744.

Prichard H.M., Gesell T.F., Davis E., 1981*, Iodine-131 levels in sludge and treated municipal wastewaters near a large medical complex.* American Journal of Public Health 71 (1), 47-52.

Punt A., Wood M., Rose D., 2007. *Radionuclide discharges to sewer – A field investigation.* Science Report – SC020150/SR2. Environmental Agency. Retrieved from: http://www.phillywatersheds.org/doc/ThamesEstuaryIodineSourceStudy.pdf

Radiation protection 97, 1998. *Radiation Protection Following Iodine-131 Therapy (Exposures due to out-patients or discharged in-patients).* European Commission. Retrieved from: https://ec.europa.eu/energy/sites/ener/files/documents/097_en.pdf

Radioactivity EU, 2017, http://www.radioactivity.eu.com/site/pages/Iodine_131.htm

Rose P.S., Smith J.P., Cochran J.K., Aller R.C., Swanson R.L., 2013. *Behavior of medically-derived I-131 in the tidal Potomac River*. Journal of Science of Total Environment, 452-453, 87-97.

Rose P.S. and Swanson R.L., 2013. *Iodine-131 in sewage sludge from a small water pollution control plant serving a thyroid cancer treatment facility.* Health Physics, 105 (2), 115-120.

Silberstein E.B., Alavi A., Balon H.R., Clarke S.E.M., Divgi C., Gelfand M.J., Goldsmith S.J., Jadvar H., Marcus C.S., Martin W.H., Parker J.A., Royal H.D., Sarkar S.D., Stabin M., Waxman A.D., 2012. *The SNM Practice Guideline for Therapy of Thyroid Disease with ^{131}I 3.0*.* Journal of Nuclear Medicine, 53 (10), 1633-1651.

SSK, 2004. *Ermittlung der Vorbelastung durch Radionuklid-Ausscheidungen von Patienten der Nuklearmedizin.* Empfehlung der Strahlenschutzkommission, Bonn (in German).

Smith J.P., Oktay S.I., Kada J., Olsen C.R., 2008. *Iodine-131: a potential short-lived, wastewater-specific particle tracer in an urbanized estuarine system*. Environmental Science and Technology, 42 (15), 5435-5440.

Sundell-Bergman S., de la Cruz I., Avila R.,Hasselblad S., 2008. *A new approach to assessment and management of the impact from medical liquid radioactive waste.* Journal of Environmental Radioactivity, 99 (10), 1572-1577.

Ulbrich S. and Fischer H.W., 2014. *An experiment to use medical I-131 as tracer in a city sewer system*. Poster session presented at the 3rd International Conference on Radioecology and Environmental Radioactivity, Barcelona, Spain.

Yin Y., Mao Q., Chen S., Li N., Li X., Li Y., 2015. *A Clinical Trial of Optimal Time Interval Between Ablation and Diagnostic Activity When a Pretherapy RAI Scanning is Performed on Patients With Differentiated Thyroid Carcinoma.* Medicine (Baltimore), 94 (31): e1308.

Chapter 2

Weser Area

In this chapter a description of the study area is given. The Weser River was selected for a variety of reasons. Most important is its proximity to the University of Bremen, enabling the collection of a plethora of samples during the limited time of the project. In its left bank, not far from the city center (only 5 km downstream) the WWTP is located which releases routinely ^{131}I contaminated effluent. Additionally it is also located in the tidal part of the river, allowing us to use ^{131}I as a readily available tracer for the study of a complex hydrological system.

2.1 The Weser River

The river Weser, with a length of 433 km (excluding the Outer Weser) and a total catchment area of 46306 km^2 (Kappenberg and Grabemann, 2001), is the longest river in northwest Germany. It originates at the confluence of the Fulda and Werra rivers, crosses the city of Bremen and discharges into the North Sea in the southernmost part of the German Bight. It can be subdivided into 4 parts; the Upper Weser flowing from the city of Hann. Münden till Minden, the Middle Weser flowing from the city of Minden till the city of Bremen, its tidal part which consists of the Lower Weser which flows from the city of Bremen till the city Bremerhaven (Inner Weser estuary) and the Outer Weser, where the estuary mouth is located. Long term average discharges (1941-2002) at the gauging station Intschede (approx. 80% of river basin catchment) are 327 m^3/s with a range of 118 to 1230 m^3/s (Cherlet, 2007). The Weser is has pluvio-nival[1] flow regime with high water flow in winter and low water flow from June to October (Galbiati et al., 2008). The geography of the region is shown in figures 2.1 and 2.2. For the protection of the hinterland (marsh) from flooding (stormsurge, tidal) a continuous line of dikes has been built next to the channel.

[1] The pluvio-nival flow regime is characterized by a period of rainfall in January, followed by a light increase in February-March, and low water in October (Musy and Higy, 2011).

Figure 2.1: The river Weser (LWL, 2018)

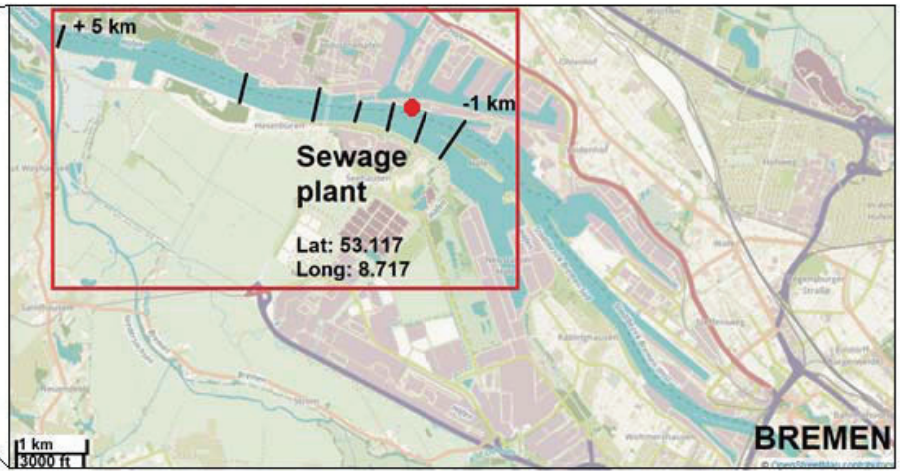

Figure 2.2: Weser River in the vicinity of the local WWTP. Red dot depicts the location of the measuring station Oslebshausen. Red rectangle indicates the sampling region (open street maps, 2017).

Lower Weser hydrology

The Inner Weser estuary has an approximate length of 70 km and width varying from 200 m up to 2 km (Grabemann et al., 1997). Despite of having many tributaries, due to significantly lower discharges than the main channel their discharges are considered negligible (Vandenbruwaene et al., 2013). It is strongly influenced by the North Sea tide up to a barrage located 4.5 km upstream of the Bremen city center (Unterwesser river km 0). The tidal range has changed significantly due to deepening of the Lower and Outer Weser and has increased since the first deepening at 1895 from approx. 0.2 m to a current level of 4.1 m at Bremen Oslebshausen (Kappenberg and Grabemann, 2001). In addition to deepening, various expansion measures and engineering structures were performed in the area leading to a mean water depth of 10 m as seen in figure 2.3.

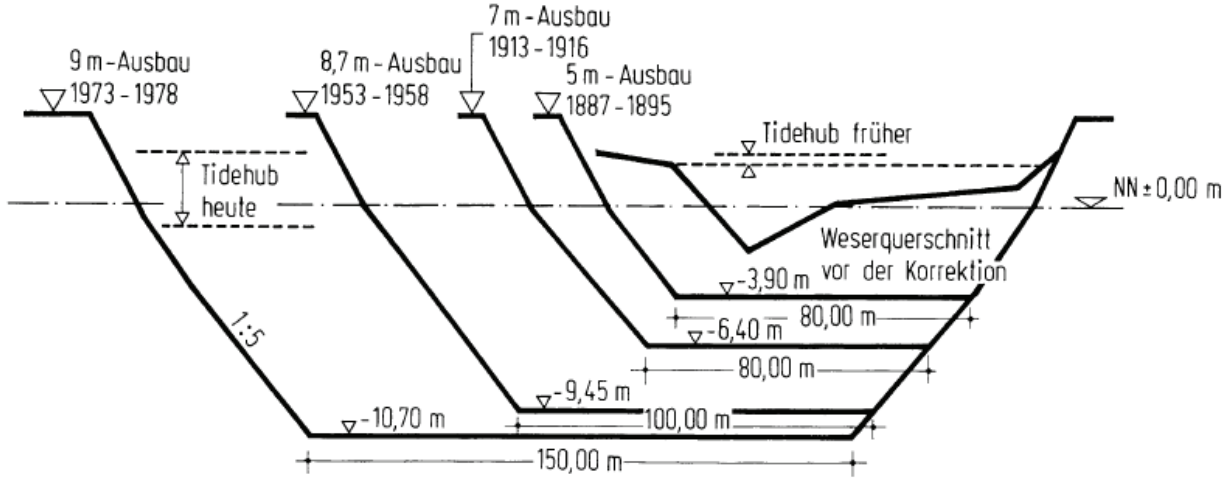

Figure 2.3: Successive deepening and widening of the Lower Weser (km 11/ Hasenbüren)(Herrling and Niemeyer, 2008).

The tides are semidiurnal (more information on §2.2) and the tidal wave slightly asymmetrical. This is due to friction at the bed and convergence of the estuary margins which lead to higher ebb current velocities and longer ebb duration (7 h and 20 min (van Rijn, 2011)) compared to the flood tide (5 h (van Rijn, 2011))(Wienberg, 2003).

Pollution and monitoring

Bremen State had already since 1928 taken measures against Weser River water pollution (keeping the salinity below certain values), since it was used for drinking and other purposes and the river had been seriously contaminated by waste water originating from potassium industries (Lammers, 1984). At 1989 the salinity of the river water varied between 0.6 and 2.0‰ depending on the discharge as a result of salt mining in the catchment area (Grabemann, 1989).

Since 1975, in the Weser River several water quality parameters are continuously monitored (chloride and other ions, metals, organic pollutants, oxygen concentration) but also water temperature and conductivity (FGG, 2017). Additionally hydrological data (such as discharge and water level height) are measured.

2.2 Tidal influence on Weser River

Tides are a result of the combined effects of the gravitational attractions and centrifugal forces within the Earth-Sun-Moon system. As tide we describe the rise and fall of the sea level and as tidal current the horizontal flow. Tides and tidal currents are superimposed on non-tidal rising and falling water levels (eg. cause by weather, seismic events, etc.) and non-tidal current (eg. river flow, floods, etc.) respectively.

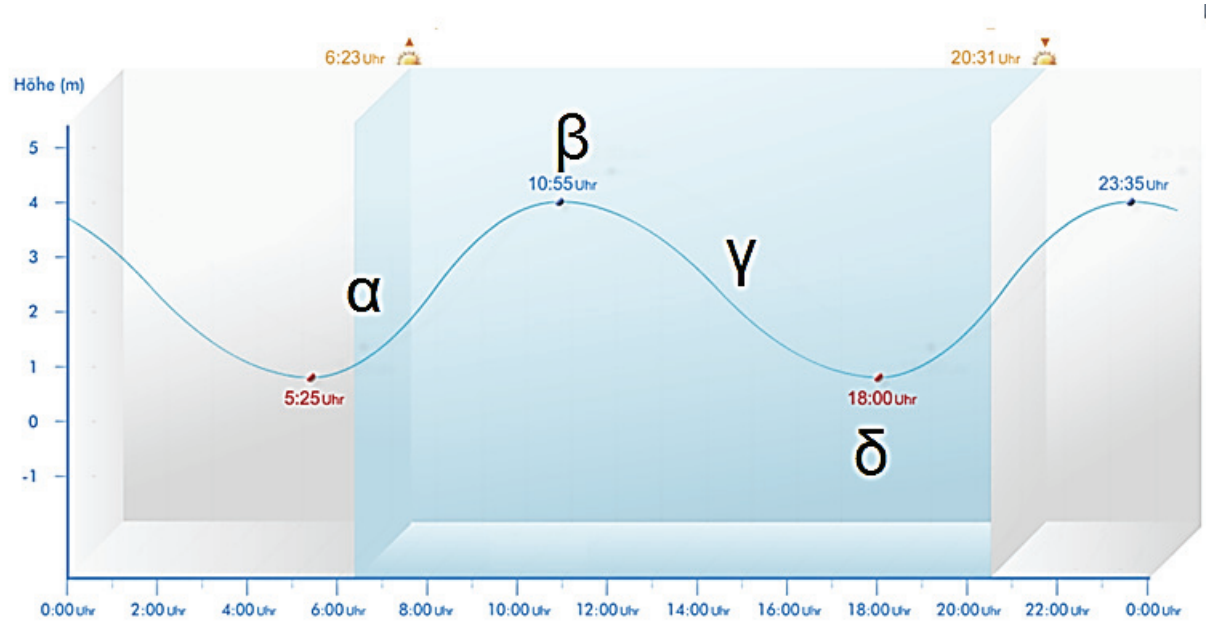

Figure 2.4: High and low tide in station Oslebshausen on 25.8.2015 (Gezeitenfisch, 2017).

At most places the tidal changes occur approximately twice a day. The sea level rises (α), covering the intertidal zone; flood tide. The water rises to its highest level, reaching high water (HW, β). Then the sea level falls (γ), revealing the intertidal zone; ebb tide, until it reaches low water (LW, δ).

The tides are classified as semidiurnal tides, with two high and two low water levels in each tidal day, such as the tides on Weser (figure 2.4), and with small differences between successive highs and lows. Apart from its type classification at a particular place, the tide exhibits many variations during the month. Approximately twice a month, during times of new and full Moon, with Earth, Moon and Sun aligning (figure 2.5), the tractive forces of the Sun and Moon are under constructive interference, resulting in the so called spring tides whose amplitudes are greater than average. Between the spring tides, during quarter moons, the tractive forces of the Sun and Moon are under destructive interference, resulting in the neap tides, with ranges less than average.

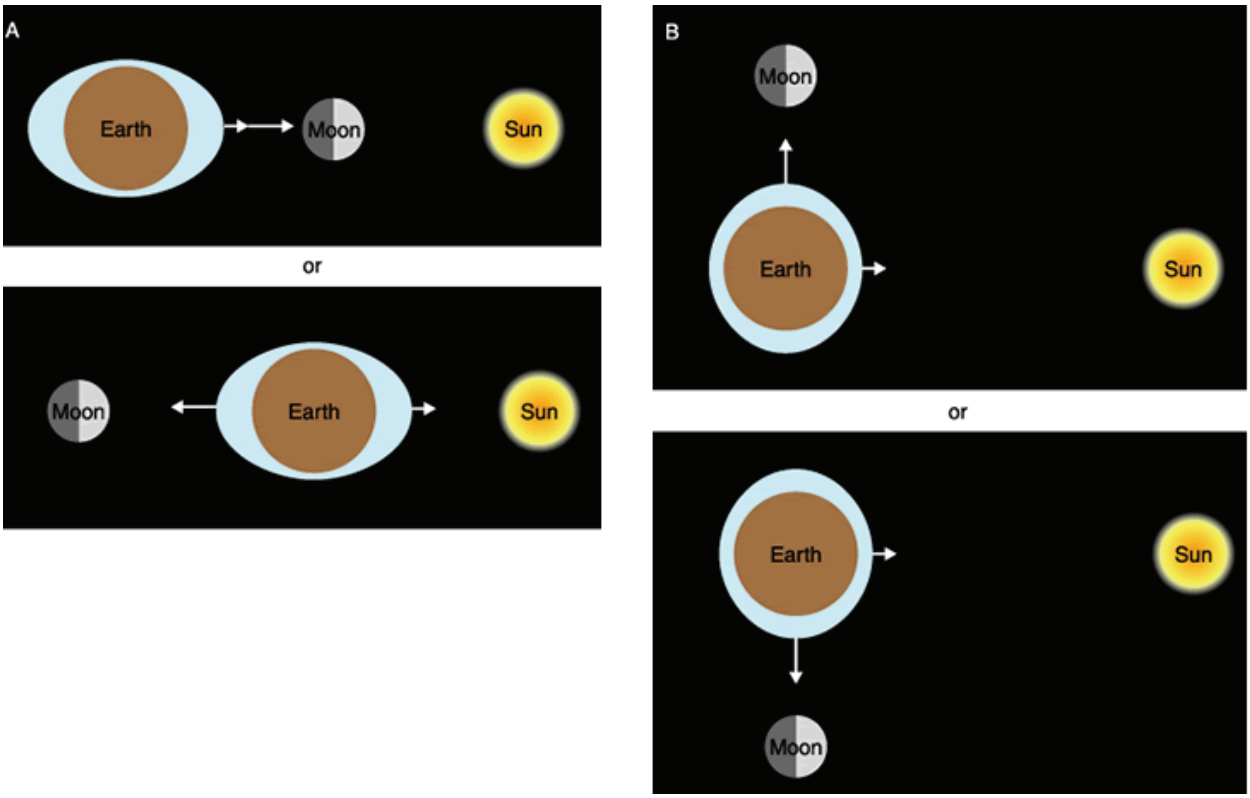

Figure 2.5: The configuration of Earth, moon and sun that is responsible for (A) spring tides and (b) neap tides (NASA , Physical Oceanography Program, 2018).

Other factors which influence the tidal range include the lunar altitude (changing distance separating Moon and Earth, minimum at perigee and maximum at apogee), solar gravitation effects, the obliquity (tilt) of the Earth's equator and rotational axis, the inclination of the plane of the lunar orbit, the elliptical shape of the Earth's orbit, Coriolis forces and land masses.

Mathematically, the tidal variations can be described as a sum of harmonic terms: any periodic motion can be resolved into a sum of a series of single harmonic motions:

$$h_i(t) = A_i \cos(\omega_i t + V_i)$$

With h_i the height of the partial tide calculated for time t, A_i the constituent amplitude (equal to one-half the constituent range). The angle $(\omega_i + V_i)$ changes uniformly and its value at any time is called phase of the constituent. The argument for the cosine includes two terms, the constituent speed or period (in solar hours), where speed=360^o/T with T the period, multiplied by time and V_i the constituent phase.

Each constituent represents a periodic change or variation in the relative positions of the Earth, Moon and Sun and by determining the tidal harmonics in one location, one can predict the tides at that place.

The most dominant tidal constituents are given in table 2.1.

Table 2.1: Most dominant tidal constituents (Parker, 2007)

Symbol	Tidal species	Period (hours)	Description
M2	Semidiurnal	12.42	Principal Lunar Semidiurnal Constituent
S2	Semidiurnal	12	Principal Solar Semidiurnal Constituent
N2	Semidiurnal	12.66	Larger Lunar Elliptic Semidiurnal Constituent
K1	Diurnal	23.93	Lunar-Solar Declinational Diurnal Constituent
O1	Diurnal	25.82	Lunar Declinational Diurnal Constituent
M4	Higher harmonics	6.21	First Overtide of M2 Constituent
M6	Higher harmonics	4.14	Second Overtide of M2 Constituent
S4	Higher harmonics	6	First Overtide of S2 Constituent
MS4	Higher harmonics	6.10	A Compound Tide of M2 and S2

For finding the harmonics (amplitude, period/speed and phase) of the constituents for the location Oslabshausen in Weser, the "Tidal fitting toolbox" by Aslak Grinsted was utilized, as a freely available software in Matlab, using as an input data (water level measured every minute) collected from the homonymous station obtained from the waterways and shipping board (Wasserstraßen- und Schifffahrtsverwaltung des Bundes, WSV, 2017) for the period 10th January 2016, 00:01 to 19th January 2016 23:51 (part of data available in Appendix 8). The HAMELS analysis (Harmonic Analysis, Method of Least Squares) fits each water level data set with the least error possible, giving the following values for the tidal constituents, presented in table 2.2.

Table 2.2: Harmonics obtained through the HAMELS analysis for Weser River – Station Oslebshausen

Harmonic Symbol	Period (period of tidal component in days)	Speed (frequency of tidal component in degrees per solar hour)	Amplitude (amplitude of the fitted component)	Phase (phase of the fitted component)
M2	0.5175	28.9841	0.6937	-2.3870
S2	0.5	30	0.0757	1.2876
N2	0.5274	28.4397	0.3134	2.5796
K1	0.9973	15.0411	0.0268	-2.0964
O1	1.0758	13.943	0.1116	1.4722
M4	0.2588	57.9682	0.2568	-0.2164
M6	0.1725	86.9523	0.1494	0.0004
S4	0.25	60	0.0085	0.7284
MS4	0.2543	58.9841	0.0775	-1.7686

In narrow bays the tidal wave entering from the open ocean gets reflected and creates a standing wave. Standing waves are composed of two waves of the same amplitude and wavelength travelling with the same speed in opposite directions:

$$n(x,t) = a\cos(kx - \omega t) + a\cos(kx + \omega t) = 2a\cos(kx)\cos(\omega t)$$

where we recall that the factor 2 comes from the constructive interference of an incoming and a reflected wave, each having the same amplitude.

Thus, the water lever is calculated as:

$$h(t)=2\cdot M2_{amp}\cdot\cos(360/M2_{phase})\cdot\cos(M2_{period}\cdot t) +$$
$$+\ 2\cdot S2_{amp}\cdot\cos(360/S2_{phase})\cdot\cos(S2_{period}\cdot t) +$$
$$+2\cdot N2_{amp}\cdot\cos(360/N2_{phase})\cdot\cos(N2_{period}\cdot t) +$$
$$+\ 2\cdot K1_{amp}\cdot\cos(360/K1_{phase})\cdot\cos(K1_{period}\cdot t) +$$
$$+\ 2\cdot O1_{amp}\cdot\cos(360/O1_{phase})\cdot\cos(O1_{period}\cdot t) +$$
$$+\ 2\cdot M4_{amp}\cdot\cos(360/M4_{phase})\cdot\cos(M4_{period}\cdot t) +$$
$$+\ 2\cdot M6_{amp}\cdot\cos(360/M6_{phase})\cdot\cos(M6_{period}\cdot t) +$$
$$+\ 2\cdot S4_{amp}\cdot\cos(360/S4_{phase})\cdot\cos(S4_{period}\cdot t) +$$
$$+\ 2\cdot MS4_{amp}\cdot\cos(360/MS4_{phase})\cdot\cos(MS4_{period}\cdot t)\ .$$

The goodness of the HAMELS fitting can be illustrated in figure 2.6, where the observed data, their fitting to the generated constituents and their residuals are shown.

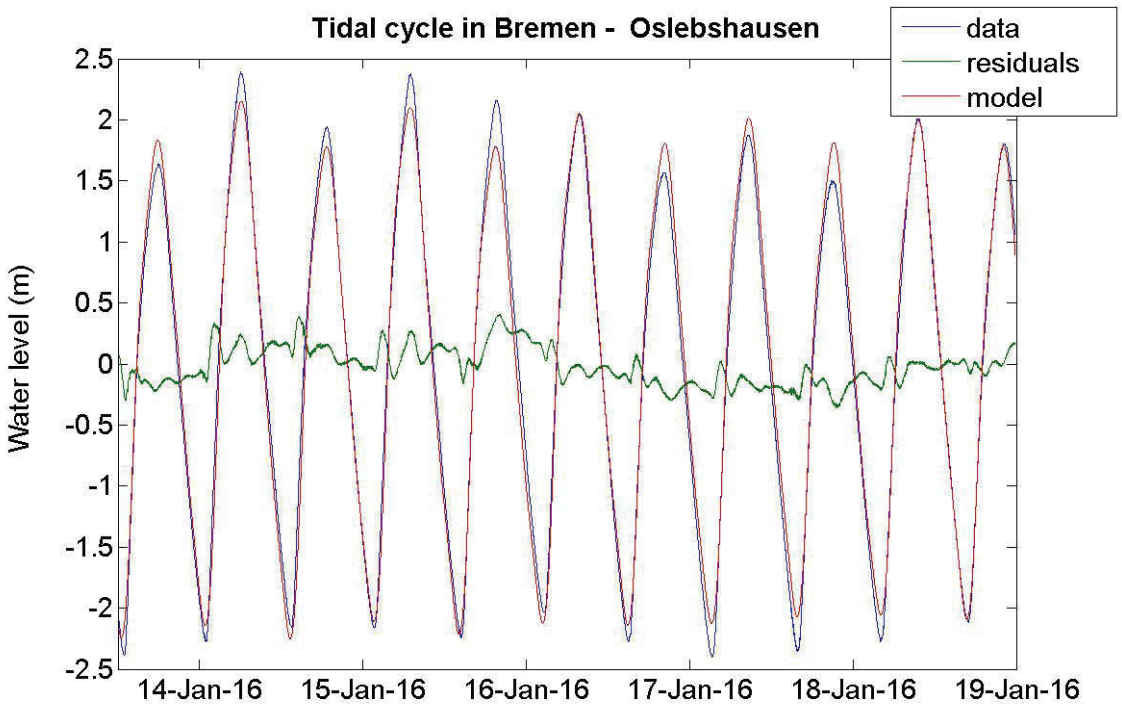

Figure 2.6: HAMELS fitting for observed data for the period 13-19 January 2016 in the station Oslebshausen.

These tidal constituents are also utilized in an effort of approximating the tidal generated currents. As tidal currents we refer to the horizontal movement of the water which accompanies the rise and the fall of the tide. One can derive mathematically (Sverdrup et al., 1942) the tidal current for a standing wave by disregarding the friction and rotation of the earth, assuming constant depth and the direction of progress of the tidal wave to be on the x-axis the equations of motion and continuity become:

$$\frac{\partial u_x}{\partial t} = -g\frac{\partial n}{\partial x} \text{ and } \frac{\partial n}{\partial t} = -h\frac{\partial u_x}{\partial x}$$

with u_x the horizontal velocity, g the acceleration of gravity, equal to 9.81m/s^2 and h the mean river depth, approximated to 12 m (Grabemann et al., 1997).

As mentioned before, for each constituent the water level would be:

$$n = 2a\cos(kx)\cos(\omega t) = n(x)\cos(\sigma t)$$

Then the velocity is derived as:

$$u_x = \frac{\partial n(x)}{\partial x}\frac{g}{\sigma}\sin(\sigma t) = -\frac{\partial n(x)}{\partial x}\frac{g}{\sigma}\cos\left(\sigma t + \frac{\pi}{2}\right)$$

$$\rightarrow u_x = -\frac{gk}{\sigma}2a\sin(kx)\cos\left(\sigma t + \frac{\pi}{2}\right) = -2a\sqrt{\frac{g}{h}}\sin(kx)\cos\left(\sigma t + \frac{\pi}{2}\right)$$

An example of a 48 hour tidal period for the simulation of water level and maximum horizontal tidal velocity for the location Oslebshausen using the harmonics from table 2.2 is given in figure 2.7. Negative values of the velocity indicate flow towards the upstream (Bremen city center) direction.

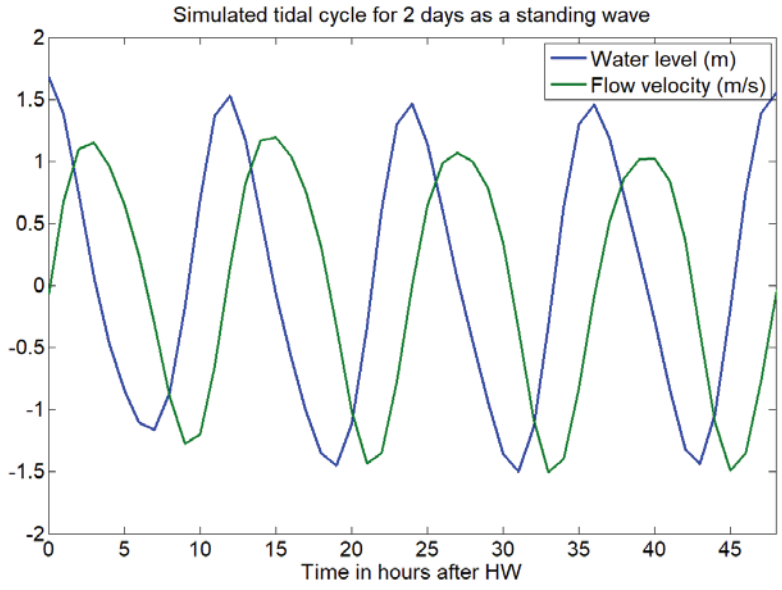

Figure 2.7: Simulated tidal cycle for 2 days as a standing wave for the station Oslebshausen. Maximum and minimum values of velocity approximately 3 hours after high and low water correspondingly.

2.3 The WWTP in Seehausen

The Bremen wastewater treatment plant *"Bremer Kläranlage Seehausen",* located 8 km downstream of the city center in the left bank of Weser River, went into operation in 1996 and since 1998 is operated by hanseWasser Bremen GMbH (Hansewasser, 2017a). It treats in daily basis approximately 130.000 m^3 of wastewater (during dry weather) of the entire city of Bremen region and neighboring communities, comprising a catchment area of 1 million population equivalent. In rainy weather, more than twice this value is treated. The largest part of waste water comes from the right bank of Weser and is conveyed through pressure pipes to the sewage treatment plant. The fed wastewater passes through a multi-stage (mechanical and biological) and a mean 45-hour cleaning process before its release in the Weser River with a mean discharge of 1.5 m^3/s (Hansewasser, 2017b). Considering a rectangular outflow channel with a width of 40 m (during high water) and depth of 4 m (see also Appendix 6) the mean discharge velocity is calculated equal to 9×10^{-3} m/s.

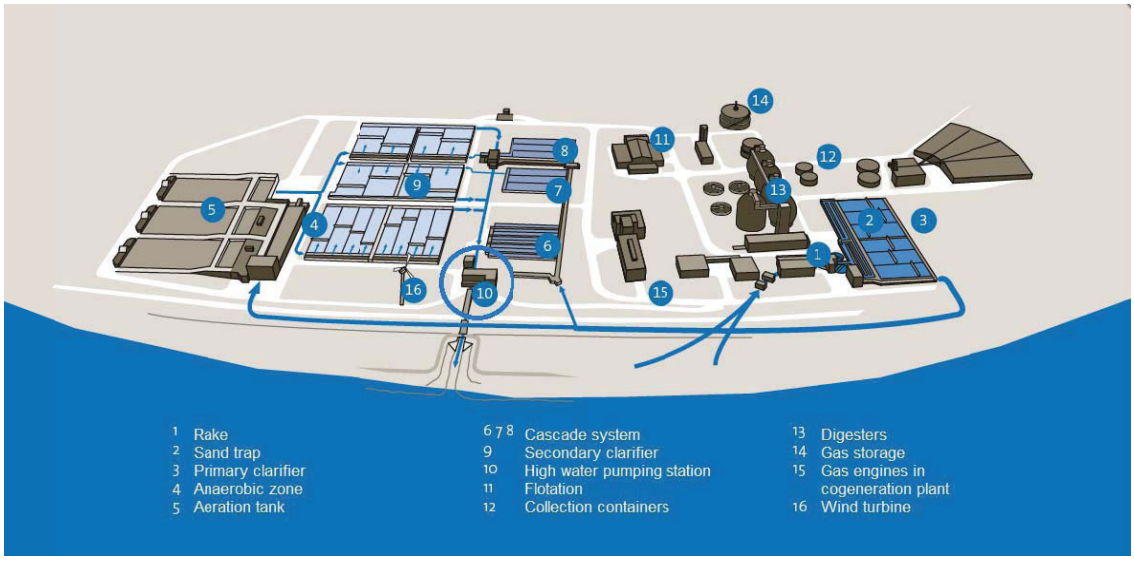

Figure 2.8: The WWTP Bremer Kläranlage Seehausen, marked location Nr.10 corresponds to the sampling point for all the effluent samples taken during this study (see Chapters 5 and 6) (adapted from *Hansewasser*, 2017b).

Hormann and Fischer (2016) reported after an 18 day sampling campaign in this specific WWTP, ^{131}I activity concentrations in the inflow between 0.33 and 1.31 Bq/L, with an average of 0.55 Bq/L and 0.21 to 0.64 Bq/L with an average of 0.36 Bq/L in the outflow. With approximately 35-45% circulating and decaying in the different compartments of the WWTP and around 48-66% released in the river water, only a small percentage ends up in the sludge with typical residence times of 3-15 days.

In the Radioactivity Measurements Laboratory in Bremen, in regular basis (approximately 4 times a year) effluent from local WWTP is measured for the German radioactivity surveillance network for environmental radioactivity "IMIS" (Weiss and Leeb, 1993), and its ^{131}I activity concentration was determined between 37 and 977 mBq/kg for the period 1994-2013 (see also Appendix 13).

2.4 Previous measurements of ^{131}I in Weser River

The interest on the ^{131}I environmental pathway in the Bremen city and consequently the Weser River developed upon the measurement of ^{131}I in river sediment in several consecutive routine samples taken within the framework of IMIS. Ulbrich[3] (2008) on her diploma thesis ("Transport von medizinischen Radionukliden mit dem Abwasser") successfully measured ^{131}I in Weser river bank sediments in both banks, up to distances of 20 km downstream and 6.5 km upstream with activity concentrations 0.45 ± 0.05 and 1.89 ± 0.16 Bq/kg (d.m.) respectively. Additionally she proved the medical origin of the isotope by sampling in the inflow and outflow of the WWTP. Following, another student of the group (P. Lysogne) performed measurements on Weser bank sediments detecting ^{131}I with activity concentration ranging between 0.38 ± 0.11 and 27.7 ± 1.1 Bq/kg (d.m.). During his study, the geographical range for both upstream and downstream directions was determined. Additionally, he collected a sample upstream the barrage, which contained no detectable amounts of ^{131}I, supporting the assumption that all the ^{131}I in the region originated from the Seehausen WWTP. These findings were thoroughly analyzed and presented by Fischer et al. (2009) on their paper "Medical radioisotopes in the environment – following the pathway from patient to river sediment". The ^{131}I profile reported along the river had a sharp maximum (122.3 ± 3.1 Bq/kg(d.m.)) at the discharge point of the WWTP and lower levels elsewhere, decreasing monotonically in the downstream direction. They also indicated the importance of the tidal current responsible for the iodine distribution in the upstream direction and concluded that a more systematic study would be required for a better insight into the dynamics of wastewater and fluvial systems.

In the Weser River water ^{131}I was more difficult to measure due to low activity concentrations (see Chapter 5) and a chemical extraction method had to be applied before measurement. Souti (2012) was able to detect it close to the left bank, up to 1.2 km downstream and 0.2 km upstream with activity concentrations 5.7 ± 2.6 and 21.9 ± 1.8 Bq/kg respectively.

[3] Exact locations and activity concentration values can be found in Appendix 10.

A further study in the area followed under the scope of the OSPAR project (Gellermann et al., 2013), where Weser was one of the four rivers (including Elbe, Ems and Rhine) covered by the project. River water and bank sediment samples were collected during the period 2012 to 2013. Sediment samples were collected in the downstream direction (locations 0, 6, 12 and 18 km of the WWTP), however except directly in the outflow of the WWTP where it was measured with a mean value of 28 Bq/kg(d.m.), in all other samples iodine was below detection limit. River water samples were collected in bimonthly basis in locations 9 km downstream and 14 km upstream the WWTP in both river banks with ranges of 0.7 to 3.4 and 1.3 to 4.1 Bq/kg correspondingly. Approximately in half of the samples ^{131}I was not present in values above the limit of detection. These values, however, may not be precise, since the chemical yield of the method used (Mundschenk, 1993) was not properly determined (see §5.3).

2.5 General comment on Chapter 2

In this chapter a general description of the study area was given. Weser River with the Bremen WWTP located on its left bank is strongly influenced by the North Sea tides leading to flow direction inversion 4 times a day. This results in detectable amounts of ^{131}I also upstream of the WWTP as reported in previous studies in the area. The continuous release of medical ^{131}I as an effluent from the WWTP allows us to use it as a readily available tracer with the aim of obtaining a better understanding on the distribution of radioisotopes in the water-sediment system.

2.6 References for Chapter 2

Cherlet M., 2007. *Experiences in Analysis of Pressures and Impacts from Agriculture on Water Resources and Developing a related Programme of Measures.* Report of the Pilot River Basin Group on Agriculture. Phase II period September 2005- December 2006. Retrieved from: http://ec.europa.eu/environment/water/water-framework/pdf/report_phase_2.pdf

Fischer H.W., Ulbrich S., Pittauerová D., Hettwig B., 2009. *Medical radioisotopes in the environment - following the pathway from patient to river sediment.* Journal of Environmental Radioactivity 200**,** 1079-1085.

Flussgebietsgemeinschaft Weser (FGG Weser) - (in German), (http://www.fgg-weser.de/, 2017).

Galbiati L., Somma F., Zaldivar-Comenges J.M., 2008. *Pilot River Basin Activity Report Phase II: 2005-2006. Water Framework Directive implementation pilot activities. Key challenges and recommendation from the Pilot River Basins.JRC Scientific and Technical Reports.* Retrieved from: https://publications.europa.eu/en/publication-detail/-/publication/abef8525-d759-43ab-92c5-893cbd142695

Gellermann R., Fischer H., Ulbrich S., Buchholz O., 2013. *Messtechnische und theoretische Abschätzung des Eintrags von I-131 in die OSPAR-Regionen aufgrund der nuklearmedizinischen Anwendungen von Radioiod in Deutschland.* Abschlussbericht. Vorhaben 3611S70013. Auftraggeber: Bundesamt für Strahleschutz. 02.12.2013.

Gezeitenfisch, 2017. http://www.gezeitenfisch.com/de/bremen/bremen-oslebshausen

Grabemann I., 1989. *Transport Processes of Suspended Matter Derived From Time Series in a Tidal Estuary.* Journal of Geophysical Research, 94, C10, 14373-14379.

Grabemann I., Uncles R.J., Krause G., Stephens J.A., 1997. *Behaviour of Turbidity Maxima in the Tamar (U.K.) and Weser (F.R.G.) Estuaries.* Estuarine, Coastal and Shelf Science, 45, 235-246.

Grinsted A., 2014, *Tidal fitting toolbox.* Retrieved from: https://de.mathworks.com/matlabcentral/fileexchange/19099-tidal-fitting-toolbox?requestedDomain=www.mathworks.com

HanseWasser, *2017a. https://www.hansewasser.de/wir-als-unternehmen/ueber-uns/historie.html*

HanseWasser, *2017b. https://www.hansewasser.de/wir-fuer-bremen/daseinsvorsorge-fuer-die-stadt/klaeranlagen.html*

Herrling G. and Niemeyer H.D., 2008. *Hydro- and Morphological Pressures and Impacts*, HARBASINS Report. Retrieved from: http://www.nlwkn.niedersachsen.de/download/70702.

Hormann V. and Fischer H.W.,2016. *A dynamic model for the transport of ^{131}I through a municipal wastewater treatment plant.* Paper presented at the 2nd International Conference on Radioecological Concentration Processes, Seville, Spain.

Kappenberg J. and Grabemann I., 2001. *Variability of the Mixing Zones and Estuarine Turbidity Maxima in the Elbe and Weser Estuaries.* Estuaries, 24, 5, 699-706.

Lammers J.G., 1984. *Pollution of International Watercourses.* Martinus Nijhoff Publishers.

LWL, 2018. Ladeschaftsverband Westfalien-Lippe. Image retrieved from: https://www.lwl.org/LWL/Kultur/Westfalen_Regional/Naturraum/Weser

Musy A. and Higy C., 2011.*Hydrology: A science of nature*. CRC Press.

Mundschenk H., 1993. *Procedure for determining radionuclides in surface water by gamma spectrometry,* C-γ-SPEKT-OWASS-01, Federal coordinating office for surface water, suspended particulate matter and sediment in inland waters.

NASA, Physical Oceanography Program, 2018. Image retrieved from: http://oceanmotion.org/html/background/tides-types.htm

Parker B.B., 2007. *Tidal Analysis and Prediction*. NOAA Special Publication NOS CO-OPS 3. Retrieved from: https://tidesandcurrents.noaa.gov/publications/Tidal_Analysis_and_Predictions.pdf

Souti M.E., 2012. *Medical ^{131}I in Weser water*, Universität Bremen, Faculty of Environmental Physics, Master Thesis. Retrieved from: http://www.iup.uni-bremen.de/PEP_master_thesis/thesis_2012/master_thesis_souti.pdf.

Sverdrup H.U., Johnson M.W., Fleming R.H., 1942. *The Oceans Their Physics, Chemistry and General Biology.* Prentice-Hall Inc.

Ulbrich S., 2007. *Transport von medizinischen Radionukliden mit dem Abwasser.* Universität Bremen, Faculty of Environmental Physics, Diploma Thesis.

Van Rijn L.C., 2011. *Comparison Hydrodynamics and Salinity of Tide Estuaries; Elbe, Humber, Schelde and Weser.*EU Project 1203583-00.Retrieved from: *www.vliz.be/imisdocs/publications/227966.pdf*.

Vandenbruwaene W., Plancke Y., Verwaest T., Mostaert F., 2013. *Interestuarine comparison: hydrogeomorphology. Hydro- and geomorphodynamics of the TIDE estuaries Scheldt, Elbe, Weser and Humber.* Version 4. WL Rapporten, 770_62b. Flanders Hydraulics Research: Antwep, Belgium. Retrieved from: http://www.tide-project.eu/downloads/WL2013R770_62b_rev4_20130220_TIDE_IC_HGM.pdf

Weiss W. and Leeb H., 1993. *IMIS- the German integrated radioactivity information and decision support system.* Radiation ProtectionDosimetry50,163-170.

Wienberg C, 2003. *The impact of dredge spoil dumping on coastal morphodynamics monitored by high-resolution acoustic measuring instruments (outer Weser Estuary, German Bight).* Doctoral dissertation, University of Bremen. Retrieved from: https://elib.suub.uni-bremen.de/diss/docs/E-Diss663_1.pdf.

WSV, 2017. *Wasserstraßen- und Schifffahrtsverwaltung des Bundes,* https://www.wsv.de/

Chapter 3

Modeling in rivers

River flow, sediment and contaminant transport are complex phenomena in nature. It is a very difficult task finding analytical solutions to most problems in river engineering and many models have been developed for this purpose. However, the basic principles are well established and presented in this chapter.

3.1 Existing models

Several models have been developed for predicting the migration of contaminants/radionuclides through rivers. The modeling of the behavior and effect of contaminants in the river requires a quantitative description of hydraulic, geo-chemical, sedimentological, ecological and anthropogenic phenomena (Monte et al., 2005).
In principle the structure of these models is based on 2 basic sub-models:
- hydrological submodel for predicting the hydrological factors which influence the contaminant migration processes, and
- radionuclide/contaminant submodel for predicting the transfer through the water and/or bottom sediments.
In some cases the models could include modules for predicting the doses to man and effects of countermeasures aimed to reduce these doses.

In the following section an overview and the fundamental characteristics of several models are presented.

Aquascope(Smith et al.,2005): Aquascope is a simplified model for predicting ^{89,90}Sr, ^{131}I and ^{134,137}Cs in surface water after a large scale radioactive fallout. It is designed for the long term assessment following deposition on the catchment area and gives averaged estimates for radionuclides in water bodies and fish.

Casteaur (Boyer and Beaugelin-Seiller, 2002): The one-dimensional Casteaur model is an operational tool to assess the impact of both accidental and routine radioactive releases on fluvial ecosystems. It includes processes of transport, diffusion, migration to sediments and uptake by fish for several fission products (eg. ^{60}Co, ^{137}Cs, etc).

Moira (Monte et al., 2001): Moira is a model-based computerized system, which identifies optimal remedial strategies for restoring radionuclide contaminated aquatic ecosystems and

drainage areas. This one-dimensional model provides monthly averages for Sr and Cs radioisotopes and includes processes of migration, transport and uptake by fish.

Rivtox (Zheleznyak et al.,2003): Rivtox, part of the RODOS[1] decision support system for nuclear emergencies, is an one-dimensional model for the simulation of the transport of radionuclides in a network of river channels. The model solves the diffusion - transport equation for fission products and natural occurring radioactive materials (NORM) and calculates the radionuclide migration to sediment by both numerical and analytical methods.

Threetox (Margvelashvili et al., 2000): Another model part of RODOS is Threetox, a numerical model which simulates the three dimensional dispersion of radionuclides in stratified water bodies (lakes, reservoirs estuaries and coastal ocean). It is an advanced surface water modeling system for hydrodynamics, sediment and radionuclide transport most appropriate for short-term and local prediction of radionuclide transport after release.
Both Rivtox and Threetox are available for download from the official RODOS-homepage for internal usage.

EFDC- Environmental Fluid Dynamics Code (EPA, 2007): EFCD is a multifunctional surface water modeling system, capable of 1, 2 and 3 dimensional spatial resolution which includes hydrodynamic, sediment, contaminant and eutrophication components. It requires several input files (grid and physical process specification, general data, control and initialization files and time series forcing and boundary condition files) for the configuration of the model. Despite the fact that it is freely available for download for Windows XP or older system versions, the configuration procedure makes it complicated to use.

River-2D (University of Alberta): Another freely available model is the River2D, a two-dimensional depth averaged model of river hydrodynamics and fish habitat. It is applicable on a limited length of the channel, typically less than ten channel widths and requires a variety of input data, such as channel bed topography, roughness, boundary and initial flow conditions. Despite its sophistication it does not include a sedimentation module.

Delft3D (Deltares Open Software): Delft3D is a modeling suite which investigates 3 dimensional hydrodynamics, sediment transport and morphology, and water quality for fluvial, estuarine and coastal environments. It is a product of Deltares, an independent institute for applied research in the field of water and subsurface. Several of its modules (flow, morphology and waves) are available in open source.

[1] RODOS is a Real-Time On-line Decision Support system for off-site emergency management in Europe. Additional information can be found in RODOS-homepage: https://resy5.iket.kit.edu/RODOS/

MIKE (Powered by DHI): MIKE is a range of software products which enable the analysis, modeling and simulation of water environments. Some of the products include 2 and 3 dimensional modeling of coast, see and river basin management, planning, data management decision and operational forecasting.

SMS– Surface-water Modeling System (Aquaveo): SMS includes several model systems for riverine and coastal simulations, a variety of numerical methods in 1 and 2 dimensions and different modules for the simulation of flow, contaminant and sediment transport.

In general the one-dimensional models describe the cross-sectional averaged flow and contaminant parameters in channels and are applicable in downstream distances from the source where the contaminant has a uniform distribution over the river cross-section.
The commercial models (Delft3D, SMS and MIKE) include not only submodels for hydrology, contaminants and sediments but also modules for tidal prediction and unstable water flows, making them more suitable in our case (see §2.1), especially since their dimensionality (2 or 3D) allows both near and far field contaminant/radionuclide predictions. On the other hand, these state of the art models require a variety of input, such as topographical maps, elevation and bathymetry data, geological and morphological information, etc, and although packaged with several user interfaces can become rather complicated to use. For this reason, the aforementioned companies offer apart from the software manuals, several webinars, training courses, on-site trainings, tutorials and consulting services for their customers.
Aside from their complexity or dimensionality, the physical processes on which all the aforementioned models are based, are well known. The equations describing the hydrological, contaminant and sediment transport processes are presented in several papers for the 1 dimensional (Smith et al., 2005, Semizhon et al., 2010, Krylov et al., 2007) or 2 and 3 dimensional (Perianez, 2004, Modenesi et al., 2004, Wang, 2004) cases. Regrettably, in the above literature, hydrodynamic equations do not consider tidal influenced flows, which increase the complexity of the equations. Papers dealing with the tidal influence on hydrological parameters (Wenli et al., 2010, Banda et al., 2009, Zhan, 2003) do not include a mathematical description of the sedimentation processes and transport.
As already stated the models Aquascope, Castreaur, Moira, Rivtox, EFDC and River-2D are not suitable in our case, the model Threetox is available for internal usage and the models Delft3D, MIKE and SMS are expensive commercial models, complicated to use. Additionally Mike and SMS provide single user license and Delft3D has limited support time. Open source software could be used from multiple users and in a variety of projects. Thus a model for predicting the dispersion of ^{131}I in Weser River (possibly applicable also in emergency situations) was developed[2].

[2] The model developed during this work is already used for a master work on ^{131}I in the Hunte River.

3.2 Model description and governing equations

3.2.1 Model description

Monte et al. (2005) name 3 main processes which control the migration of contaminants in rivers:

1. Transport caused by the water current;
2. Diffusion of the dissolved pollutant within the water due to thermal molecular movements and to the turbulent motion of water (eddy diffusion);
3. Interaction of pollutant with sediment and suspended matter and consequent transport.

Guided by these processes and considering the models described by Zheleznyak et al (2003) and Perianez (2004) a model for predicting the dispersion of ^{131}I in Weser River was developed. It consists of two major sub-models; the hydrodynamic sub-model and the radionuclide transport sub-model which is further subdivided for the components of river water and sediments (figure 3.1).

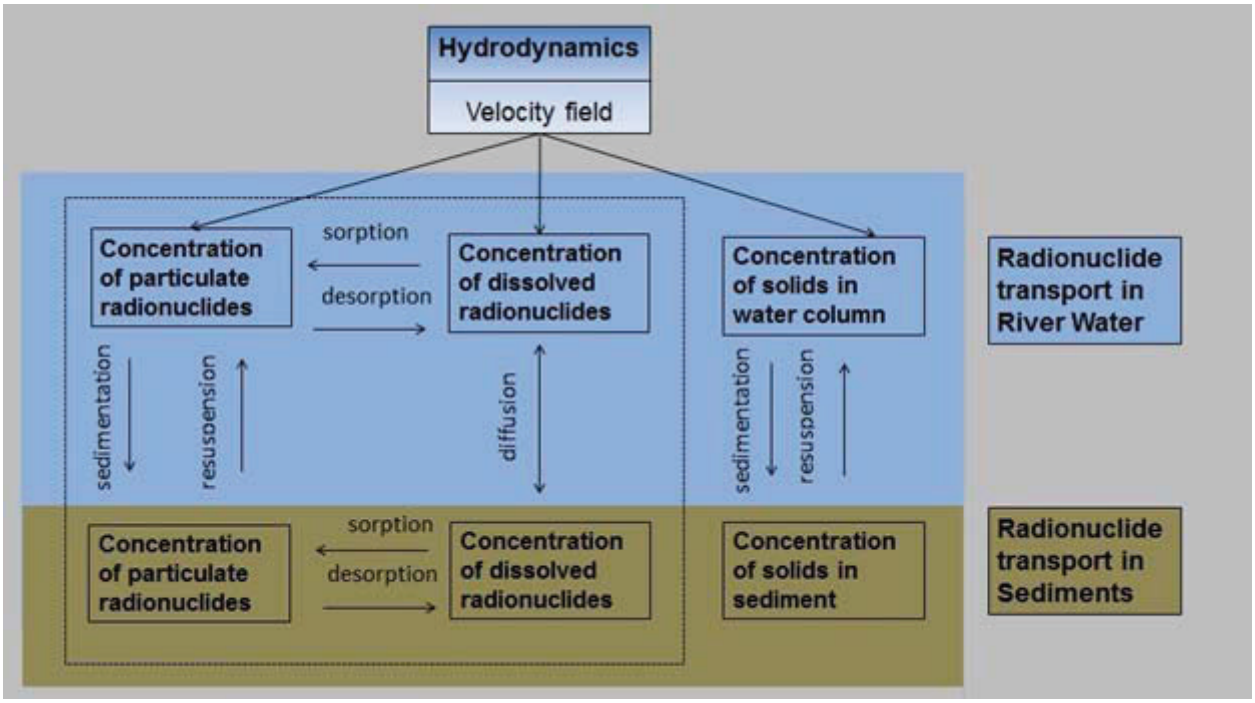

Figure 3.1: Scheme of the model including information on the hydrodynamic and radionuclide transport sub-models (blue represents the river water and brown the sediments).

Hydrodynamics sub-model: The hydrodynamics sub-model calculates the velocity field in the river domain by solving numerically the 2 dimensional steady state Navier Stokes equations implemented on Matlab with the aid of the IFISS (Incompressible Flow & Iterative Solver Software) software package (Silvester et al., 2015). The tidal influence on the velocity field is estimated by calculating maximum current speed and water level for standing waves (see §2.2).

Radionuclide transport sub-model: The radionuclide transport is described by the advection-diffusion equation taking into account the exchanges between radionuclide concentration in solute, suspended sediments and bottom deposition specified by the processes of adsorption-desorption, sedimentation-resuspension and mass transfer between the water column and the pore water of bed sediment. In addition, first order degradations are taken into account describing the radioactive decay.

Although flow and sediment transport are 3 dimensional phenomena, which should be more realistically simulated using 3 dimensional models, due to being time-consuming, simplifications such as section-, depth- and width averaging allow the use of 2 dimensional models which achieve feasible solutions in engineering practices (Wu, 2008). In the case of the Weser river, the deepening and widening of the waterway (see figure 2.3), provides constant depth along the modelled area allowing us to use a 2 dimensional model.

The model dataset includes initial data, boundary information and data representing the parameters of the calculation as input and provides the 2 dimensional (horizontal) fields of velocity and radionuclide concentration in river water as well as radionuclide concentration in river bank sediments for selected locations as output.

3.2.2 Governing equations

3.2.2.1. Hydrodynamics

The Navier Stokes equations are describing the motion of fluids and may be used to model weather, the movement of air in the atmosphere, ocean currents, water flow, air flow around a wing, as well as many other fluid flow phenomena. Basically, they are the continuity equations derived from the conservation principles of mass, momentum and energy.

The conservation form of the equations of continuum motion for a Newtonian fluid[4], also known as Cauchy momentum equation, is:

$$\frac{\partial}{\partial t}(\rho \mathbf{u}) + \nabla \cdot (\rho \mathbf{u} \otimes \mathbf{u}) = -\nabla \cdot P\mathbf{I} + \nabla \cdot \boldsymbol{\tau} + \rho \mathbf{f} \qquad \textit{eq. 3.1}$$

where ρ the fluid density, $\mathbf{u}$ the flow velocity and $\mathbf{u} \otimes \mathbf{v} = \mathbf{u}\mathbf{v}^T$[3] its outer product, P is the pressure, $\boldsymbol{\tau}$ the deviatoric stress tensor[5], $\mathbf{f}$ the body acceleration acting on the fluid (eg. gravity, inertial acceleration, electrostatic acceleration etc.), ∇ is the divergence and $\mathbf{I}$ the identity matrix. For incompressible flows of isotropic and homogeneous fluids the following assumptions can be made:

- The density is constant with respect to both time and spatial coordinates, hence $\nabla \cdot \mathbf{u} = 0$.
- The stress does not depend directly on the flow velocity but on the spatial derivatives of the flow velocity, thus the stress variable is the tensor gradient $\nabla \mathbf{u}$.
- The fluid is isotropic and consequently $\boldsymbol{\tau}$ is an isotropic tensor and can be expressed in terms of the dynamic viscosity μ[6]: $\boldsymbol{\tau} = 2\mu\boldsymbol{\varepsilon}$, where $\boldsymbol{\varepsilon} = \frac{1}{2}\left(\nabla \mathbf{u} + \nabla \mathbf{u}^T\right)$ is the rate of strain tensor, so $\boldsymbol{\tau} = \mu\left(\nabla \mathbf{u} + \nabla \mathbf{u}^T\right)$. Since the fluid is incompressible the divergence of the stress is $\nabla \boldsymbol{\tau} = 2\mu \nabla \cdot \boldsymbol{\varepsilon} = \mu \nabla \cdot \left(\nabla \mathbf{u} + \nabla \mathbf{u}^T\right) = \mu \nabla^2 \mathbf{u}$.

[3] As Newtonian fluids we describe fluids whose viscous stresses arising from their flow are linearly proportional to the local strain rate (rate of change of deformation over time) at every point.

[4] The divergence of the outer product equals: $\nabla(\mathbf{u} \otimes \mathbf{u}) = (\nabla \cdot \mathbf{u})\mathbf{u} + (\mathbf{u} \cdot \nabla)\mathbf{u} = \mathbf{u} \cdot \nabla \mathbf{u}$ for incompressible flow

[5] The stress tensor, $\boldsymbol{\sigma}$ ($\boldsymbol{\sigma} = -P\mathbf{I} + \boldsymbol{\tau}$), can be expressed as a sum of a mean hydrostatic stress tensor (pressure) which tends to change the volume of the stressed body and a deviatoric stress $\boldsymbol{\tau}$, which tends to distort it and for incompressible flow is only a shear effect.

[6] The dynamic (shear) viscosity expresses the resistance of a fluid to shearing flows.

The equation 3.1 under these assumptions and by introducing the kinematic viscosity $v = \frac{\mu}{\rho}$ and absorbing the constant density into the pressure $p = \frac{P}{\rho}$ takes the following form:

inertia per volume *divergence of stress*

$$\overbrace{\frac{\partial \mathbf{u}}{\partial t} + \mathbf{u} \cdot \nabla \mathbf{u}}^{} - \overbrace{v \nabla^2 \mathbf{u}}^{} = -\nabla p + \mathbf{f} \qquad \textit{eq. 3.2}$$

The term $\frac{\partial \mathbf{u}}{\partial t}$ describes the variation on time, $\mathbf{u} \cdot \nabla \mathbf{u}$ the convection and $v \nabla^2 \mathbf{u}$ the diffusion, while the terms ∇p and $\mathbf{f}$ define the internal and external sources respectively.
In the situation of steady state conditions, the time-derivative term is zero, thus:

$$\mathbf{u} \cdot \nabla \mathbf{u} - v \nabla^2 \mathbf{u} = -\nabla p + \mathbf{f} \qquad \textit{eq. 3.3}$$

$$\nabla \cdot \mathbf{u} = 0 \qquad \textit{eq. 3.4}$$

Equation 3.3 along with the continuity equation (eq. 3.4) are collectively known as the steady state Navier-Stokes equations. In two dimensions the velocity, $\mathbf{u} = (U, V)$, along with the pressure are 3 unknown variables. Since we also have 3 equations to describe our system, for a well-defined problem one has to set also boundary conditions (in the case of the unsteady state Navier Stokes equations one must also set initial conditions; the velocity field at the initial time $\mathbf{u}(t = 0) = \mathbf{u_0}$).

Non-dimensional form of Navier-Stokes equations

The Navier-Stokes equations often are put in a non-dimensional form by normalizing the system (equations 3.3 and 3.4) with respect to the size of the domain ($\mathbf{x}^* = \frac{\mathbf{x}}{L}$) and the magnitude of the velocity ($\mathbf{u}^* = \frac{\mathbf{u}}{U_0}$). Accordingly the pressure is selected as $p^* = \frac{p}{U_0}$ leading to:

$$\mathbf{u}^* \cdot \nabla \mathbf{u}^* - \frac{1}{\mathrm{Re}} \nabla^2 \mathbf{u}^* = -\nabla p^* + \frac{L}{U_0^2} \mathbf{f} \qquad \textit{eq. 3.5}$$

and

$$\nabla \cdot \mathbf{u}^* = 0 \qquad \textit{eq. 3.6}$$

where the relative contributions of convection and diffusion are defined by the Reynolds number, $\mathrm{Re} := \frac{U_0 L}{\nu}$. If Re ≤ 1 then the flow is diffusion dominated and its solution uniquely defined. In contrast for Re >> 1 the flow problem is convection dominated.

The system (eq. 3.5 - 3.6) is supplemented by the boundary conditions; Dirichlet[7] ($\partial\Omega_D$) or Neumann[8] ($\partial\Omega_N$) boundaries, where the boundary is such that $\partial\Omega = \partial\Omega_D \cup \partial\Omega_N$ and $\partial\Omega_D \cap \partial\Omega_N = \emptyset$.

Due to their complexity these equations only admit a limited number and simplified analytical solutions, eg. flow between two parallel plates or flow in a circular pipe, while numerical methods (see §3.3) have to be applied in more complicated geometries.

[7] The Dirichlet or first type boundary condition specifies the values that a solution needs to take along the boundary of the domain. It is called an essential boundary condition. Imposing a Dirichlet boundary condition in a one dimensional domain (eg. a metal bar) is fixing the value for the temperature for the solution in that edge.

[8] The Neumann or second type boundary conditions specifies the values in which the derivative of a solution is applied within the boundary of the domain. It is called a natural boundary condition. Imposing a Neumann boundary condition in a one dimensional domain (eg. a metal bar) is fixing the value for the flux of heat through that edge; if the Neumann boundary condition is set to zero it means that the edge is isolated and no flux enters or exits the bar.

3.2.2.2 Radionuclide transport

The processes governing the radionuclides transport and reactions in rivers may be simulated in one, two or three dimensions depending on the application desired. In general, a contaminant injection at the bank of the river will be mixed laterally and vertically and get transported by current velocity (downstream or upstream depending on the flow conditions and in the lateral direction). Assuming the contaminant is completely mixed in the vertical direction (see § 6.5.2), the conservation of mass for a radionuclide around a control volume $h\Delta x\Delta y$, where h the depth of the water column in m, yields the advection-reaction-dispersion equation:

$$\frac{\partial C}{\partial t} = \underbrace{-u_i \frac{\partial C}{\partial x_i}}_{\text{advective transport}} + \underbrace{\frac{\partial}{\partial x_i} E_i \frac{\partial C}{\partial x_i}}_{\text{dispersive transport}} \pm R \qquad \textit{eq. 3.7}$$

with

C = radionuclide concentration, Bq/L
t = time, s
E_i = dispersion coefficient in the x, y directions
u_i = average velocities in the x, y directions, m/s
R =reaction terms
x = longitudinal distance, m
y = lateral distance, m

The total concentration in water, $C_{T,w}\,(Bq/L)$, and in bed sediment, $C_{T,b}\ (Bq/L)$ are expressed as the sum of the soluble and particulate concentrations: $C_{T,w} = C_{s,w} + C_{p,w}$ and $C_{T,b} = C_{s,b} + C_{p,b}$ correspondingly, with $C_{s,w}\ (Bq/L)$ and $C_{s,b}\ (Bq/L)$ the soluble radionuclide concentration in water column and sediment and $C_{p,w}\ (Bq/L)$ and $C_{p,b}\ (Bq/L)$ the particulate radionuclide concentration in water column and sediment accordingly.

Considering the role of water/sediment partitioning and processes of sedimentation/resuspension, adsorption/desorption and radioactive decay, as illustrated in figure 3.1 and assuming no additional source terms for the soluble ($C_{s,w}$) and particulate adsorbed ($C_{p,b}$) radionuclides and suspended solids (S_w) to the water column, the final set of six equations adapted from Schnoor, (1996) in accordance to eq. 0-95 (Chapter 7.4) become:

$$\frac{\partial C_{s,w}}{\partial t} = -u_x \frac{\partial C_{s,w}}{\partial x} + \frac{\partial}{\partial x}\left(E_x \frac{\partial C_{s,w}}{\partial x} \right) - u_y \frac{\partial C_{s,w}}{\partial y} + \frac{\partial}{\partial y}\left(E_y \frac{\partial C_{s,w}}{\partial y} \right)$$
$$- k_1 C_{s,w} S_w - \lambda C_{s,w} + k_2 C_{p,w} + \frac{k_L}{h}\left(C_{s,b} - C_{s,w} \right)$$

eq. 3.8

$$\frac{\partial C_{p,w}}{\partial t} = -u_x \frac{\partial C_{p,w}}{\partial x} + \frac{\partial}{\partial x}\left(E_x \frac{\partial C_{p,w}}{\partial x} \right) - u_y \frac{\partial C_{p,w}}{\partial y} + \frac{\partial}{\partial y}\left(E_y \frac{\partial C_{p,w}}{\partial y} \right)$$
$$- k_s C_{p,w} + \alpha \frac{S_b r}{\gamma} + k_1 C_{s,w} S_w - k_2 C_{p,w}$$

eq. 3.9

$$\frac{\partial S_w}{\partial t} = -k_s S_w + \frac{\alpha}{\gamma} S_b - u_x \frac{\partial S_w}{\partial x} + \frac{\partial}{\partial x}\left(E_x \frac{\partial S_w}{\partial x} \right) - u_y \frac{\partial S_w}{\partial y} + \frac{\partial}{\partial y}\left(E_y \frac{\partial S_w}{\partial y} \right)$$

eq. 3.10

$$\frac{\partial C_{s,b}}{\partial t} = -k_3 C_{s,b} S_b + k_4 r S_b - \lambda C_{s,b} - \frac{k_L}{d}\left(C_{s,b} - C_{s,w} \right)$$

eq. 3.11

$$\frac{\partial r}{\partial t} = k_3 C_{s,b} - k_r r + k_s \frac{C_{p,w}\gamma}{S_b} - \alpha r$$

eq. 3.12

$$\frac{\partial S_b}{\partial t} = k_s S_w \gamma - \alpha S_b$$

eq. 3.13

Where

$C_{s,w}$ = soluble radionuclide concentration in the water column, Bq/m^3

$C_{p,w}$ = particulate radionuclide concentration in the water column, Bq/m^3

$C_{s,b}$ = soluble radionuclide concentration in the sediment, Bq/m^3

$C_{p,b}$ = particulate radionuclide concentration in the sediment, Bq/m^3

S_b =solids concentration in the bed, kg/m^3

S_w =solids concentration in the water column, kg/m^3

r =radionuclide concentration in sediments, Bq/kg(d.m.)

t = time in seconds

u_x = the longitudinal component of the velocity field, m/s

u_y = the lateral component of the velocity field, m/s

x = the longitudinal (downstream) distance, m

y = the lateral distance from the left bank, m

E_x =the longitudinal dispersion coefficient, m^2/s

E_y =the lateral dispersion coefficient, m^2/s

k_1 = adsorption rate constant from dissolved to particulate concentration in water, $m^3kg^{-1}s^{-1}$

k_3 = adsorption rate constant from dissolved to particulate concentration in sediment, $m^3kg^{-1}s^{-1}$

k_2 = desorption rate constant from dissolved to particulate concentration in water, s^{-1}

k_4 = desorption rate constant from dissolved to particulate concentration in sediment, s^{-1}

λ = the radioactive decay constant, s^{-1}

k_L = the mass transfer coefficient between water column and pore water of bed sediment, m/s

k_s = the sedimentation rate (v_w / h , mean particle settling velocity divided by depth h), s^{-1}

α = the scour/resuspension rate, s^{-1}

d =depth of active sediment layer, m

γ =ratio of water depth to depth of active sediment layer

Under the assumption of instantaneous equilibrium, the amount of radionuclide that is sorbed to the bottom sediments can be related to the dissolved radionuclide concentration using a linear adsorption isotherm (at low concentrations, adsorption is a linear process, where the amount adsorbed is directly proportional to the amount in solution (Mohr et al., 2010)) and the sediment/water partition coefficients can be expressed as the ratio of the adsorption rate constant to the desorption rate:

$K_{p,w} = \frac{k_1}{k_2}$ and $K_{p,b} = \frac{k_3}{k_4}$ with $K_{p,w}$ and $K_{p,b}$ are the partition coefficients (kg/m^3) in the water column and in the bed respectively.

The scour coefficient, with the assumption of constant solids concentration in the river and the bed, is calculated through steady-states conditions ($\frac{dS_b}{dt} = 0$) to be equal to $\alpha = \frac{k_s S_w \gamma}{S_b}$.

Assuming constant horizontal eddy diffusivity[9] (E) in the same manner as Margvelashvili et al., (2000) and Perianez (2004), the six compartment model can be reduced to a system of 2 differential equations describing the activity concentration of the radionuclide in the water column and sediments (Schnoor, 1996):

x-direction advection dispersion; y-direction advection dispersion

$$\frac{\partial C_T}{\partial t} = -u_x \frac{\partial C_T}{\partial x} + E\frac{\partial^2 C_T}{\partial x^2} - u_y \frac{\partial C_T}{\partial y} + E\frac{\partial^2 C_T}{\partial y^2}$$

$$-\underbrace{\lambda\left(\frac{C_T}{1+K_{p,w}S_w}\right)}_{\text{radioactive decay}} - \underbrace{k_s\left(\frac{K_{p,w}S_w}{1+K_{p,w}S_w}\right)C_T}_{\text{sedimentation}} + \underbrace{\frac{k_L}{h}\left(\frac{r}{K_{p,b}} - \frac{C_T}{1+K_{p,w}S_w}\right)}_{\text{pore-water diffusion}} + \underbrace{\alpha\frac{S_b r}{\gamma}}_{\text{resuspension}} \qquad \textit{eq. 3.14}$$

radioactive decay; sedimentation; resuspension

$$\frac{\partial r}{\partial t} = -\lambda\frac{r}{\left(1+K_{p,b}S_b\right)} + k_s\left(\frac{K_{p,w}S_w/\left(1+K_{p,w}S_w\right)C_T\gamma}{\left(S_b+1/K_{p,b}\right)}\right) - \alpha S_b\frac{r}{\left(S_b+1/K_{p,b}\right)}$$

$$-\underbrace{\frac{k_L\left(r/K_{p,b} - C_T/\left(1+K_{p,w}S_w\right)\right)}{d\left(S_b+1/K_{p,b}\right)}}_{\text{pore water diffusion}} \qquad \textit{eq. 3.15}$$

[9] It is common to model the turbulent transport, which is significantly more effective than molecular diffusion in respect to momentum, hear and tracer transport, by defining an effective diffusion coefficient called eddy diffusivity.

In the case of 1 hour simulations for the river water, the terms of radioactive decay, sedimentation, resuspension and pore water - sediment diffusion are negligible compared to the terms of advections and dispersion (see Appendix 14), thus equation 3.14 becomes:

$$\frac{\partial C_T}{\partial t} = -u_x \frac{\partial C_T}{\partial x} + E \frac{\partial^2 C_T}{\partial x^2} - u_y \frac{\partial C_T}{\partial y} + E \frac{\partial^2 C_T}{\partial y^2} \qquad \textit{eq. 3.16}$$

Under steady state conditions it has the following form:

$$- u_x \frac{\partial C}{\partial x} + E \frac{\partial^2 C}{\partial x^2} - u_y \frac{\partial C}{\partial y} + E \frac{\partial^2 C}{\partial y^2} = 0 \qquad \textit{eq. 3.17}$$

Or

$$- \varepsilon \nabla^2 C + \mathbf{u} \cdot \nabla C = 0 \qquad \textit{eq. 3.18}$$

with C the total radionuclide concentration in the river water, being transported along a stream moving with flow velocity $\mathbf{u}$, also subject to diffusive effects regulated by the horizontal eddy diffusivity ε.

Due to its complexity equation 3.18 has to be solved with the aid of numerical methods, such as the finite element method (see §3.3.1, §3.3.2).

When the activity concentration of the radionuclides in the water is known, equation 3.15 can be solved analytically (Appendix 12) with the activity concentration in river sediments given as:

$$r(t) = \exp\left[-\int_0^t \left(\frac{\lambda}{1 + K_{p,b} S_b} + \frac{\alpha(t) S_b}{S_b + \frac{1}{K_{p,b}}} \right) dt \right] +$$

$$+ \int_0^t \exp\left[-\int_0^{t'} \left(\frac{\lambda}{1 + K_{p,b} S_b} + \frac{\alpha(t) S_b}{S_b + \frac{1}{K_{p,b}}} \right) dt' \cdot C \left(\frac{k_s(t) K_{p,w} S_w}{S_b + \frac{1}{K_{p,b}}} \frac{1}{\left(1 + K_{p,w} S_w\right)} \gamma \right) dt \right] \qquad \textit{eq. 3.19}$$

where both the sedimentation and resuspension terms are tidal related parameters (due to the tidal varying water depth, see also §2.2).

3.3 Numerical methods

The nonlinear differential equations describing river flow and sediment transport have been studied extensively and many solution techniques have been developed. The complexity of these natural systems excludes the use of purely analytical methods, and solutions can only be achieved through numerical analysis. The differential equations are solved by discretizing the equations and bringing them into a finite- dimensional subspace. Three major concepts of this analysis include (Wu, 2008):

- Convergence: whether the approximate solution of the discretized algebraic equations approaches the exact solution of the original differential equation for each dependent variable as the grid spacing approaches zero.
- Consistency: whether the system of discretized equations is equivalent to the differential equation at each grid point when the grid spacing approaches zero.
- Stability: whether the cumulative effect of the error produced during the numerical algorithm application is negligible.

Widely used discretization methods include the finite difference method, the finite volume method and the finite element method. In the finite difference method the differential equations are discretized by approximating the differential operators by difference operators at each point. The most commonly considered forms are the forward, backward and central differences schemes. The finite volume method is based on integrating the differential equations over each control volume, holding the conservation laws of mass, momentum and energy. The method is easily formulated to allow calculations for unstructured meshes, thus used in many computational fluid dynamic packages. The finite element method (FEM) approximates solutions to boundary value problems by subdividing the problem into smaller and more simple parts. These simplified equations are then assembled into a larger system of equations that model the system.

The finite difference method is often regarded as the simplest method to use. Along with the finite volume methods, they adopt structured regular meshes and encounter difficulties in complicated geometries, while the finite element method can conveniently handle irregular domains and any type of boundary conditions. Other advantages of the FEM include stability (in contrast with the finite differences, where stability can be difficult to establish), convergence (the quality of the approximation generally follows the best approximation results) and accounting for inhomogeneity problems (Desai and Kundu, 2001). For these reasons the FEM was the numerical method selected for solving the Navier-Stokes and the advection-dispersion equations (see §3.2.2.1 and 3.2.2.2).

3.3.1 The Finite Element Method (FEM)

The finite element method is a function/basis-based approach for solving partial differential equations (PDEs). Its fundamental concept, as stated from Champion and Ensminger (1988), is that any continuous quantity can be approximated by a discrete model composed of a set of piecewise continuous functions defined over a finite number of sub-domains or elements. The interpretation of the finite element discretization can be done both physically (the continuous physical model is divided into finite sub-domains called elements and the laws of nature are applied to the generic element; when recombined the results represent the continuum) and mathematically (the differential equation representing the system is converted into a variation form approximated by a linear combination of a finite set of trial functions).
The PDEs are described by their strong form, which holds all the partial derivatives and boundary condition requirements and when solved provides the exact solution of the problem. The Galerkin method weakens the differentiability requirements and satisfaction of boundary condition requirements on the Dirichlet part of the domain by providing an alternative representation of the differential equation, the weak form. The weak formulating turns the differential equation into an integral equation which when solved provides an approximate solution of the problem. Both formulations are mathematically equivalent.

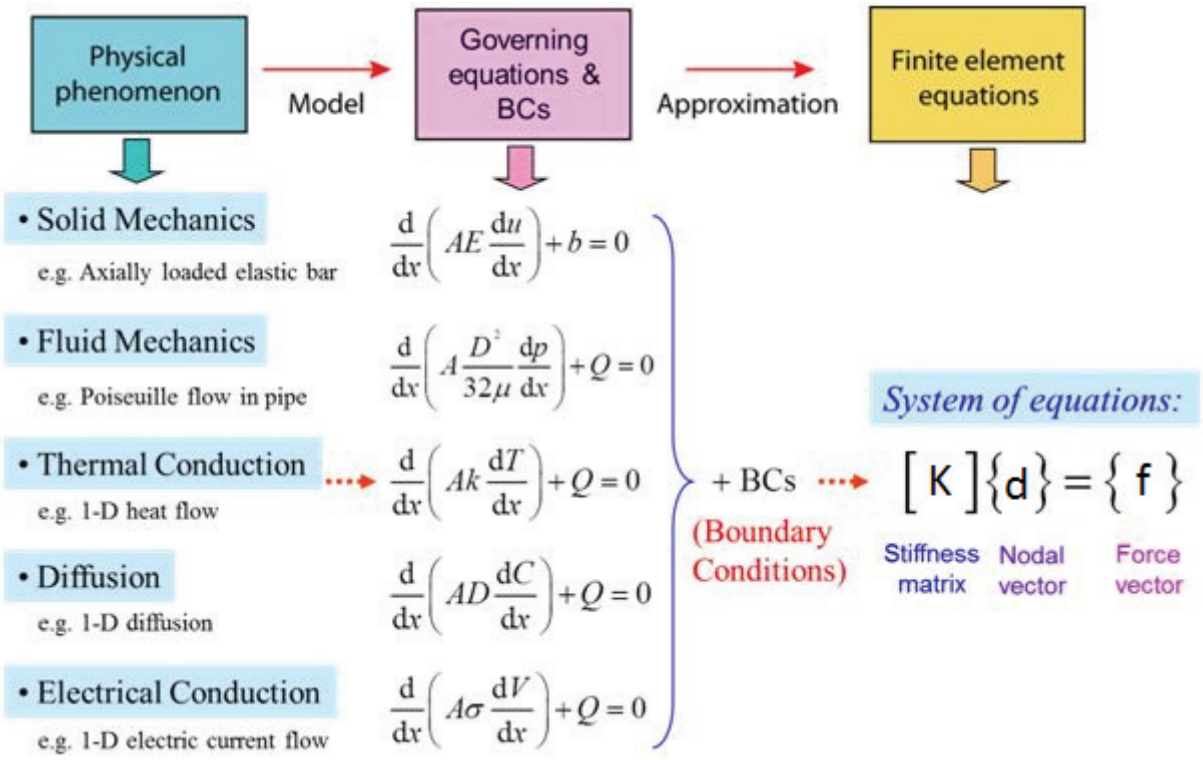

Figure 3.2: The FEM premise description for a range of common physical phenomena and their 1-D governing equations in differential form (Adapted from University of Cambridge, 2017, https://www.doitpoms.ac.uk/tlplib/fem/intro.php).

Some of the main steps in a finite element implementation include:

1. *Partitioning into finite elements*: A domain Ω is partitioned into m non-overlapping sub-domains (elements) such that $\Omega = \bigcup_{e=1}^{m} \Omega_e$, known as mesh. The elements are assumed to be connected to one another only in interconnected joints, the nodes. The mesh and nodal coordinates form an element connectivity matrix which indicates the nodes connected to a specific element and has dimensions $m \times n$ (m is the number of elements and n the number of nodes per element); for linear elements in one dimension the element connectivity matrix is a $m \times 2$ matrix.

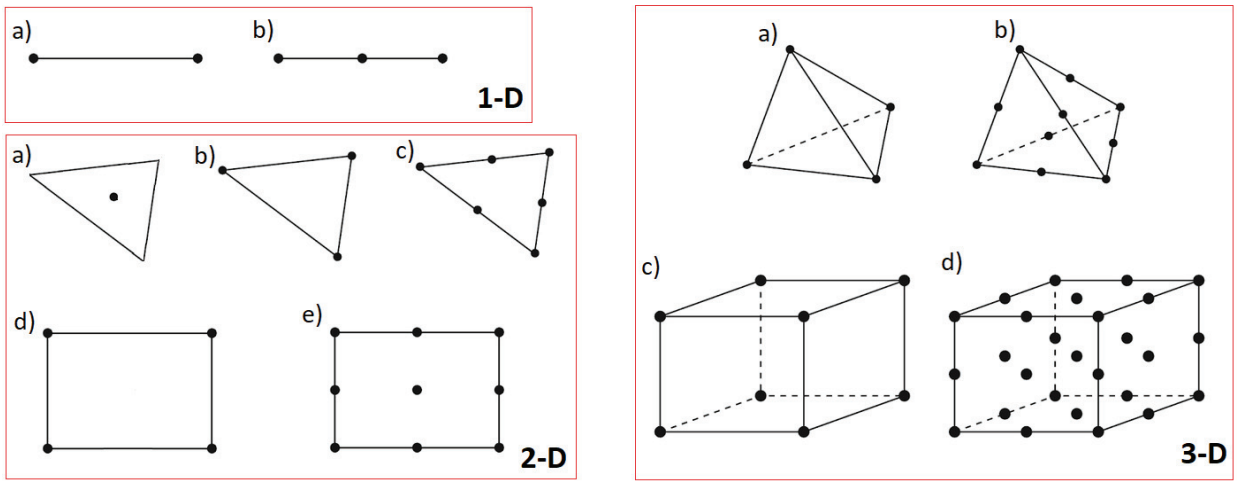

Figure 3.3: Examples of finite elements in 1-D (a: 2 nodes, b: 3 nodes), 2-D (a: triangle 1 nodes; P_0, b: triangle 3 nodes; P_1, c: triangle 6 nodes; P_2, d: rectangular 4 nodes; Q_1, e: rectangular 9 nodes; Q_2) and 3-D (a: tetrahedral 4 nodes; P_1, b: tetrahedral 10 nodes; P_2, c: brick 8 nodes; Q_1, d: brick 27 nodes; Q_2).

2. Finite element shape functions: If the domain is described by n nodes, we can approximate the solution $u(x)$ by $u^h(x)$ for the 1-D case where h is a measure of the nodal-spacing (or element size) with $u^h(x) = \sum_{j=1}^{n} \phi_j(x) u_j$, where $\phi_j(x)$ are the basis functions and define a set of trial functions (often called shape functions) and u_j are nodal values (for example the value of temperature at x_j for the thermal conduction PDE).

These functions have a very simple form, most common piecewise polynomials of low order and for each node are non-zero only over the element while their value diminishes to zero on the nodes, i.e. they have a local character. The shape functions are constructed in a reference element $\xi \in \Omega_0 = [-1.1]$. For the one dimensional case the linear finite element shape functions are: $N_1(\xi) = (1-\xi)/2$ and $N_2(\xi) = (1+\xi)/2$.

3. Isoparametric mapping: The calculations can be significantly simplified by utilizing a coordinate transformation; every point of the original coordinate system can be mapped to a corresponding point in the transformed system using a linear relationship.

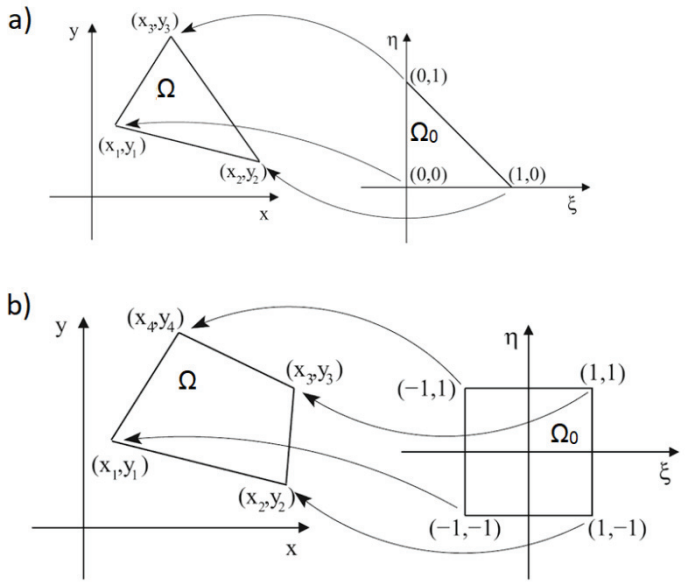

Figure 3.4: Isoparametric mapping of a: a P_1 element and b: a Q_1 element (Adapted from Elman et al., 2014b).

4. Calculation of integrals: The stiffness matrix $\mathbf{K}$[10] (system of linear equations that must be solved in order to ascertain an approximate solution to the differential equation) and the force vector $\mathbf{f}$ are assembled on element basis, for the case of 1-D thermal conduction given as $\mathbf{K} = \sum_e k^e$ and $\mathbf{f} = \sum_e f^e$ where $k_{ij}^e = \int_{\Omega_e} aN_i' N_j' dx$ and $f_i^e = \int_{\Omega_e} bN_i dx$ with a the conductivity coefficient and b the source term. The stiffness matrix is a square and symmetric matrix with dimensions ruled by the number of nodes and the unknown variables per node (mentioned as degrees of freedom in many textbooks).

The integrals over Ω_e are transformed to Ω_0 using the Isoparametric transformation and the chain rule is used for computing the derivatives of the shape functions. The evaluation of the integrals on Ω_0 is done through numerical integration (Gauss quadrature[11]).

[10] The finite element method was first used to deal with the elastic deformation of solids, so for historical reasons the square matrix $\mathbf{K}$ is called stiffness matrix, although this name has no physical significance when working with non solid problems (Novak et al., 2010).

[11] The Gaussian quadrature is an approximation of a definite integral of a function to a weighted sum of function values at specific points in the domain of integration (Press et al., 1989).

5. *Matrix-Vector weak form:* After assembling the stiffness matrix and force vector, the boundary conditions are incorporated and the linear system $\mathbf{Kd} = \mathbf{f}$ is solved to obtain $\mathbf{d}$ the vector of unknown nodal values of u, where $\mathbf{d} = \{u_1, u_2, ..., u_m\}^T$, the finite element solution is computed using $u(x) = \sum_{j=1}^{n} \phi_j(x) u_j$.

3.3.2 The Incompressible Flow & Iterative Solver Software (IFISS)

The Incompressible Flow & Iterative Solver Software (IFISS) is an open-source software package distributed by the University of Manchester (http://www.maths.manchester.ac.uk/~djs/ifiss/, 2017). It is a graphical package which allows the study of incompressible flow problems run under Matlab or Octave. It includes algorithms for discretization by a combination of finite element methods and a posteriori error estimation of the computed solutions, together with state of the art preconditioned iterative solvers for the discrete linear systems that arise (Elman et al., 2014b). A large number of build-in test problems, all based on common PDEs, are available. IFISS focused mainly on four specific PDEs that arise in modeling natural phenomena: the Poisson equation, the convection-diffusion equation, the Stokes and Navier-Stokes equations.

The Navier-Stokes equations

In IFISS package, for solving the Navier-Stokes equations the use of a mixed Q_1-P_0 discretization of the domain (see figure 3.3) for the velocity and pressure respectively is suggested (Silvester et. al, 2015). This mixed approximation gives rise to a non-linear system of algebraic equations in which initial velocity estimates are required to start the iterative process of solving a linearized problem at each step. Thus, given an "initial guess[12]" a sequence of iterates is computed with the goal of converging to the solution of the weak formulation.

[12] The "initial guess" in IFISS is the solution to the corresponding Stokes problem (inertial forces are negligible in comparison to the viscous forces).

In IFISS three iterative procedures for solving the Navier-Stokes equations are implemented (Rehman et al., 2006):

Newton iteration: The convective term can be linearized as:

$$u^{k+1}\nabla u^{k+1} = u^{k+1}\nabla u^{k} + u^{k}\nabla u^{k+1} - u^{k}\nabla u^{k}$$

Where u^{k+1} the solution we want computed at a present iteration level k+1. If the initial estimate is good, Newton iteration converges quadratically, if not iterations converge slowly or may diverge.

Picard iteration: In this method the convection term is approximated by:

$$u^{k+1}\nabla u^{k+1} \approx u^{k}\nabla u^{k+1}$$

This method does not require an accurate initial estimate and converges linearly.

Hybrid method: This method utilizes both properties of the Newton and Picard methods. Based on Picard iterations, Newton method gets a good initial estimate.

The hybrid method is used for our modeling (see §7.3).

The Convection-diffusion equation

When solving numerically equation 3.18 by applying the Galerkin finite element method, using the Q_1 approximation (see figure 3.3) for discretization, often it results in a discrete solution that exhibits non physical oscillations. In IFISS the discrete problem is stabilized by adding diffusion in the streamline direction, i.e. using the streamline diffusion method as described by Hughes and Brooks (1979).

The streamlines or characteristic curves are associated with the advection and are defined to be the parameterized curves that have tangent vector at every point of the curve. If $f = 0$ then the solution is constant along streamlines.

The implementation is done by using the Streamline Upwind Petrov-Galerkin (SUPG) stabilization (Elman et al., 2007b). The streamline diffusion method only adds diffusion in the streamline direction, which is also known as upwinding. The SUPG method is a residual-based upwinding technique in which the stabilized finite elements are formed by adding variational terms to the standard Galerkin method, which are mesh dependent; i.e. controlled by the so-called element Peclet number: $P_h^k := \frac{|\vec{u}_k| h_k}{2\varepsilon}$ with $|\vec{u}|$ the Euclidean norm of the flow velocity at the element centroid, ε the eddy diffusivity as defined in eq. 3.18, h_k a measure of the element length in the direction of $\vec{u}$ (Rehman et al., 2006).

Clearly this means that the stabilization depends on the element size. As stated by Elman et al., (2014b) the streamline diffusion approach limits the damage caused by poor resolution and leads to more accurate solutions. Additional information on the SUPG method can be found in Pearson and Wathen (2013).

3.4 Errors in modeling

Any model despite its physical level of detail is by definition a simplification of reality. Although computational simulations give direct, cost-effective predictions their reliability depends on how well done were: a) the conceptual modeling of the physical system, b) the mathematical description, through governing equations, boundary conditions and empirical formulas, of the conceptual model, c) the discretization and algorithm selection for the mathematical model using numerical schemes, d) the computer programming of the discrete model, e) the numerical solution of the computed program model, using direct or iterative solution methods and f) the representation of the numerical solution (see figure 3.5).

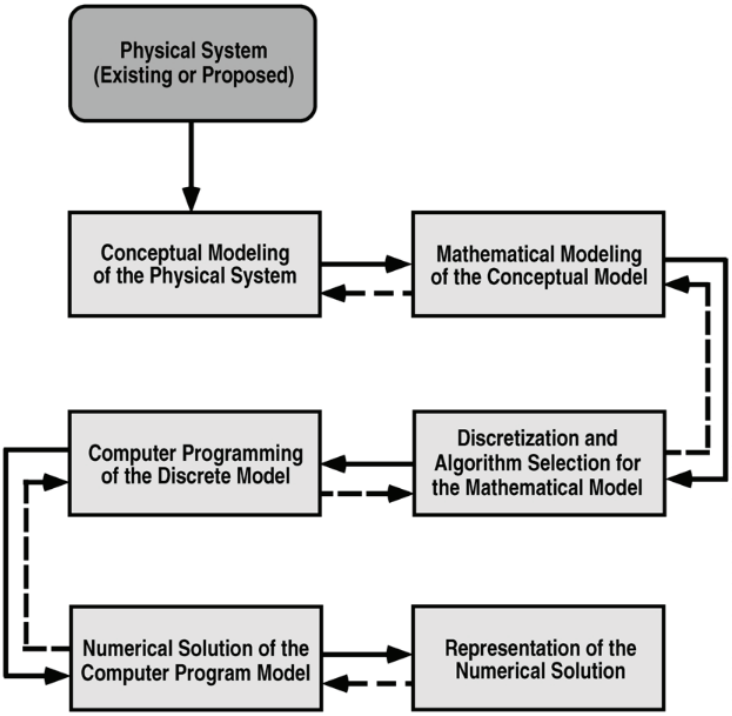

Figure 3.5: Proposed phases for computational modeling and simulation (Oberkampf et al., 2002).

More detailed, in each phase of the modeling uncertainties and errors can occur:

Conceptual modeling:
In the conceptual phase of the modeling, where the system/environment is specified, errors can develop depending on which processes one considers and which assumptions are made regarding the system under consideration (eg. dimensionality, type of flow i.e. laminar, turbulent, steady, unsteady or quasi-steady, bed load, suspended load, etc.).

Mathematical modeling:
During the description of the physical phenomena of the study, epistemic uncertainty (aka systematic uncertainty, defined as potential inaccuracy due to lack of knowledge) and/or unacknowledged error (representing mistakes on modeling and simulation as a result of human error) can arise as a result of improper specification of all PDEs, auxiliary, initial and boundary conditions. Additional sources of error include restrictions (constraints on the range of selected values) as well as values based on a subjective assessment when insufficient data are available, computational resources, availability on computer codes and technical issues.

Discretization and algorithm selection for the mathematical model:
The discretization focuses on converting the differential equations to equivalent algebraic equations held to approximate the exact solution locally.

Computer programming of the discrete model:
The potential for errors in this phase is enormous, including mistakes in input preparation, module design and coding, compilation and linkage. In addition to coding bugs there is the subtler problem of unidentified code behavior influencing error connected with the libraries and compilers of the selected programming language.

Numerical solution of the computer program model:
In this step of the process the spatial grid distribution and the time step (in case of unstable PDEs) are specified, thus two types of error arise, the truncation error caused by a truncated Taylor series expansion replacing the spatial and time derivatives and the round-off error which occurs because of the computing device's inability to deal with certain numbers which need to be rounded off to some near approximation. The round-off error is device dependent while the order of the truncation error is proportional to the grid size (Δx) and timestep (Δt), implying that as Δx and Δt decrease, the error decreases. However decreased grid size and timestep result in an increased number of computational operations leading to additional round-off errors.

Representation of the numerical solution:
This phase includes the graphical/animation visualization of a solution, where errors can be introduced when constructing what-appears-to-be continuous functions based on the discrete solutions obtained by the model.

Unfortunately, time limitations did not allow an extensive error determination of the model, topic briefly discussed in §7.4 and 8.3.

3.5 General comment on Chapter 3

This chapter presented the physical processes and basic equations of a 3 compartment model for computing the ^{131}I behaviour in a tidal river. The complexity of PDEs, describing mathematically the motion of the river water and the advection-dispersion of the radionuclides require highly sophisticated numerical methods for acquiring their solutions. These equations are solved with the numerical method of the finite elements and are implemented on Matlab with the aid of the IFISS software. The parameterization and the simulation results are presented in Chapter 7 along with a basic assessment of the model.

3.6 References for Chapter 3

Aquaveo– *SMS 12.2-The Complete Surface-water Solution.* Info: http://www.aquaveo.com/software/sms-surface-water-modeling-system-introduction, 2017

Banda M.K., Seaid M., Thömmes G., 2008, *Lattice Boltzmann simulation of dispersion in two-dimensional tidal flows.* International Journal for numerical methods in engineering, 77, 878-900.

Boyer P., Garnier-Laplace J., Adam C., 2002, *CASTEAUR: a simple tool to assess the transfer of radionuclides in waterways.*Health Physics, 83 (4), 539-42.

Boyer P., Beaugelin-Seiller K., Ternat F., Anselmet F., Amielh M., 2005, *A dynamic box model to predict the radionuclide behaviour in rivers for medium and long-term periods.* Radioprotection, 40,S307-S313.

Champion E.R., Ensminger J.M., 1988. *Finite Element Analysis with Personal Computers (Mechanical Engineering).* Marcel Dekker , INC.

Desai C.S., Kundu T., 2010, *Introductory Finite Element Method*. CRC Press, Taylor & Francis Group.

Deltares Open Software, *Delft3D*. Info: https://oss.deltares.nl/web/delft3d

Elman H.C., Ramage A., Silvester D.J., 2007, *Algorithm 866:IFISS, A Matlab Toolbox for Modelling Incompressible Flow.* ACM Transaction on Mathematical Software, 33, 2, 14.

Elman H.C., Ramage A., Silvester D.J., 2014a, *IFISS: A Computational Laboratory for Investigating Incompressible Flow Problems,* Society for Industrial and Applied Mathematics, 56, 2, 261-273.

Elman H., Silvester D., Wathen A., 2014b, *Finite Elements and Fast Iterative Solvers with Applications in Incompressible Fluid Dynamics,* Second Edition, Oxford Science Publications.

EPA, 2007, *Environment Fluid Dynamics Code (EFDC),* Info: https://www.epa.gov/exposure-assessment-models/environment-fluid-dynamics-code-efdc-download-page

Hughes T.J.R., Brooks A.N., 1979, *A Multidimensional Upwind Scheme with no Crosswind Diffusion.* American Journal of Computational Mathematics, 6, 3, 19-35.

Krylov A.L., Nosov A.V., Kryshev A.I., Kryshev I.I., Kiseliev V.P., 2007, *Assessment of Concentration of Radionuclides in River Water and Bottom Sediments.* Russian Meteorology and Hydrology, 32, 7, 470-478.

Margvelashvili N., Maderich V., Zheleznyak M., *2000, THREETOX- numerical model to simulate the three-dimensional dispersion of radionuclides in stratified water bodies* .RODOS-WG4-RP(96)04. Retrieved from: https://resy5.iket.kit.edu/RODOS/Documents/Public/HandbookV6/Volume3/THREETOX_04.pdf

MIKE, Powered by DHI. Info: https://www.mikepoweredbydhi.com/

Modenesi K., Furlan L.T., Tomaz E., Guirardello R., Nunez J.R., 2004, *A CFD model for pollutant dispersion in rivers. Brazilian Journal of Chemical Engineering,* 21, 04, 557-568.

Mohr T.K.G., Stickney J.A., DiGuiseppi W.H., 2010, *Environmental Investigation and Remediation 1.4-Dioxane and other Solvent Stabilizers.* Taylor & Francis Group, LLC.

Monte L., Van der Steen J., Bergstroem U., Gallego E., Hakanson L., Brittain J.E., 2001, *The project MOIRA: A model-based computerized system for management support to identify optimal remedial strategies for restoring radionuclide contaminated aquatic ecosystems and drainage areas.* Retrieved from: https://www.researchgate.net/publication/235675821_The_project_MOIRA_A_model-based_computerised_system_for_management_support_to_identify_optimal_remedial_strategies_for_restoring_radionuclide_contaminated_aquatic_ecosystems_and_drainage_areas

Monte L., Boyer P., Brittain J.E., Hakanson L., Lepicard S., Smith J.T., 2005, *Review and assessment of models for predicting the migration of radionuclides through rivers.* Journal of Environmental Radioactivity, 79, 273-296.

Novak P., Guinot V., Jeffrey A., Reeve D.E., 2010. *Hydraulic Modelling -an Introduction: Principles, Methods and Applications.* Spon Press, Taylor & Francis Group.

Oberkampf W.L., DeLand S.M., Rutherford B.M., Diegert K.V., Alvin K.F., 2002, *Error and uncertainty in modeling and simulation.* Reliability Engineering and System Safety, 75, 333-357.

Pearson J.W. and Wathen A.J., 2013. *Fast Iterative Solvers for Convection-Diffusion Control Problems*. Electronic Transactions on Numerical Analysis, 40, 294-310.

Perianez R., 2004, *Modelling the dispersion of radionuclides by a river plume: Application to the Rhone river.* Continental Shelf Research 25, 1583-1603.

Press W.H., Flannery B.P., Teukolsky S.A., Vetterling W.T., 1989. *Numerical Recipes in Pascal: The Art of Scientific Computing.* Cambridge University Press.

Rehman M., Vuik C., Segal G.., 2006, Report 06-06, *Study report of IFISS PACKAGE (VERSION 2.1)*, DELFT UNIVERSITY OF TECHNOLOGY. Retrieved from: https://repository.tudelft.nl/islandora/object/uuid%3Ac5c4780c-9236-4c70-a9eb-8a4831836874

Schnoor J.L., 1996. *Environmental Modeling: Fate and Transport of Pollutants in Water, Air and Soil*. John Wiley & Sons

Semizhon T., Röllin S., Spasova Y., Klemt E., 2010, *Transport and distribution of artificial gamma-emitting radionuclides in the River Yenisei and its sediment*. Journal of Environmental Radioactivity, 101, 385-402.

Silvester D.J., Elman H.C., Ramage A., 2015, *Incompressible Flow Iterative Solution Software (IFISS) Installation & Software Guide,* Version 3.4. Retrieved from: http://www.maths.manchester.ac.uk/%7Edjs/ifiss/ifiss_guide_3.5.pdf

Smith J.T., Belova N.V., Bulgakov A.A., Comans R.N., Konoplev A.V., Kudelsky A.V., Madruga M.J., Voitsekhovitch O.V., ZiboldG., 2005, *The „AQUASCOPE" simplified model for predicting 89,90St, 131I, and 134,137Csin surface waters after a large-scale radioactive fallout.* Health Physics, 89 (6), 628-44.

University of Alberta, River 2D software. Info: http://www.river2d.ualberta.ca/

University of Cambridge, 2017. Retrieved from: https://www.doitpoms.ac.uk/tlplib/fem/intro.php

Wang S.S.Y., Wu W., 2004, *River sedimentation and morphology modeling- the state of the art and future development.* Proceedings of the Ninth International Symposium on River Sedimentation, October 18-21, 2004, Yichang, China.

Wenli W., Rong G.W., Liu Y.L., 2010. *Simulation for 2D Flows and Water Quality in Curvilinear Coordinates.* International Conference on Computational and Information Sciences, 17-19 December 2010, Chengdu, China.

Wu W., 2008, *Computational River Dynamics*, Taylor and Francis/Balkema.

Zhan X., 2003, *Simulation of unsteady flow and solute transport in a tidal river network.* Engineering Computations, 20, 5/6, 754-767.

Zheleznyak M., Donchytz G., Hygynyak V., Marinetz A., Lyashenko G., Tkalich P., 2003, *RIVTOX-one dimensional model for the simulation of the transport o radionuclides in a network of river channels.* RODOS-WG4-TN(97)05. Retrieved from: https://resy5.iket.kit.edu/RODOS/Documents/Public/HandbookV6/Volume3/RIVTOX.pdf

Chapter 4

Gamma Spectroscopy

In this work, ^{131}I activity concentration (in both river water and sediments) is measured by gamma spectroscopy. Thus, it is necessary to present the basic background physics and instrumentation allowing us to perform some measurements.

4.1 Radioactive decay

The nucleus consists of uncharged neutrons and positively charged protons; both called nucleons. The number of protons (atomic number Z) defines the element while the total number of nucleons (mass number; A=Z+N with N being the number of neutrons) defines the isotope of the element. In general an assembly of nucleons, with its associated electrons is called nuclide (X) and is specified as ${}^{A}_{Z}X$. All elements have radioactive isotopes and most of them have one or more stable isotopes (figure 4.1).

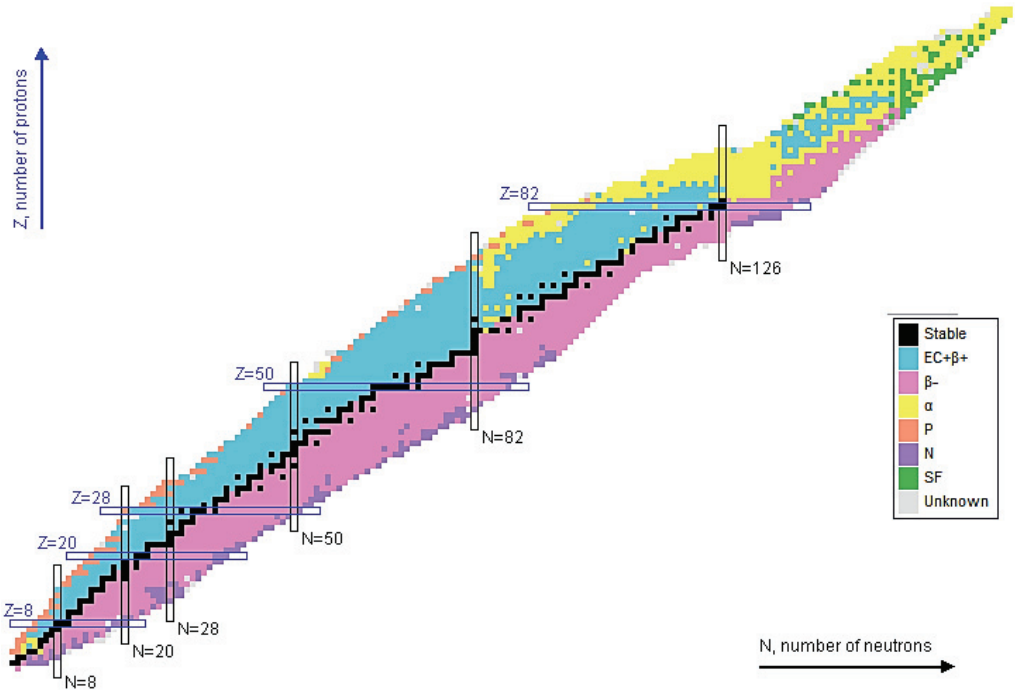

Figure 4.1: Chart of nuclides. (Adapted from National Nuclear Data Center, 2017)

Radioactive isotopes, also called radionuclides, undergo a process called radioactive decay in which a spontaneous change occurs inside the nucleus and results in the emission of particles and/or electromagnetic radiation.
The radioactive decay is driven by mass change of the nucleus, referred to as parent isotope, resulting in lowest energy for the products. This energy difference is determined by Einstein's equation:

$$\Delta E = \Delta m \cdot c^2 \qquad \textit{eq. 4.1}$$

with the energy difference in Joules, the mass is kilograms and the speed of light in m/s.
The radioactive decay is a stochastic process and according to quantum theory it is impossible to predict when a particular nucleus will decay, however for a collection of radioisotopes the expected decay is characterized in terms of half-life or decay constant. Given such a collection with *N* number of atoms, the number of decay events *dN* expected to occur in a small interval of time *dt* is proportional to the number of radionuclides present;

$$\left(-\frac{dN}{dt}\right) = \lambda \cdot dt \;\rightarrow\; N(t) = N_0 \cdot e^{-\lambda t} \qquad \textit{eq. 4.2}$$

where
N(t): the number of atoms after time *t*,
N_0: the initial number at time t=0 and
λ *:* the decay constant, inversely proportional to the half-life $T_{1/2}$ as $\lambda = \frac{\ln 2}{T_{1/2}}$.
The activity of a radioactive source is defined from the number of disintegrations per second:
$A = \lambda N$
measured in Becquerel: 1Bq=1 disintegration/s. An older unit is Curie: 1 Ci= 3.7×10^{10}Bq.

4.2 Modes of radioactive decay

The most common modes of radioactive decay include alpha, beta and gamma decay processes.

4.2.1 Alpha decay

The emission of alpha particles is a process mainly occurring in heavy nuclei (Z > 83), where an alpha particle (^{4}He nucleus) is emitted by penetrating the Coulomb barrier of the heavy nucleus through quantum mechanical tunneling.

An example is the decay of the most common isotope of radium:

$$^{226}_{88}Ra \rightarrow ^{222}_{86}Rn + ^{4}_{2}He + Q$$

Q represents the energy release equal to the difference in mass between the initial nuclides and products.
The alpha particles are mono-energetic with energies ranging between 2 and 10 MeV, depending on the parent and daughter isotopes. In many cases the emission of an alpha particle can result in excited states of the daughter isotope.

4.2.2 Beta decay

The radioactive decay process resulting in the emission of beta particles (electrons and positrons) is called beta decay.

β^- decay

A β^- decay is caused by the transformation of a nucleus with neutron surplus, to a nucleus with an extra proton and the same mass number accompanied by the emission of an electron and an electron antineutrino. An example of a β^- decay is:

$$^{14}_{6}C \rightarrow ^{14}_{7}N + e^- + \overline{\nu}_e + Q$$

the reaction involving the transformation of a free neutron to a proton:

$$n \rightarrow p + e^- + \overline{\nu}_e$$

β^+ decay

A β^+ decay is caused by the transformation of a nucleus with a neutron deficiency, to a nucleus with an additional neutron and the same mass number accompanied by the emission of a positron and an electron neutrino. An example of a β^+ decay is:

$$^{23}_{12}Mg \rightarrow ^{23}_{11}Na + e^+ + \nu_e + Q$$

the reaction involving the transformation of a proton to a neutron:

$$p \rightarrow n + e^+ + \nu_e$$

Positron emission is only possible if there is sufficient energy difference, i.e. mass difference between the consecutive nuclides. The emitted positron, after emission, is rapidly slowed down

and after reaching kinetic energy close to zero the annihilation process occurs, where the positron interacts with an electron and both annihilate creating two 511 keV photons.

The energy range of the emitted electrons/positrons is continuous, varying between some keV to a maximum energy of some MeV, which corresponds to the difference between the parent and daughter isotopes, leading to continuous energy spectra caused by the distribution of energy between the produced particles (electron- electron antineutrino, positron- electron neutrino).

Electron capture

Due to the fact that this process (β^+ decay) can occur if more than 1022 keV of decay energy is available, neutron deficient nuclides close to stability can decay by electron capture. In this type of decay the electron needed to convert the proton is captured by the nucleus from one of the electron shells. As the K-shell is closest to the nucleus, it is more probable that a K-electron will be captured leaving a vacancy which is filled by an electron dropping from a higher shell with the excess energy released as an X-ray in what is referred to as fluorescence. An example of an electron capture is:

$$^{81}_{36}Kr + e^- \rightarrow ^{81}_{35}Br + v_e$$

the reaction involving the transformation of a proton and an electron to a neutron:

$$p + e^- \rightarrow n + v_e$$

4.2.3 Spontaneous fission

This type of decay is a natural process in which a heavy nucleus spontaneously splits into two large fragments, a process prevented in all but very large nuclei by the fission barrier, the required energy in order to deform the nucleus from a sphere to a situation where two fission product nuclei can split off. An example of a spontaneous fission is:

$$^{252}_{98}Cf \rightarrow ^{140}_{54}Xe + ^{108}_{44}Ru + n + Q$$

In addition to these decay modes, some other rather uncommon exist with no particular interest to gamma spectrometrists such as delayed neutron and proton emission, double beta and two proton decay and emission of ‘heavy ions’ or ‘clusters’, as ^{14}C and ^{24}Ne.

4.2.4 Gamma decay

In contrast to the aforementioned decay modes, gamma decay does not alter the nucleons, rather than the energy state of the nuclei. The process is solely that of losing the excess energy, as the transition of an excited nuclear state to another energy state (intermediate ground state) is accompanied with the emission of gamma-rays (photons). Gamma radiation is electromagnetic radiation with energies of some keV to several MeV, with the energy of the emitted gammas being mono-energetic and characteristic for the parent nuclei. In practical gamma spectroscopy, for most cases, the interest lies in the region of 30 keV to 2 MeV.

The de-excitation of a nuclear level can occur through two additional processes: the pair production and the internal conversion.

Pair production is a rather uncommon form of gamma decay only possible when the energy difference between two levels is greater than 1022 keV, used to create an electron-positron pair. The particles are ejected from the nucleus and share the remainder energy as kinetic energy between them.

Internal conversion is very common. In this process the excitation energy of the nucleus is transferred to an atomic electron which is ejected from the atom. This is an internal conversion electron, mono-energetic with energy equal to the transition energy less the electron binding energy and a small nuclear recoil energy. The vacancy of the ejected electron will be filled by an electron from a higher shell leading to the emission of X-rays and Auger electrons. Due to the fact that there is no change in the number of neutrons, the atomic or mass numbers, the X-rays produced are characteristic of the parent isotope in contrast to electron capture where the X-rays produced are characteristic of the daughter isotope.

4.2.5 Other sources of photons

Other sources of photons include the annihilation radiation, the bremsstrahlung, the prompt gammas and the X-rays.

Annihilation radiation

Following β^+ decay and attenuation, a positron reaches kinetic energy close to zero and interacts with an electron producing two 511 keV photons, i.e. annihilation radiation. Due to the Doppler effect, the annihilation peak in the spectrum is approximately 2 keV wider than full energy peaks, making it rather unsuitable for peak shape calibration purposes.

Bremsstrahlung

Bremsstrahlung is the electromagnetic radiation produced when fast electrons interact with the Coulombic field of the nucleus and lose energy which appears as a continuum of photons, largely apparent in the X-ray region with the maximum energy being that of the corresponding beta particle. The effect is inversely proportional to the square of the charged particle mass, making

the effect significant with light particles. In the gamma spectrum it can be observed due to the raise of the general background continuum and decreases with increasing energy.

Prompt gammas
Elements irradiated with a beam of neutrons, absorb some of the neutrons and reach an excited state. The de-excitation of the neutron activated nucleus happens quickly with the emission of prompt gamma rays as the exited nucleus falls into ground state. This de-excitation is unrelated to the gamma emissions of radioactive decay and their energies are often greater than those of beta decay gammas and can reach over 10 MeV.

X-rays
As already mentioned, after electron capture and internal conversion the vacancy in the electron shell created leads to the rearrangement of the atomic electrons and the excess energy is emitted as photons (X-radiation). Most often vacancies occur in the K-shell which only has one energy level, while higher shells like L-series and M-series have sub-shell levels and their radiation is much lower in energy than the K-series. Since the X-rays are due to changes in the atomic structure rather than the nuclear structure only information as to the element involved is available but not the isotope since the arrangement of the atomic electrons is determined by the atomic number. X-rays are mono-energetic, characteristic for the daughter nucleus (only in the case of internal conversion they identify the parent nucleus) and their energy range is between ca. 100 eV to 100 keV.

4.3 Interaction of gamma radiation with matter

Gamma spectroscopy is based on the indirect ionization the photons cause when they interact with matter. For practical gamma spectroscopy the photoelectric effect, the Compton scattering and the pair production are the most important processes.

4.3.1 Photoelectric absorption

Photoelectric absorption is the process where a photon undergoes an interaction with one of the bound electrons in an atom. The photon completely disappears by transferring all its energy to an electron which is ejected from its shell with a kinetic energy, E_e, equal to:

$$E_e = E_\gamma - E_b$$

With E_γ the photon energy and E_b the binding energy of the electron in its shell.

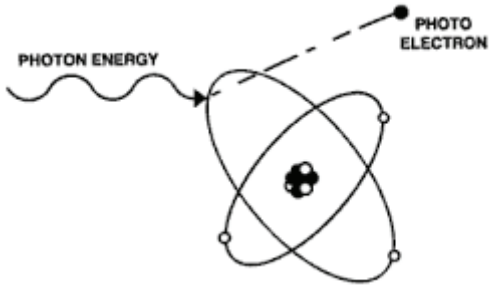

Figure 4.2: Gamma interaction by Photoelectric effect (FAS, 2017).

The atom is left in an exited state and may de-excite by redistributing the excess energy between its remaining electrons, leading to release of further electrons from the shells (Auger electrons) or a higher-energy electron can fill the vacancy left by the ejection of the photoelectron with the emission of a characteristic X-ray (X-ray fluorescence).

4.3.2 Compton scattering

Compton scattering is a direct interaction of the incident photon and an electron, thus creating a scattered gamma-ray and a recoil electron. The energy of the incident photon is divided between the recoil electron, which is ejected from its shell, and the scattered photon. The energy of the scattered photon is given as,

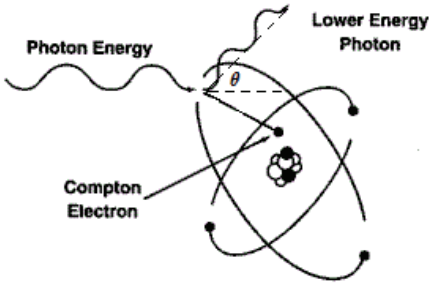

Figure 4.3: Gamma interaction by Compton effect (FAS, 2017).

$$E_{\gamma'} = E_{\gamma} \frac{1}{1 + E_{\gamma}\left(1 - \cos\theta\right)/ m_0 c^2} \qquad \textit{eq. 4.3}$$

and depends on the scattering angle. Thus, when θ=0 the scattered photon retains all its energy and the recoil electron gains no energy, while when θ=180^o the incident gamma ray is backscattered and the recoil electron moves along the direction of incidence with a maximum energy lower than E_γ. The highest energy of the recoil electron, corresponding to θ=180^o,is referred to as the Compton edge. At intermediate values of the scattering angle, the amount of energy the scatter photon has must be between those two extremes.

4.3.3 Pair production

The process takes place in the Coulomb field of the nucleus provided that the gamma ray energy exceeds twice the electron rest mass (1.022 MeV), resulting in the conversion of a gamma-ray into an electron-positron pair.

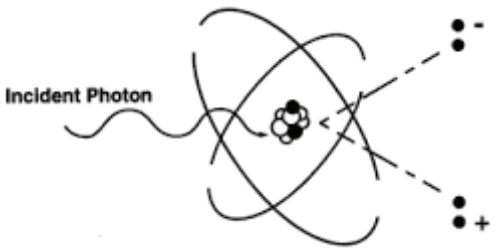

Figure 4.4: Gamma interaction by pair production (FAS, 2017).

The electron and positron created share the same excess gamma-ray energy, losing it to the medium as they are slowed down. Following when the energy of the positron is reduced near to its thermal energy it interacts with an electron and both annihilate creating two 511 keV photons.

Each of these interaction processes results in the transfer of photon energy to electrons in the absorbing medium. Other process of interaction of gamma radiation with matter includes coherent scattering (also known as Bragg or Rayleigh scattering).

4.4 Detection of gamma radiation

The detection of gamma radiation is possible through several different systems, i.e. gas detectors, scintillators and semiconductor detectors. Their operation is based on the indirect ionization photons cause when they interact with matter as their energy is converted to kinetic energy of electrons (and positrons), leading to the production of charge carriers (electron-ion pairs, electron-hole pairs) or light (emitted during the de-excitation of the molecular states by these electrons) which is collected and measured. For higher probability of complete transfer of the total photon energy, a high absorption coefficient of the detector material is desired, thus ruling out gas detectors. For practical gamma-ray spectroscopy scintillation and semiconductor detectors are widely used.

4.4.1 Scintillation detectors

In scintillation detectors the ionization is produced by the primary electrons which raise secondary electrons to the conduction band leaving holes in the valence band. The energy given to the electrons in some cases might not be sufficient to raise them to the conduction band resulting in entities called excitons, i.e. pairs of electrons and a holes remaining electrostatically attracted to each other. During the de-excitation of electrons by falling back to the valence band, electromagnetic radiation is emitted and if it is in or near optical wavelengths it can be detected by photomultipliers. Scintillation detectors are made from inorganic crystals as sodium iodide (NaI), cesium iodide (CsI), calcium fluoride (CaF_2), bismuth germanate (BGO) and lanthanum halides. In order to ensure that the band gap will be inside the visible range an activator is used eg. thallium or sodium impurities in the crystal (eg. NaI(Tl) the most common used scintillator material, CsI(Tl) and CsI(Na)) which give rise to extra levels within the forbidden band (between valence and conduction bands). These extra levels get populated by capturing electrons, holes and excitons which with a mean life of the order of 0.1 μs de-excite (Gilmore, 2008) and emit light which is collected and measured so to produce an electrical signal. The number of light photons emitted in such event is proportional to the energy lost by the initial charged particle in that event, thus the gamma-ray which interacted with the detector crystal.

4.4.2 Semiconductor detectors

In semiconductor detectors the primary ionization of the detector medium is broadly the same, however the collection process differs. The interaction of a gamma-ray with the semiconductor material will produce primary electrons with energies greater than the thermal energies. Interaction will raise secondary electrons from the conduction band, leaving positively charged vacancies in the valence band, i.e. holes. The electrons in the conduction band can respond to electric field when high voltage is applied and move to the positive contact. The vacancies in the valence band can be filled in with adjacent electrons, forming in turn other vacancies and creating a positive charge to the negative contact. Both electrons and holes carry charge, therefore contribute to the conductivity of the material and create an electric signal.

Germanium is by far the most common gamma-ray detector material and since it has a higher atomic number than other semiconductor material like silicon for example, it can detect higher energy radiation (Gilmore, 2008). With a band gap of 0.7 eV, energy similar to the energies achievable by thermal excitation, germanium detectors must be operated at low temperatures in order to allow an easier detection of the excitation due to the gamma-ray interactions, since thermally induced electrons moving to the conduction band would create a background current.
As it is not possible to have completely pure material, even high purity germanium detectors (HGe) have impurities which have a significant effect upon the conductivity. Impurities (eg. lithium) which result in one electron too few to maintain overall electronic configuration, i.e. a hole, give rise to extra energy states above the valence band, and germanium with this configuration is called p-type germanium. Impurities (eg. boron) resulting on one electron in excess of that required for electronic uniformity create donor states just below the conduction band and germanium with such impurities is called n-type germanium. N-type detectors have extended low-energy measurement capability and are more resistant to neutron damage, however come at a higher cost and have greater potential for true coincidence summing[1] problems (Gilmore, 2008). The layer on the face of the detector can be n+ contact by diffusing lithium on the detector surface (which creates a 700 μm dead layer[2]) or p+ contact by ion-implantation of boron atoms onto the surface (which creates 0.3 μm dead layer). Detector caps are constructed typical of aluminum limiting the detectors use below 40 keV, thus carbon composite end caps are also available which have higher efficiency at low energy (Gilmore, 2008). Figure 4.5 shows different configuration of gamma detectors, along with an indication of the energy range over which they might be used (efficiency curves are to give a general impression, since they depend on the size and type of detector).

[1] True coincidence summing is a source of error as a consequence of summing gamma-rays emitted almost simultaneously from the nucleus, important effect when nuclides with complicated decay schemes with cascades of gamma-rays in them are measured.

[2] Dead layer is a layer of impure germanium where the absorbed photons are not registered.

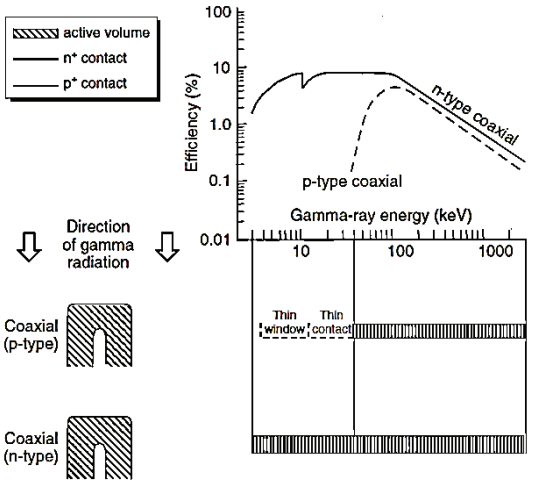

Figure 4.5: Configurations of detector generally available, together with schematic efficiency curves and an indication of the energy range over which they might be used (Adapted from Gilmore,2008).

4.4.2.1 Detectors in the laboratory

In the laboratory 3 different types of germanium detectors are available, all produced by CANBERRA Industries. Their performance and physical characteristics are given in tables 4.1 and 4.2.

Table 4.1: Performance characteristics of detectors 3 - 6 in the laboratory.

Detector name	Det3	Det4	Det5	Det6
Description	Reverse p-type coaxial Ge detector	P-type coaxial Ge detector	N-type coaxial Ge detector	N-type coaxial Ge detector
Model number	GX5019	GC5021	GR5021	GR5021
Relative efficiency[3] (%)	51.2	45.8	50.8	50.9
Full Width at Half Maximum[4] (FWHM) (keV)	at 22 keV: 0.9 at 88 keV: 1.0 at 1.3 MeV: 1.9	at 122 keV : 1.2 at 1.3 MeV: 2.1	at 122 keV : 1.00 at 1.3 MeV: 2.1	at 122 keV : 1.00 at 1.3 MeV: 2.1
Peak to Compton ratio[5] (P/C)	64:1	56	58	58

[3] Relative efficiency is a measure of the general performance of the detector, relating its efficiency of detection of the ^{60}Co gamma emission at 1332 keV to that of a standard sodium iodide scintillation detector (a 3 in. by 3 in. diameter).

[4] Full width at half maximum is the width of the photon peak at half of the highest point on the peak and it is used to express detector resolution.

[5] Peak to Compton ratio is an indication of detector performance for measuring lower energy gamma-rays in the presence of higher energies.

Table 4.2: Physical characteristics of detectors 3 - 6 in the laboratory.

Detector name	Det3	Det4	Det5	Det6
Geometry	Coaxial one open end, closed end facing window			
Diameter (mm)	67	64.4	64	63.5
Length (mm)	60.5	60.8	60	63.5
End-cap	Cu endcap with C epoxy window	Al endcap	Cu endcap with C epoxy window	Cu endcap with C epoxy window
Distance from window (outside) (mm)	5	6	5	5
Shielding[6]	Pb: 92 mm Cu: 10 mm Cd: 1.3 mm PMMA: 5 mm	Pb: 100 mm Cu: 2.0 mm	Pb: 92 mm Cu: 10 mm Cd: 1.3 mm PMMA: 5 mm	Pb: 100 mm Cu: 10 mm

During operation the germanium detector must be cooled in order to avoid leakage current induced noise which destroys the energy resolution. The temperature is reduced to 77 K with the use of a dewar in which reservoir of liquid nitrogen is kept in contact with the detector (via a coldfinger). More information on the detectors can be found in CANBERRA Industries website (http://www.canberra.com/products/detectors/).

4.4.2.2 Photon interactions within the detector

In gamma spectroscopy of environmental samples, energies may vary between a few keV up to several MeV, where all type of interactions can take place with the photoelectric effect dominating in lower energies and the Compton effect at intermediate energies and pair production in high energies. When a detector is bombarded with a large number of gamma-rays (with energies greater than 1022 keV, so that the pair production is taken into account) (figure 4.6), we can expect some Compton scattering events, some pair production events and photoelectric absorption (creating the nuclide specific full energy peaks).

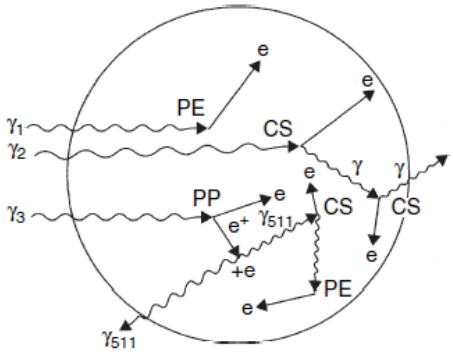

Figure 4.6: Additional possibilities for interaction within a detector (Gilmore, 2008).

[6] The detectors are enclosed in 92-100 mm of lead shielding in order to reduce the amount of radiation from background sources, mainly natural radioisotopes and cosmic radiation, reaching the detector.

There are also other possibilities which give rise to identifiable features in our spectrum, such as the single and double escape peaks, created due to the loss of energy absorbed caused by the escape of one or both annihilation photons, multiple Compton events appearing in the spectrum between the Compton edge and the full energy peak, backscatter peak caused by the backscattering of gamma rays by the detector shielding and pile-up, seen as a continuum above the full energy peak caused not by the interaction of gamma-rays with the detector itself, rather than from summing of the energy of more than one gamma-rays arriving in the detector simultaneously (random summing).

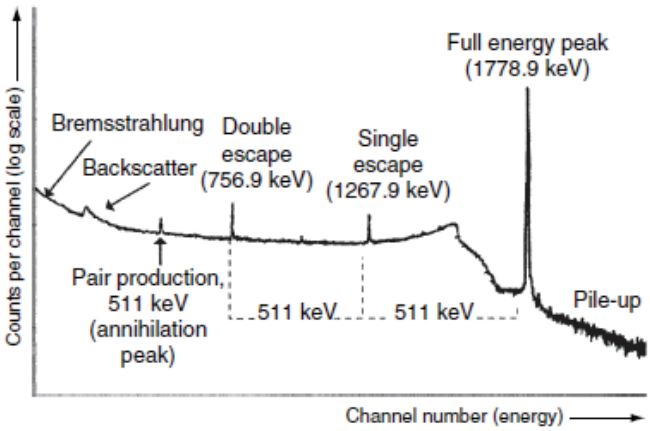

Figure 4.7: ^{28}Al spectrum illustrating the various spectral features expected (Gilmore, 2008).

4.4.2.3 Electronics for gamma spectrometry

The purpose of the electronics of a gamma spectroscopic system is the transfer of the electrical charge, proportional to the amount of gamma-ray energy absorbed by the detector, from the detector to the multichannel analyzer (MCA) with as little alternation as possible.

More specifically, high voltage is applied in the detector crystal which sweeps the electrons and collects the charge created by the interaction of photons with the detector. The bias voltage must be as high as possible, since the charge collection improves with increasing voltage and at the same time low enough to avoid breakdown. The bias supply in our lab detectors is set between 4 and 5.2 keV. The charge arrives in the preamplifier which is part of the detector assembly and is converted to a voltage. The pulse is then sent to the amplifier where it is shaped and its size increased, with the height of the pulse being proportional to the amount of charge collected in the detector and if photoelectric absorption took place then it should be proportional to the energy of the incident photon. The pulse is afterwards converted to digital information in the analog to digital converter (ADC) and transferred to the MCA. The MCA analyzes the stream of pulses, by sorting them according to pulse height and counting the number of pulses within individual pulse height intervals. This information is stored as a spectrum of number of events vs pulse-height which relates linearly to energy, in our spectroscopic systems. A computer is required for the visualization of the spectrum and for performing analysis using spectrum analysis software; Genie 2000 Spectroscopy Software by Canberra used in our laboratory has the capabilities for acquiring and analyzing spectra from MCAs. Examples of two spectra from samples collected

from river water and river sediments follow in figures 4.8 and 4.9. In the spectra several lines are visible corresponding to specific isotopes, the activity of which is calculated and reported after analysis of the spectrum (see §4.5).

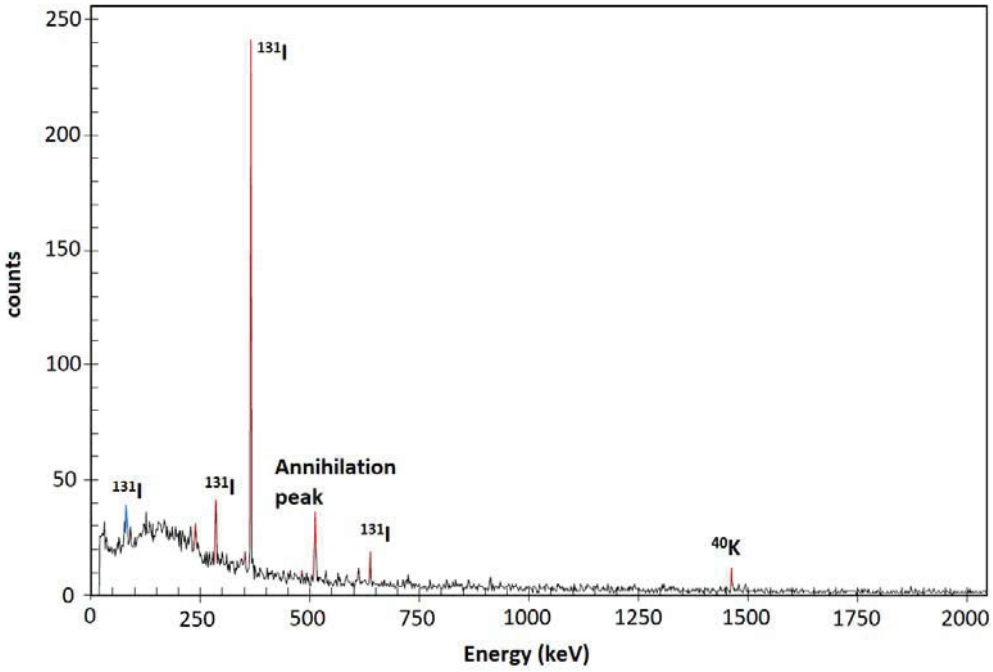

Figure 4.8: Water sample spectrum. Multiple lines of ^{131}I are visible along with natural ^{40}K.

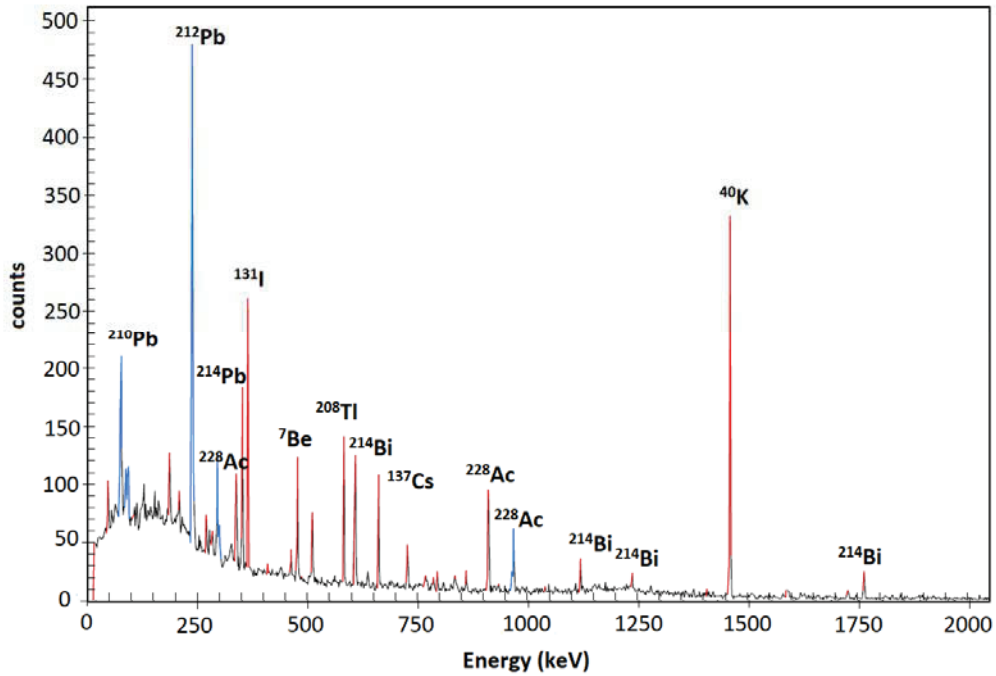

Figure 4.9: Sediment spectrum. Several natural isotopes (^{210}Pb, ^{212}Pb, ^{214}Pb, ^{212}Bi, ^{214}Bi, ^{208}Tl, ^{228}Ac and ^{40}K) and manmade ^{131}I and ^{137}Cs are present.

4.5 Gamma spectrum analysis

For the determination of the activity of the radionuclides present in our samples, several steps during spectra analysis need to be taken into account, available in the Genie 2000 software offered by Canberra, further described in this section.

4.5.1 Calculation of calibration curves

Energy calibration

Energy calibration allows the gamma spectrum to be interpreted in terms of energy through a linear relationship (see §4.4.2.3) by relating the peak position in the spectrum to the corresponding gamma-ray:

$$E = a \cdot ch + b \qquad \textit{eq. 4.4}$$

Where

E the energy of the gamma-ray in keV,
ch the channel number of the MCA,
a the gradient and
b the offset of the linear relationship.

For the energy calibration of our spectra most common lines used were ^{131}I at 364.5 keV, the annihilation peak at 511 keV and the ^{40}K at 1460.8 keV. Since only two peaks are necessary for the determination of the gradient and offset, the annihilation peak was used for energy calibration when the ^{131}I peak's centroid was not clearly visible. Upon calibration other full energy peaks present in the spectrum could be identified and used for an additional confirmation of proper energy calibration (eg. ^{137}Cs, ^{7}Be, ^{212}Pb etc).

Peak shape calibration

The **peak shape calibration** uses a modified Gaussian function to describe the peaks (calculation of peak centroid, height, FWHM and possibly tail parameter values) and has the capacity of recognizing overlapping peaks. Genie's automated peak search and fitting (Canberra, 2006) is done by relating the peak full-width at half-maximum (FWHM in units of channels) as a function of energy:

$$FWHM = \frac{F_0 + F_1\sqrt{E}}{a} \qquad \textit{eq. 4.5}$$

where

E is the energy in keV,
F_1 and F_0 are the coefficients of the FWHM equation and
a the 'gain' term from the energy calibration equation.

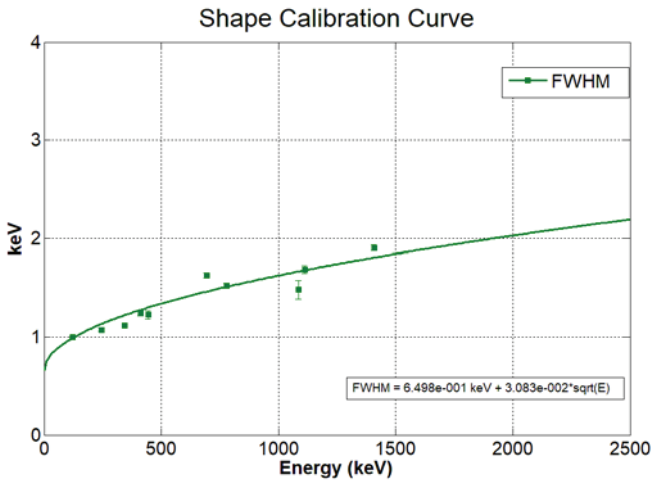

Figure 4.10: Shape calibration curve in Genie 2000. Measured FWHM data points are fitted using equation 4.5.

Gilmore (2008) argues that the Genie 2000 fit is clearly not satisfactory opting for a square root or simple quadratic fit. In the case of a non satisfactory fit (visual representation of the fit available through the Interactive Peak Fit function of Genie) there is the possibility of manual interventions.

Full energy efficiency calibration

The **full energy peak efficiency (FEP) calibration** relates the peak area at a particular energy to the number of gamma-rays emitted by the source and depends on the geometrical arrangement of the source and detector and the sample matrix. The determination of the efficiency curve for a specific geometry and matrix can be done by experimental (i.e. physical) and/or by mathematical calibration.

Regardless of the data used (experimental or mathematical), Canberra software (Canberra, 2006) fits the calibration curve with a polynomial of the form:

$$\ln(\varepsilon) = \sum_{i=0}^{n} b_i \cdot (\ln(E))^i \qquad \textit{eq. 4.6}$$

where

b_i the coefficient to be determined by the calculation and

ε the FEP efficiency at the photopeak energy E.

An extension, called the dual function offers the possibility of either one single curve or two curves, one for the low and one for the high energy region with a single "crossover point" common to both curves. The latter option is used for all the calibration curves used in this work.

The experimental calibration is based on the use of a source or solution of known activity which is measured in different geometries and matrices and the calculation of the full energy peak efficiency for each nuclide (in the case of a multinuclide solution) is done as:

$$\varepsilon(E) = \frac{S}{t_L f A U_f K_w} \qquad \textit{eq. 4.7}$$

where
$\varepsilon(E)$ is the efficiency at energy E,
S the net peak area of the calibration peak,
t_L the live time[7] of the measurement,
f the branching ratio[8] of the calibration nuclide at this energy,
A the source activity at the source reference time (certificate time) and
K_w is the decay correction factor to correct the activity A to the activity at the time of the start of acquisition equal to $K_w = \exp(-\ln 2 \cdot t_w / T_{1/2})$, with t_w the decay time of the calibrations source and $T_{1/2}$ the half life of the calibration nuclide.

Experimental efficiency curves have been constructed for the detectors 4, 5 and 6 in our lab with the standard geometries being the Marinelli beaker in several sizes (0.5, 1 and 2 L) for water (density ρ =1 g/cm^3) and soil samples (ρ=1.5 g/cm^3), the plastic bottle of 0.5 L (PE-LD bottles) in different filling heights for both water and soil samples, filters (diameter 55 mm) and pressed tablets for soil samples (diameter 20 mm, varying height 5, 10 and 20 mm).
Mathematical methods are especially useful in the calibration of non-standard geometries, creating ad hoc calculated efficiencies for each specific sample, instead of creating pre-defined source-geometries with calibration solutions which would increase the cost of materials and (especially) labor. Monte Carlo computer codes, as MCNP (Monte Carlo N-Particle Transport code), can be used to model the source and the detector, however the software is complex and requires the use from experts, while the generation of the efficiency data with acceptable precisions could take hours or even days. Ray tracing methodology is another approach and although one can simulate the efficiency responses at different gamma-ray energies, there is lack of consideration on the multiple interactions that take place inside a gamma detector (Venkataraman and Nakazawa, 2012).
A combination of these two methods is the ISOCS (In Situ Object Counting System) program by Canberra, which calculates efficiency curves for user-defined source geometries. An improved version, LabSOCS (Laboratory Sourceless Calibration Software) allows measurements at close geometry and has improved attenuation corrections, is offered by Canberra since 1999. Several

[7] Live time is the total counting time minus the dead time (total time during which the signals of individual decay events are processed and no other events can be registered).
[8] Branching ratio is the ratio of the number of nuclei of an isotope decaying via a specific decay mode with respect to the total nuclei of the same isotope which decay via all decay modes.

papers and studies (Bronson, 2003), (Venkataramann et al., 2005), (Venkataraman and Nakazawa, 2012) are devoted to the validation of the accuracy of the LabSOCS software for germanium detectors. Bronson (2003) showed that the LabSOCS mathematical efficiency calibration creates results that are accurate to within 4 - 5 % at energies greater than 400 keV (for energies between 150 and 400 keV the uncertainty rises to 6 %), which comparing to 3 - 5 % of total uncertainties that source-based efficiency calibration typically have, seems acceptable for most laboratory assay processes.

LabSOCS can only be used in connection with a detector that has been characterized by Canberra by MNCP and measurements with point sources. The characterization is done at the factory where all the information on the detector's dimensions, its mounting and housing hardware are given to a MCNP model. Then a large data set on point computations covering energy range of 50 - 7000 keV and space range of 0 - 50 meters distance and 0-360^{o} angular angle is produced and combined into a series of mathematical equations whose parameters are detector specified. Calibrations can then be performed for the specific characterized detector for many different shapes (cylindrical objects viewed from end or the side, box-shaped objects and Marinelli beakers), different matrices (of any elemental composition and density) in different locations on the detector axis or offset from it and/or aligned or at different angle with the sample axis.

In our laboratory detector 3 is the only detector characterized by Canberra[9]. Examples on efficiency curves produced by LabSOCS for different geometries are given in the figures 4.11-4.14.

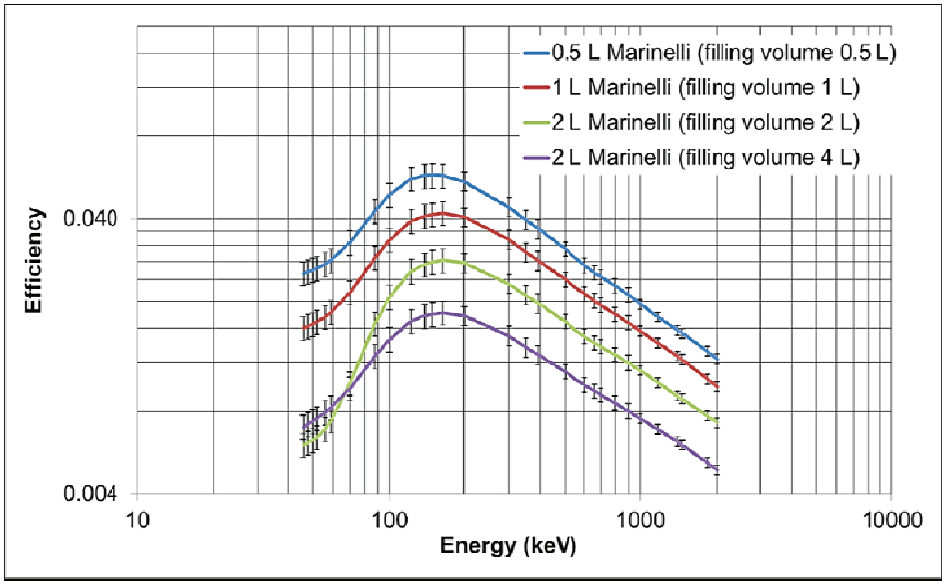

Figure 4.11: Efficiency calibration curves for different Marinelli geometries with filling volumes of 0.5, 1, 2 and 4 L produced by LabSOCS for detector 3.

[9] Detector 2 in our laboratory is also characterized by Canberra, however it is not used for any measurements of this work.

In total more than 70 efficiency curves were produced for the samples measured in this work. The WWTP effluent was measured in 2 L Marinelli (filled up to a volume of 4 L corresponding to a filling height of 163 mm), 0.5 and 1 L Marinelli were used when measuring bentonite precipitate, 2 L Marinelli for the Fe precipitate or for the combined Ca and bentonite precipitate (see §5.3.12). Additionally, 0.5 L Marinelli beakers were used for measuring bank sediment samples (see §6.6). The majority of the created efficiencies (43), were developed for the measuring of the precipitate formed from the river water samples (see §6.5) in geometries of 0.5 L Plastic bottles with varying sample height (20 - 100 mm) and density (0.8 - 1.3 g/cm^3). Pittauerova (2013) studied the effect of the sample height and distance from the detector on a PMMA dish filled with water. Similarly in an effort to produce as precise results as possible a comparison of efficiency calibration curves for different filling heights and densities on a 0.5 L plastic bottle follows (figures 4.12 and 4.13).

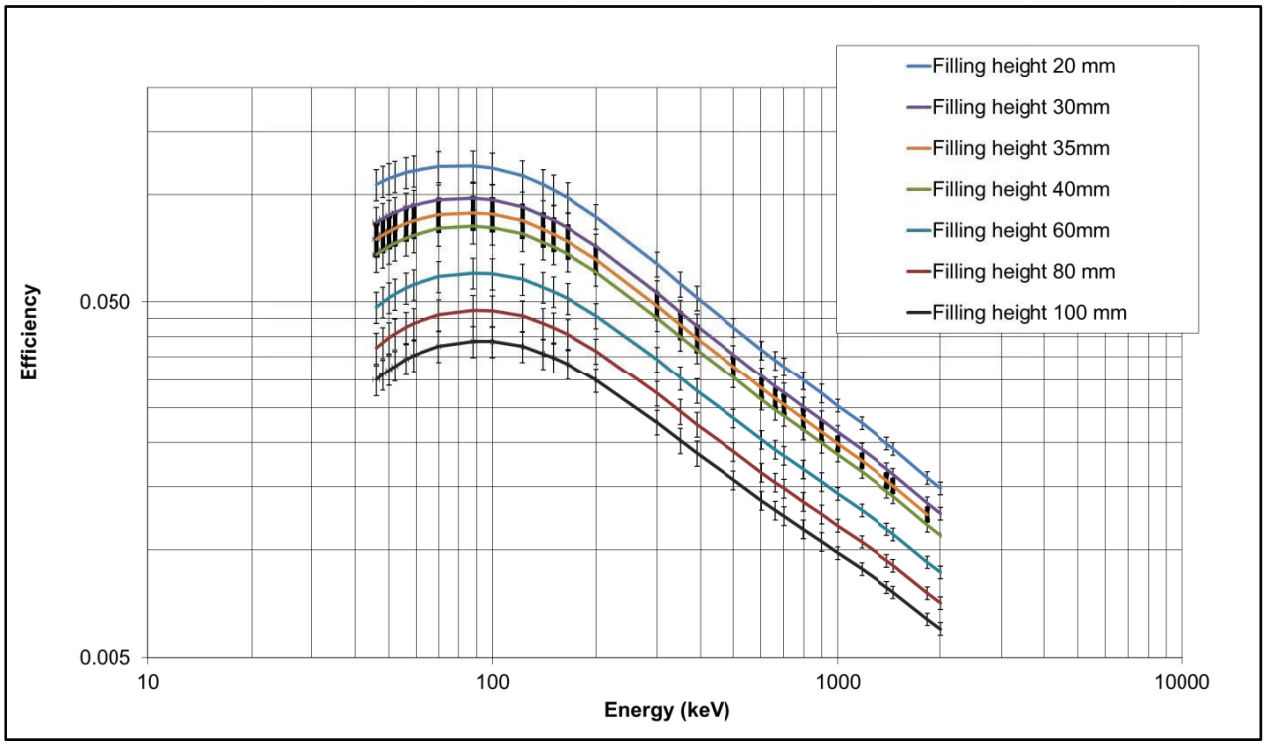

Figure 4.12: Efficiency calibration curves for different filling heights on a 0.5 L plastic bottle with constant density of 1.0 g/cm^3 produced by LabSOCS for detector 3.

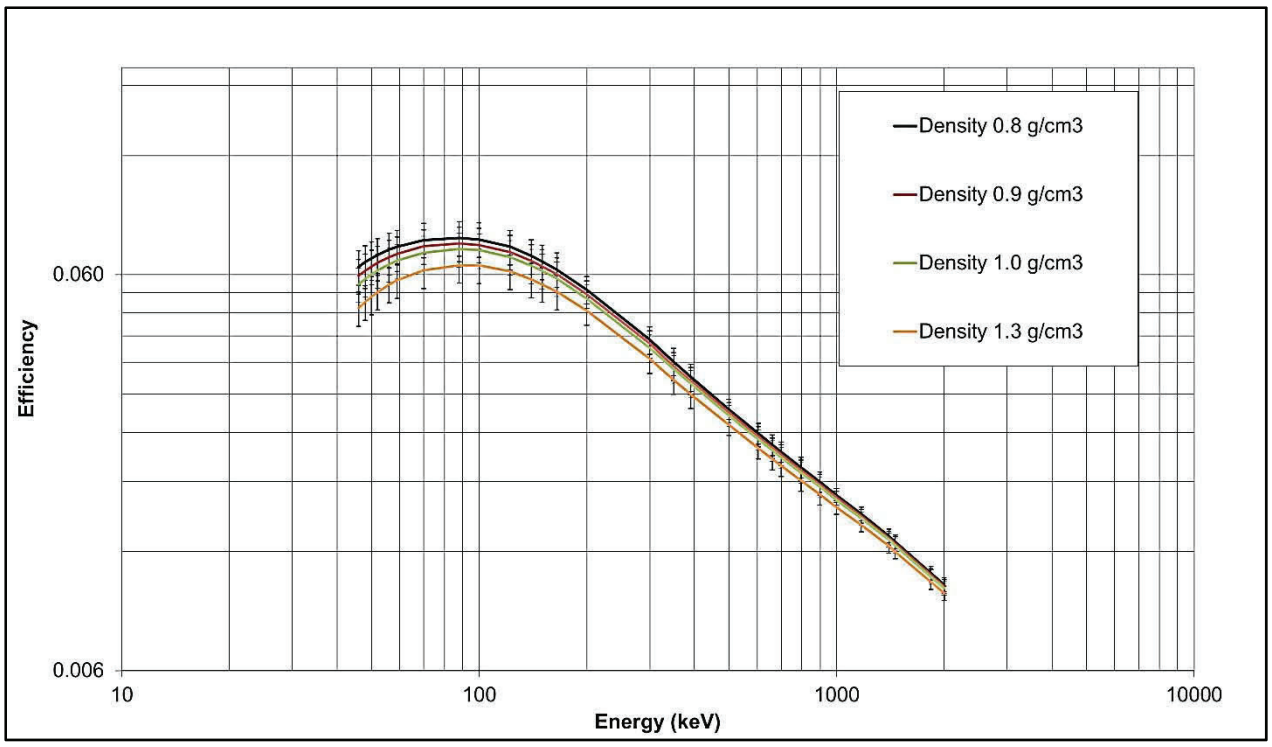

Figure 4.13: Efficiency calibration curves for different filling densities on a 0.5 L plastic bottle with constant filling height of 50 mm produced by LabSOCS for detector 3.

It is evident that for the same density, different filling heights (20 – 100 mm) cause the efficiency to vary by a factor of 6 (figure 4.12), which can influence our results significantly. For the same filling height and different densities (0.8 – 1.3 g/cm^3) the effect is not so pronounced. For each filling height and density a corresponding efficiency could be created, however it would be time taking and unnecessary. It is more practical to group the geometries with the criterion of overlapping error bars of efficiency A with the values of efficiency B. For example in figure 4.12 the error bars of efficiency (A) with filling height 35 mm and density 1.0 g/cm^3 (illustrated with bold lines), overlap the values of efficiency (B) with filling height 40 mm and density 1.0 g/cm^3. Thus in an effort to be as accurate and precise as reasonable the grouping of the efficiencies was done for 5 mm filling height and 0.1 g/cm^3 density.
The efficiency values for each measurement done in this work can be found in appendices 1, 2 and 6.

4.5.2 Peak location and area

Genie 2000 locates all peaks in the search region significantly above the continuum by using a generalized second difference method. The gamma spectrum analysis method used is the SAMPO80, method best suited for applications where the radionuclides present in the sample are not known in advance (Canberra, 2006). The algorithm locates the peaks of the spectrum above specified threshold levels and identifies their centroids by finding positions of the function's

seconds difference minima. In combination with the "Sum Non-Linear Least Squares Fit" peak analysis function, the limits of the peak region are defined and the peak areas along with their uncertainties are calculated for both singlet and multiplets. The calculation is done by assuming a best fit function, through the set of data point belonging in the peak region (channel number and counts per channel) and determining its free parameters. The free parameters are determined by minimizing the sum of weighted differences between the counts per channel at each channel of the peak region and the function's output for each corresponding channel.
Each individual peak defined and its fitting can be further inspected and if necessary corrected through the "Interactive Peak Fit" subprogram. The corrections made under the scope of this work fitted the 364.5 keV peak as a singlet with a fixed FWHM and fixed low tail. An example of such correction is given in figure 4.14.

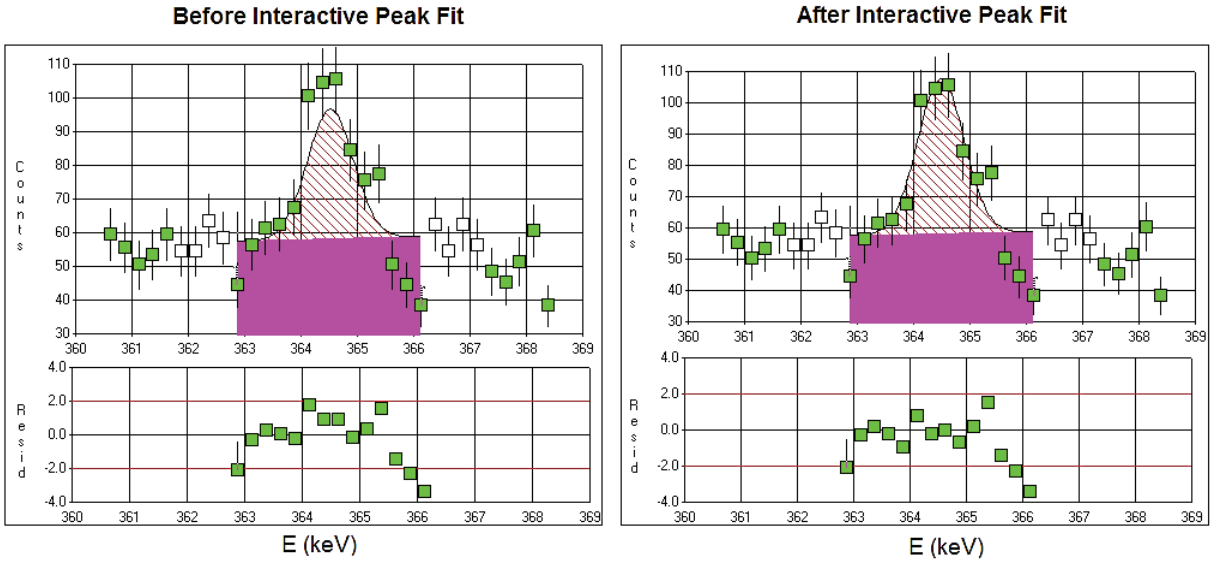

Figure 4.14: An example of interactive peak fit use. Wrongly fitted 364.5 keV peak can be corrected by setting the FWHM and the low tail as fixed parameters. The FWHM was corrected from 0.96 to 0.97 keV, the peak area uncertainty was reduced from 32.7% to 14.7 % resulting in ^{131}I activity change from (1.05 ± 0.34)mBq/kg to (1.48 ± 0.22)mBq/kg.

These corrections were done for 38 cases (from a total of 122 measurements), corresponding to measurements on ^{131}I activity concentrations on river water. The activity concentration before and after the fitting along with the difference is given in Appendix 14. By fitting the peaks and recalculating the activity and its uncertainty, one can achieve reduction in the uncertainty from 0.3 up to 64 % which provides better accuracy in our experimental results.

4.5.3 Background subtraction

The calculation of the net peak area and its uncertainty is done by using the following formulas (Canberra, 2006):

$$S = (G - B) - I \qquad \textit{eq. 4.8}$$

and

$$\sigma_S = \sqrt{\sigma_G^2 + \sigma_B^2 + \sigma_I^2} \qquad \textit{eq. 4.9}$$

where:

G and σ_G the gross counts and its uncertainty in the peak region of interest (ROI),

B and σ_B the continuum subtracted from the gross counts which gives the net area and its uncertainty.

I and σ_I the number of counts above the continuum due to the environmental background and the corresponding uncertainty, in the case of ^{131}I there is no environmental background (in contrast to natural isotopes, eg. ^{40}K).

Background measurements are regularly performed in the lab, approximately once a month and a typical spectrum is given in the following figure. One can observe several lines corresponding to natural radioisotopes, such as ^{40}K, ^{214}Bi and ^{214}Pb. In the energy region close to 364 to 365 keV no characteristic line exists.

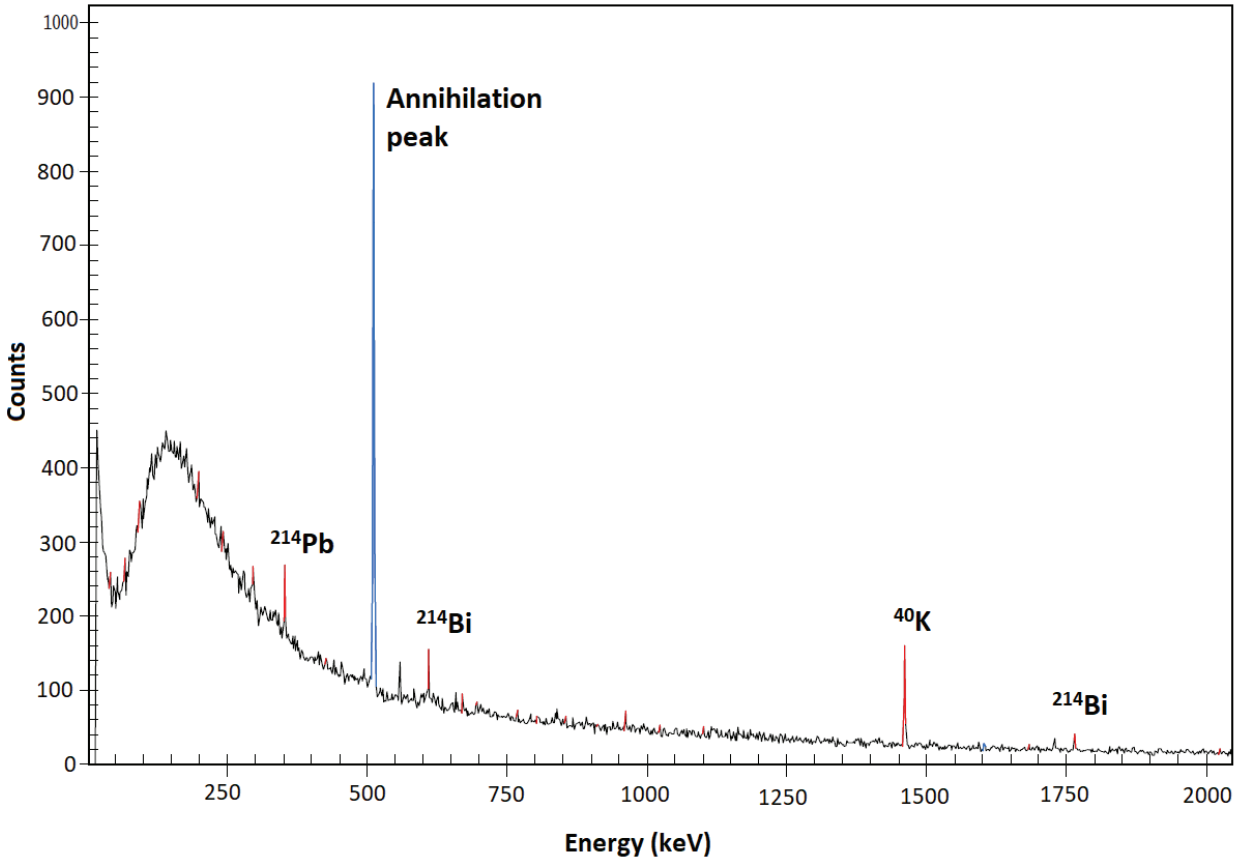

Figure 4.15: Background spectrum from detector 3 (t_L=505524 s).

4.5.4 Efficiency correction

For each of the located peaks the efficiency and its uncertainty are obtained. For dual efficiency calibration curves, as in our cases, equation 4.6 is used for the calculation of the energy dependent efficiency.

4.5.5 Nuclide Identification

The selection of the appropriate nuclide library is necessary for the calculation of the activity of the radionuclides present in our sample. Canberra (2006) calculates the specific activity (C) and its uncertainty (σ_C) utilizing the following equations:

$$C = \frac{S}{V \cdot \varepsilon \cdot y \cdot T_l \cdot K_C \cdot K_w} \qquad \textit{eq. 4.10}$$

and

$$\sigma_C = C\sqrt{\left(\frac{\sigma_R}{100}\right)^2 + \left(\frac{\sigma_S}{S}\right)^2 + \left(\frac{\sigma_V}{V}\right)^2 + \left(\frac{\sigma_\varepsilon}{\varepsilon}\right)^2 + \left(\frac{\sigma_y}{y}\right)^2 + \left(\frac{\sigma_K}{K}\right)^2} \qquad \textit{eq. 4.11}$$

with

S: the net peak area and σ_S its uncertainty

V: the sample volume or mass and σ_V its uncertainty

ε: the efficiency and σ_ε its uncertainty,

y: the emission probability of the peak energy and σ_y its uncertainty

T_l: the live time of measurement in seconds

K_c and K_w the correction factors for the nuclide decay during measurement and from the time of sampling to the start of the gamma measurement respectively, calculated as $K_C = \frac{T_{1/2}}{\ln(2)t_C}\left(1 - e^{\left(-\frac{\ln(2)t_C}{T_{1/2}}\right)}\right)$ and $K_W = e^{\left(-\frac{\ln(2)t_W}{T_{1/2}}\right)}$ with $T_{1/2}$ the half-life of the radionuclide, t_C the elapsed real time and t_W the elapsed time from the time of sampling to the start of the measurement. All the samples collected were decay corrected to the sampling date and time.

σ_K: the uncertainty of the composite decay correction factor K; $\sigma_K = K\sqrt{\left(\frac{\sigma_{K_C}}{K_C}\right)^2 + \left(\frac{\sigma_{K_W}}{K_W}\right)^2}$ with σ_{Kc} and σ_{Kw} the uncertainties for the decay correction factors K_C and K_W respectively.

In the case of multiple lines per radionuclide or interference with lines of other nuclides, additional calculations are made. Pittauerova (2013) suggests using multiple lines of the same radionuclide for activity determination with the aim of reducing the counting uncertainty. However in the majority of our samples only the 364.5 keV line of ^{131}I is detectable and is used for the isotope quantification.

4.5.6 Minimum Detectable Activity (MDA) determination

Currie (1968) on his paper on the limits for qualitative detection and quantitative determination defines the critical limit, $L_{C,}$ as the net signal level above which an observed signal may be recognized as detected and the detection limit, $L_{D,}$ as the net signal level which may be a-priori expected to lead to detection.

In Canberra (2006) the critical level test criterion is calculated as:

$$L_C = k\sqrt{B + \left(\frac{T_S}{T_B}\right)\cdot I_b + \left(\frac{N}{2n}\right)^2 (B_1 + B_2) + \left(\frac{T_S}{T_b}\right)^2 \sigma_{I_b}} \qquad \textit{eq. 4.12}$$

where

k: the k-value dependent on the confidence level, at the 95% confidence level equal to 1.645 for α=0.05 (first kind error: wrongly deciding a signal present when its not) and 1-β=0.95 (second kind error: wrongly deciding a signal is not present when it is) .

B: the value of the continuum subtracted

T_s: the live time of the sample measurement

T_b: the live time of the background measurement

I_b: the net peak area of the background measurement and σ_{Ib} its uncertainty

N: the number of channels in the peak region

n: the number of channels each side of the peak region used for determination of the continuum counts

B_1: the sum of counts in the n-channels left of the peak region

B_2: the sum of counts in the n-channels right of the peak region

If the net peak area is less than L_C then a "non-detected" decision is made and if greater a "detected" decision is made.

The detection limit is calculated according to the German Nuclear Safety Standards Commission (KTA, 2017) as:

$$L_D = 0.5\cdot(2k)^2 + 2\cdot L_C \qquad \textit{eq. 4.13}$$

Genie algorithm calculates the MDA using eq. 4.10 by replacing the net peak area by the detection limit. Similar calculations can be done for the detection threshold, where the net peak area is replaced by the critical limit. Both L_C and L_D are given then in activity concentration terms. A simple approximation valid for our measurements gives a difference of a factor of two between the Genie MDA and the detection threshold.

4.6 Quality Assurance of Gamma Detectors

To ensure reliability of our gamma measurements, quality assurance measurements are preformed periodically using the Genie 2000 QA module, which offers the capability of monitoring the performance of our spectroscopic systems. Additionally, statistical analysis, reporting and plotting options are provided for tracking the system performance and stability over time (Canberra, 2002). On a monthly frequency parameters such as the peak centroid, FWHM and energy at 60, 105 and 1274 keV, along with the mean activity of both isotopes are tested for consistency, with a test source of ^{155}Eu/^{22}Na (1μCi/1μCi; manufactured at 25.02.2004) in a predetermined geometry ((10 ± 0.2) cm distance from the detector) and live time (300 s). The result is illustrated in a control chart.

In a similar way, for ensuring non-contaminated status of the detectors, background spectra are analyzed and control charts are created for the natural isotopes ^{214}Bi (609 keV, 1764 keV), ^{214}Pb (351 keV) and ^{40}K (1461 keV).

In addition to the QA tests, our laboratory participates in several yearly intercomparison tests in different matrices (soil, water, milk etc.) with the radionuclide standards provided by accredited laboratories for the preparation of standards and the Federal Office for Radiation protection (Bundesamt für Strahlenschutz).

Furthermore the nuclear data used are frequently updated and compared to the latest reference data from internationally evaluated nuclear data files offered by Nucleonica and the Brookhaven National Laboratory.

4.7 General Comment on Chapter 4

This chapter focused on presenting the theoretical background on gamma spectroscopy; the physics of radiation, the gamma spectroscopic system and its electronics and the analysis of gamma spectra. Each of the subchapters is only a glance of the covered topic and whole books have been dedicated to them. Although the topics are covered in this chapter are the tip of the iceberg for what is called gamma spectroscopy, they are presented in a precise, compact and comprehensible way offered as background material on the experimental methods and instrumentation used.

4.8 References for Chapter 4

Bronson F. L., 2003. *Validation of the accuracy of the LabSOCS software for mathematical efficiency calibration of the Ge detectors for typical laboratory samples.* Journal of Radioanalytical and Nuclear Chemistry, 225,1, 137-141.

Canberra, 2002. *Model S505 QA Software. User's Manual*.

Canberra, 2006. *Genie 2000 Spectroscopy Software – Customization Tools*.

Canberra, 2008. *Genie 2000 Quality Assurance Software.*

Currie L.A., 1968*, Limits for qualitative detection and quantitative determination. Application to radiochemistry*. Analytical Chemistry, 40 (3), 586-593.

Debertin K. and Helmer R., G., 1988. *Gamma and X-ray Spectrometry with Semiconductor Detectors*. Elsevier Science Ltd.

FAS, *2017, Federation of American Scientists, https://fas.org/nuke/guide/usa/doctrine/dod/fm8-9/1ch2.htm*

Gilmore, G., 2008. *Practical gamma-ray spectrometry*, Second Edition, John Wiley & Sons Ltd.

KTA, 2017. *KTA 1504 Überwachung der Ableitung radioaktiver Stoffe mit Wasser.*Retrieved from: http://www.kta-gs.de/d/regeln/1500/1504_r_2015_11.pdf

National Nuclear Data Center, 2017. Retrieved from: https://www.nndc.bnl.gov/chart/reColor.jsp?newColor=dm

Pittauerova D., 2013. *Gamma Spectroscopy for chronology of recent sediments.*PhD-Thesis, Department of Physics and Electrical Engineering, University of Bremen. Retrieved from: https://elib.suub.uni-bremen.de/edocs/00103560-1.pdf

Venkataraman R., Bronson F., Atrashkevich V., Field M., Young B. M., 2005. *Improved detector response characterization method in ISOCS and LabSOCS*. Journal of Radionalytical and Nuclear Chemistry, 264, 1, 213-219.

Venkataraman R., and Nakazawa D., 2012. *The Role of Mathematical Methods in Efficiency Calibration and Uncertainty Estimation in Gamma Based Non-Destructive Assay – 12311*. WM20152 Conference, February 26-March 1, 2012, Phoenix, Arizona, USA. Retrieved from: http://www.wmsym.org/archives/2012/papers/12311.pdf

Chapter 5

Chemical extraction of ^{131}I

In Weser river water, ^{131}I concentrations have been detected as low as 0.7 – 4 mBq/kg (Souti, 2012), (Gellermann et al., 2013) requiring low detection limits to be reached for successful ^{131}I detection. For example, a 4 L sample measured in 2 L Marinelli container (as described in §2.5) can reach a detection limit of 50 mBq/kg on a 24 h measurement, while for the same measuring time a 50 L sample in a 0.5 L plastic bottle with filling height of 50 mm (volume: 217 cm^3) can reach 1.5 mBq/kg as detection limit. Thus a chemical extraction of ^{131}I in bulk river water samples is necessary, which will not only reduce the volume of the river water samples for measuring purposes (50 L samples do not fit in our gamma detectors) but will increase the efficiency of the measurement (in detector 3, the efficiency of a 4 L water sample measured in 2 L Marinelli container at energy of 364.5keV is 0.01323, while the efficiency for the same sample in a 0.5 L plastic bottle with filling height of 50 mm is 0.03365).

5.1 Iodine Chemistry

Iodine is a member of the halogen family (fluorine, chlorine, bromine, iodine and astatine). It is solid at room temperature and is the least abundant of the stable halogens. Although it is the least reactive of the stable halogens, it is still one of the most reactive elements, exhibiting complex biogeochemical behavior with six major oxidation states (-1, 0,+1,+3,+5 and +7). It occurs in various species with unique hydrophilic, atmophilic and biophilic characteristics.
Elementary iodine reacts slowly with metals, eg. magnesium, which form non-volatile iodides, and forms compounds with all the elements except the noble gases, sulfur and selenium, but only reacts indirectly with carbon, nitrogen and oxygen (Lyday, 2012).
In freshwater the dominant inorganic forms of iodine are iodide, I^- (oxidation state -1) and iodate, IO_3^- (oxidation state +5) in which iodine exists stably under oxic conditions for most pH values (Nagata and Fukushi, 2010). Figure 5.1 illustrates the major chemical forms of inorganic iodine in aqueous solutions. In addition to the aforementioned dominant forms several other exist (periodate; IO_4^-, iodic acid; HIO_3, periodic acid; HIO_4, hydroxyperiodate; HIO_5^-, hydroperoxyperiodate; HIO_6^-).

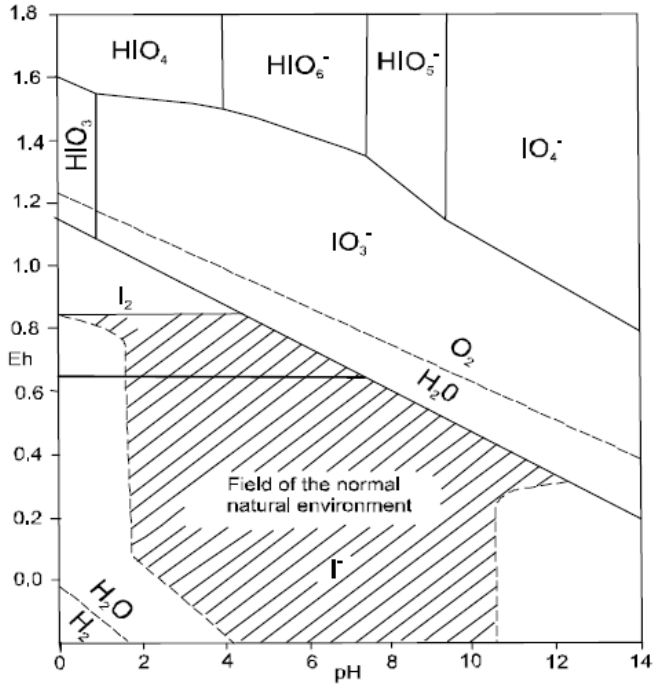

Figure 5.1: The major chemical forms of inorganic iodine in aqueous solutions (Bunprapob, 2010).

However, a significant fraction of the total iodine in environmental aqueous systems is organically bound. Hu et al. (2005) found up to 50% of the total iodine as organic iodine under environmental conditions, while Kulyukhin et al. (2010) report values up to 67 % in samples from estuaries, rivers and rain.

Hu et al. (2005) report that the inorganic iodine can be incorporated into humic substances with the aid of microorganisms (also present in WWTPs) and change its physio-chemical characteristics, finding additionally supported by Rädlinger and Heumann (2000). Hormann and Fischer (2017) suggest the most dominant species of ^{131}I in the outflow of the WWTP to be inorganic or low molecular organic.

5.2 Iodine separation methods

In gamma spectroscopy and the application of semi-conductor detectors, chemical separation of radionuclides is seldom required. However, in cases of short half-lives and low concentrations, where more precise methods such as mass spectroscopy[1] cannot be used, chemical separation of radionuclides in bulk samples allows a considerable reduction of the minimum detectable activity in the samples.

[1] Mass spectroscopy is used for ^{129}I determination, since its long half-life (1.57×10^7 y) allows time taking preparation techniques.

In the literature, the same traditional methods used for chemical separation of stable isotopes are also used for radionuclides, since nearly always they behave chemically identically. The most common methods used in inorganic analysis include precipitation, ion exchange and liquid extraction (Lehto and Hou, 2011).

Several methods have been developed for the use of ion resins in the extraction of the inorganic compounds of iodine (I_2, I^-, IO_3^-) with high chemical yields. Zulauf et al. (2010) describe a separation method using Ag^+ loaded Cl resin with a yield of (92 ± 9) % for ^{129}I, while Decamp and Happel (2013) prepare mixed-bed columns using the aforementioned resin in combination with a non-polar resin (XAD-4 resin) used to remove molecular iodine from solution reaching a higher iodine recovery of (95 ± 3) %. Parekh et al. (2003) report recovery of ^{129}I almost quantitatively (> 99 %) with the use of Dowex 1x8 (50 - 100 mesh) Cl-form resin. Lehto et al. (2012) report separation of iodide and iodate ^{129}I species of approximately 74 % (range: 63 - 81 %) from sea, lake and rain waters using the BIO-RAD AG1 anion exchanger.

Another common method for the extraction of iodine includes its precipitation as AgI, CuI or co-precipitation with AgCl and $Ag_4[Fe(CN)_6]$. Mundschenk (1993) describes an easy procedure for surface waters, where ^{131}I precipitates as AgI with a yield of (90 ± 4) % (see also §5.3). Kulyukhin et al. (2010) achieved iodine recovery by co precipitating with AgCl of (97 ± 2) % from solutions simulating nuclear power plant trap waters[2]. Fan et al. (2012) report a method used for the extraction of ^{129}I from water samples which includes anion exchange chromatography followed by solvent extraction and directly AgI precipitation, where a recovery higher than 70 % is reached.

Apart from these commonly used methods found in literature, inorganic iodine separation has been achieved with high chemical yields using static polyurethane foam column with (95 ± 1) % recovery (Palagyi, 1985) and using solid phase extraction disks impregnated with polyvinylpyrrolidone (PVP) with (95 ± 7) % recovery for I_2, (101 ± 5) % for I^- and (91 ± 3) % for IO_3^- (Grogan and DeVol, 2013).

For determining the speciation or for recovering of total iodine in water samples additional steps need to be realized, to the use of ion exchange resins or precipitation of AgI, which target the organically bound iodine. Reifenhäuser and Heumann (1990) developed a method to determine both inorganic and organic iodine species in aquatic systems by decomposing the organic compounds by UV irradiation followed by AgI precipitation. To determine iodine speciation, Schwehr and Santschi (2003) used dehydrohalogenation (NaOH+EtOH), heat and ultra-sonication for organic iodine in water samples before reduction to iodide and use of anion exchange resin and spectrophotometric detection. Muramatsu and Ohmomo (1988) separated elemental and organic iodide from their water samples with the addition of carbontetrachloride (CCl_4).

[2] Nuclear power plant rap waters include wastes from occasional leakage of the heat carrier, solutions from decontamination of the equipment and solutions formed by washing of building structures contaminated with radionuclides (Kulyukhin et al., 2010).

An alternative method which can be used for bulk samples (in contrast to UV decomposition, heat and ultra-sonication, and with no adverse health effects that may be caused by CCl_4) includes the precipitation of organic iodine along with the total dissolved organic matter (DOM) which can be induced by interaction with metals (Al, Fe, Ca). These metal ions (coagulants) when added to the water, destabilize the particles' charges by neutralizing the negative charges on dispersed non-settable solids (eg. clay and organic substances) since they have opposite charges to those of suspended solids. This charge neutralization allows the small suspended particles to stick together and form slightly larger particles, called microflocs. Further mixing can cause bonding between the microflocs, producing larger flocs whose size continues to build through additional collisions and interaction with inorganic polymers formed by the coagulant, leading to the production of microflocs, masses large enough to settle. Nierop et al. (2002) report Fe(III) creating stronger flocculation than Al at pH=3.5 and Leenheer and Reddy (2008) suggested Ca as a practical application of removing DOM from water samples. This finding is further supported by Sindelar et al. (2015), who conducted a set of experiments in the interactions of phosphorus, calcium and dissolved organic carbon (DOC) and concluded that at high pH values (8.5 – 9.5), DOC can co-precipitate with Ca.

5.3 ^{131}I extraction methods tested in this work

Effluent samples were taken from the local WWTP (Hansewasser Bremen GmbH). Immediately after collection, solid sodium sulfite (Na_2SO_3) was added (20 mg/L) to each of the samples in order to prevent oxidation of I^- to IO_3^-, and they were stirred for 10 minutes. Part of the samples (4 L) was transferred in a 2 L Marinelli beaker (see § 4.5) and measured in a gamma spectrometer overnight in order to obtain the ^{131}I concentration, used as a reference (100 %) value for the extraction experiments. Following the measurement, a chemical extraction method was applied to 20 L samples, as described in the next paragraph.

Published by the Federal coordinating office for surface water, suspended particulate matter and sediment in inland waters, the following method is still the recommended procedure for ^{131}I analysis of surface waters in routine and emergency environmental monitoring in Germany. The procedure developed by Mundschenk (1993) can be easily performed by technical staff, is also applicable in bulk samples and requires chemicals commonly found in chemistry labs, therefore was selected as a starting point in the investigation of ^{131}I extraction methods.

Mundschenk method – Procedure for determining radionuclides in surface water by gamma spectrometry (MM)

The method is based on the precipitation of several nuclides from large volumes (^{54}Mn, ^{58}Co, ^{65}Zn, ^{88}Y, ^{109}Cd, ^{133}Ba, ^{134}Cs, ^{144}Ce, ^{131}I) with the help of flocculants. By excluding the carriers for all isotopes, but ^{131}I, and omitting the steps 3.3.1.3 and 3.3.1.4 of the method a silver iodide precipitate is formed which can be measured directly in wet or dry form. More precisely the following chemicals are added under continuous stirring (stirring speed of 500 - 600 rpm):

Step 1 – 16 µmol/L potassium iodide (KI)
Step 2 – 18.5 µmol/L of silver nitrate ($AgNO_3$)
Step 3 – 1.2 g/L of disodium hydrogen phosphate ($Na_2HPO_4 \cdot 2H_2O$)
Step 4 – 8 ml/L Flygtol A solution (activated montmorillonite - 20 g/L)
Step 5 – Ammonium hydroxide (NH_4OH) (10 mol/L) solution, until pH ≥ 8 and stirred continuously for 30 minutes
Step 6 – 4 ml/L of a flocculating agent (Kerafloc A 4005 S) solution (polyelectrolyte - 2 g/L).

The sample is allowed to settle for at least 1 h, preferably overnight, in order to form a distinguishable precipitate (figure 5.2). After the settling of the precipitate, the supernatant is siphoned off or drawn off and discarded. The precipitate is poured into a 1 L Marinelli beaker and measured in wet state with the addition of cellulose to ensure homogeneity of the sample[3].

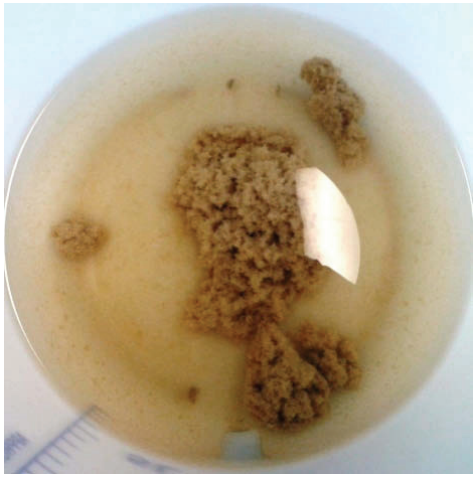

Figure 5.2: ^{131}I precipitate. Container diameter 27.8 cm.

Figure 5.3: Homogenized sample in gamma spectrometer.

[3] Settling of precipitate inside the Marinelli beaker would create a two layer sample with different material –precipitate and water- and different densities thus altering the efficiency.

However, extensive testing of this method reported that ^{131}I attached to DOM is not reliably extracted, since the overall chemical yield of the method varied from (25 ± 4) % to (87 ± 8) % (Ulbrich et al., 2013). This result spurred the need to establish and assess an efficient chemical extraction method for ^{131}I in sewage effluent and river water, applicable to large volumes. In the following paragraph, 12 different approaches in this direction are presented with the majority of the separation methods used being a variation of the Mundschenk method[4] with extensions for precipitating dissolved organic iodine. Each method was tested multiple times and the mean value (calculated as $\bar{x} = \frac{1}{N} \cdot \sum_{1}^{N} x_i$) and range of the chemical yield is determined.

Additional information on the experimental results can be found in Appendix 1.

5.3.1 Method I: MM followed by Fe induced precipitation

This procedure is based on the precipitation of inorganic iodine with the Mundschenk method (formation of 1st precipitate) followed by a Fe induced precipitation for the extraction of ^{131}I bound to organic matter (formation of 2nd precipitate).

More specifically, the supernatant after the Mundschenk procedure is not discarded, rather treated with 4 M nitric acid (HNO_3) until the pH is adjusted to 3 (Nierop et al., 2002). With the addition of 285 mg/L of iron (III) chloride hexahydrate ($FeCl_3 \cdot 6H_2O$), stirring for 10 minutes and allowing to settle overnight, a second precipitate is formed (figure 5.4), collected after siphoning off the supernatant and measured in a wet state in a 1 L or 2 L Marinelli beaker (depending on mass of the precipitate formed) with the addition of cellulose.

Both precipitates are measured in gamma spectrometers (see § 4.5).

Figure 5.4: Fe precipitate after the Mundschenk method

The method was repeated for 13 samples, the mean value of the chemical yield was 94% with a range of (75 ± 15) - (144 ± 46) %.

[4] Methods V, VI and VII include variations of the MM related to step 2, method X to step 3 and method III to step 4.

5.3.2 Method II: Fe induced precipitation followed by MM

This procedure is similar to the method I with the variation of the precipitation step sequence, i.e. first the Fe precipitate is formed and on the supernatant the Mundschenk method is applied. However, the Fe precipitation allowed too many suspended flocs to remain in the solution (figure 5.5) hampering its collection and measurement. Both precipitates are measured in gamma spectrometers (see § 4.5).

Figure 5.5: Fe precipitate before the Mundschenk method.

The method was repeated for 3 samples, the mean value of the chemical yield was 48% with a range of (39 ± 6) - (61 ± 12) %.

5.3.3 Method III: MM (use of specially manipulated Bentonite) followed by Fe induced precipitation

In this variation, the Flygtol A solution added on step 4 is replaced by a solution of the same concentration but different clay material, a special manipulated bentonite provided to us by the Institute of Radioecology and Radiation Protection from the Leibniz University in Hannover (IRS). Michel et al. (2008) prepared the bentonite by dispersing 20 g of clay in a chloride solution for organophilization, stirring for 24 hours, filtering the suspension, washing with distilled water and freeze drying.

After separation of the inorganic iodine a Fe precipitation is induced and a second precipitate is formed. Both precipitates are measured in gamma spectrometers (see § 4.5).

The method was repeated for 3 samples, the mean value of the chemical yield was 88% with a range of (78 ± 13) - (96 ± 13) %.

5.3.4 Method IV: Fe induced precipitation followed by MM (formation of 1 precipitate)

As described in method II, the Fe precipitate formed allowed too many suspended flocs to remain in the solution and in an attempt to produce better results the Mundschenk method was applied directly afterwards providing one precipitate overall, measured in a gamma spectrometer (see § 4.5).

The method was repeated for 3 samples, the mean value of the chemical yield was 47% with a range of (36 ± 5) – (71 ± 10) %.

5.3.5 Method V: MM (use of 10 times higher concentration of $AgNO_3$) followed by Fe induced precipitation

As a result of incomplete separation of iodine in method I, a variation of the step 2 by using a 10 times higher concentration of $AgNO_3$ and following the procedure as before was done, creating 2 precipitates which were measured in gamma spectrometers (see § 4.5).
The method was repeated for 3 samples, the mean value of the chemical yield was 80% with a range of (62 ± 12) - (100 ± 24) %.

5.3.6 Method VI: MM (use of AgOH instead of $AgNO_3$) followed by Fe induced precipitation

A variation of the step 2 in method I was done by adding 0.1 g/L of previously prepared silver oxide (AgOH) instead of $AgNO_3$ based on the findings of Kulyukhin et al. (2010). The preparation of AgOH was done by adding equal quantities of 0.1 M $AgNO_3$ and sodium hydroxide (NaOH) in a beaker while stirring, followed by filtering and washing with distilled water and ethanol. The chemical extraction procedure follows the same steps as mentioned before creating 2 precipitates which were measured in gamma spectrometers (see § 4.5).
The method was repeated for 14 samples, the mean value of the chemical yield was 96% with a range of (75 ± 12) - (132 ± 33) %.

5.3.7 Method VII: MM (use of AgOH additional to AgNO3) followed by Fe induced precipitation

In this procedure the same steps as for method I take place where after the $AgNO_3$ addition (step 2) a supplementary step follows; addition of 0.1 g/L of previously prepared AgOH. Two precipitates are formed, which were measured in gamma spectrometers (see § 4.5).
The method was repeated for 4 samples, the mean value of the chemical yield was 97% with a range of (82 ± 12) - (121 ± 20)[5]%.

[5] The value appears to be >100 %, however is due to mathematical rounding of the values presented in appendix 1. When using values rounded up to the second significant digit, the overall chemical yield is (120 ± 20) %.

5.3.8 Method VIII: ^{131}I extraction with use of Dowex 1x8 resin followed by Fe induced precipitation

Motivated by the almost quantitative recovery of iodine reported from Parekh et al. (2002) we performed their procedure as described with one modification. Instead of passing the water sample through the resin column, we added the prepared resin to the sample, stirred for 2 hours and left to precipitate overnight. This alteration reduces the preparation time (Parekh et al. (2002) pass the sample with a flow rate of 10 – 12 ml/min and our sample would need 83 h to pass through the resin volume with the same flow rate).

After collecting the resin, it is washed twice with distilled water and 100 ml of 2 M sodium chloride (NaCl) before it is placed on a PMMA dish (diameter 70mm - filling height 20 mm) for measurement. The supernatant is treated with the Fe induced precipitation procedure and the 2nd precipitate is measured in a Marinelli beaker after the addition of cellulose.

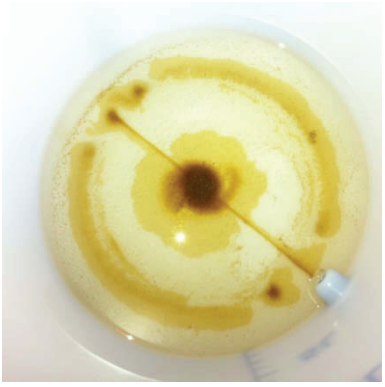

Figure 5.6: Resin precipitate

Figure 5.7: Collection of resin precipitate

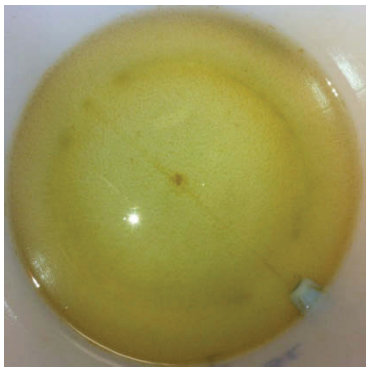

Figure 5.8: Fe precipitate after ^{131}I resin extraction

The method was repeated for 3 samples, the mean value of the chemical yield was 29% with a range of (27 ± 5) - (30 ± 9) %.

5.3.9 Method IX: ^{131}I extraction with use of mixed bed silver loaded Cl resin and XAD-4 resin followed by Fe induced precipitation

Prompted also by the high chemical yield (96 %) reported by Decamp and Happel (2012) a mixed bed of silver loaded Cl resin and XAD-4 resin was prepared for the ^{131}I separation. By repeating the same modification as in method VIII[6], a resin precipitate was formed and measured in 1 L Marinelli beaker after the addition of cellulose. Following the supernatant is treated with the Fe induced precipitation and the 2nd precipitate is also measured in the same geometry.

Due to limited availability of required materials, the method was preformed once giving a chemical yield of (60 ± 10) %.

[6] Decamp and Happel (2012) report higher flow rate than Parekh et al. (2002), 150 ml/min, but still out sample would need close to 6 h to pass through the resin volume.

5.3.10 Method X: MM (excluding the addition of $Na_2HPO_4 \cdot H_2O$) followed by Fe induced precipitation

This procedure is similar to the method I with the variation of excluding step 3, the addition of $Na_2HPO_4 \cdot H_2O$. Both precipitates appeared to have different texture than in method I and especially the Fe precipitate allowed too many suspended flocs to remain in the solution (figures 5.9 and 5.10). Both precipitates were measured in Marinelli beakers with the addition of cellulose for homogenization in gamma spectrometers (see § 4.5).

Figure 5.9: Bentonite precipitate formed with method X

Figure 5.10: Fe precipitate formed with methodX

The method was repeated for 4 samples, the mean value of the chemical yield was 82% with a range of (59 ± 25) - (103 ± 18) %.

5.3.11 Method XI: MM followed by Ca induced precipitation

This procedure is similar to the method I with the variation of organically bound iodine precipitation which is induced with the aid of calcium chloride dehydrate ($CaCl_2 \cdot 2H_2O$). Once collecting the supernatant after the bentonite precipitation the pH value of the solution is adjusted to larger than 8 (Sindelar et al., 2015) by the addition of NH_4OH. Afterwards approximately 175 mg/L of $CaCl_2 \cdot 2H_2O$ is added, the solution gets stirred for 10 minutes and is left to precipitate overnight. Following, the 2nd precipitate formed is collected and measured in a 1 L or 2 L Marinelli beaker in a wet state with the addition of cellulose.

The method was repeated for 3 samples, the mean value of the chemical yield was 86% with a range of (78 ± 12) - (98 ± 15) %.

5.3.12 Method XII: Mundschenk method followed by Ca induced precipitation (formation of 1 precipitate)

This method combines both precipitation methods in one procedure with the formation of one precipitate, minimizing the time required for both chemically extracting and measuring afterwards in the gamma detectors. In more detail, the unfiltered surface water sample gets stirred under a speed of 500 - 600 rpm and the following chemicals are added: 16 μmol/L of KI, which enables the AgI colloid formation, followed by 18.5 μmol/L $AgNO_3$, for creating AgI colloids and an excess of Ag^+ which leads to a positive charge of the almost insoluble AgI particles formed by the reaction $KI + AgNO_3 \rightarrow AgI + KNO_3$. Next 1.2 g/L of $Na_2HPO_4 \cdot 2H_2O$ is added which promotes the cation precipitation. Next the stirring is stopped and 8 ml/L of FlygtolA (20g bentonite per liter) is added which is a substance with a large surface and high adsorptivity. Then the pH of the sample is set to a value higher than 8 by adding NH_4OH and is gets stirred for 30 minutes. Kim (2003) measured the point of zero charge[6] of bentonite to be at pH value of 8, thus the negative surface charge formed on the bentonite particles enhances the AgI colloids to attach. For enhancing the DOM precipitation and hence the iodine bound in organic matter particles, 175 mg/L of $CaCl_2 \cdot 2H_2O$ is added under constant stirring for 10 minutes. Finally 4 ml/L of Kerafloc solution (2g/L) is added and stirred for 3 more minutes. Kerafloc brings about agglomeration of the small primary flocs (after less than a minute of stirring), as a result of charge exchange; the large flocs thus formed settle rapidly. The sample is left (to precipitate) overnight. Then the combined bentonite - Ca precipitate is collected and measured in a wet form in a 2 L Marinelli beaker. The method was tested on 36 samples and the results are given in table 5.1.

Table 5.1: Values of ^{131}I activity concentration in original WWTP water, calculated from the precipitate after the extraction using method XII and the subsequent determination of chemical yield (see Appendix 1).

Original WWTP effluent ^{131}I activity concentration (mBq/kg)	WWTP effluent ^{131}I activity concentration calculated from the precipitate (mBq/kg)	Chemical yield (%)
168 ± 18	143±6	85±13
454 ± 28	413±15	92±9
501±32	440±24	88±10
199±22	165±8	83±13
238±24	164±9	69±11
194±20	161±11	83±14
191±20	142±9	74±12
171±21	153±11	89±17
250 ±27	158±10	63±11
217 ±23	146±10	67±12
167±20	174 ±10	104±18
207±25	166±10	80±15
170±19	158±9	93±16
191±21	172±8	90±14
215±21	168±7	78±11
201±21	166 ±7	83±12
214 ±21	158 ± 12	74±13
214±17	153±13	71±12

Original WWTP effluent ^{131}I activity concentration (mBq/kg)	WWTP effluent ^{131}I activity concentration calculated from the precipitate (mBq/kg)	Chemical yield (%)
217±24	136±11	63±12
162±21	160±13.	99±21
115±20	104±7	90±22
119±21	110±5	92±21
111±14	99±5	89±16
80±15	105±5	131±31
106±21	103±8	97±27
83±13	102±10	123±31
120±12	100±8	83±15
138±20	96±9	70±17
146±21	97±10	66±16
100±14	99±9	99±23
122±20	98±10	80±21
172±19	154±8	90±15
165±21	156±10	95±18
198±21	170±8	86±13
188±19	158±9	84±13
169±25	160±10	95±20

The mean value of the chemical yield was 86% with a range of (63 ± 12) - (131 ± 31) %.
This rapid method, easily applicable to large volumes of samples with a high chemical yield, creates one precipitate thus reduces the measuring time at least by half compared to the other methods. It was therefore chosen as the chemical extraction procedure applied in river water samples taken under the scope of this work.
For this reason further analysis of the chemical yield values follows.

5.4 Statistical analysis of chemical yield

The dataset originating as experimental results from the chemical extraction (method XII) performed on 36 discrete samples can be evaluated with the aid of statistical tests in order to define its structure and properties.
There is a wide range of statistical tests available depending on the distribution of the data, the type of variable and the research design. Most common statistical tests include correlation tests (eg. Pearson, Spearman, Chi-square) which test for the strength of the association between variables, comparison of means tests (eg. paired and independent T-test, ANOVA) which look for the differences between the means of variables, regression tests (eg. simple and multiple regression) which assess if change in one variable predicts the change in another and non-parametric tests (eg. Wilcoxon rank-sum and sign-rank tests, sign-test) which are used when the available data do not meet assumptions required for parametric tests.
A common non-parametric test of the equality of continuous, one-dimensional probability distributions used to compare a sample with a reference probability distribution (normal distribution in our case) is the Kolmogorov-Smirnov test (K-S test or KS-test). The K-S test tries to determine if a sample is drawn from a given distribution by quantifying the distance D, between the empirical cumulative distribution function of the sample and the cumulative distribution function of the reference distribution, under the null hypothesis. The null hypothesis, H_0, assumes that the data follow the specified distribution (in our case the normal distribution) and if the test statistic D, is greater than the critical value obtained from a table (O'Connor and Kleyner, 2012) it is rejected in favor of an alternative hypothesis, H_A, that the data do not follow the specified distribution.
Thus we get for a sample of N= 36 values, a mean ($\bar{x}$) of 86 and a standard deviation (σ) of 15, calculated as:

$\bar{x} = \frac{1}{N}\sum_{i=1}^{N} f_i x_i$ and $\sigma = \sqrt{\frac{1}{N-1}\left(\sum_{i=1}^{N} f_i x_i^2 - N\bar{x}^2\right)}$ respectively, which allows us to build the table in order to carry out the K-S test, as seen in table 5.2.

Table 5.2: Kolmogrov-Smirnov calculations

Midpoint value (x_i)	Frequency (f_i)	Cumulative frequency values (k_i)	Cumulative distribution function $Sn(x_i)$	Z-score	Cumulative distribution function $F(x_i)$	Difference D_i
60	0	0	0	-1.867	0.031	0.031
65	4	4	0.111	-1.529	0.063	0.048
70	3	7	0.194	-1.191	0.117	0.078
75	2	9	0.250	-0.854	0.197	0.053
80	3	12	0.333	-0.516	0.303	0.030
85	7	19	0.528	-0.178	0.439	0.098
90	8	27	0.750	0.159	0.563	0.187
95	4	31	0.861	0.497	0.690	0.171
100	2	33	0.917	0.835	0.798	0.119
105	1	34	0.944	1.172	0.879	0.065
110	0	34	0.944	1.510	0.934	0.010
115	0	34	0.944	1.848	0.968	0.023
120	0	34	0.944	2.185	0.986	0.041
125	1	35	0.972	2.523	0.994	0.022
130	1	36	1	2.861	0.998	0.002

where the cumulative distribution function $S_n(x_i)$ is calculated as $S_n(x_i)=\frac{k_i}{n}$, the Z-score as standardized values according to the mean and standard deviation, i.e. $Z_i=\frac{x_i-\bar{x}}{\sigma}$, the cumulative distribution function $F(x_i)$ is calculated as $F(x_i)=\frac{1}{\sqrt{2\pi}}e^{-\frac{z^2}{2}}$ and the difference D_i is calculated as the absolute difference value between the two cumulative distribution functions. The maximum value of the difference between the two distributions is $D_{max}=0.187$. From the Kolmogorov-Smirnov table for significant level of 5%, we get $D_{36,0.05}=0.221$ (O'Connor and Kleyner, 2012). Since $D_{max}<D_{36,0.05}$we conclude there is no significant difference between the data and the data, which can be assumed to be normally distributed.

Matlab can also be used to run this test (command line: kstest(x), where x the vector containing our experimental dataset). It returns a test decision for the null hypothesis that the dataset comes from a standard normal distribution against the alternative that it does not at the 5% significance level with an additional visual representation (figure 5.11) of both empirical ($Sn(x_i)$) and theoretical ($F(x_i)$, normal distribution with mean of 86 and standard deviation of 15) cumulative distribution functions.

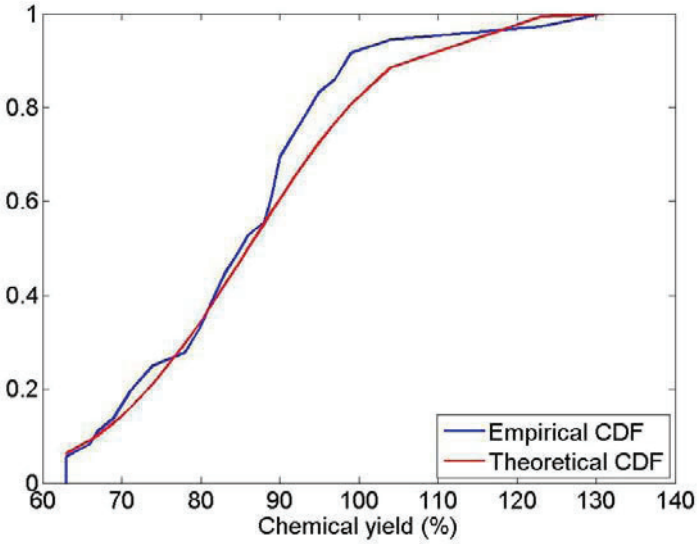

Figure 5.11: Theoretical and empirical cumulative distribution functions for the chemical yield values.

5.5 Influence of physical and chemical properties of WWTP effluent on the chemical yield

Several factors can affect the physical and chemical form of radionuclides in aqueous solutions. According to Lehto and Hou (2011) the most important of these are solution pH, redox potential, dissolved gases, ligands forming complexes with metals, humic substances, colloids, the source and mode of generation of radionuclides. The following parameters (conductivity, salinity, pH (see Appendix 1) and the time between sampling and beginning of the chemical extraction) were determined in order to detect a possible influence on the chemical yield of the chosen extraction method (method XII).

Conductivity and Salinity

The conductivity (also referred to as electrical conductivity) of water is an expression of its ability to conduct electric current, a property related to the ionic content of the sample. These conductive ions are dissolved salts and inorganic materials such as alkalines, chlorides, sulfides and carbonate compounds (Fondriest Environmental, 2014). Salinity is the total concentration of all dissolved salts in water and a strong contributor to conductivity. It is not measured directly but derived from the conductivity measurement, referred to as practical salinity.

Salinity is important in particular since it affects dissolved oxygen solubility with higher salinities leading to lower dissolved oxygen concentration. Dissolved oxygen and carbon dioxide play a major role in the speciation of metals in natural waters, in the oxidation of organic matter

and formation of carbonic acid or carbonate ions depending on the pH respectively (Lehto and Hou, 2011). Additionally, it can affect the Ag^{+}/Cl^{-} molar ratio thus the precipitation of inorganic iodine (Hormann and Fischer, 2017).

pH

By definition pH is the negative of the logarithm to base 10 of the activity of the hydrogen ion concentration in a solution and it used to specify the acidity or basicity of a liquid. The pH can influence the form of radionuclides in several ways by directly affecting the hydrolysis and redox reactions of metals and indirectly the binding of metals to oxide and silicate surfaces and the formation of complexes (Lehto and Hou, 2011).

Time between sampling and chemical extraction

Another possible influence on the ^{131}I extraction investigated was the time between the sampling and the beginning of the chemical extraction method. WWTP water contains microorganisms and bacteria which can influence the speciation or iodine eg. microbiological formation of CH_3I by methylation of I^- by aerobic bacteria (Kulykhin et al., 2010). In addition, slow reactions might take place during longer time intervals possibly influencing its separation during the extraction method.

Due to the fact that our existing equipment was not proper for insitu measurements, samples were brought back to the lab, kept in plastic containers at room temperature and processed within 48 h. Prior to the chemical extraction, approximately 20 - 50 ml of sample were analyzed with the aid of a conductivity/pH meter instrument (inoLab Cond Level 1, pH Level 1 by WTW GmbH & Co. KG), for the parameters of conductivity, salinity and pH. The calibration of the instrument for the conductivity cell constant was done using 3 M KCl solution and for the pH electrode using buffer solutions by AVS TITRINORM with pH values of 4, 7 and 9. All the measurements were performed at room temperature varying between 20 - 25^{o}C. The results are given in figure 5.12.

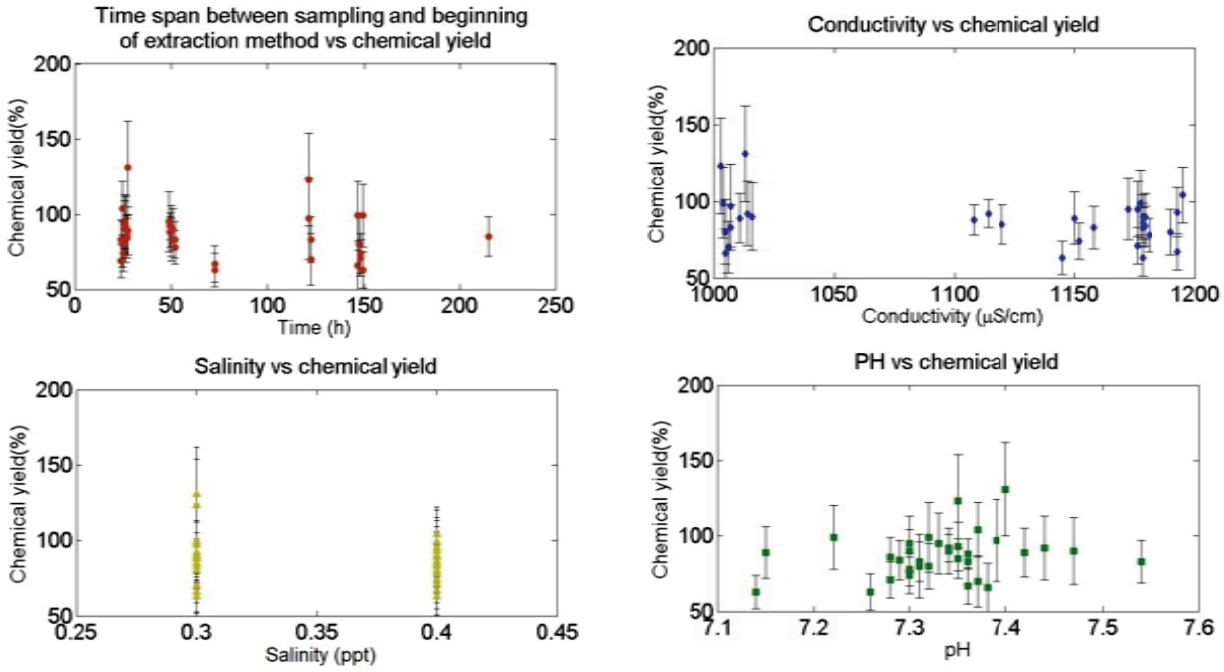

Figure 5.12: Scatter plots of measured time span between sampling and beginning of extraction method, conductivity, salinity and pH values over the corresponding chemical yield values.

It is obvious from figure 5.12 that there is no apparent correlation of the chemical yield with any of the aforementioned properties. Thus the ^{131}I extraction is not influenced by the time span 24 to 215 hours between sampling and beginning of the procedure, by conductivity values varying between 1003 and 1195 µS/cm, salinity from 0.3 to 0.4 ppt and pH values ranging from 7.14 to 7.54, as were found across the totality of samples.

5.6 Repeatability and Reproducibility

The two components of precision in a measurement system are repeatability and reproducibility. Repeatability is defined as the agreement between measurement results of the same quantity from several samples taken and measured under the same conditions. In an effort to credit repeatability in our experimental results, 3 samples of river water were taken simultaneously, at the same location approximately from the upper 30 cm of the water column, processed using the same chemicals, centrifuged to obtain the ^{131}I precipitate and measured in gamma detectors around 24 hours, details given in table 5.3.

Table 5.3: Repeatability of the chemical extraction method on 3 river water samples

Sampling date	Type of sample	Total sample mass (kg)	Total ^{131}I activity concentration (mBq/kg)
5.10.15	River water #1.1	18.64	104± 14
5.10.15	River water #1.1	20.00	94 ± 13
5.10.15	River water #1.1	20.50	103 ± 16

The ^{131}I activity concentration values reported are equal within the regions of their uncertainties supporting the repeatability of our experimental procedure.

Reproducibility is defined as the agreement between measurement results of the same quantity from several samples taken and measured under the different conditions. To examine the reproducibility of the chemical yield, results from the OSPAR II project (Gellermann et al., 2017) were used, given in table 5.4.

Table 5.4: OSPAR II measurements on the chemical yield

WWTP location/ Sampling date	spectrum	Mass (kg)	Measuring time (s)	WWTP ^{131}I effluent activity (mBq/kg)	Combined Bentonite and Ca^{131}I precipitate activity (mBq/kg)	Combined chemical yield (%)
Emscher	62382	3.98	58824	116± 10		
27.06.16	31849	4.93	31849		122 ± 10	105 ± 18
Hamburg	62365	3.97	84731	236 ± 13		
13.06.16	31832	4.93	239993		214 ± 16	91 ± 12
Hamburg	52255	3.96	66217	186 ± 12		
13.07.16	52262	4.56	172391		171 ± 5	92 ± 9
Gütersloh	52266	3.90	68368	222 ± 13		
20.07.16	52269	5.08	256613		235 ± 6	106 ± 9

The aforementioned samples (app. 5 L samples) were collected from 3 different WWTPs (Emscher, Hamburg and Gütersloh) as effluent from the plants (4 L samples), measured directly in Marinelli beakers of 2 L and subsequently ^{131}I was extracted as a combined precipitate. Subsequently, the chemical yield of the procedure was determined, which agrees with the previously determined mean value of (86 ± 15) % (see §5.4), thus indicating the reproducibility of our method.

5.7 General comment on Chapter 5

Finding the most suitable chemical extraction method for ^{131}I from surface waters was a necessary and unexpected long procedure, requiring a lot of effort and time at the lab. The selected method was shown that it is suitable for high volume samples as well as a rapid and cost effective method; the chemical extraction can be completed in 2 hours. It's a simple and environmental friendly procedure which can be easily performed by technical staff and does not include hazardous chemicals such as CCl_4. It is sensitive and specific; it's applicable in large sample volumes of samples, with a high extraction yield of (86 ± 15) %, targeting inorganic and organically bound iodine at the same time, independent of natural pH, salinity and conductivity. The method is sufficient to give reliable and reproducible results applicable in both WWTP effluent from different plants but also to river water. Its most important advantage in comparison with the other tested methods is the formation of 1 precipitate, which reduces significantly not only the preparation but also the measuring time.
Utilizing this method the measuring geometry the efficiency of the river water measurements is improved and the detection limit for ^{131}I can be lowered to 0.5 mBq/kg for a cylindrical geometry (diameter 70 mm, filling height 20 mm) for a 50 L river water sample and a measuring time of 4 days in our detectors (see specifications § 4.4.2.1) allowing us to successfully measure ^{131}I activity concentration in Weser water.

5.8 References for Chapter 5

Bunprapob S., 2010, *New methods for the speciation analysis of radioactive iodine in aqueous Samples,* University of Southampton, School of Chemistry, Master Thesis.
Retrieved from:https://eprints.soton.ac.uk/191327/1/Thesis_of_Supamatthree.pdf

Decamp C. and Happel S., 2013, *Utilization of a mix bed column for the removal of iodine from radioactive process waste solutions*, Journal of Radionaalytical and Nuclear Chemistry, 298, 2, 763-767.

Fan Y., Hou X., Zhou W., 2012, *Progress on ^{129}I analysis and its application in environmental and geological researches,* Desalination, 321, 32-46.

Fondriest Environmental, Inc., 2014, "*Conductivity, Salinity and Total Dissolved Solids*." Fundamentals of Environmental Measurements. Retrieved from http://www.fondriest.com/environmental-measurements/parameters/water-quality/conductivity-salinity-tds/

Grogan K. and DeVol T., 2013, *Development of a Novel Method for the determination of Aqueous inorganic ^{129}I Speciation,* Analytical Chemistry, 85 (9), 4658-4665.

Hormann V. and Fischer H.W., 2017*, The physiochemical distribution of ^{131}I in a municipal wastewater treatment plant,* Journal of Environmental Radioactivity, 178-179, 55-62.

Hu Q., Zhao P., Moran J.E., Seaman J.C., 2005, *Sorption and transport of iodine species in sediments from the Savannah River and Hanford Sites,* Journal of Contaminant Hydrology, 78, 185-205.

Kim Dong-Su, 2003, *Measurement of point zero charge of bentonite by solubilization technique and its dependence of surface potential on pH,* Environmental Engineering Research, 8, 4, 222-227.

Kulyukhin S., Konovalova N.A., Rumer I.A., Gorbacheva M.P., Mizina L.V.., 2010, *Recovery of ^{131}I and ^{137}Cs from a Solution Simulating NPP Trap Waters,* Radiochemistry, 52, 5, 515-522.

Leenheer J. and Reddy M., 2008, *Co-precipitation of dissolved organic matter by calcium carbonate in Pyramid Lake, Nevada,* Annals of Environmental Science, 2, 11-25.

Lehto J. And Hou X., 2011*, Chemistry and Analysis of Radionuclides: Laboratory Techniques and Methodology,* WILEY-VCH Verlag & Co.

Lehto J., Rätz T., Hou X., Paatero J., Aldahan A., Possnert G., Flinkman., Kankaanpää H., 2013, *Speciation of ^{129}I in sea, lake and rain waters*, Science of the total Environment, 419, 60-67.

Lyday P. A., 2012, *Iodine and Iodine Compounds*, Wiley-VCH Verlag GmbH & Co.

Michel R., Riebe B., Meleshyn A., Dultz S., Schampera B., 2008, *Stabilität von Organotonen als Anionenadsorber unter Endlagerbedingungen- Experiment und Modellierung,* Abschlusbericht zum BMWi-Project FKY 02E10025.

Mundschenk H., 1993, *Procedure for determining radionuclides in surface water by gamma spectrometry,* C-γ-SPEKT-OWASS-01, Federal coordinating office for surface water, suspended particulate matter and sediment in inland waters.

Muramatsu Y. and Ohmomo Y., 1988, *Tracer experiments for the determination of chemical forms of radioiodine in water samples,* Journal of Radionanalytical and Nuclear Chemistry, 124, 1, 123-134.

Nagata T. and Fukushi K., 2010*, Prediction of iodate adsorption and surface speciation on oxides by surface complexationmodeling,* Geochimica et Cosmochimica Acta, 74, 21, 6000-6013.

Nierop K.G, Jansen B., Verstraten J.M., 2002, *Dissolved organic matter, aluminium and iron interactions: precipitation induced by metal/carbon ratio, pH and competition,* Science of the total environment, 300(1-3), 201-11.

O'Connor P. D. T. and Kleyner A., 2012, *Practical Reliability Engineering*, John Wiley & Sons, Ltd.

Gellermann R., Fischer H., Ulbrich S., Buchholz O., 2013. *Messtechnische und theoretische Abschätzung des Eintrags von I-131 in die OSPAR-Regionen aufgrund der nuklearmedizinischen Anwendungen von Radioiod in Deutschland.* Abschlussbericht. Vorhaben 3611S70013. Auftraggeber: Bundesamt für Strahleschutz. 02.12.2013.

Gellermann R., Fischer H., Keil A., Ahrens C., 2017. *Messtechnische und modellbasierte Abschätzung des Eintrags von I-131 in die OSPAR-Regionen aufgrund der nuclear-medizinischen Anwendung von Radioiod in Deutschland.* Abschlussbericht Vorhaben Nr. 3614S5001. Auftraggeber: Bundesamt für Strahlenschutz. 31.10.2017.

Palagyi S., 1985*, Determination of Radioiodine in Drinking Water and Milk Using Separation on the Static Polyurethane Foam Column,* Isotopenpraxis, 21,130.

Parekh P., Bari A., Harris P., 2002, *Rapid radiochemical analysis of ^{131}I in environmental samples using a well- type Ge-detector,* Journal of Radioanalytical and Nuclear Chemistry, 256, 2, 225-230.

Rädlinger G. and Heumann K.G., 2000, *Transformation of Iodide in Natural and Wastewater Systems by Fixation on Humic Substances*, Environmental Science & Technology, 34, 3932-3936.

Reifenhäuser C. and Heumann K., 1990, *Development of a definitive method for iodine speciation in aquatic systems,* Fresenius Journal of Analytical Chemistry, 336, 559-563.

Schwehr K. and Santschi P., 2003, *Sensitive determination of iodine species, including organo-iodine, for freshwater and seawater samples using high performance liquid chromatography and spectrophotometric detection,* Analytical Chimica Acta, 482, 59-71.

Sindelar H.R., Brown M.T., Boyer T.H., 2015, *Effects of natural organic matter on calcium and phosphorus co-precipitation*, Chemosphere, 138, 218-224.

Souti M.E., 2012, *Medical ^{131}I in Weser water*, Universität Bremen, Faculty of Environmental Physics, Master Thesis. Retrieved from: http://www.iup.uni-bremen.de/PEP_master_thesis/thesis_2012/master_thesis_souti.pdf.

Ulbrich S., Hormann V., Souti M.E., Toma E., Igbinosa A., Hettwig B., Fischer H.W., 2013, *Method for the determination of 131I in surface water,* 15. Fachgespräch zur Überwachung der Umweltradioaktivität, Bremen, 5-10 March, 2013. (http://www.bmub.bund.de/fileadmin/Daten_BMU/Download_PDF/Strahlenschutz/umweltradioaktivitaet_tagungsband_15_fachgespraech_bf.pdf).

Zulauf A., Happel S., Mokili M.B., Bombard A., Jungclas H., 2010, *Characterization of an extraction chromatographic resin for the separation and determination of ^{36}Cl and ^{129}I,* Journal of Radionalytical and Nuclear Chemistry, 286, 2, 539-546.

Chapter 6

^{131}I activity concentration in Weser River

Understanding of pollutant transport in rivers is aided by performing tracer experiments where several physical processed can be studied (eg. advection, diffusion, etc.) and/or an estimation of related parameters (eg. flow velocity, dispersion coefficient, etc.) is possible. Tracers may be artificially introduced in the system or they may be natural occurring. Artificially introduced tracers include fluorescent dyes (eg. fluorescein, rhodamine WT, etc. (Tazioli, 2011)), chemicals (eg. SF_6 (Ho et al., 2002)), or radioisotopes (eg. ^{3}H (Clark and Fritz, 1997)). Natural occurring tracers can also be chemicals (eg. NaCl), or radioactive tracers of cosmogenic origin (^{7}Be, ^{14}C, ^{3}H).
Previous measurements of ^{131}I in Weser River area (see §2.4) along with its routine releases into the water body of the river with WWTP effluent, motivated us on performing a systematic study, spanning between autumn 2014 to autumn 2015 by utilizing ^{131}I as a readily available tracer. This chapter focuses on presenting the results of 17 different sampling campaigns which quantified the concentration of ^{131}I in both river water and sediments with the aims of obtaining a better understanding on the distribution of radioisotopes in the water-sediment system and of developing and assessing a model for predicting the dispersion of radionuclides in Weser River (see Chapter 7).

6.1 Sampling methods

The appropriate sampling method for water and sediments of a river depends on the type of the study. One of the prime considerations prior to establishing a sampling campaign is ensuring the representativeness of the samples. In order to achieve that, a large number of sites is preferable since more information is provided. Another important factor in terms of representativeness is the sampling frequency. However due to limited time of most research studies, one can only collect a small number of samples.
For river water samples, usually grab samples from the surface of water layer (0-5 cm from the surface) at the center of the main flow are collected. Water quality sampling on Yukon River (Whitfield, 1983) was performed at 5 equidistant points across the river in locations where the river was traveling in a generally straight manner and where no tributary was in the immediate vicinity upstream. Facchi et al. (2007) suggest a different approach, namely the collection of composite samples, especially when the river water quality fluctuates over short periods of time

with respect to the sampling frequency since the collection of grab samples may be inappropriate for characterizing average water quality. Composite samples are created by pooling a number of grab samples of a given volume over a period of time (high frequency grab samples) and/or over the full depth and width of the river (depth-and width- integrated composites).
For water-sediment linked studies, the same sampling locations for both media should be preferred. Shelton and Capel (1994) present several guidelines for collecting and processing sediment samples, focusing on samples of fine-grained surficial sediments during low-flow conditions and on compositing samples from several depositional zones which represent various flow regimes (left bank, right bank and center of channel).

6.2 Selection of sampling locations on Weser River[1]

As a starting point, due to lack of river water data, some rather simple calculations were used for estimating the ^{131}I activity concentration from bank sediments to river water with the goal of selecting sampling locations where ^{131}I could be detected in water samples. Already published data in Weser river sediments[2] (Fischer et al., 2009), for both river banks in different locations upstream and downstream the WWTP were used. Rearranging the formulas 1-3 in the aforementioned publication:

$$C_{sm} = k_F C_w$$

$$O = \frac{\rho_s}{\lambda_r} v_s C_{sm} \left(1 - e^{-\lambda_r t_s}\right)$$

$$a = \frac{O}{d\rho_s}$$

where

C_{sm}: activity concentration of the isotope in suspended matter (Bq/kg(dry mass; d.m.))

k_F: concentration factor (10^4 L/kg)

C_w: concentration of isotope in water (Bq/L)

O: sediment deposition density (Bq/m^2)

ρ_s: sediment density (kg/m^3)

λ_r: radioactive decay constant (s^{-1})

v_s: sedimentation growth rate (m/s)

[1] Detailed information on the sampling area can be found in §2.1

[2] River sediment samples were collected and measured during S. Ulbrich's thesis (see also Appendix 10).

t_s : time allowed for sedimentation (s)

a : activity concentration of sediment (Bq/kg(d.m.))

d : thickness of sampled sediment layer (m)

By adopting the same parameter values (a : varying depending on location as given in table 1, $d = 5mm$, $\lambda_r = 10^{-6}$ s^{-1}, $v_s = 2.1 \times 10^{-10}$ m·s^{-1} and t_s equal to 1 month), one can calculate the ^{131}I activity concentration C_w in river water (in Bq/l):

$$C_w = \frac{a \cdot d \cdot \lambda_r}{v_s \cdot k_F \cdot \left(1 - e^{-\lambda_r \cdot t_s}\right)} \qquad \textit{eq. 6.1}$$

As a result of the calculations one gets table 6.1 and figure 6.1.

Table 6.1: ^{131}I activity concentration in the sediments and calculated values for river water in different locations on both banks. Negative distance indicates direction upstream the WWTP.

Left bank			Right bank		
Distance from the WWTP [km]	^{131}I activity in sediments [Bq/kg(d.m.)]	Calculated ^{131}I activity in water [mBq/L]	Distance from the WWTP [km]	^{131}I activity in sediments [Bq/kg(d.m.)]	Calculated ^{131}I activity in water [mBq/L]
12.75	0.65±0.08	1.43	20	0.45±0.05	0.99
9.75	0.63±0.10	1.39	17.5	0.84±0.11	1.85
5	0.46±019	1.01	14	0.75±0.07	1.65
1.75	3.74±0.18	8.24	9.75	0.73±0.07	1.61
0	98.71±2.28	217.43	4.5	2.73±0.28	6.01
0	122.30±3.11	269.39	0.5	1.75±0.47	3.85
-2	2.51±0.87	5.53	-2.25	1.50±0.39	3.30
-2.5	1.80±0.27	3.96	-6.5	1.60±0.26	3.52
-4.5	2.34±0.38	5.15			
-6.5	1.89±0.16	4.16			

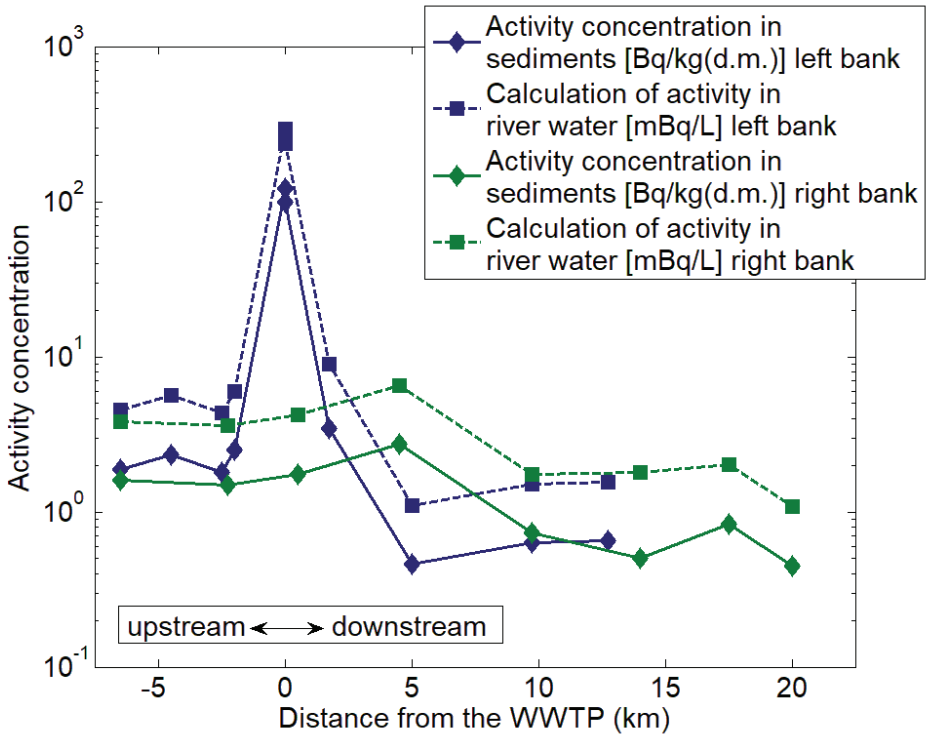

Figure 6.1: ^{131}I activity concentration in the sediments and calculated values for river water in different locations on both banks.

According to these calculations one would expect to find iodine in all locations (except 20 km downstream on the left bank) with activity concentrations higher than 1 mBq/L. The most promising region however is close to the WWTP and in distances up to 6.5 km upstream and 5 km downstream where the activities are expected to be higher than 3 mBq/L.

6.3 Sample collection and treatment

For determining the ^{131}I activity concentration in river water, sediment and suspended matter different sampling procedures and treatments were applied depending on the medium under investigation. All sampling locations were determined with the aid of GPS. The measuring results and their analysis follow in the next paragraphs.

6.3.1 River water samples

The samples were collected from a rigid inflatable boat equipped with an outboard engine with the help of a GARDENA electric water pump (figure 6.2). The samples collected in the first two sampling campaigns (see § 6.4) were depth-integrated samples with the remaining samples (see § 6.6) being collected from the upper 30 cm of the water column.
All the samples were treated with the ^{131}I chemical extraction procedure described in §5.3.12, centrifuged for 15 min at 2000 rpmin order to decrease the volume and measured in 0.5 L plastic bottles.

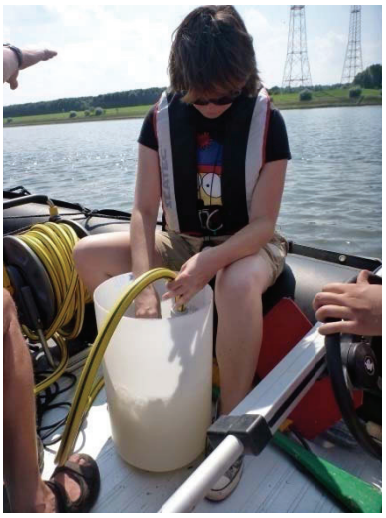

Figure 6.2: River water sampling.

6.3.2 Sediment samples

Bottom sediment sampling (see also § 6.7.1)
The sampling device used was a Ponar 'grab' sampler (figure 6.3), a modified Van Veen type self-tripping sampler acquired from Rickly Hydrological Co. This type of sampler is used universally since it is adequate for most substrates, in deep lakes, rivers and estuaries and it is useful for sand, silt or clay. The standard Ponar is quite heavy (app. 30 kg) and requires winch for operating, however, it is available in several sizes. The 'Petite Ponar', which was used in this study, can be operated from a small boat since it weighs about 12 kg. It can reach sediment depths between 0 to 10 cm and samples volume up to 1 L. An important disadvantage of this sampler is its susceptibility to incomplete closure leading to loss of sample.

Figure 6.3: Petite Ponar grab.

Bank sediments (see also § 6.7.2)
Most of the rocks in the river banks (see also §2.1) were covered by a 5 mm layer of sediment which was scratched of (figure 6.4) 1 hour before and after high water.

Figure 6.4: Sampling of sediments on the river bank

All sediment samples collected were measured in a wet state and dried afterwards until constant mass at 105ºC.

6.3.3 Suspended matter samples

For the quantification of ^{131}I bound to suspended matter in the Weser River we follow the instructions as given from Mundschenk (1993) on the recommended procedure for gamma spectroscopic determination of radionuclides in suspended matter of surface waters in routine and emergency environmental monitoring in Germany (see also §6.8).
A sample of 50 L is filtered through a 589/2 Whatman filter paper with pore size of 4-12 μm, designed for gravimetric analysis (figure 6.5). The suspended matter deposited on the filter is dried till constant mass at 105ºC and then at 200ºC for 4 hours. The temperature selection is made in order to prevent volatilization of iodine in the sample (Herod et. al., 2014). The sample is then ground to fine dust in a mortar to achieve homogeneity and measured in gamma spectrometer in PMMA geometries of 36 and 70 mm diameter (figure 6.6).

Figure 6.5: Filtering device

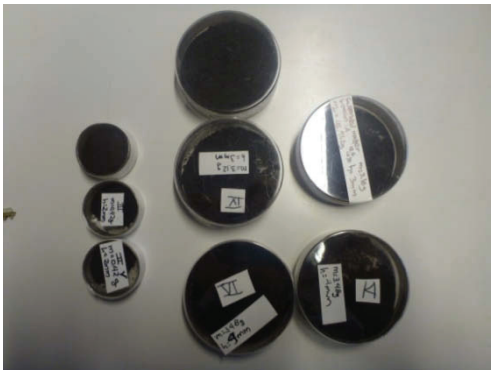

Figure 6.6: Suspended matter samples

An additional method was applied where a 50 L sample was mildly stirred (< 2000 rpm) after the addition of 200ml of a commercial flocculent solution "Flockfix® flüssig" (Waterman GmBH, Wendlingen, Germany) which contains aluminiumchlorohydrate and was let to precipitate overnight (figure 6.7).

Figure 6.7: Suspended matter precipitate. Container diameter 34.6 cm

6.4 1st and 2nd sampling campaigns

The first and second sampling campaigns took place at the 23rd of September and 6th of October 2014. Samples were collected at the same sampling points both times, at 5 equidistant locations across the river, 0 km distance from the WWTP (figure 6.8). Detailed information on the exact sampling locations can be found in Appendix 2. All samples were depth integrated (see §6.3.1), with the depth of the water column varying between 5 and 13 m.

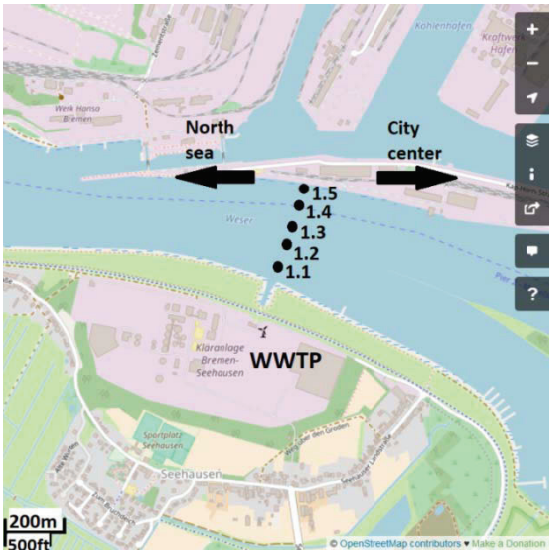

Figure 6.8: Sampling points for the 1st and 2nd sampling campaigns (open street maps).

During the first sampling campaign (13:40-15:20), the flow of the river was towards the Bremen city – upstream direction (low water at 10:25/ high water at 15:45), and during the second (16:08-17:28) towards the North Sea – downstream direction (high water at 13:47/ low water at 21:08). All samples were prepared and analyzed within a week from sampling to avoid additional decay losses and were measured on average for 3 days. The measuring results are can be found in Appendix 3. The ^{131}I activity concentration of the WWTP effluent for the 1st and for the 2nd sampling campaigns is 67 ± 12 mBq/kg (sampling time: 12:00) and 90 ± 17 mBq/kg (sampling time: 14:30) respectively[2].

[2]The time difference between sampling in the WWTP and in the river (app. 1.5 hours) is justified due to the sampling procedure. When reaching the area (figure 6.15), first WWTP effluent is collected, then a small rubber boat (app. 5 m length) is launched from a ramp from the harbor "Hasenbüren" and loaded with the necessary sampling equipment. The water samples are gathered by traveling to a maximum distance of 7 km once or twice (due to the large volume of the samples collected), thus the sampling time span is close to an hour for the river water samples, especially when sampling in sections (see §6.2.2). During the sampling period the WWTP effluent activity concentration does not change drastically as can be seen in Appendix 4.

All measurements except one are below the detection limit. Furthermore, the ^{131}I activity concentration on sampling point 1.1 (at the boundary between WWTP outflow channel and river) is 1.13 ± 0.40mBq/kg, much lower than expected (see table 6.1) since the activity in sediments for the same location had been measured to be between 98 and 122 Bq/kg(d.m.). Additionally previous measurements in the river water (see §2.4) resulted in ^{131}I activity concentrations of 4.45 mBq/kg 9.7 km downstream the WWTP (Gellermann et al., 2013), 50.3 mBq/kg only app. 60 m away from location 1.1 and 5.7 mBq/kg 1 km downstream the WWTP (Souti, 2012). This large discrepancy, the measurements below the detection limit and the fact that ^{131}I had been successfully measured in water surface samples, lead to reconsideration of the sampling method (see §6.5).

The initial idea about this difference was based on the type of samples collected. A possible slow mixing in the vertical direction could lead to lower activity concentration values. However, this hypothesis was rejected (see §6.6.2). The reason for the discrepancy turned out to be a slight difference in the sampling location directly in the outflow of the WWTP. As illustrated in figure 6.9, only a few meters distance (app. 15 m) do matter, since the plume is deflected towards the downstream bank.

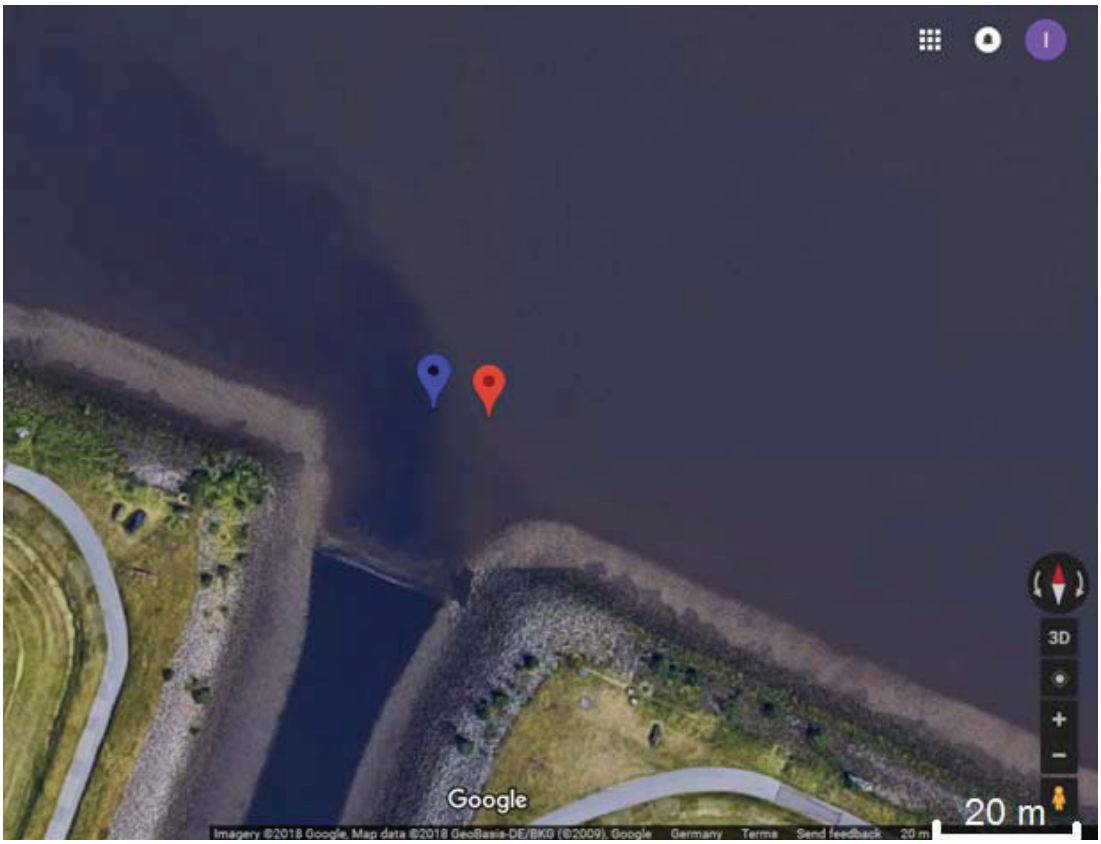

Figure 6.9: Sampling locations during the first two sampling campaigns (red marker) and the revised ones (blue marker). The outflow plume of the WWTP is also visible deflected towards the downstream bank (different coloration between plume and river water). Image acquired from Google maps (2018).

6.5 CORMIX simulations

For the selection of sampling locations, the CORMIX (9.0 version) software, licensed and distributed solely by MIXZON INC, was used. CORMIX predicts mixing behaviors and plume geometry by classifying momentum and buoyancy of the discharge in relation to boundary interactions (eg. flow surface or bottom contact or terminal layer in formation in density stratified ambient currents). Detailed descriptions of the mathematical formulations of this model can be found on the Technical reports of CORMIX1, CORMIX2 or CORMIX3 (http://www.mixzon.com/downloads/, 2017). It can model single-port, multiport and surface discharge sources. The effluents under consideration may be conservative, non-conservative, heated, brine discharges or contain suspended sediments with application to steady as well as unsteady ambient currents/tides or stagnant ambient conditions.
For the simulation of a pollutant discharged into a river channel, the user needs to provide input information on the effluent, the discharge type, the ambient water and the mixing zone. The output of the simulation is given as a visual (3D and 2D near and far field visualizations by CorVue) and as a report file including simulation details, project summary, processing record and description of the flow and design recommendations.

In our case the following parameterization was done:
Effluent
Non conservative with first order decay ($\lambda = \ln(2)/\tau_{1/2} = 0.086\ day^{-1}$).
Discharge concentration: 1 mBq/kg (in the software the units are given as mg/l), thus the results are given as normalized concentration.
Effluent flow rate: 1.5 m^3/s (Hansewasser, 2017).
Effluent density: calculated[3] using the mean temperature 12.6^oC (www.fgg-weser.de, 2017) and salinity 0.35 ppt (mean of 33 values in the period 2013-2014, measurement in our lab (see figure 5.12 in §5.5/ Appendix 1)).

[3]CORMIX density calculator tool is based on the specified Effluent Temperature and Salinity, using the UNESCO (1981) Equation of State for fluids/water (Millero and Poisson, 1981). Input: effluent temperature in ^oC and effluent salinity in ppt, Output: computed effluent density in kg/m^3.

Discharge

Location of discharge: left bank

Flush type of discharge with horizontal angle of 90^{o} and bottom slope of 50^{o} (calculation based on figure 5 "Successive deepening and widening of the Lower Weser" from the HARBASINS report (Herrling and Niemeyer, 2008).)

Discharge outlet width 40 m, (measurements during HW).

Local depth at discharge outlet: 4 m (own measurement, available data in Appendix 3).

Ambient (River water)

Geometry: average depth 12m (Grabemann et. al, 1996).

Depth at discharge: 4 m (own measurement, see Appendix 3).

Wind speed: 2 m/s (recommended value, Doneker, 2008).

Manning value[4]: 0.025 (typical value for clean and straight natural rivers, Doneker, 2008/ for the same region Stoschek and Matheja (2001) use similar values (0.025-0.030)).

Ambient density data calculated using the mean temperature 12.6^{o}C (www.fgg-weser.de, 2017) and salinity 0.7 ppt (own measurement mean of 10 values from the depth integrated measurements, available data in Appendix 3).

Bounded channel with uniform width of 340 m.

Unsteady flow with period 12.42 h, maximum velocity of 1.3 m/s and tidal velocities depending on the time of the tidal cycle given as seen in figure 6.10.

[4]Manning's n value is a measure of the roughness characteristics in the channel. CORMIX internally converts the n value to a f friction value (Darcy-Weisbach friction factor) using the following equation: $f = 8g\frac{n^2}{HA^{1/3}}$ where g=9.81m/s^2 the gravitational acceleration and HA the average ambient depth (Jirka et al., 1996).

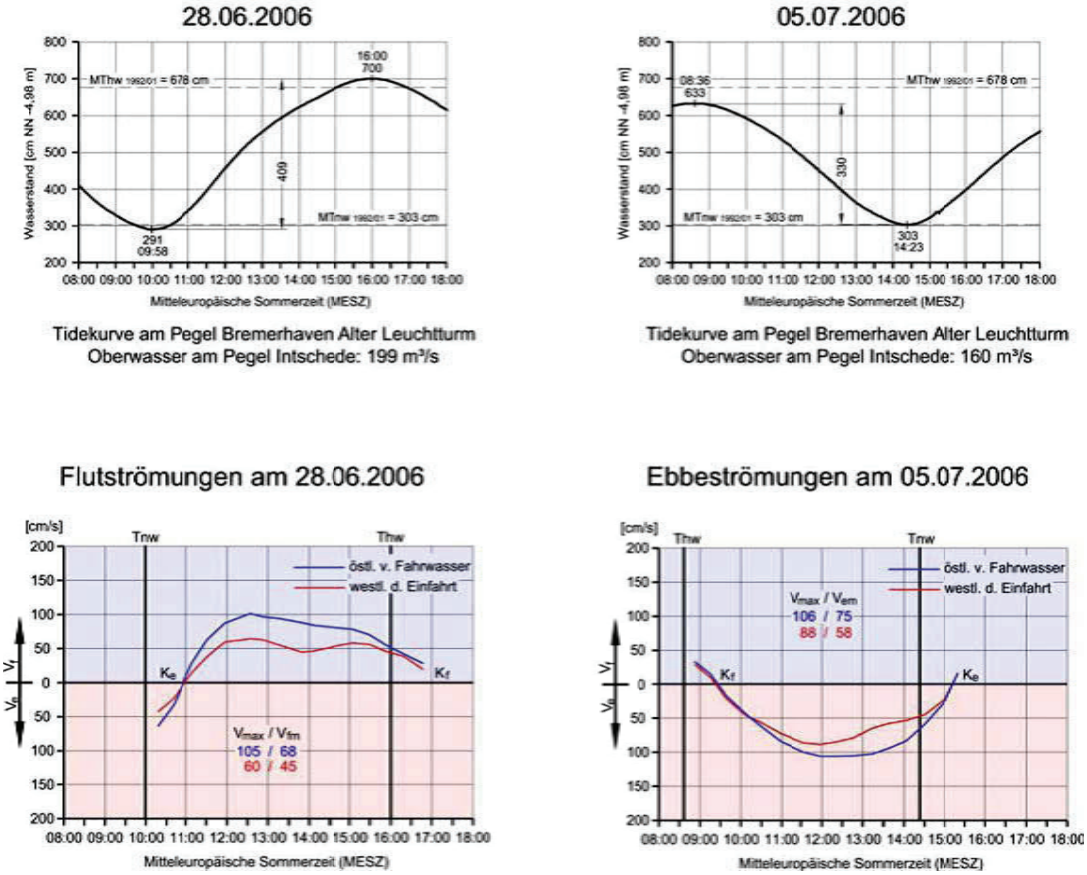

Figure 6.10: Tide curves and corresponding flood and ebb current velocities for the station Bremerhaven Alter Leuchtturm[5] on the 28th of June and 5th of July 2006 respectively (Hochschule Bremen, 2011).

The region of interest for the simulations was from 0 to 5000 m distance from the WWTP (see § 6.2) and the ^{131}I activity concentration in the river water during different times in the tidal cycle are given in figure 6.11.

[5] Despite the fact that the width of the river at this location (> 2000 m, Grabemann et. al, 1996) is larger than in the area of interest (Oslebshausen station), leading to discrepancies in the values of the ebb and flood current velocities, the lack of data for the Oslebshausen station limited our options.

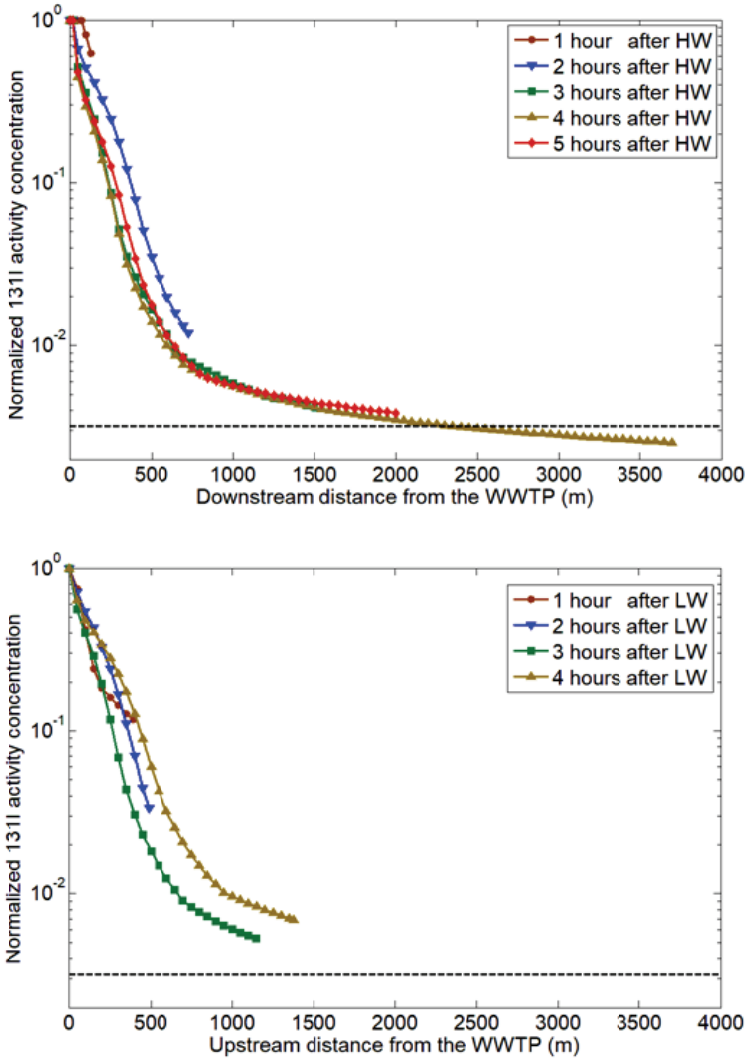

Figure 6.11: Simulation results for CORMIX simulations with the aforementioned input (figure 6.10), for the left bank during different times of the tidal cycle. The dashed line indicates a normalized value (to a mean WWTP effluent value of 250 mBq/L) of detection limit for a water sample of 49.8 L measured for 2.8 days in cylindrical geometry (filling height 30mm).

The predictions were terminated before reaching the distance of 5000 m downstream/upstream the WWTP, due to the unsteadiness of the ambient current (river flow) during the tidal reversal. CORMIX is a steady state model and in the tidal mode it accounts for re-entrainment of the plume remaining from the previous tidal cycle, leading to pollutant build up. However, if unsteady build up over multiple tidal cycles is likely (as in our case, see formation of ^{131}I background concentration, §6.6.2), additional methods of analysis may be necessary.

At distance of 3700 m downstream where the predictions terminated the normalized activity concentration was 0.0025, yielding 0.55 mBq/kg for a mean WWTP outflow of 216 mBq/kg (IMIS average for the years 1993-2014, details in Appendix 13) with a range of 0.09 to 2.49 mBq/kg according to the range of the WWTP effluent values (37 to 977 mBq/kg). In the

upstream direction at a distance of 1375 m, a normalized concentration of 0.007 under the same considerations leads to 1.75 mBq/kg for a mean ^{131}I activity concentration in the WWTP effluent. For a water sample of 49.8 L measured for 2.8 days in a 0.5 L Plastic bottle with a filling height of 30 mm a detection limit of 0.7 mBq/kg was reached (see table 6.2), thus depending on the activity concentration of the effluent ^{131}I can be detected 3700 m downstream and 1375 m upstream the WWTP.

The flow, as defined in the flow class description file, consists of the following flow regimes a far field (> 500 m distance from the WWTP) buoyant spreading and passive ambient diffusion; the plume spreads laterally along the surface while being advected downstream with the ambient current with a small mixing rate, while the ambient turbulence becomes the predominant mixing process. The plume will grow in both vertical and horizontal directions at a rate dependent on the magnitude of the ambient turbulence. The values of the vertical and horizontal diffusivities are given in the prediction file equal to 0.012 and 0.015 m^2/s correspondingly.

Additionally, in the processing record the following information was given:
1. There is intrusion of river water into the outflow channel and
2. The discharge plume, in the presence of strong ambient flow, becomes rapidly deflected towards the left bank. Shoreline attachment of the plume generally leads to decreased dilutions and higher pollutant concentrations along the bank. These conditions occur due to the discharge geometry (depth, horizontal angle and aspect ratio (depth/width)). By increasing the discharge depth, the bottom interaction and subsequently downstream bank attachment is discouraged, while when decreasing the aspect ratio, the discharge is encouraged to propagate further into river channel. Last the larger the angle between the downstream bank and discharge channel, the less likely shoreline attachment will occur.

As illustrated in figure 6.11, the activity concentration over downstream distance depends on tidal flow. For detecting ^{131}I activity concentrations larger than 1mBq/kg in downstream distances from the WWTP greater than 2 km, the optimum sampling time during the tidal cycle appears to be 4 hours after high water. For this time of the tidal cycle, after tidal reversal, mixed water from the previous half-cycle becomes re-entrained into the near field of discharge, increasing the pollutant concentrations compared to steady state predictions. For the upstream direction, sampling 4 hours after low water to distances up to 1350 m appears to be the most favorable time for detecting ^{131}I activity concentrations above detection limit.

Despite its limitation on the prediction of complicated tidal flows the CORMIX software appears to be a useful tool, allowing us to get estimation on the concentration of ^{131}I in the river water and determining accordingly our sampling locations.

6.6 ^{131}I activity concentration in Weser River water

6.6.1. Tidal influence

In an attempt to verify the simulation results obtained through CORMIX and select the most favorable sampling time during the tidal cycle, river water samples were collected at the same downstream locations (0 km to 5 km close to the left bank) for different times after high water; 0.5 - 1 h (samples collected at locations 0 and 1 km downstream the WWTP), 3 - 3.5 h, 4 - 4.5 h (samples collected during two campaigns, since in the first one (illustrated with dashed line in figure 6.14) samples were collected at locations 0 and 0.5 km downstream the WWTP) and 5 - 5.5 h (samples collected only at locations 0, 0.5 and 1 km downstream the WWTP) hours after high water (see figure 6.12). The results of 5 sampling campaigns are given in figure 6.14, as normalized ^{131}I activity concentration (the normalization is done according to the effluent ^{131}I activity concentration as samples before and after each sampling campaign were collected from the WWTP). Detailed results can be found in Appendix 3.

As predicted from the CORMIX simulations, there must be a pre-dilution of the effluent inside the WWTP outlet channel, probably due to intrusion of "fresh" river water. The difference[5] between the activity concentration of the WWTP effluent and of river water collected at the boundary between WWTP outlet and river, depending on the time on the tidal cycle varies between 29 and 115%. Additional support of this assumption (i.e. pre-dilution of the effluent) is the different coloration of the river bank (due to dry and wet states) in this location (figure 6.13), indicating the water level during high water. In order to back our supposition, when the water level was high enough for the boat to have access (0.5 - 1 hour after high water), a sample was additionally taken inside the WWTP outlet channel. The ^{131}I activity concentration at this location (187 ± 33 mBq/kg) is lower than the effluent (358 ± 19 mBq/kg), substantiating our assumption on pre-dilution of the WWTP effluent before reaching the river.

During similar times in the tidal cycle (4 - 4.5 hours after high water) the ^{131}I has similar activity concentrations within the uncertainty region of the respective value, indicating reproducibility of our measurements.

[5] Calculation is done using the following formula: $D = \frac{A_{WWTP} - A_{river}}{\left(A_{WWTP} + A_{river}\right)/2} \times 100\,(\%)$ with A_{WWTP} the ^{131}I activity concentration of the WWTP effluent and A_{river} the ^{131}I activity concentration in river water.

As expected from the aforementioned simulations, the most favorable time for measuring ^{131}I in the downstream direction with activity concentrations larger than 1 mBq/kg is 4 hours after high water.

Figure 6.12: Sampling locations; 0: Outlet, 1.1: Outlet-River boundary, 2.1: 0.5 km downstream, 3.1: 1 km downstream and 4.1: 2 km downstream the WWTP (open street maps).

Figure 6.13: WWTP outlet with visible height of the high water reach.

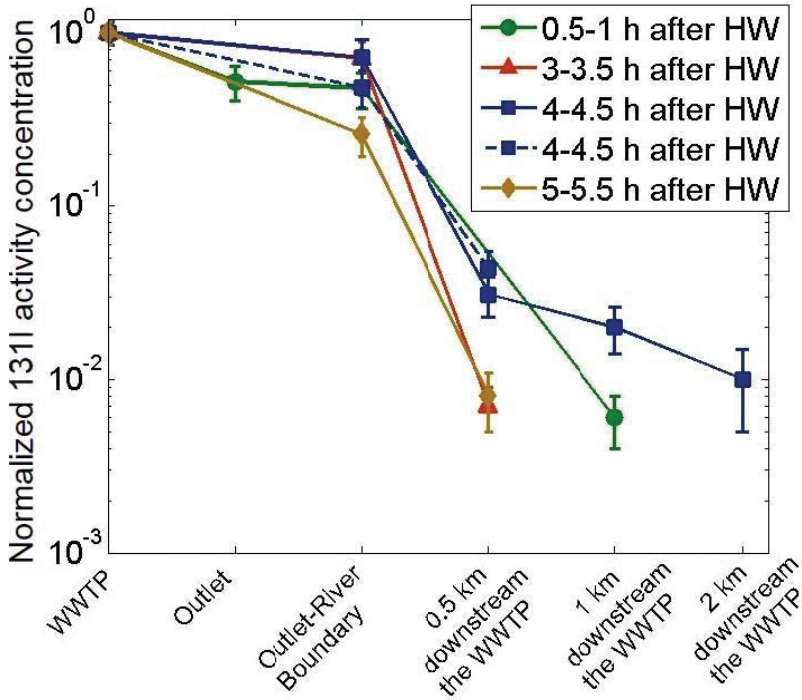

Figure 6.14: Normalized ^{131}I concentration over downstream distance close to the left bank (corresponding locations illustrated in figure 6.13) during different times in the tidal cycle. True scale figure available in Appendix 3 (figure A.1).Values below detection limit not included.

Taking into consideration these results, along with the CORMIX simulations, 3 to 4 hours (selected time span sufficient for sampling, see also footnote 2) after high (for the downstream direction) and low water (for the upstream direction) was selected for sampling in 5 equidistant locations across the river (figure 6.15).

6.6.2 ^{131}I activity concentration in Weser water 3 to 4 hours after high/low water

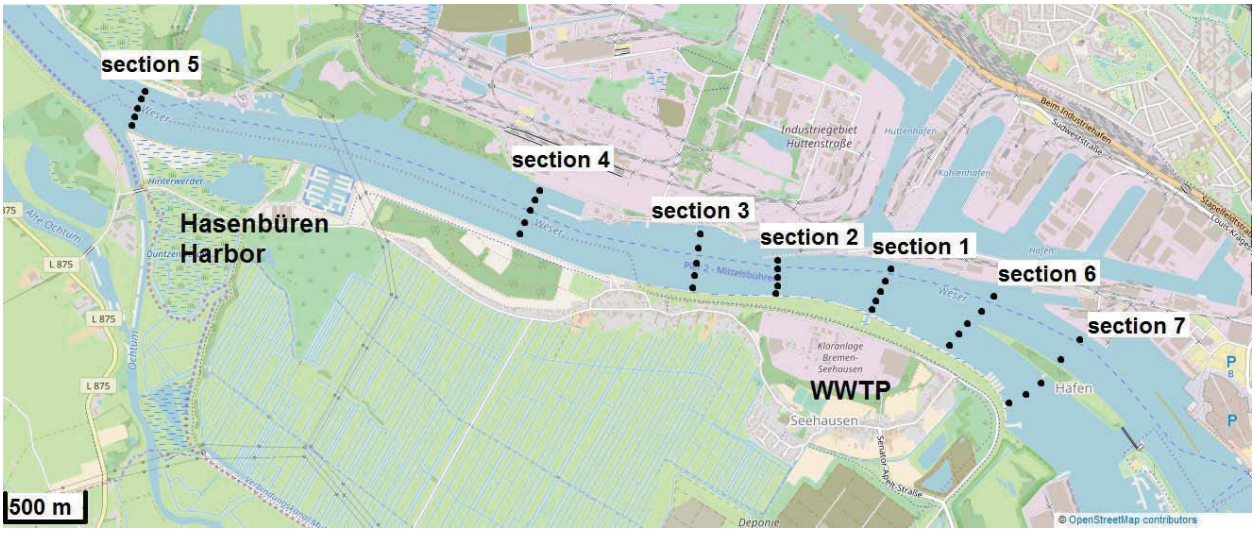

Figure 6.15: Sampling locations on 7 sections, each with 5 equidistant sampling points across the Weser River ; Section 1: 0 km, Section 2: 0.5 km downstream, Section 3: 1 km downstream, Section 4: 2 km downstream, Section 5: 5 km downstream, Section 7: 1 km upstream, Section 6: 0.5 km upstream from the WWTP (open street maps).

All samples were taken during 3 to 4 hours after high (downstream direction) and low (upstream direction) water as described in §6.3.1.

The ^{131}I activity concentrations are given in the following semi-logarithmic figures (6.16 and 6.17) as normalized concentrations to the WWTP effluent activity concentration, detailed values and linear plots (figures A2 and A3) can be found on Appendix 3. The majority of the collected samples was from the surface of the water body with the exception of locations close to the left bank, where samples were taken also close to the bottom of the river in order to get a better understanding of the vertical mixing of the WWTP effluent plume (see below).

The experimental results have several interesting features:

Verification of the origin/source of ^{131}I:
As expected the highest concentrations of ^{131}I are found at the boundary between WWTP outlet and river (normalized activity of 0.27). Similar results obtained from the sediments (§ 6.7) verify the WWTP as source.

Fast vertical mixing:
Water samples from both the surface and bottom of the river close to the left bank have similar profiles and activities (range of normalized activity: 0.01 - 0.27) indicating a rather fast homogenization in the vertical direction.

Mixing in the horizontal direction:
The WWTP discharges its effluent with a mean rate of 1.5 m^3/s (Hansewasser, 2017). As predicted by CORMIX, in the river (mean river discharge: 327 m^3/s, see also §2.1) the activity plume is rapidly deflected towards the left bank, where the ^{131}I is detected in higher activity concentrations than in the center of the river and right bank. As the effluent plume moves in the downstream direction it gets dispersed also in the lateral direction, and in distance of 5 km downstream of the WWTP ^{131}I is detected with similar normalized activity concentrations (range: 0.002 – 0.008) in all 5 sampling points across the river.

^{131}I upstream the WWTP:
The presence of ^{131}I upstream the WWTP is must be due to the tidal nature of the river. As the river flows towards the city of Bremen it transports the ^{131}I in the upstream direction where it is detected up to 1 km with normalized activity concentrations between 0.005 and 0.014.

Formation of ^{131}I background concentration:
The traveling time of water parcels in the Weser River, affected by the diurnal tide according to Grabemann et. al.(1996) can vary from 3 to 27 days for the inner part of the estuary (app. 65 km length) depending on the river discharge. This forward/backward movement of the plume causes iodine not only to appear in the upstream direction but also in locations the “fresh” plume does not reach. Other parcels containing ^{131}I, transported by the original effluent plume downstream travel upstream, due to water inversion, until the tide reverses the flow direction (app. 6 hours later) and downstream once more. This complex flow pattern tends to level out ^{131}I activity concentrations, resulting in similar values in both up and downstream directions of the WWTP and in both left and right banks of the river, visible in figures 6.16 and 6.17.

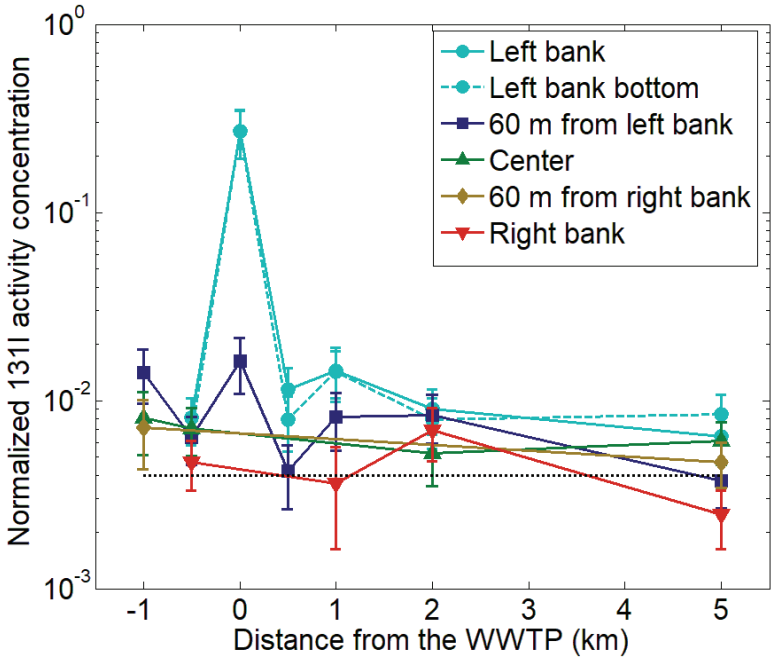

Figure 6.16: Normalized ^{131}I activity of surface samples, 3 to 4 hours after high and low water, on 5 equidistance points across the river in locations -1, -0.5, 0, 0.5, 1, 2 and 5 km distance from the WWTP. Negative values indicate upstream locations. On the left bank additionally bottom samples were analyzed. Values below detection limit not included. Dotted line indicates the ratio between the mean WWTP discharge (1.5 m^3/s – Hansewasser 2017) and the mean river discharge (327 m^3/s - Cherlet, 2007).

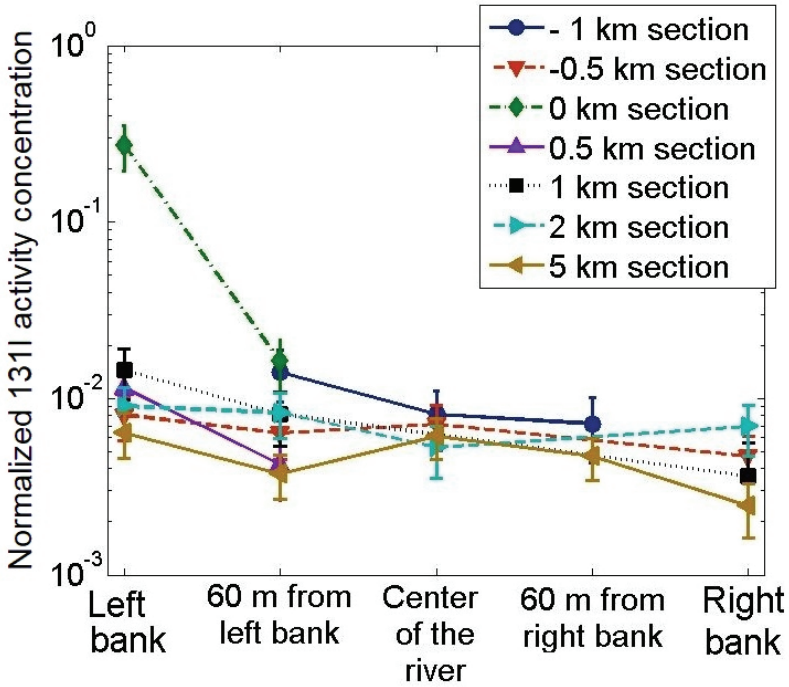

Figure 6.17: Normalized ^{131}I activity of surface samples, 3 to 4 hours after high and low water, on 5 equidistance points across the river in sections -1, -0.5, 0, 0.5, 1, 2 and 5 km distance from the WWTP. Values below detection limit not included.

6.7 ^{131}I activity concentration in Weser River sediments

6.7.1 Bottom sediments

In this water-sediment linked study an attempt was made to obtain bottom sediments in the same sampling points where water samples were taken. The sampling campaigns took place on the 12th and 18th of March 2015. In our case we expect to find iodine in bottom sediment layer depths smaller than 1 cm. In figures 6.18 and 6.19 bottom sediment sampling locations and samples in wet state are illustrated.

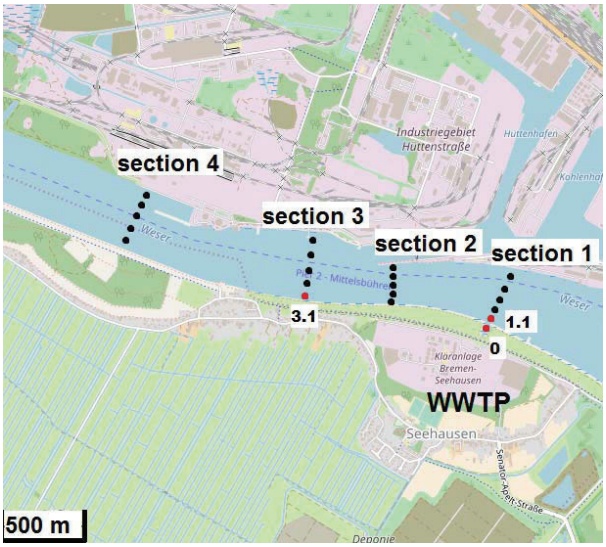

Figure 6.18: Sampling locations for bottom sediments. Red dots represent the locations where samples were successfully collected (open street maps).

Figure 6.19: Bottom sediment samples(in wet state) in drying pans from locations 0 (left sample- darker color) and 3.1 (right sample – lighter color).

Out of all sampling locations, only from 3 (figure 6.18), bottom sediment samples were obtained. Most of the sampling attempts provided mostly mussels and stones (figure 6.20) or no sample at all. One of the reasons for not obtaining bottom sediment samples could be the sampler itself, since the possibility of not proper closing can cause sample loss when moving the device upwards. On the other hand, the fact that stones and mussels instead of silt or clay bottom sediments were obtained indicates the absence of fine material in the bottom of the river. Schrottke et al. (2006) observed that the constructions made in the area of groins, sheet pilings (figure 6.21) and subaqueous embankments canalize the tidal currents and reduce sediment deposition in the navigation channel. In fact many engineering structures performed in the area (see also §2.1) were done in order to minimize the sedimentation thus maintaining constant depth of the channel and avoiding periodic dredging.

Figure 6.20: Sampled stone, mussels and sand from the bottom of the river.

Figure 6.21: Industrialized area of the Weser River with sheet pilings on the right bank.

The results from the gamma measurements are given in the following table. More information can be found in appendix 6.

Table 6.2: ^{131}I activity concentration on bottom sediments

Sampling location	Distance from the WWTP (km)	Date of sampling	^{131}I activity concentration [Bq/kg(d.m.)]
0	0	18.3.15	0.47 ± 0.03
1.1	0	12.3.15	6.45 ± 0.62
3.1	1	18.3.15	< 0.40

The ^{131}I activity concentration in bottom sediments is lower than expected (see §2.4) and more than 10 times lower as measured by Fischer et. al. (2009) in 2008 (eg. in location 1.1 in bank sediments the activity was 98.7 ± 2.3 and 122.3 ± 3.1 Bq/kg(d.m.)). Especially 1 km downstream the activity was below detection limit, where in 2008, in 1.75 km distance downstream in the left bank the activity was more than 10 times higher than the detection limit (see table 6.1). Additionally the comparability of the samples could not be established (although the number of samples was limited) since in different locations the samples had discrepancies not only on their activity but also on their color (figure 6.19) and smell.

6.7.2 Bank Sediments

Since the sampling of bottom sediments did not provide any fruitful results, two additional sampling campaigns on the 26th of March and 8th of April 2015 were carried out. Sediment samples were taken from both banks (see §2.1) in locations up to 2 km upstream and 5 km downstream the WWTP. Some locations, notably on the right bank, were inaccessible due to the industrialization of the area (figure 6.21). In all sampled locations ^{131}I was detected above

detection limit with activity concentration between 0.9 to 36 Bq/kg(d.m.). Its profile is similar to the one in river water as illustrated in figure 6.22.

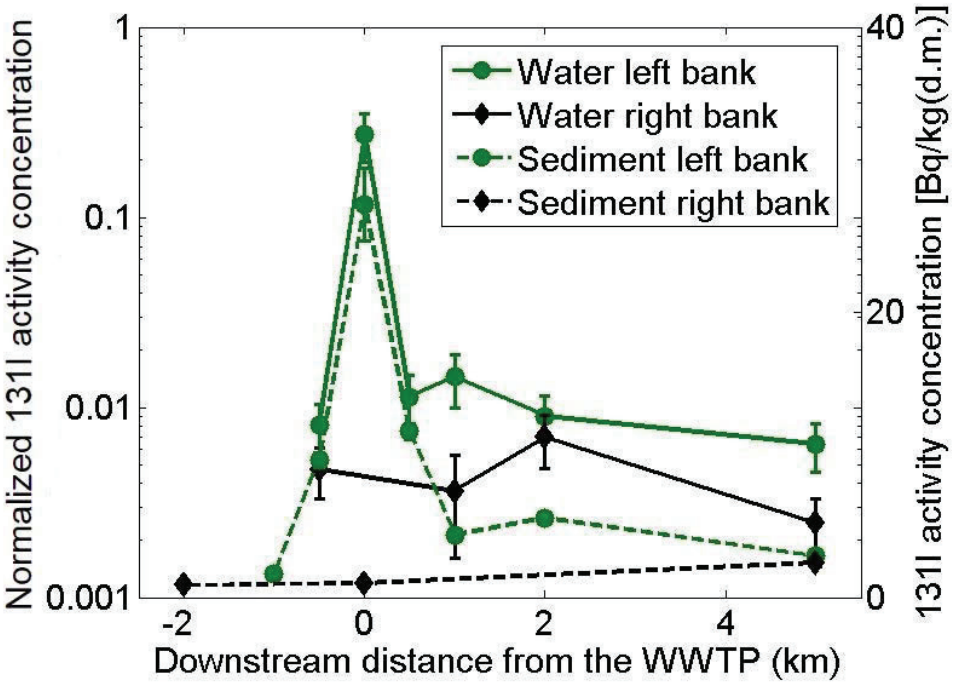

Figure 6.22: ^{131}I activity concentration in bank sediments(in Bq/kg(d.m.)) and normalized activity concentrations in river water in left and right bank and distances -1 to 5 km from the WWTP.

As expected, the highest concentrations are close to the WWTP outlet, decreasing with increasing distance from the source. The presence of ^{131}I in the upstream direction and in the right bank is due to the tidal effect of the river. In distance 5 km downstream in both banks the concentrations, 2.89 ± 0.27 Bq/kg(d.m.) on the left bank and 2.44 ± 0.26 Bq/kg(d.m.) on the right bank are similar, additionally supporting our earlier assumption of full horizontal mixing (see §6.6.2). Moreover the hypothesis explaining the background ^{131}I concentrations (as defined in §6.6.2) is further substantiated by the sediment data, where similar concentrations are detected in the upstream direction and in whole right bank.

Comparing with older data on sediment from the same locations (Fischer et al., 2009) one can observe in figure 6.23, that the ^{131}I background concentration is rather low compared to close proximity of the WWTP discharge.

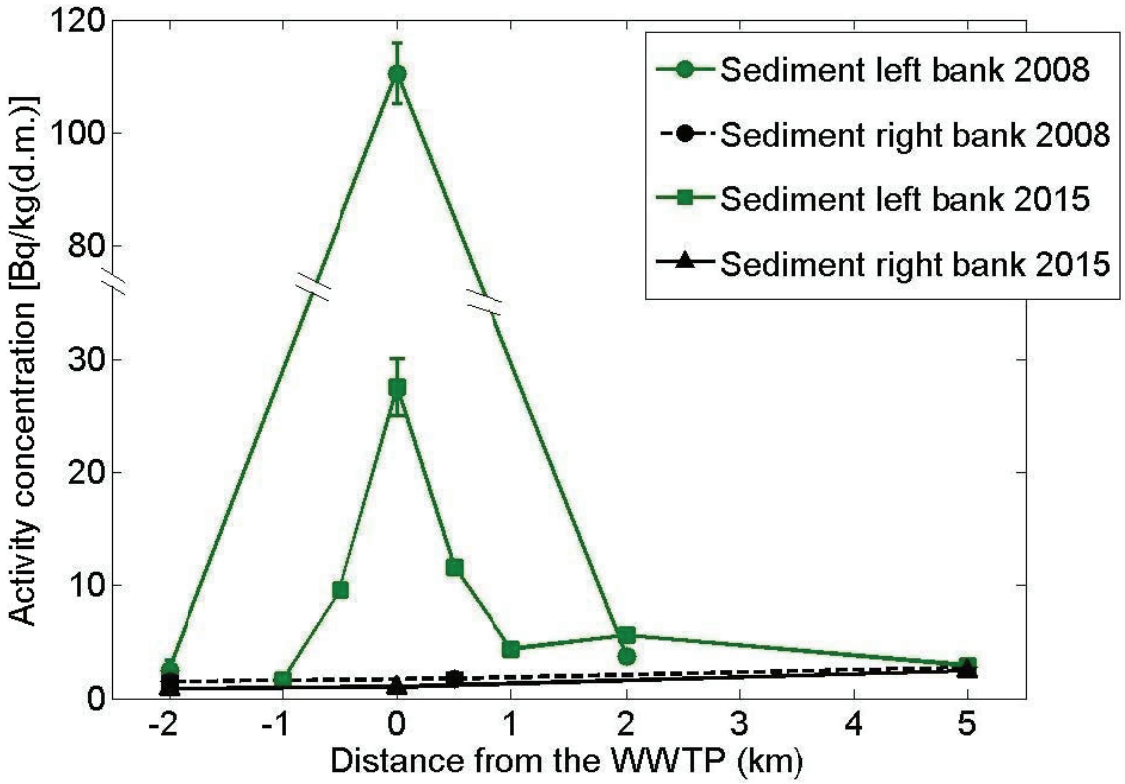

Figure 6.23: ^{131}I bank sediment activity concentration (in Bq/kg(d.m.)) of 2015 and 2008 sampling campaigns.

On the location directly on the boundary between the river and the WWTP, a discrepancy (35.72 ± 1.44 and 19.39 ± 1.01 Bq/kg(d.m.) in the 2015 samples and 98.71 ± 2.28 and 122.30 ±3.11 Bq/kg(d.m.) in the 2009) is observed. This can be attributed to slightly different sampling spots (figure 6.24); sediments collected closer to the outflow have higher ^{131}I activity concentrations than further away.

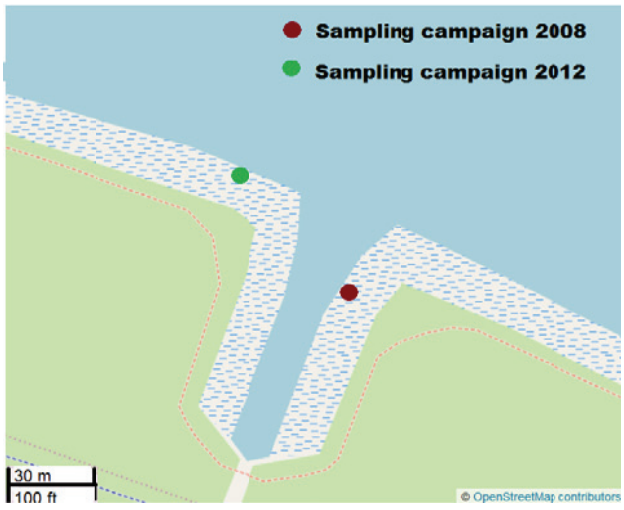

Figure 6.24: Sampling locations on the outflow of the WWTP of 2008 and 2015 sampling campaigns.

In addition to ^{131}I, a variety of natural and manmade isotopes were detected in both banks of the river (figure 6.25).

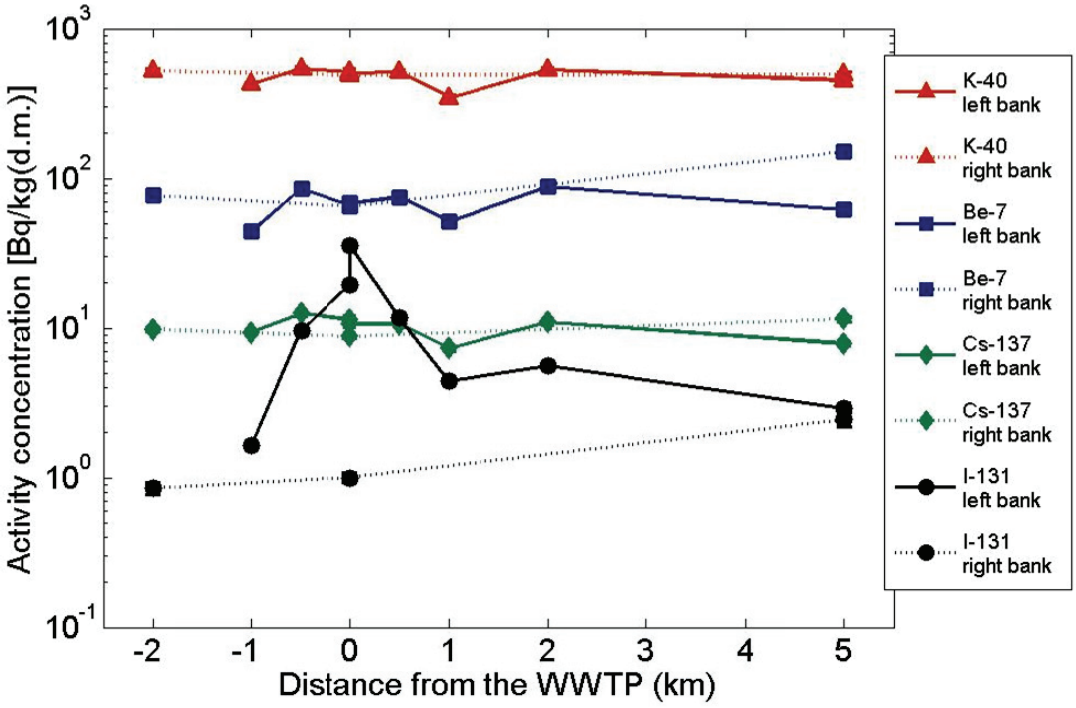

Figure 6.25: Natural and manmade radioisotopes in Weser bank sediments.

Both ^{40}K, ^{7}Be and ^{137}Cs, with half lives of 1.3×10^{9} years, 53 days and 30.2 years respectively, show a rather constant concentration in both upstream and downstream the WWTP irrelevant of the river bank (left or right). This is to be expected, since they have different environmental pathways than iodine, not originating from the WWTP, rather than processes of wet/dry deposition and erosion.

More specifically, the natural radioisotope ^{7}Be is created in the lower stratosphere and the upper troposphere where cosmic rays interact with nuclei of oxygen and nitrogen atoms (spallation). After this production, it is attached to aerosols and these are transported to the ground through wet (mainly) and dry deposition. The depositional flux of ^{7}Be in the Bremen region between January 2013 and July 2015 was between 16.4 and 177 Bq/m^2/week (Souti et al., 2015).

The concentrations of both ^{40}K and ^{137}Cs in wet and dry deposition are negligible. ^{40}K as a natural isotope is present in soils with average concentrations of 332 Bq/kg(d.m.),(Souti et al., 2015). ^{137}Cs is a manmade radioisotope and fission product, deposited in Bremen soils from the Chernobyl accident and nuclear weapons fallout, with average activity concentrations in the surface of 11.5 Bq/kg(d.m.),(Souti et al., 2015). While the main origin of ^{7}Be in river water appears to be the wet and dry deposition, both ^{40}K and ^{137}Cs reach the river by erosion processes, subsequently get attached to particles and sediment, creating a rather stable profile along the river length.

6.8 ^{131}I bound to suspended matter in Weser River

As stated in §5.1, iodine in river water can occur in both inorganic and organic forms. Especially under aerobic conditions, iodine can become incorporated into dissolved organic matter, colloids and particles through processes of uptake by fresh water algae, particle surface interactions, colloidal flocculation and coprecipitation, which "trap" a fraction of the dissolved radioiodine in the particulate phase (Smith et. al, 2008). Therefore, the quantification of the ^{131}I bound to the suspended matter is of importance, since once associated with the particulate phase ^{131}I can be deposited in sediments.

The ^{131}I in suspended matter was determined through 4 sampling campaigns where WWTP water and surface river water in the WWTP - river boundary were collected. The selection on the sampling locations (figure 6.26), was based on fact that in the boundary there is a minimum dilution of the original ^{131}I effluent activity. The results are given in table 6.3. Additional information can be found in Appendix 7.

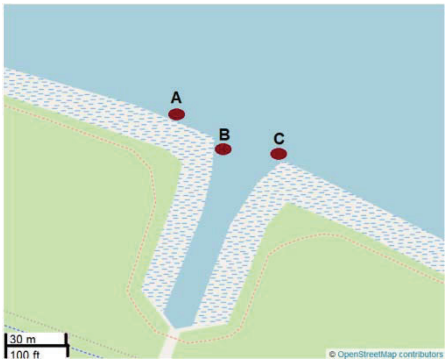

Figure 6.26: Sampling locations for suspended matter measurements (open street maps).

Table 6.3: ^{131}I bound to suspended matter results for WWTP effluent and river water.

Sampling date	Type of sample	Total ^{131}I activity concentration in the sample [mBq/kg]	Total sample mass [kg]	Total activity measured in suspended matter [mBq]	Radioactive analysis (^{131}I in suspended matter[mBq]/total ^{131}I in sample[mBq]) [%]
Samples treated with Mundschenk method					
6.5.14	WWTP effluent	149±24	19.24	72±11	2.51
6.5.14	WWTP effluent	197±21	17.94	39±6	1.10
6.5.14	WWTP effluent	198±19	18.92	47±9	1.25
20.5.14	WWTP effluent	315±25	48.16	128±16	0.84
20.5.14	WWTP effluent	272±24	48.52	158±19	1.20
20.5.14	WWTP effluent	306±28	47.44	119±18	0.82
18.6.14	River water- A	63±14	49.64	< 20	< 0.64
18.6.14	River water- B	136±19	48.46	< 15	< 0.23
Sample treated with Flockfix®					
12.11.14	River water- C	175 ± 20	51.20	20 ± 1	11.51

The results of the radioactive analysis reveal small to non-detectable amounts of ^{131}I bound to suspended matter in river water. For the WWTP effluent measurements the fraction of ^{131}I bound to suspended matter reaches up to 2.5%. Only when applying the precipitation with Flockfix we are able to detect a bit more than 10% of the total iodine in the precipitate, however this precipitate is formed not only by suspended matter but also with smaller particles, such as colloids and macromolecules larger than 2000 Dalton (Hormann and Fischer, 2017).
In spite of the limited set of data, one can expect that with ^{131}I activity concentrations of some mBq/kg in the Weser river water, the ^{131}I bound to suspended matter (< 10 %, even as low as 2%) is highly unlikely to be measured. This leads to describing the partitioning of ^{131}I between water and suspended matter in terms of distribution coefficients, as found in literature (see Table 7.3).

6.9 General comment on Chapter 6

Medically derived ^{131}I is regularly released into the water body of the Weser River, with WWTP effluent, and partially attaches to particles and becomes confined in sediments.
Large amounts of data were obtained in the framework of this study and are in good agreement with previous measurements done in the region (Fischer et al., 2009). The ^{131}I activity concentration in river water is strongly dependent on the tidal cycle of the river and its profile appears to be analogous to that of the sediment, identifying the WWTP as the main source, a finding additionally supported when comparing with the rather steady sediment profiles of ^{40}K, ^{7}Be and ^{137}Cs.
Due to the complexity of the hydrological system, results are less easy to interpret since temporal variations are dependent on many parameters. Nonetheless, ^{131}I can be used as a readily available tracer for the study of such a complex system, allowing us a better understanding of the processes of convection, diffusion and sedimentation.

6.10 References for Chapter 6

Cherlet M., 2007. *Experiences in Analysis of Pressures and Impacts from Agriculture on Water Resources and Developing a related Programme of Measures.* Report of the Pilot River Basin Group on Agriculture. Phase II period September 2005- December 2006. Retrieved from: http://ec.europa.eu/environment/water/water-framework/pdf/report_phase_2.pdf

Clark I.D., Fritz P., 1997. *Environmental Isotopes in Hydrogeology.* CRC Press LLC.

Doneker R.L., 2008, *CORMIX Input/Output*, Mixing Zone Model Workshop. Retrieved from: http://www.ifh.uni-karlsruhe.de/science/envflu/research/brinedis/WS/9-CORMIX%20Input-Output.pdf

Facchi A., Gandolfi C., Whelan M.J., 2007, *A comparison of river water quality sampling methodologies under highly variable load conditions*. Chemosphere 66, 746-756.

Fischer, H.W., Ulbrich, S., Pittauerová, D., Hettwig, B., 2009. *Medical radioisotopes in the environment-following the pathway from patient to river sediment.* Journal of Environmental Radioactivity200**,** 1079-1085.

Flussgebietsgemeinschaft Weser (FGG Weser) - (in German), (http://www.fgg-weser.de/, 2017).

Grabemann, I., Kuehle, H., Kunze, B., Mueller, A., 1996. *Studies on Transport Times and Water Quality in the Weser Estuary (Germany)*, in Mixing in estuaries and Coastal Seas, American Geophysical Union, Washington, D.C..

HanseWasser, *2017. https://www.hansewasser.de/wir-fuer-bremen/daseinsvorsorge-fuer-die-stadt/klaeranlagen.html*

Herrling G., Niemeyer H.D., 2008.*Hydro- and Morphological Pressures and Impacts*, HARBASINS Report. Retrieved from: http://www.nlwkn.niedersachsen.de/download/70702.

Herod M.N., Cornett R.J., Clark I.D., Kieser W.E., St. Jean G., 2014.*Extraction of ^{129}I and ^{127}I via combustion from organic rich samples using ^{125}I as a quantative tracer*, Journal of Environmental Radioactivity , 138, 323-330.

Ho D.T., Schlosser P., Caplow T., 2002. *Determination of Longitudinal Dispersion Coefficient and Net Advection in the Tidal Hudson River with a Large-Scale, High Resolution SF6 Tracer Release Experiment.* Environmental Science and Technology, 36 (15), 3234-3241.

Hormann V. and Fischer H.W., 2017*, The physiochemical distribution of ^{131}I in a municipal wastewater treatment plant,* Journal of Environmental Radioactivity, 178-179, 55-62

Hochschule Bremen- *InstitutfürWasserbau, 2011. In situ Messungen im Bereich des geplanten Offshore Terminals Bremerhaven (OTB). (in German).* Retrieved from: http://www.bauumwelt.bremen.de/sixcms/media.php/13/13.04%20In%20situ%20Messungen%20im%20Bereich%20des%20geplanten%20OTB.pdf.

Jirka G.H., Doneker R.L., Hinton S.W., 1996. *User's manual for CORMIX: A hydrodynamic mixing zone model and decision support system for pollutant discharges into surface waters.* Retrieved from: https://www.epa.gov/sites/production/files/2015-10/documents/cormix-users_0.pdf

Millero F.J., Poisson A., 1981. *International one-atmosphere equation of state of seawater.* Deep Sea Research Part A, Oceanographic Research Papers, 28 (6), 625-629.

Mundschenk H., 1993. *Verfahren zur gammaspektrometrischen Bestimmung von Radionukliden in Schwebstoffproben*, Leitstelle für Oberflächenwasser, Schwebstoff und Sediment in Binnengewässern. (in German), Retrieved from: http://www.bmub.bund.de/fileadmin/Daten_BMU/Download_PDF/Strahlenschutz/leitstelle_c-gamma-spekt-schwe-01.pdf

Gellermann R., Fischer H., Ulbrich S., Buchholz O., 2013. *Messtechnische und theoretische Abschätzung des Eintrags von I-131 in die OSPAR-Regionen aufgrund der nuklearmedizinischen Anwendungen von Radioiod in Deutschland.* Abschlussbericht. Vorhaben 3611S70013. Auftraggeber: Bundesamt für Strahleschutz. 02.12.2013.

Schrottke K., Becker M., Bartholomä A., FlemmingW.,Hebbeln D., 2006. *Fluid mud dynamics in the Weser estuary turbidity zone tracked by high-resolution side-scan sonar and parametric sub-bottom profiler*, Geo-Marine Letters, 26,3,185-198.

Shelton L.R., Capel P.D., 1994.*Guidelines for collecting and processing samples of stream bed sediment for analysis of trace elements and organic contaminants for the National Water-Quality Assessment Program*, Open-File Report 94-458. Retrieved from: https://pubs.usgs.gov/of/1994/0458/report.pdf

Smith J.P., Oktay S.D., Kada J., Olsen C.R., 2008. *Iodine-131: A potential Short-Lived, Wastewater-Specific Particle Tracer in an Urbanized Estuarine System*. Environmental Science and Technology, 42 (15), 5435-5440.

Souti M.E., 2012.*Medical ^{131}I in Weser water*, Universität Bremen, Faculty of Environmental Physics, Master Thesis. Retrieved from: http://www.iup.uni-bremen.de/PEP_master_thesis/thesis_2012/master_thesis_souti.pdf.

Souti M.E., Anesiadou A., Amoo P.B., Fischer H.W., 2015. *Be-7 in various environmental media in the Bremen Region*, Extended abstract available from Envira 2015 Conference.

Stoschek O. and Matheja A., 2001, *Simulation von Sedimenttransportprozessen in Tidebeeinflussten Hafengebieten*. Franzius Inst. F. Wasserbau u. KüsteningenieurwesenUni Hannover, Heft 86/01, 18-56

Tazioli A., 2011, *Experimental methods for river discharge measurements: comparison among tracers and current meter*. Hydrological Sciences Journal, 56:7, 1314-1324.

Whitfield P., 1983. *Evaluation of water quality sampling locations on the Yukon River.* Water Resources Bulletin, American Water Resources Association, 19, 1, 115-121.

Chapter 7

Modeling ^{131}I in Weser River

The majority of existing radionuclide distribution and transport models in rivers are applicable in short duration releases and /or in distances with uniform distribution of the contaminant over the river section downstream a source, unsuitable to our case (tidal nature of river, short half-life of ^{131}I, see §3.1). This spurred the need for developing and assessing a model for predicting the dispersion of ^{131}I in Weser River, presented in this chapter.

7.1 ^{131}I dispersion-sedimentation model in Weser River

The mathematical model used for the simulation of the dispersion and sedimentation of ^{131}I in Weser River (figure 7.1), as described in §3.2, consists of 2 major coupled sub-models: the hydrodynamic (2 dimensional horizontal model) and the radionuclide transport, which is subdivided for the components of river water (2 dimensional horizontal model) and bank sediments (1 dimensional longitudinal model). Due to the complexity of the partial differential equations (see §3.2.2) the solution for the hydrodynamic and radionuclide transport in river water is approached with the finite element method, implemented in Matlab with the aid of the IFISS software package (see §3.3.2).
Tidal related parameters are calculated by fitting measured data from the nearby Oslebshausen station, acquired from the Waterway and Shipping administration of the federal government (WSV, 2017)[appendix 8], using the HAMELS method (Harmonic Analysis, Method of Least Squares) with the aid of the Tidal fitting toolbox (see §2.2). All MatLab files used for this work are given in Appendix 15.

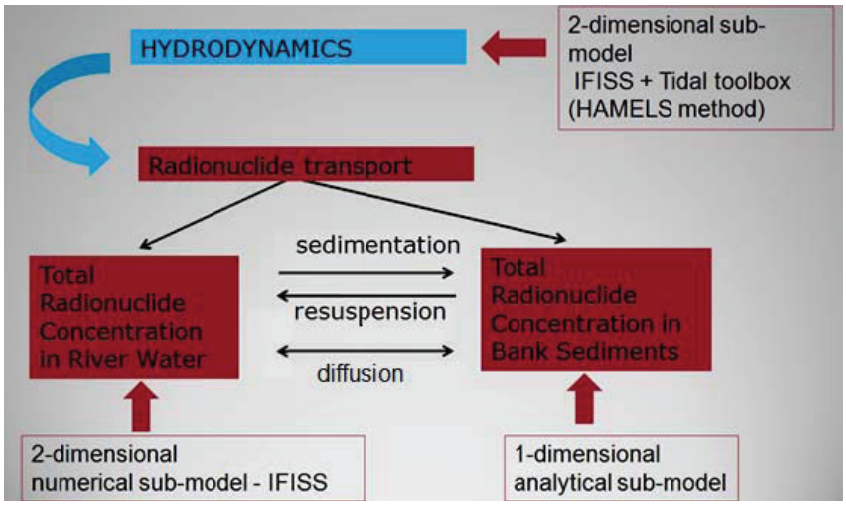

Figure 7.1: Simplified scheme of the model. Detailed version figure 3.1(see §3.2.1).

7.2 Grid approximation

In advance of the numerical calculations of the river flow velocity and activity concentration in river water and sediments it is of importance to define the domain by a grid which provides information (specifically, node point coordinates and element connectivity information) as an approximation of the actual region, as seen in figures 7.2 and 7.3.

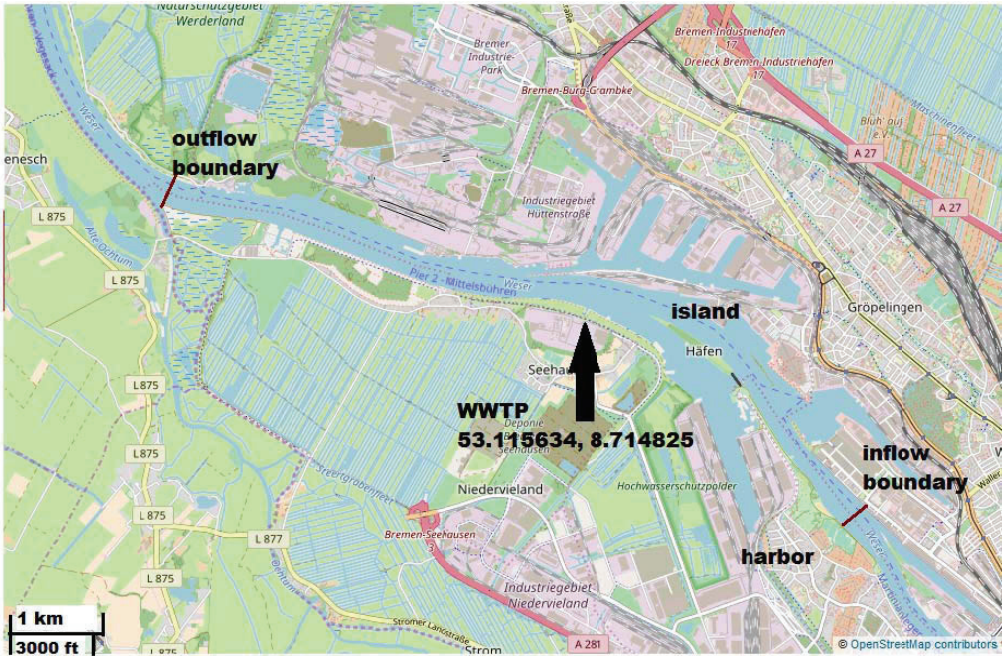

Figure 7.2: Weser River in the vicinity of the WWTP (open street maps).

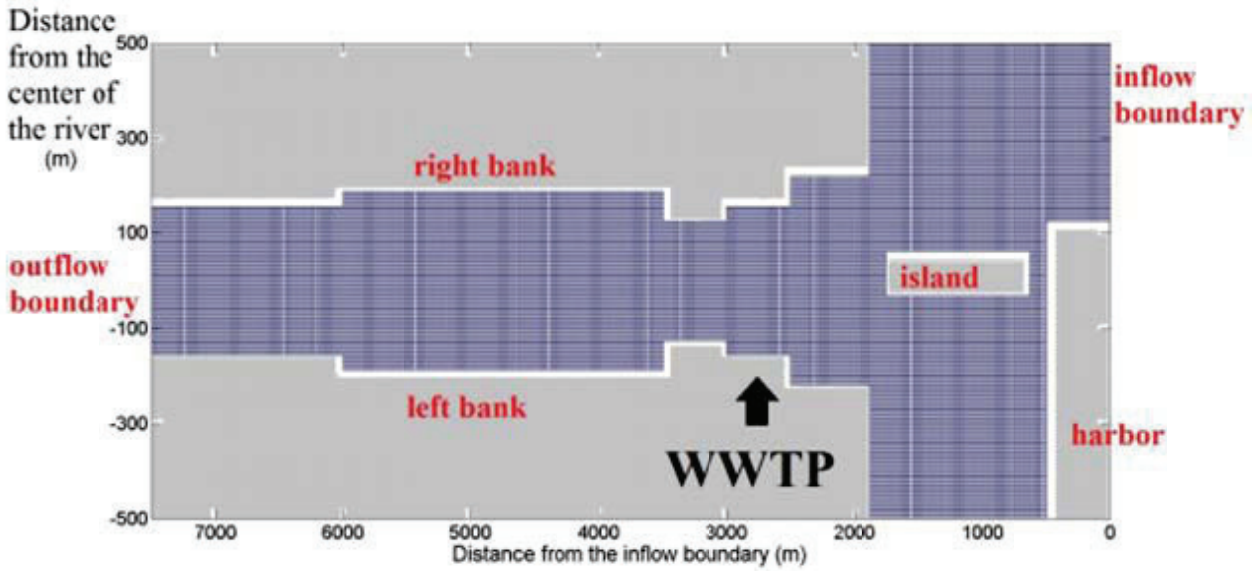

Figure 7.3: Weser domain discretization.

The grid consists of 10 rectangles with length between 125 m to 2.5 km and width of 250 m to 1 km, as seen in table 7.1 and figure 7.4. In the longitudinal direction (min 0, max 7.5 km) the resolution (restricted by the computer's specification: Intel Core i5-3330 CPU @ 3.00GHz with a RAM of 4.00GB) is 65.5 m and in the lateral (min 0, max 1 km) 31.25 m.

Table 7.1: Grid dimensions

Rectangle	Range of x (m)	Range of y (m)
I	[0,500]	[125,500]
II	[500,1875]	[-500,500]
IIIa	[500,625]	[-500,500]
IIIb	[625,1750]	[-500,-31.25]
IIIc	[625,1750]	[62.5,500]
IIId	[1750,1875]	[-500,500]
III	[1875,2500]	[-218.75,218.75]
IV	[2500,3000]	[-156.25,156.25]
V	[3000,3500]	[-125,125]
VI	[3500,6000]	[-187.5,187.5]
VII	[6000,7500]	[-156.25,156.25]

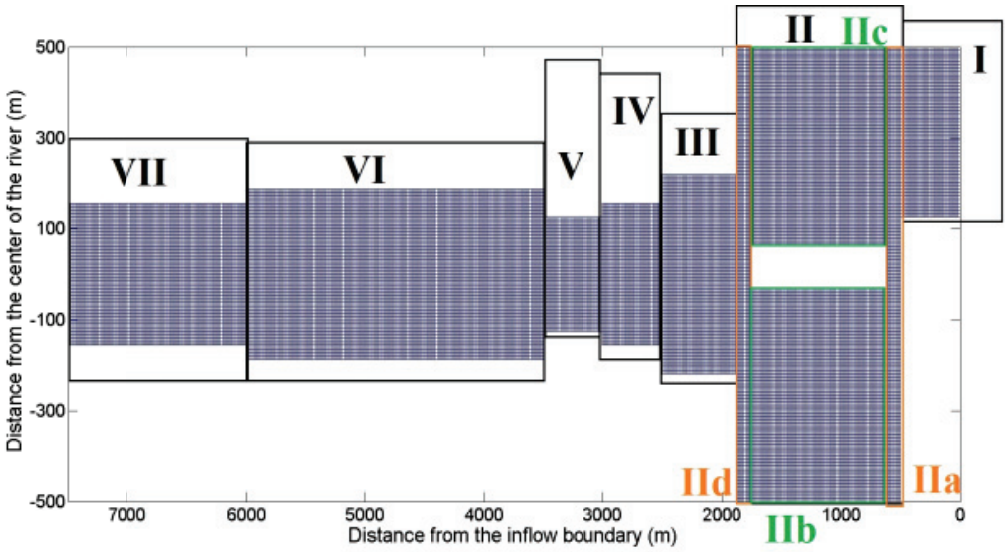

Figure 7.4: Grid approximation as sum of rectangles

Boundaries

At coordinate x=0 km, the inflow boundary is located and at x=7.5 km the outflow. On the outflow, Neumann boundary conditions are applied (see §3.2.2.1), while for the inflow, banks and remaining boundaries Dirichlet boundary conditions are set (figure7.5). In total the grid consists of 7000 (2x2 macro) elements with 28708 nodes. In the Dirichlet boundary 688 macroelement edges face with more than 1300 nodes.

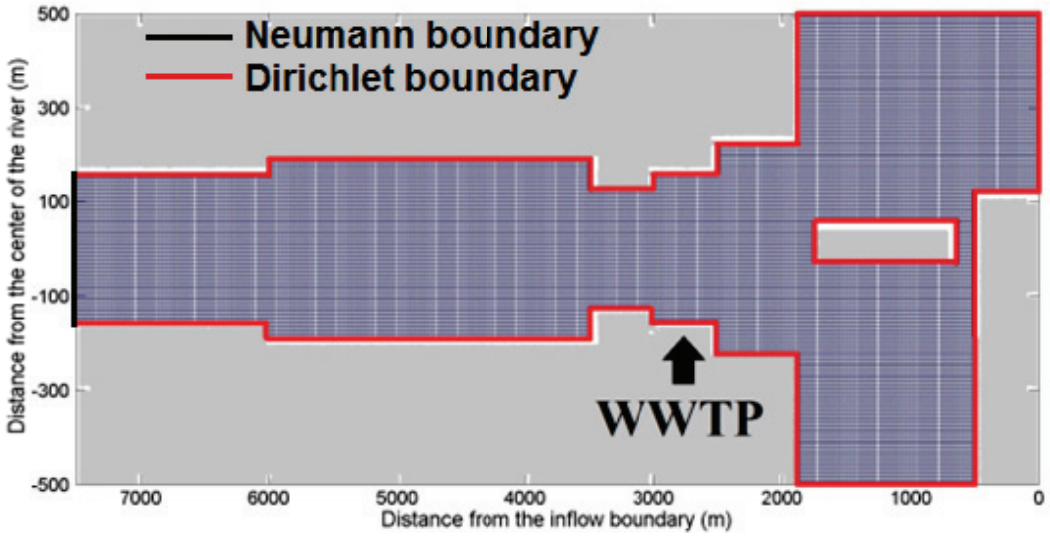

Figure 7.5: Dirichlet and Neumann boundaries.

7.3 Hydrodynamic sub-model

For the simulation of the water flow in Weser River the non dimensional form of steady state 2 dimensional Navier Stokes equations were used (see eq. 3.5-3.6, §3.2.2):

$$\mathbf{u}^* \cdot \nabla \mathbf{u}^* - \frac{1}{\mathrm{Re}} \nabla^2 \mathbf{u}^* = -\nabla p^* + \frac{L}{U_0^2} \mathbf{f} \qquad \textit{eq.3.5/7.1}$$

$$\nabla \cdot \mathbf{u}^* = 0 \qquad \textit{eq.3.6/7.2}$$

where $\mathbf{u}^* = \frac{\mathbf{u}}{U_0}$ and $p^* = \frac{p}{U_0}$ the normalized, with respect to the size of the domain ($\mathbf{x}^* = \frac{\mathbf{x}}{L}$), velocity and pressure accordingly, $\mathrm{Re} := \frac{U_0 L}{\nu}$ the Reynolds number(with ν the kinematic viscosity) and $\mathbf{f}$ a forcing term.

Applying a particular set of boundary conditions, such as Dirichlet and Neumann boundary conditions on boundary $\partial\Omega = \partial\Omega_D \cup \partial\Omega_N$:

$$\mathbf{u}^* = \mathbf{w} \quad \textit{on the Dirichlet boundary, } \partial\Omega_D \qquad \textit{eq.7.3}$$

$$\nu \frac{\partial \mathbf{u}^*}{\partial n} - \mathbf{n} p^* = \vec{0} \quad \textit{on the Neumann boundary, } \partial\Omega_N \qquad \textit{eq.7.4}$$

where $\mathbf{n}$ is the unit vector normal to the boundary $\partial\Omega$.
The domain discretization was done by the Q1-P0 approximation (see §3.3.1). This approximation represents bilinear basis functions for the velocity and constant approximation for the pressure. This mixed approximation gives rise to a non-linear system of algebraic equations in which initial velocity estimates are required to start the iterative process of solving a linearized problem at each step. In complex domains, such as the Weser River approximated domain, Elman et. al. (2014) suggests the use of a hybrid method (see §3.3.2) with a maximum of 6 Picard iterations followed by 5 Newton iterations or until the nonlinear convergence test with a tolerance of 10^{-8} is satisfied.

The Dirichlet boundary is characterized by a no-flow (zero velocity) condition on the walls of the domain (right and left banks, island) and a Poiseulle flow imposed on the inflow boundary (x=0 m)[appendix 9]. The outflow boundary (x=7500 m) satisfies the natural outflow condition (eq. 7.4).

In IFISS the reference velocity and lengths are preset to unity (Elman et al., 2014), so that the Reynolds number of the flow is given by $R = 1/\nu$,with v > 0 the kinematic viscosity. The Reynolds number indicates whether the flow is laminar or turbulent, with values below 500 indicating laminar flow in a river with very low average velocities and extremely shallow depths and reflects the predominance of viscous forces over inertia forces. When Re > 2000 the flows become fully turbulent with chaotic movement of water masses. Flows with Reynolds numbers between 500 and 200 are considered transitional (Mount, 1995). Since the kinematic viscosity of the water is $10^{-6} m^2/s$, the Reynolds number is $\sim 10^6$, thus turbulent flow. For river flow, this low viscosity of the water means that disturbances due to irregularities along the channel can cause the water flow to become turbulent and in all but small rivulets the flow is turbulent. Under conditions of turbulent flow however, the flow behavior is determined more by the momentum of the fluid than its viscosity, expressed as frictional resistance generated along the boundaries (eddy viscosity). The aforementioned normalization can lead to a wide range of Reynolds numbers depending on the selection of the characteristic length scale in the domain, making it a function of the grid size.

Elman et al., (2014) state in reference problem 8.1.2 of an L shaped domain with parabolic inflow boundary condition and natural outflow boundary condition, that in the case of unstable flow it makes little sense in trying to compute steady solutions, result observed also in our simulations (figures 7.6, 7.7).
By running simulations for different values of the viscosity parameter we get figures 7.6 and 7.7 for the longitudinal and lateral components of the velocity respectively.

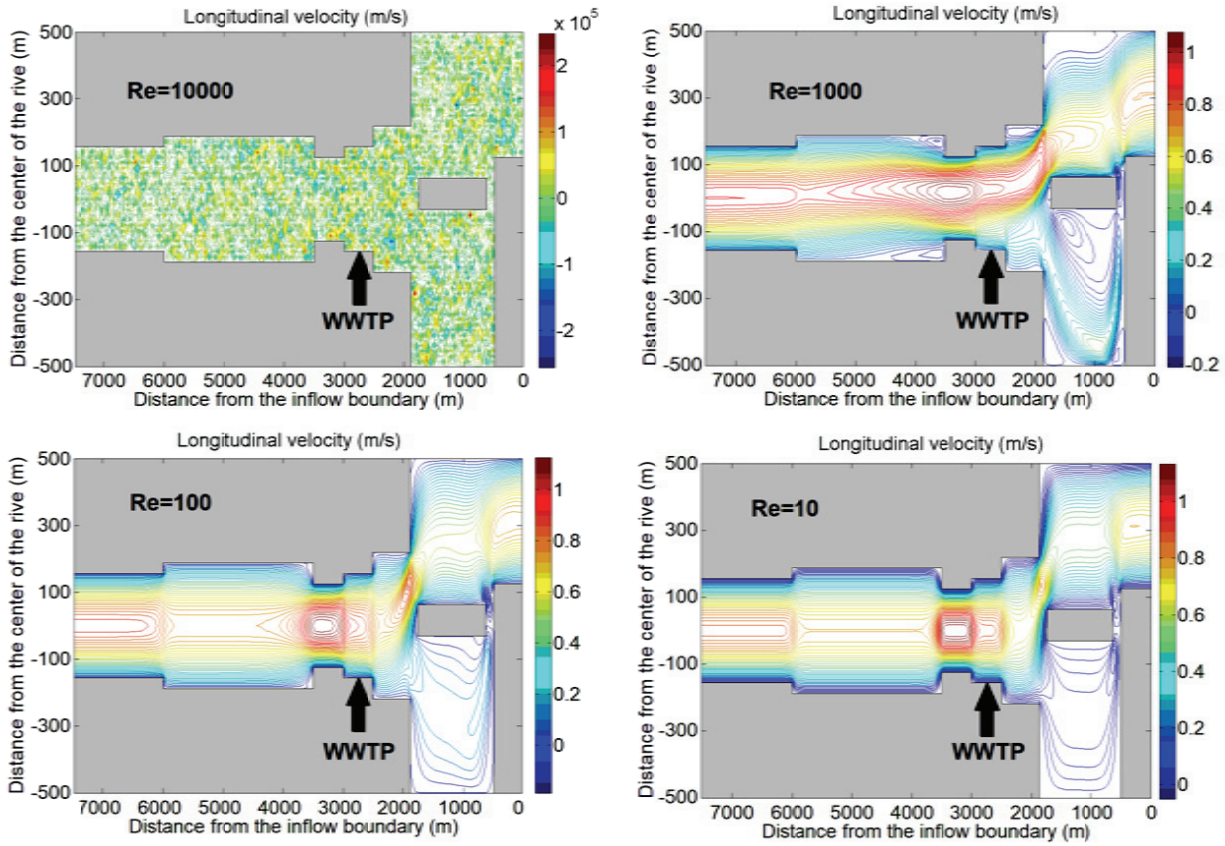

Figure 7.6: Simulations for the longitudinal component of the velocity for different viscosity parameters. Different coloration of zero and negative velocities.

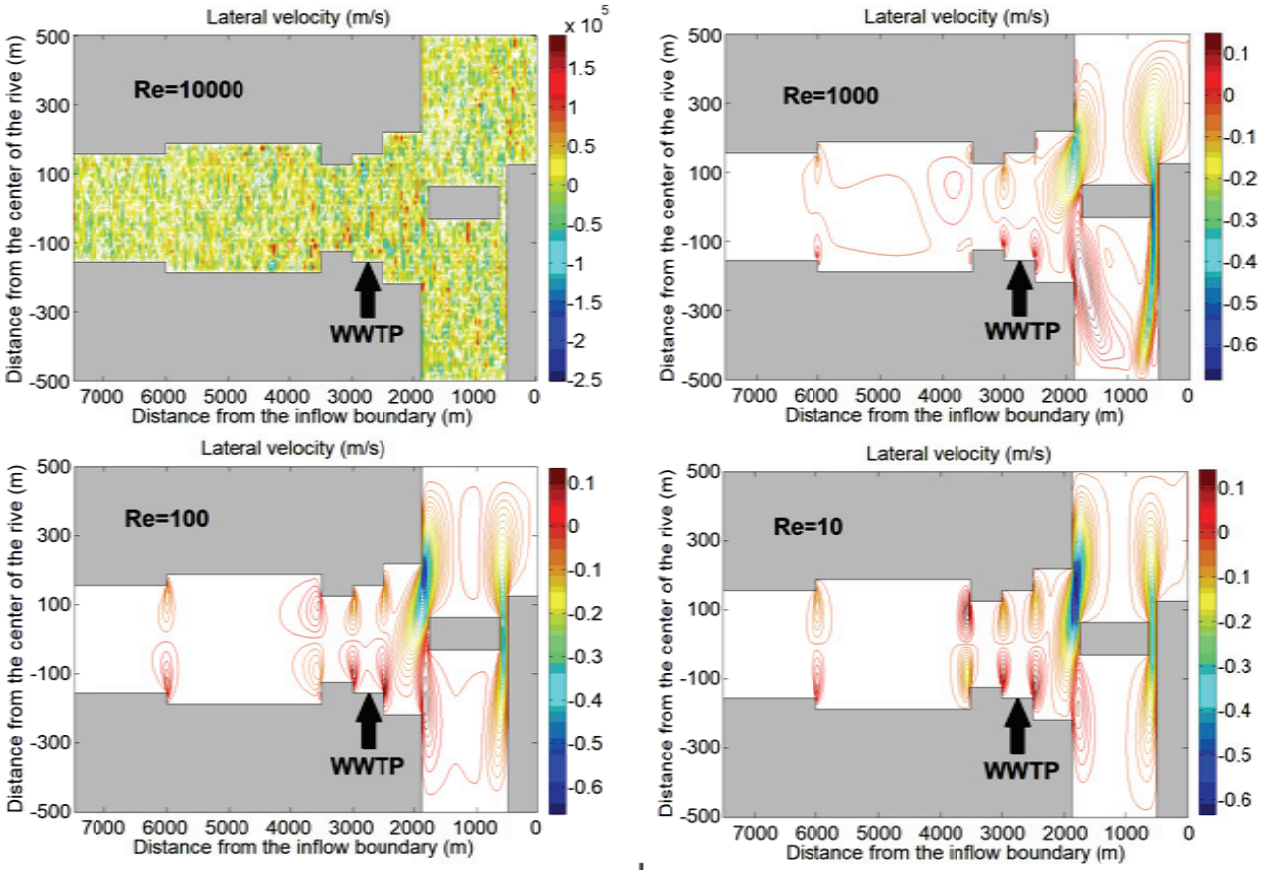

Figure 7.7: Simulations for the lateral component of the velocity for different viscosity parameters. Different coloration of zero and negative velocities.

In IFISS the Galerkin approximations are restricted to steady flows, occurring at low Reynolds numbers, since solving flows at higher numbers would necessitate the introduction of stabilization methods. Thus we set the Reynolds number equal to 1000, indicating a transitional flow. Additional to the Reynolds number the values of the horizontal velocity are influenced by the tide. Maximum current speed and water level are calculated for standing waves (see §2.2), taking into consideration a mean river depth of 12 m (Grabemann, 1996). Thus for Reynolds number equal to 1000 and in different times during the tidal cycle we get varying maximal values of the velocity as illustrated in figure 7.8.

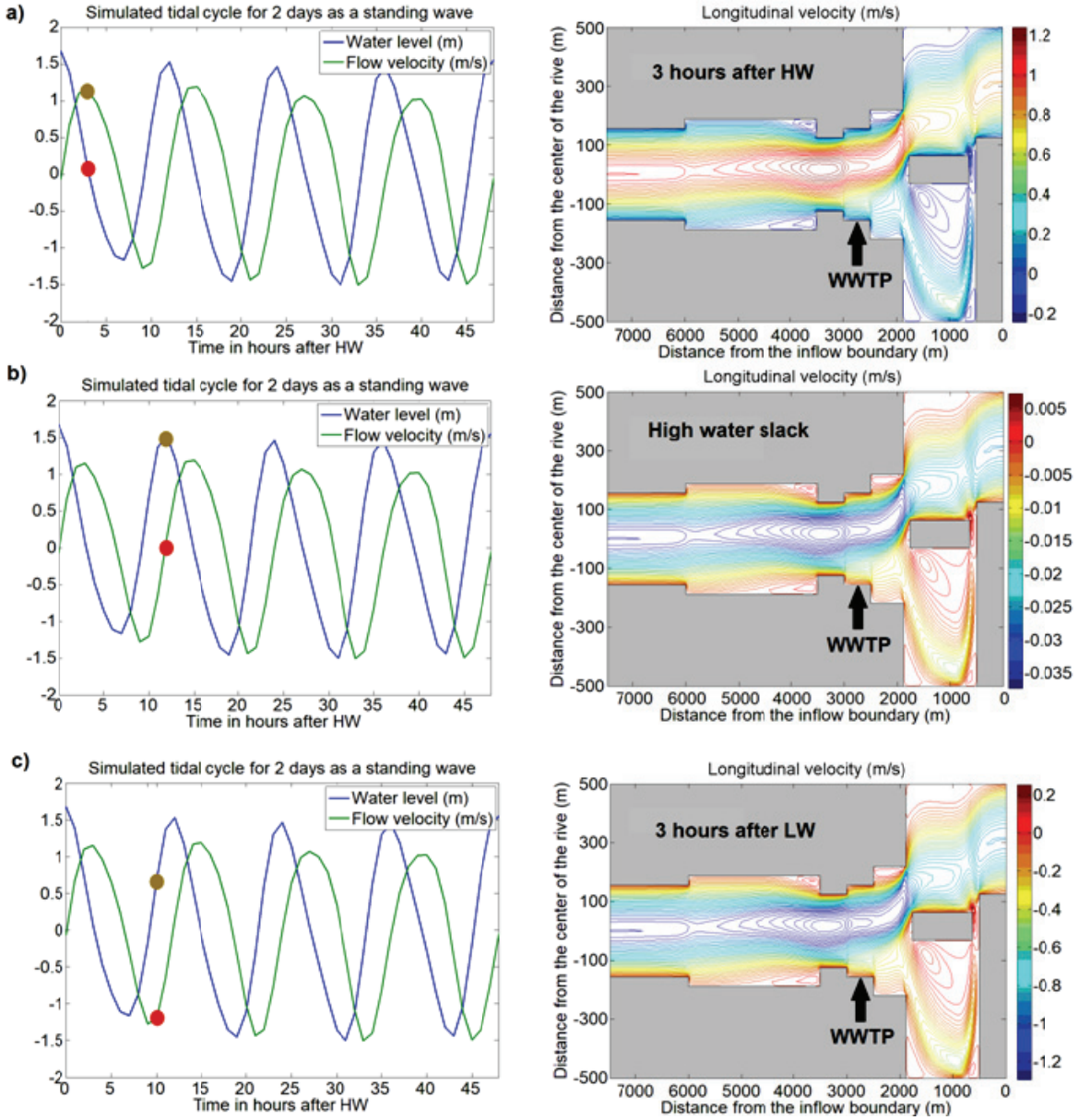

Figure 7.8: Simulated tidally influenced longitudinal velocities with maximum values (indicated by red dots)of a) 1.150 (3 hours after HW), b) -0.035 (LW close to slack) and c) -1.199 (3 hours after LW).

As observed and expected, the tide leads to fluctuations of the maximum velocity values between close to 0 m/s (slack time) to maximum values of 1.2 m/s (3 hours after high or low water – ebb and flood currents). Maximum values of water flow are located in the central part of the river, while the flow diminishes to zero close to the river banks (according to the boundary conditions). Negative values refer to upstream direction of the flow and current inversions which are present in locations south of the island, with values close to 10 times lower than the maximum values of the river flow.
The lack of hydrological data during our study, does not allow a direct assessment of the simulated data, however the results appear realistic. Similar values can be found in literature, i.e. Grabemann et al. (1996) report velocities ≈0.5 - ≥1 m/s, Schuchartdt et al. (1993) mention current velocities within the tidal cycle can reach up to 1.2 m/s with a mean of about 1.0 m/s and Vandenbruwaene et al. (2013) present mean and maximum ebb and flood flow velocities respectively ranging between 0.1 and 0.6 m/s and between 0.2 and 1.3 m/s in agreement with our simulation data.

7.4 Radionuclide submodel

7.4.1 Radionuclide submodel for river water
For a uniform channel, a steady state advection-dispersion equation (eq. 3.18, see §3.2.2.2) may be applied to describe the process of a pollutant with concentration C being transported along a stream moving with flow velocity $\mathbf{u}$, also subject to diffusive effects described by the horizontal eddy diffusivity ε.

$$-\varepsilon\nabla^2 C + \mathbf{u}\cdot\nabla C = 0 \qquad \textit{eq.3.18/7.5}$$

with boundary conditions

$C = g_D$ *on the Dirichlet boundary,* $\partial\Omega_D$ *eq.7.6*

$\frac{\partial C}{\partial n} = g_N$ *on the Neumann boundary,* $\partial\Omega_N$ *eq.7.7*

where n is the unit vector normal to the boundary $\partial\Omega$. The Dirichlet boundary sets the concentration equal to zero in the river banks with the exception of the location where the WWTP is located. The concentration is set as 1, in order to express our results as normalized concentrations (see §6.4). The velocity vector ($\mathbf{u}$) used as input is the simulated river flow obtained from the hydrodynamic sub-model adjusted according to the tidally influenced maximum value (example figure 7.8). In addition, the lateral transport of the effluent on the

WWTP location is taken into account by setting the lateral velocity on this specific location equal to 9×10^{-3} m/s (see §2.3).

The eddy diffusivity can be determined experimentally for specific river segments using the dispersion of non-toxic substances (dyes, etc, see Chapter 6) and may depend on local flow conditions and other factors thus not being constant along the river (Zhang, 2008). In all following simulations a constant value is assumed for simplicity. Fisher et. al (1979) state the following equation to be true for practical purposes in rivers describing the eddy diffusivity:

$$\varepsilon / Hu_* = 0.6 \pm 50\% \qquad eq.7.8$$

where H the mean river depth and u_* the shear velocity calculated as $u_* = \bar{u}\sqrt{f/8}$ with $\bar{u}$ the cross-sectional mean velocity and f the Darcy-Weisbach friction factor (see also footnote 4 §6.5) defined as $f = 8g\frac{n^2}{H^{1/3}}$ where g=9.81 m/s^2 the gravitational acceleration and n the Manning's value.

The cross-sectional mean velocity, approximated for trapezoid channel is calculated as: $\bar{u} = Q/A$ with Q the daily mean river discharge with values between 101 and 293 m^3/s on our sampling dates (see Appendix 5) and A[1] the river cross-section with values between 3780 and 2280 m^2.

Stoschek and Matheja (2001), on their work on sediment transport in the same area as in this work (see figure 3.2-1 in their publication), use for their simulations Manning's values between 0.025 and 0.040.

By utilizing equation 7.8 with the aforementioned parameters one obtains the eddy diffusivity value in the range of 0.001 and 0.25.

[1] The cross sectional area of a trapezoidal channel is calculated as $A = wh + zh^2$, where w the width of the channel as specified in our grid (see table 7.1), h the mean river depth equal to 12 m (Grabemann, 1996) and z equal 5 (Herrling and Niemeyer, 2008).

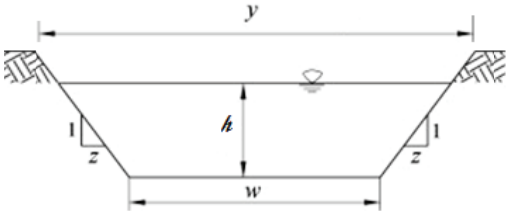

By running simulations for different values of the eddy diffusivity, using the velocity values obtained through the hydrodynamic model and setting the maximum tidal velocity equal to 1, we get for the normalized activity concentration of ^{131}I in the Weser River figures 7.9 and 7.10. The selection of the maximum tidal velocity is done based on the fact that it corresponds to tidal times of 3 hours after high water, were we know from our experimental results (see §6.5.2) the locations where ^{131}I can be found.

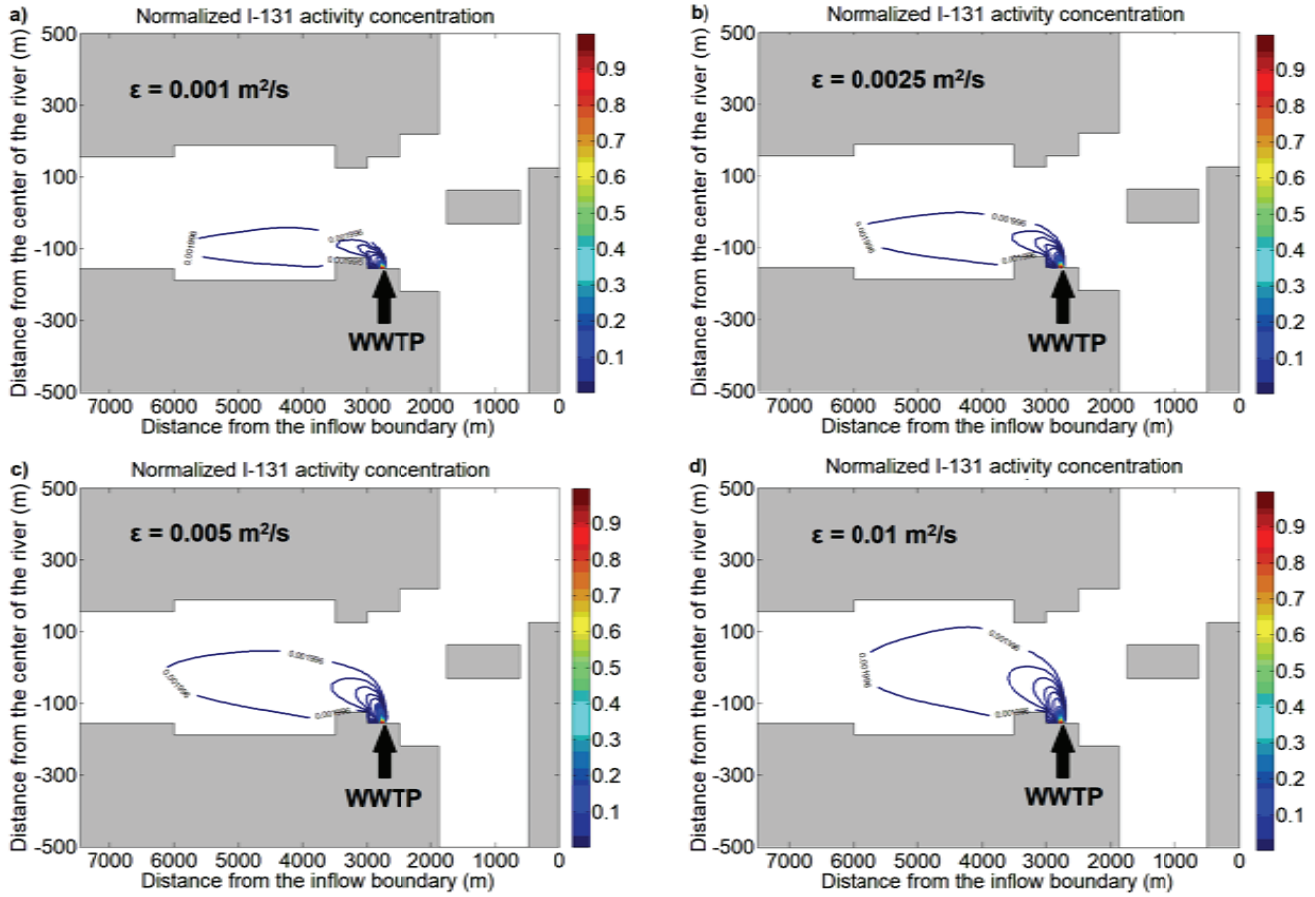

Figure 7.9: Simulated normalized ^{131}I activity concentration for different values of eddy diffusivity (a. ε=0.001 m^2/s, b. ε=0.0025 m^2/s, c. ε=0.005 m^2/s, d. ε=0.01 m^2/s) at the same time during the tidal cycle (3 hours after HW). The outermost contour corresponds to normalize activity concentration of 0.002.

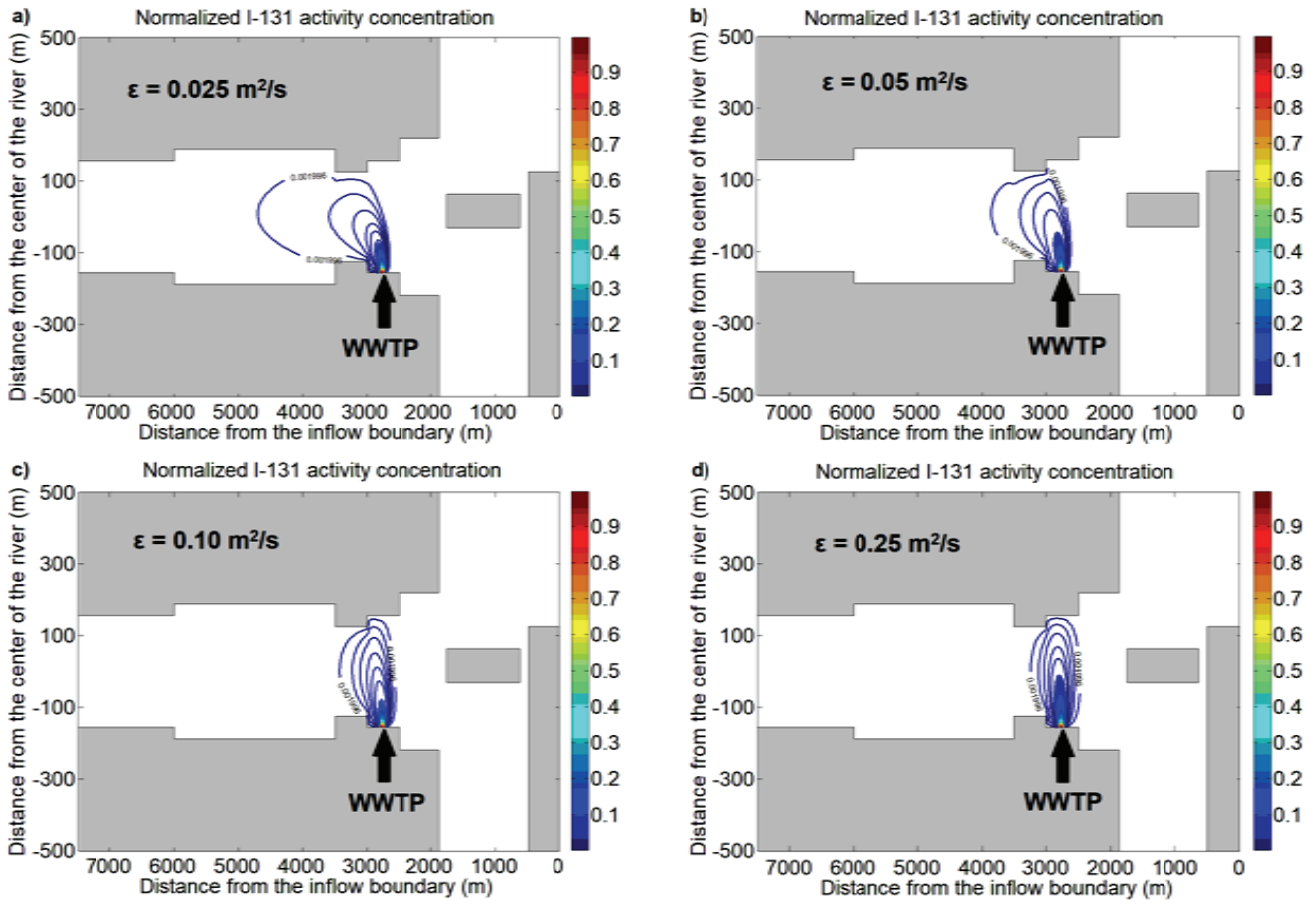

Figure 7.10: Simulated normalized ^{131}I activity concentration for different values of eddy diffusivity (a. ε=0.025 m^2/s, b. ε=0.05 m^2/s, c. ε=0.10 m^2/s, d. ε=0.25 m^2/s) at the same time during the tidal cycle (3 hours after HW). The outermost contour corresponds to normalize activity concentration of 0.002.

It is obvious from the simulations that as the eddy diffusivity increases its value the diffusion process dominates and the advection plays a secondary role. For the selection of its value a comparison with our experimental data was done for ε= 0.01, 0.0025 and 0.005 m^2/s (figures 7.12 and 7.13). Eddy diffusivity with ε= 0.01 m^2/s was selected as more appropriate on the grounds of smallest residual sum of squares (RRS) between simulated and experimental values ($RRS_{\varepsilon= 0.005\ m2/s}$=0.579, $RRS_{\varepsilon= 0.0025\ m2/s}$=0.746, $RRS_{\varepsilon= 0.01\ m2/s}$=0.470, available data on Appendix 11).

The selection of this value is also supported by the CORMIX mixing model (see §6.5) for a preliminary calculation of the ^{131}I concentration in river water, which was used as a helping tool for identifying possible sampling locations.
Including the tidal influence to our simulations, for different times in the tidal cycle we can observe how the outflow plume is transported and dispersed in the river (figure 7.11).

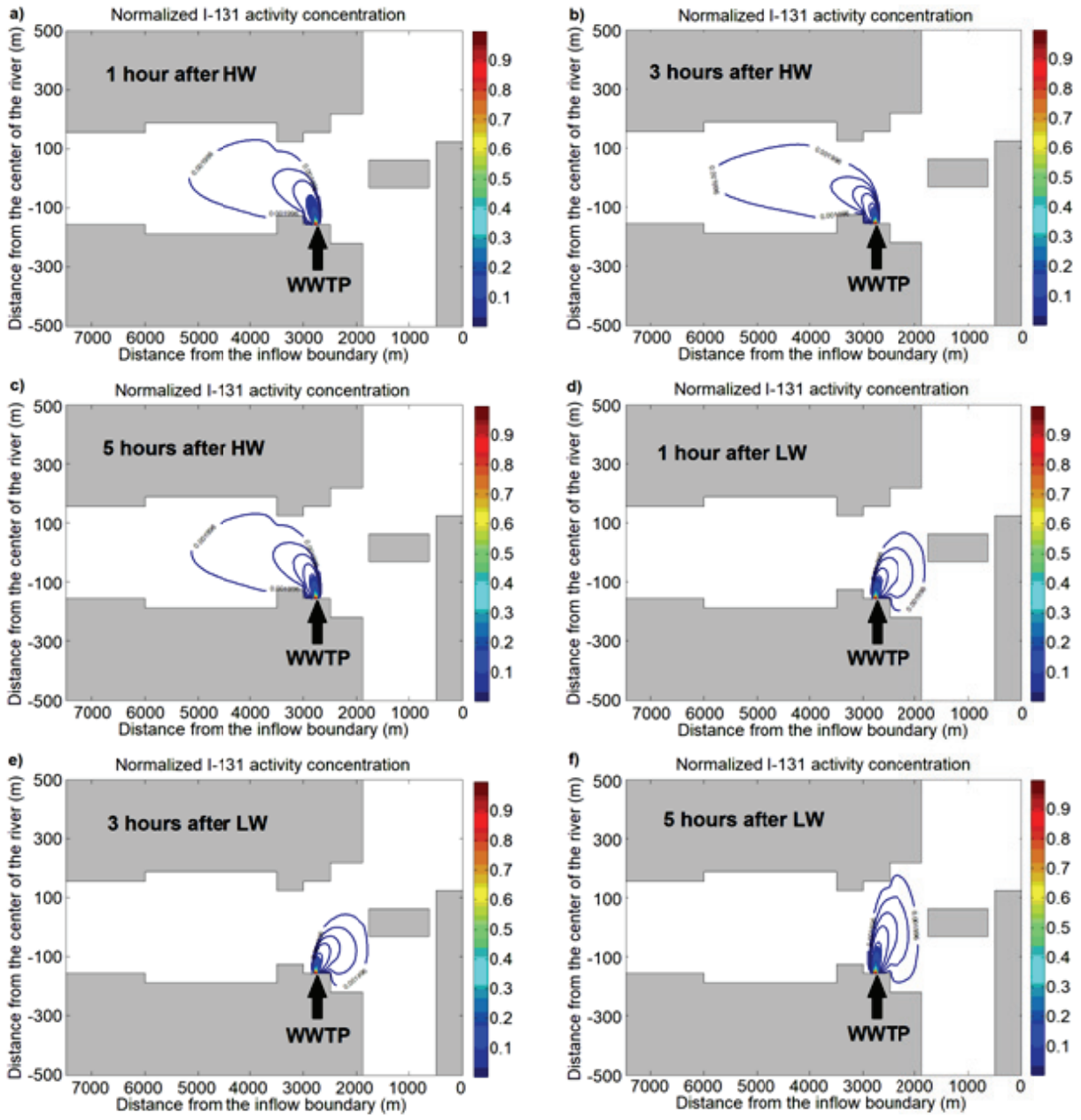

Figure 7.11: Simulated normalized ^{131}I activity concentration 1,3 and 5 hours after high and low water with eddy diffusivity equal to $\varepsilon = 0.01\ m^2/s$.

By selecting the same time on the tidal cycle (3 hours after high water for the downstream direction from the WWTP (figure 7.11 b) and 3 hours after LW for the upstream (figure 7.11 e)) and comparing simulation results with experimental data (figure 6.16, see §6.5.2) for the locations where we obtained river water samples we get figure 7.12.

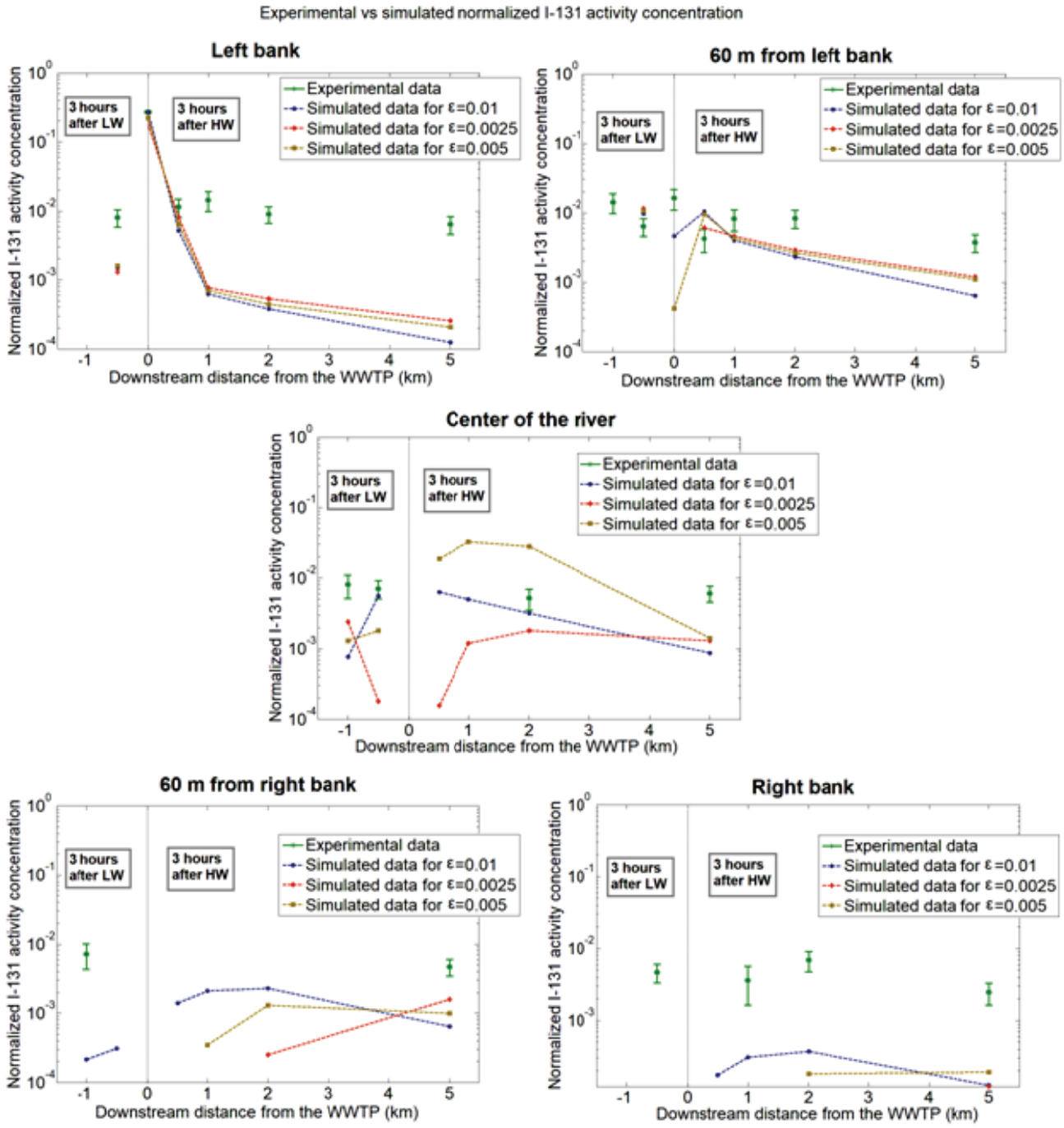

Figure 7.12: Comparison of simulation results with eddy diffusion of 0.01, 0.0025 and 0.005 m^2/s with experimental data, 3 hours after high/low water, in locations -1, -0.5, 0, 0.5, 1, 2 and 5 km distance from the WWTP: a. close to the left bank, b. 60 m away, c. on the center of the river, d. 60 m from the right bank and e. close to the right bank. Only the simulations values above 0.0001 of non-dimensionalized concentration are shown while missing experimental values correspond to measurements under detection limit.

By comparing the simulation (ε=0.01 m^2/s) with the experimental data in 6 locations (0 km left bank, 0.5 km left bank, -0.5 km 60 m from the left bank, -0.5 km centre of the river and 2 km downstream centre of the river) the difference is less than 20% (see also Appendix 11). There is a systematic underestimation of ^{131}I, more than an order of magnitude, in distances larger than 2 km downstream the WWTP and in the lateral direction, notably in the right bank. This is expected, considering that the simulated outflow plume is centrally located and does not reach distances greater than 3 km with normalized concentrations larger than 0.002 (see figure 7.11 b). In reality this plume is deflected towards the left bank (see also figure 6.9), possibly due to differences in discharge rates of the river (mean value of: 223 m^3/s) and the WWTP outflow (mean value of: 1.5 m^3/s), differences in temperature and salinity (0.35 ppt for the outflow plume and 0.7 ppt for the river water, see also Appendix 3) which can create gradients and stratified flow. Additionally several simplifications of the model do not necessarily represent adequately the reality, eg. grid. Large discrepancies can also be observed during different times in the tidal cycle between simulated and experimental data in the left bank (figure 7.13).

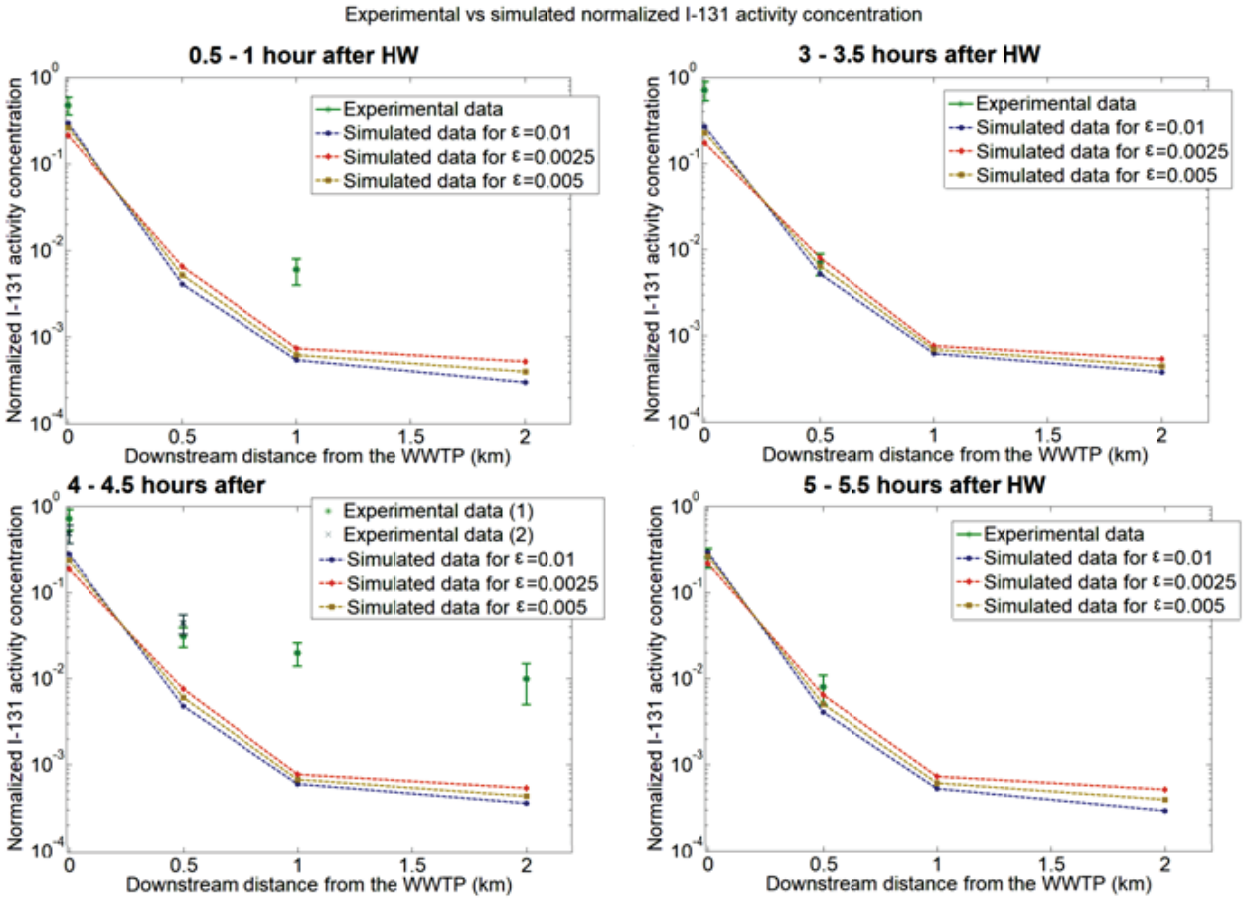

Figure 7.13: Comparison of simulation results with eddy diffusion of 0.01, 0.0025 and 0.005 m^2/s with experimental data for different times during the tidal cycle. Missing experimental values correspond to either not measured or values below detection limit (see also figure 6.14).

Overall, out of 52 experimental measurements, 35 were above detection limit (see Appendix 3) which when compared to model simulations agreed within a 10% difference with 9% of the data, within a 30% difference with 26% of the data and within 50% with 31% of the data. Additionally when including the 17 experimental values under detection limit, 16 of simulation values were lower than the corresponding detection limit, allowing validation. When including all values above and below detection limit, there is an agreement within a 50% difference of 52% of the data (see also Appendix 11).

A common method on evaluating environmental models is to perform regression analysis on simulated vs. experimental values. Pineiro et al. (2008) argue that experimental/observed (in the y-axis) vs. simulated/predicted (in the x-axis) (OP) regressions should be used for a proper model evaluation since significantly different results may be produced from an alternative approach (PO). An illustration of an OP regression can be seen in figure 7.14.

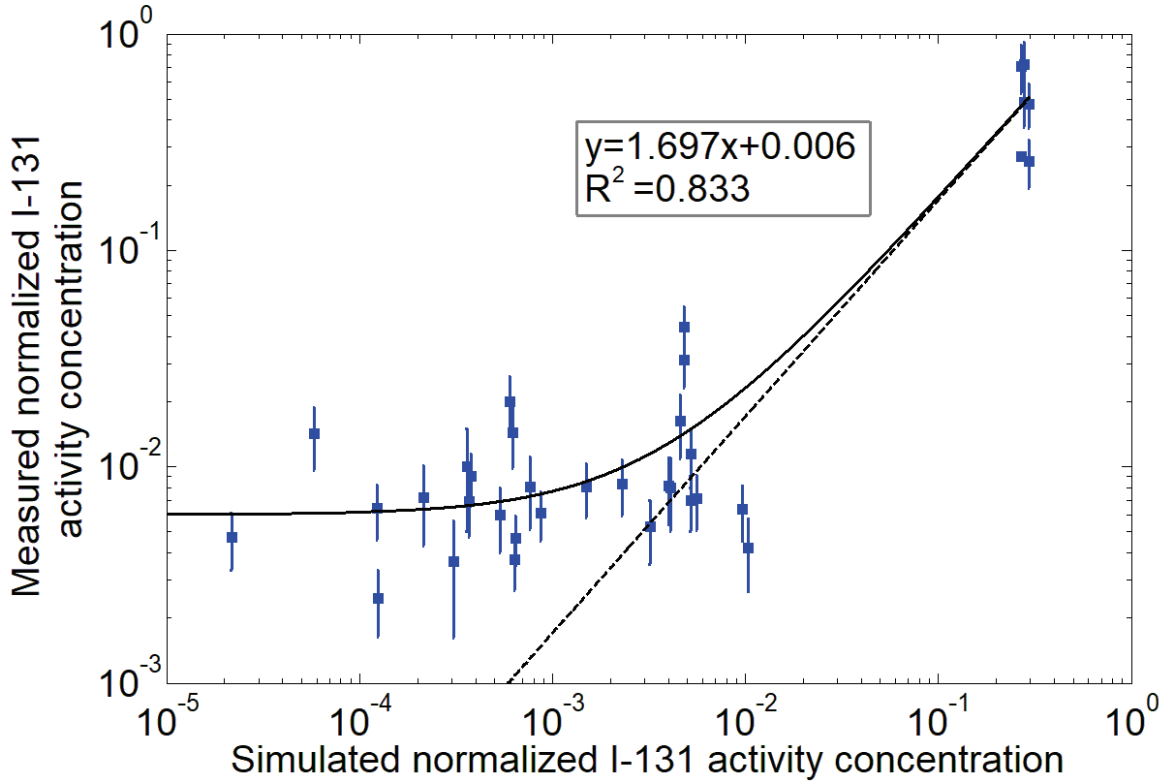

Figure 7.14: Scatter plot of simulated vs. experimental normalized ^{131}I activity concentrations. The black line represents the regression line ($y = 1.697x + 0.006$). The dashed line represents the regression line without zero intercept. Logarithmic scale in both axis used for better visualization.

The regression line is calculated using the formula $y = a + bx$ where a the slope and b intercept are: $a = \frac{\left(\sum_i^N y_i\right)\left(\sum_i^N x_i^2\right) - \left(\sum_i^N x_i\right)\left(\sum_i^N x_i y_i\right)}{N\left(\sum_i^N x_i^2\right) - \left(\sum_i^N x_i\right)^2}$ and $b = \frac{N\left(\sum_i^N x_i y_i\right) - \left(\sum_i^N x_i\right)\left(\sum_i^N y_i\right)}{N\left(\sum_i^N x_i^2\right) - \left(\sum_i^N x_i\right)^2}$, with N the number of simulated-measured pairs, x_i the simulated values and y_i the measured values. The slope and the intercept describe the consistency and the model bias, respectively.

The standard error of the regression is calculated as $S = \sqrt{\frac{\sum_{i=1}^N \left(y(x_i) - x_i\right)^2}{N}}$ equal to 0.082. This error is a measurement of the accuracy of our simulations and represents the average distance that the simulated values fall from the regression line. In the same manner the standard error of our simulation values is calculated equal to 0.020 and represents the average distance the simulated values have from the experimental data. This value is only an estimate since our data do not correspond to normal distributions (see below).

The R^2 value equals $R^2 = 1 - \frac{Res_SS}{Tot_SS} = \frac{Reg_SS}{Tot_SS}$ where Res_SS the residual sum of squares, Reg_SS the regression sum of squares and Tot_SS the total sum of squares which equals the sum of residual and regression sum of squares. It is calculated as $R^2 = \left(\frac{N\sum_{i=1}^N x_i y_i - \sum_{i=1}^N x_i \sum_{i=1}^N y_i}{\sqrt{\left[N\sum_{i=1}^N x_i^2 - \left(\sum_{i=1}^N x_i\right)^2\right]\left[N\sum_{i=1}^N y_i^2 - \left(\sum_{i=1}^N y_i\right)^2\right]}} \right)^2$ equal to 0.834. The R^2 value shows the proportion (83.4%) of the total variance explained by the regression model (and also how much of the linear variation in the simulated values is explained by the variation in the measured values). The correlation coefficient is then R=0.913, indicating a strong positive relationship between simulated and measured data. A high R^2 value doesn't necessarily mean that the model has a good fit. One should evaluate R^2 values in conjunction with residual plots.

Using residual (difference between the regression's predicted value and the simulated value) plots one can easily assess whether the observed error (residuals) are randomly distributed. In the case of predictability of the residuals, the model should be rejected since it would be systematically incorrect.

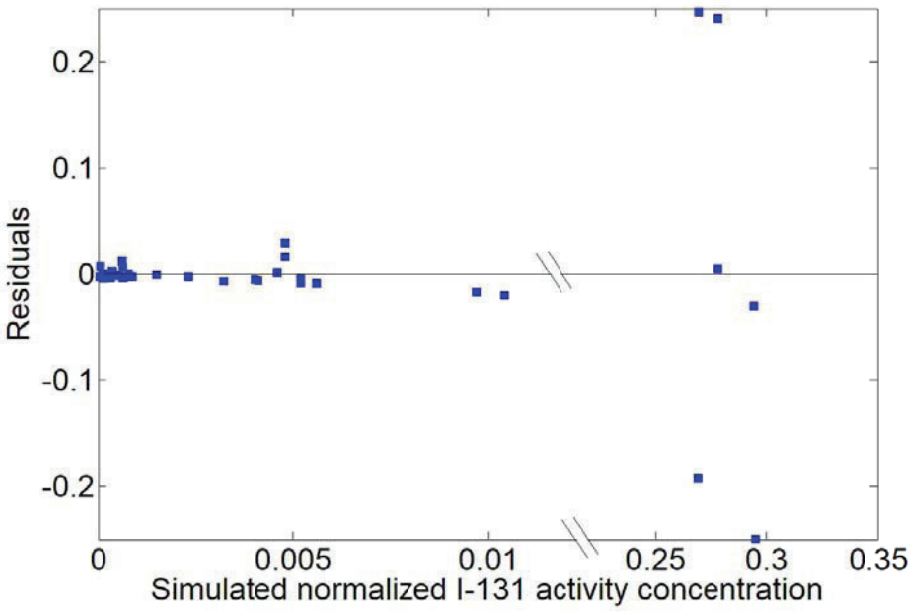

Figure 7.15: Residuals vs. simulated values plot for assessing the goodness of our model.

Figure 7.15 appears to have heteroscedasticity; the residuals are close to zero for small simulated values and increase for large simulation values. This is not unexpected when observing also figure 7.13 closer in the location of the WWTP outflow. The most common reason for this effect is due to an omitted variable. This omitted variable causes this type of error because the portion of the omitted effect is not represented. Such effects could be physical and chemical processes not taken into account. Additional turbidity in the region, due to discharges from tributaries, breakwaters, shipping, more complex geometry of the domain, bottom shear and wind stress could influence the transport and dispersion of the outflow plume leading to such discrepancies. Since the effect is present in less than 10% of the data, for the purpose of this study we consider it as acceptable.

The importance of this analysis lies to the intercept evaluation; the model bias. Physically this would be interpreted as a pre-existing ^{131}I activity concentration to the river water. As explained in §6.6.2, the tide influences the activity concentration in both upstream and downstream directions by varying the retention time[2] of a water parcel and creating a background value of ^{131}I activity concentration in locations as far as 5 km downstream and 1 km upstream from the source in both banks of the river. This lack of memory the system has of previous states is an important effect which contributes to the model bias and is not taken into account during the simulations. The regression analysis evaluates this model bias; thus the background normalized ^{131}I activity concentration with a value of 0.006. Considering the mean ^{131}I activity concentration of the WWTP outflow as 209 mBq/kg (see Appendix 4) this background concentration in the river water becomes 1.25 mBq/kg (value close to our detection limits, see also Appendix 3).

[2] Retention time is defined as the average time spent by a water parcel from time of inflow to that of outflow (Cushman-Roisin, 2014).

A measurement of ^{131}I in river water in location downstream the WWTP during river flow toward the upstream direction would (if the measurement is above the detection limit) not only verify the presence of the background ^{131}I activity concentration but also quantify it. Due to the fact that such measurements were beyond this work and not performed, adding this normalized background concentration value (0.006) in our river water simulations is not deemed appropriate. For this verification a series of measurements in the area under different flow conditions (when the presence of ^{131}I background concentration is having an effect on the measurements) and in different locations (where ^{131}I background is present under these conditions) are necessary. For example the presence of ^{131}I background activity concentration appears straightforward during river flow in the upstream direction (what was transferred downstream is transferred once more upstream). Even so the background concentration may vary depending in the location significantly; one would expect higher concentrations close to the WWTP (for the part not influenced directly from the outflow).
For locations in the downstream direction during flow towards the same direction is not clear if a background concentration is present (in locations 5 km downstream one can conclude that the presence of iodine is from previous tidal cycles since 1 hour travelling time for the ^{131}I originating from the WWTP is not sufficient for reaching such large distances even in cycles such as 3-4 hours after high water, where the velocity in the centre of the river reaches its maximum value of 1.2 m/s (see also figure 7.6) and if its value is significantly altered due to dilution effects with fresh river water.

7.4.2 Radionuclide submodel for bank sediments

Steady-state conditions (see Appendix 16) may be sufficient to describe our system concerning advection and dispersion of the radionuclide in the river water, due to the short-term (1 hour) period simulations where the time scales of the processes are much smaller than of the radioactive decay, pore-water diffusion or sedimentation.

However, when considering processes such as sedimentation, which require longer-term simulations, the assumption of steady-state conditions is not valid and equation 3.19 (see §3.2.2.2) is used for the calculation of the total activity concentration of ^{131}I in the sediments:

$$r(t) = \exp\left[-\int_0^t \left(\frac{\lambda}{1 + K_{P,b} S_b} + \frac{\alpha(t) S_b}{S_b + \frac{1}{K_{P,b}}} \right) dt \right] +$$

$$+ \int_0^t \exp\left[-\int_0^{t'} \left(\frac{\lambda}{1 + K_{P,b} S_b} + \frac{\alpha(t') S_b}{S_b + \frac{1}{K_{P,b}}} \right) dt' \cdot C(t) \left(\frac{k_s(t) K_{P,W} S_W}{S_b + \frac{1}{K_{P,b}}} \frac{1}{(1 + K_{P,W} S_W)} \gamma \right) \right] dt$$

eq. 3.19/7.8

The total activity concentration in the river water C, along with the sedimentation rate k_S and resuspension rate α are time dependent (thus written from now on as C(t), $k_S(t)$ and α(t) correspondingly), and their value depends on the time of the tidal cycle.

Due to the fact that the total activity concentration in the river water C(t) ,obtained as a solution of the radionuclide sub-model in river water, is given as normalized concentration one must multiply it with the WWTP outflow activity concentration. The approach of normalized ^{131}I activity concentration values for the sediment is not possible since the WWTP outflow activity concentration and its variation was not known during the sedimentation period. Thus for comparing our simulation data with the experimental values we need to express them in units of Bq/kg(d.m.) (same unit as our experimental values, see also §6.7). The WWTP outflow ^{131}I activity concentration is measured during our study with a mean value of 209 mBq/kg and a range between 56 and 603 mBq/kg (see Appendix 4). In figure 7.16 the variation of the normalized ^{131}I activity concentration 0.5 km downstream the WWTP during the sedimentation period is illustrated.

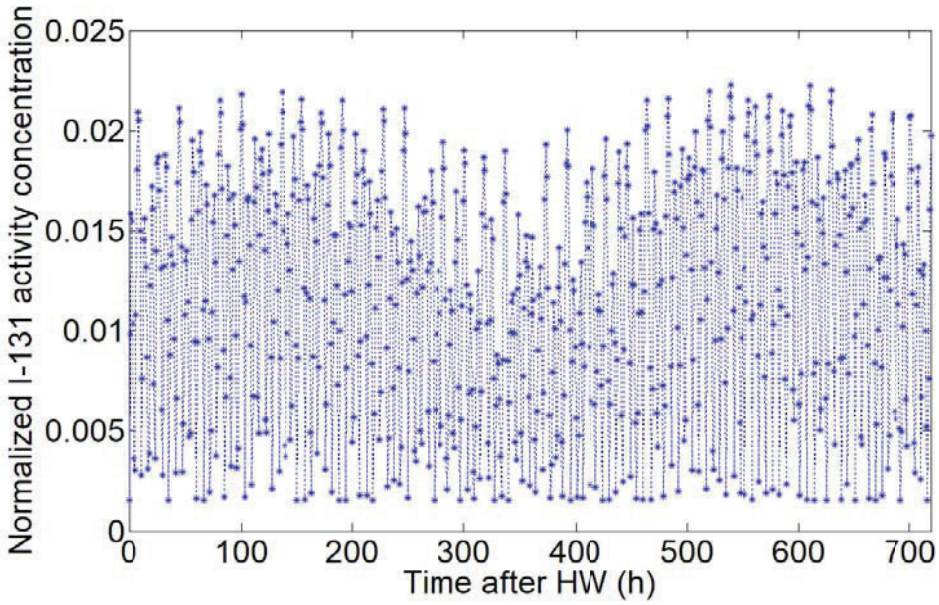

Figure 7.16: Variation of the normalized ^{131}I activity concentration 0.5 km downstream the WWTP during the sedimentation period.

The sedimentation rate, given as $k_S = v_W / h(t)$, mean particle settling velocity divided by depth, is inversely proportional to the depth of the river water (or height) on the banks, calculated using the tidal constituents given by the "Tidal fitting toolbox" (see §2.2). Stoschek and Matheja (2001) on their report on the simulation of sediment transportation processes in tidally influenced harbour areas, studied the same region as in this project. On table 3.4-2 of the aforementioned publication they report the percentage distribution of sediment classes in the different sampling areas, as illustrated in their figures 3.4-7 to 3.4-9, based on results from sampling campaigns in the region (sampling campaigns at 25.10.1989 and 07.07.1993). These results are presented in table 7.2, where 2 particle sizes[3] for the sediments are considered (sand and silt) along with their percentage of each constituent to the total sediment. As they proposed, these particles have mean diameters of 0.1 mm and 0.018 mm, which result in sedimentation velocities of 0.007 m/s and 0.00015 m/s. respectively.

[3] The selection of 2 particle sizes for the sediments assumes equal concentrations of ^{131}I in sand and silt, while it may be that iodine does not get adsorbed in the same way for both sizes and constitutes a source of error.

Table 7.2: Percentage distribution of sediment classes in the various model/sampling areas (Stoschek and Matheja, 2001)

Sampling site	Distance from WWTP (km)	Sand (%)	Silt (%)
7.1	-1	52	48
6.1	-0.5	62	38
1.1/1.5	0	46	54
2.1	0.5	4	96
3.1	1	3	97
4.1	2	45	48
5.1/5.5	5	45	48

The resuspension (scour) rate is given as $\alpha(t) = \frac{k_s(t) S_w \gamma}{S_b}$, proportional to the sedimentation rate and inversely proportional to the depth of the river water.

The depth of the active[4] bed sediment is calculated as the product of sedimentation growth rate v_s ($v_s = 2.1 \times 10^{-10}$ m/s, Fischer et al., 2009) with time. Considering that after 10 half-lives all of the ^{131}I will have decayed, the depth of the active bed sediment is calculated as 1.5×10^{-3} m.

The solids concentration in the bed sediment, S_b, is calculated from our experimental data (see Appendix 6) as $S_b = \rho_s(1-f)$ (Trento and Alvarez, 2014, Thibodeaux, 1996), with ρ_s the density of the sediment and f the porosity, resulting in a mean value of 400 kg/m^3 and a range (140-560) kg/m^3.

The ratio of the water depth to the depth of the active bed sediment, γ is calculated equal to 2300, when considering the depth of the water on the river banks where our samples were collected. As the tidal range is 4 m and the samples were taken 1 hour before/after low water, the depth of the river water is approximately 3.5 m.

The values of the all the variables used in the model are given on table 7.3. Those not directly measured or derived from our experimental data were found on the literature

[4] Depth of active bed sediment or exchange layer sediment is the part of the bed sediments involved in exchange processes with the water column (Parker and Garcia, 2006).

Table 7.3: Model parameter values given in literature

Parameter - description	Value	Literature reference
v_w – mean particle settling velocity	Sand: 0.007 m/s Silt: 0.00015 m/s	Stoschek and Matheja, 2001
λ –radioactive decay constant	10^{-6} s^{-1}	
K_{pw} – distribution (partition) coefficient in water column	0.01 m^3/kg	Zheleznyak et al.,2003
K_{pb} – distribution (partition) coefficient in sediment	0.01 m^3/kg	Zheleznyak et al.,2003
k_L - mass transfer coefficient between water column and pore water of bed sediment	10^{-8} m/s	Schnoor, 1996
S_w – solids concentration in the water column	0.04 kg/m^3	Kappenberg,2001 Grabemann, 2001 Schuchardt, 1993 Mueller,1992
S_b – solids concentration in the sediment	400 kg/m^3	Mean value – own measurements (Appendix 6)
γ – ratio of water depth to depth of active bed sediment	2300	
d- depth of active bed sediment	1.5×10^{-3}m	
C – ^{131}I activity concentration in the river water (normalized concentration $\times^{131}$I activity concentration of the WWTP outflow, C_{WWTP})	Location and time dependent	Simulated from the radionuclide in the river water model (see §7.4.1) or experimentally determined (see Appendix 3)
C_{WWTP}	210 mBq/kg	Mean value – own measurements (Appendix 4)

For solving equation 7.8, especially since the water level is given as a sum of several cosines, the Simpson numerical method for integration is applied and the simulation is done via Matlab. The corresponding m-file is given in Appendix15.

The simulations were run for a 30 day period (time allowed for sedimentation where the equilibrium is reached, Fischer et al., 2009) in hourly time steps for a mean value of the WWTP concentration of 209 mBq/l and excluding the time period of 1 hour before to 1 hour after low water (this is the same as our sampling period (see §6.7.2) where the sediments are not covered by river water, thus none of the aforementioned processes (see §3.2.2.2), eg. sedimentation take place). By using as an input not the ^{131}I activity concentration in the river water as given from the radionuclide model in the river water, but instead our experimental values for locations close to the bank 3 hours after high and low water (see Appendix 3 and figure 6.16, §6.6.2) we get similar results. The simulation results are displayed in figure 7.17.

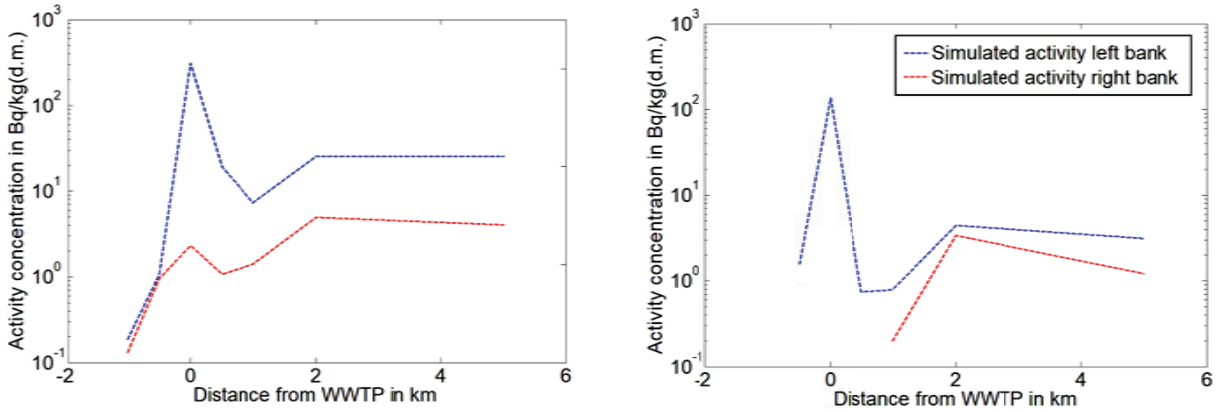

Figure 7.17: Simulated activity concentration in sediment (Bq/kg(d.m.)) in both left and right river banks, using as input the simulated (on the left) or the measured (on the right) ^{131}I activity concentration in river water.

As a first approach to improving our simulations we consider the formed ^{131}I activity concentration background by adding the normalized background value of 0.006 (corresponding to mean background activity concentration value of 1.2 mBq/kg, value close to the detection limit) to the values of the ^{131}I activity concentration in river water for the times in the tidal cycle when the river water moves to the upstream direction (thus carrying with it already parcels containing iodine (see §6.6.2)). This background concentration value was determined through regression analysis applied to the radionuclide submodel for the river water (see §7.4.1). For the simulations which use as input our experimental values a similar idea is followed, since in locations where the ^{131}I activity concentration was below detection limit the simulations provided zero values. Additionally, we have no information on the ^{131}I activity concentration of the river water in locations downstream the WWTP during upstream flow. For these reasons, as before, the ^{131}I activity concentration background was added to the values of the ^{131}I activity concentration in river water for the times in the tidal cycle when the river water moves to the upstream direction. The results of these simulations are depicted in figure 7.18.

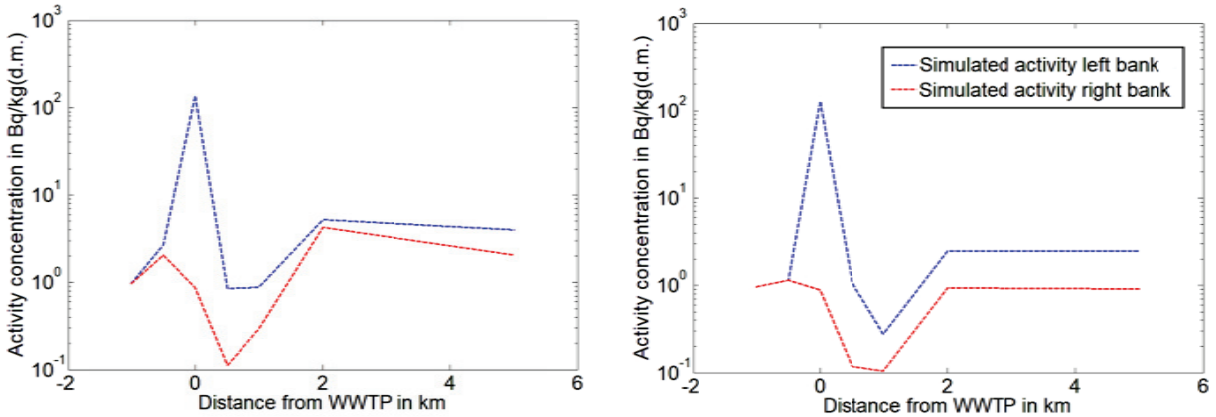

Figure 7.18: Simulated activity concentration in sediment (Bq/kg(d.m.)) in both left and right river banks, taking into account a background concentration of 1.2 mBq/kg and using as input the simulated (on the left) or the measured (on the right) ^{131}I activity concentration in river water.

Comparing with our experimental data (see §6.6.2), as well as with values obtained from the 2008 sampling campaign (see §2.4) for same locations with input of experimental and simulation data in the river water we get figure 7.19.

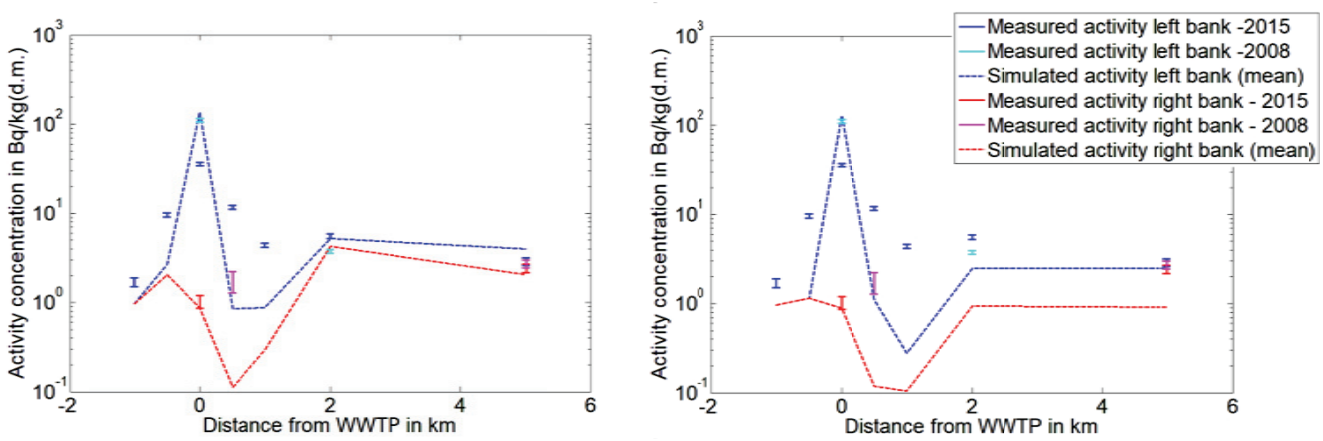

Figure 7.19: Comparison of activity concentration in sediment (Bq/kg(d.m.)) in both left and right river banks, taking into account a background concentration of 1.2 mBq/kg and using as input the simulated (on the left) or the measured (on the right) ^{131}I activity concentration in river water, with experimental data in the selected locations, collected at 2008 and 2015 campaigns.

A visual comparison of our model simulations with our experimental data (collected at 2008 and 2015 campaigns) using as an input the simulated or the measured ^{131}I activity concentration in river water it is easy to observe that the simulations behave in a similar way as expected for both inputs. Additionally in some locations the simulations results appear to be in agreement with our measured values. For evaluating our simulations two methods are applied, regression and sensitivity analysis.

Regression analysis

In a similar manner as done for the river water simulations, an OP regression is performed for the simulations in the river sediments for the following cases:

A: Measured ^{131}I activity concentration in the river water, no background considered

B: Measured ^{131}I activity concentration in the river water, normalized background considered (0.006)

C: Simulated ^{131}I activity concentration in the river water, no background considered

D: Simulated ^{131}I activity concentration in the river water, normalized background considered (0.006)

The regression and residual plots are similar in all cases and for demonstration purposes case D is presented in figure 7.20.

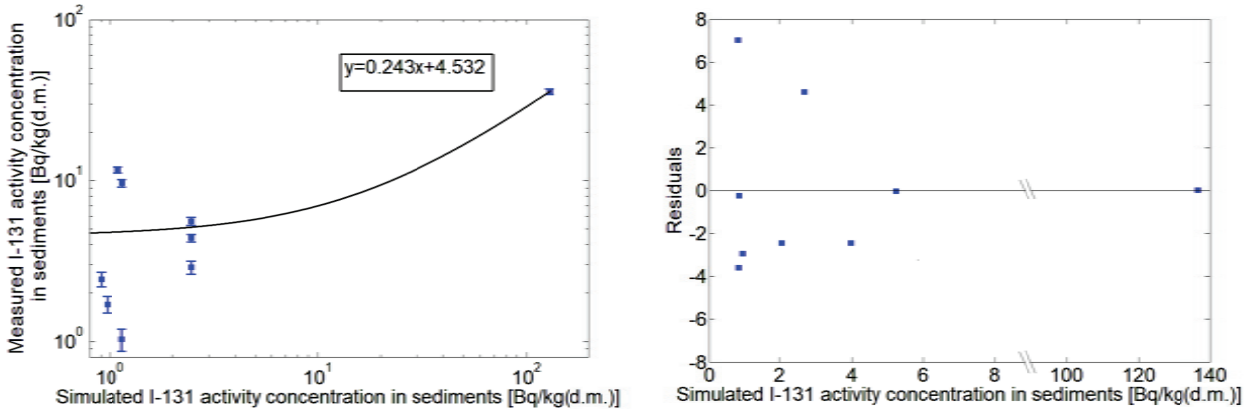

Figure 7.20: Regression and residual plots for OP regression analysis of simulated ^{131}I activity concentration in the bank sediments with normalized background considered (0.006) and experimental data.

The residual plots appear to have randomness, thus the results of the regression analysis are reliable. Additionally, the F-test of overall significance in regression analysis is calculated as the ratio of the variation between sample means and variation within the samples. The test is performed by stating the following hypotheses: null hypothesis (the fit of the intercept-only model and our model are equal) and the alternative hypothesis (the fit of the intercept-only model is significantly reduced compared to our model). The F value is calculated as $F = \frac{\mathrm{Re}g_SS / \mathrm{Re}g_df}{\mathrm{Re}s_SS / \mathrm{Re}s_df}$, where Reg_SS and Res_SS are the regression and residual sum of squares and Reg_df and Res_df the regression and residual degrees of freedom equal to 1 and 7 in our case, respectively. If F is lower than the critical value at the p=0.05 level of significance (in our case 5.59 (Dougherty, 2002)) then the null hypothesis is rejected in favour of the alternative hypothesis. In all cases we conclude that our model provides a better fit that the intercept-only model. The results of the regression analysis are given in table 7.4.

Table 7.4: Regression analysis for OP regression of simulated and measured data in Weser sediments.

Regression analysis case	Regression line	Standard error of regression	Standard error of simulations	R^2 value	P value for the F-test
A	y=0.229x+4.575	3.820	33.72	0.892	1.34E-04
B	y=0.229x+4.435	3.856	33.96	0.891	1.26E-04
C	y=0.240x+4.470	4.375	31.33	0.859	3.29E-04
D	y=0.243x+4.532	3.872	31.27	0.889	1.38E-04

As can be observed from table 7.4 the models have similar performances. Setting as a criterion the lowest standard error of simulations, case D is selected for sensitivity analysis.

Sensitivity analysis

Sensitivity analysis is an important step in our modelling process. Only a few critical values account for most of the uncertainty in our simulations and sensitivity analysis identifies the influence these critical variables have. Hamby (1994) reports several sensitivity analysis methods found in the literature, addressing them in 3 groups: those that operate on one variable at the time, those that rely on the generation of an input matrix and an associated output vector and those that require a partitioning of a particular input vector based on the resulting output vector. In this study the first two methods are applied.

The first step towards our analysis is identifying which of the input variables in the model, given in table 7.3, have a range of values rather than a fixed one.

- Studies on the sorption and desorption processes of iodine in soil and sediment have shown a large range on values depending on the sediment type and the pH. Wilhem (2004), on the EPA report about the understanding of the variation in the partition coefficient values of iodine, recommends site-specific calculations. This recommendation is not limited to iodine but to all contaminants since the reported partition coefficient values in the literature may vary by as much as six orders of magnitude. Both Wilhem (2004) and Sheppard et al. (2009) report a wide range of partition coefficient values between 4×10^{-6} m^3/kg and 4 m^3/kg.

- The solids concentration in the water column is also a quantity that varies and is correlated to the river discharge (Schuchardt, 1993). The hydrographic book for the year 2014 (Deutsches Gewässerkundliches Jahrbuch Weser- und Emsgebiet) reports the solids concentrations on the Weser river water on the measuring station Intschede to be between 0.038 and 0.851 kg/m^3 for the years 1970 to 2014.

- The mass transfer coefficient between the water column and the pore water of the bed sediment was found in literature to vary between 10^{-8} - 10^{-5} m/s (Semizhon et al., 2010).
-
- The solids concentration in the bed sediment, S_b, is calculated from our experimental data, resulting in a range of (140-560) kg/m^3.

- Last, the WWTP outflow ^{131}I activity concentration measured during our study has a range between 56 and 603 mBq/kg (see Appendix 4). Summarizing these results we obtain table 7.5.

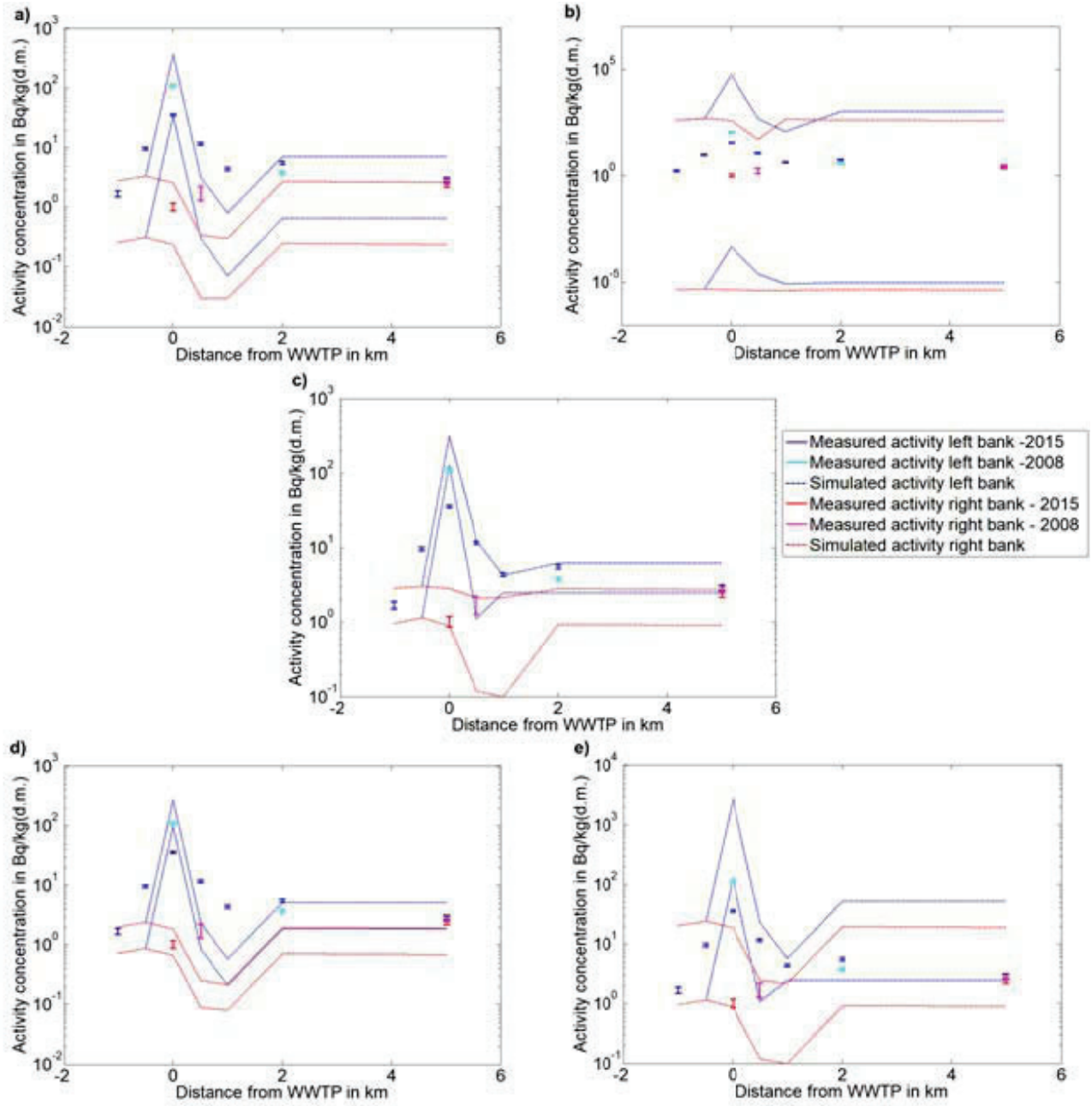

Figure 7.21: Comparison of simulated activity concentration in sediment (Bq/kg(d.m.)) in both left and right river banks, taking into account normalized background concentration of 0.006, using as input the simulated ^{131}I activity concentration in river water, with experimental data in the selected locations, collected at 2008 and 2015 campaigns. Dotted lines represent model output when using the minimum and maximum values of the range of a) ^{131}I activity concentration of the WWTP outflow, b) distribution coefficients in river water column and sediment, c) mass transfer coefficient between water column and pore water of bed sediment, d) solids concentration in the sediment and e) solids concentration in the water column, as input (see table 7.4). Values available in Appendix 11.

Table 7.5: Range of model parameter values

Parameter - description	Range of values	Literature reference
Distribution coefficients in river water column and sediment K_{pw}, K_{pb}	$(4\times10^{-6} – 4)$ m^3/kg	Wilhem (2004) Sheppard et al. (2009)
Mass transfer coefficient between water column and pore water of bed sediment k_L	$(10^{-8} - 10^{-5})$ m/s	Semizhon et al., 2010
S_w – solids concentration in the water column	(0.038 – 0.851) kg/m^3	Deutsches Gewässerkundliches Jahrbuch Weser - und Emsgebiet, 2014
S_b – solids concentration in the sediment	(140 - 560) kg/m^3	own measurements (Appendix 6)
C_{WWTP} - ^{131}I activity concentration of the WWTP outflow	(56 – 603) mBq/kg	own measurements (Appendix 4)

Simulating the ^{131}I activity concentration in the river sediments taking into account the range of these values we obtain figure 7.21. In each case an "uncertainty band" is formed where most of the experimental values fall in. When varying the ^{131}I activity concentration of the outflow (figure 7.21a), 77% of the experimental data are within the uncertainty band. Similar results we get when varying the solids concentration in the sediment (figure 7.21d). In the case of the distribution coefficients in river water column and sediment (figure 7.21b) all values are within the uncertainty band, however the distribution coefficient values cover a six order of magnitude range. The mass transfer coefficients between the water column and the pore water of the sediment cover a smaller range (2 orders of magnitude) and 85% of the experimental data are within this uncertainty band (figure 7.21c). When varying the solids concentration in the water column between the values 0.038 – 0.851 kg/m^3, we get an uncertainty band which covers 92% of our experimental data (figure 7.12e).

To determine the importance of each of these variables the sensitivity index is calculated as suggested from Till and Meyer, (1983):

$$SI = \frac{D_{\max} - D_{\min}}{D_{\max}},$$

Where Dmin and Dmax represent the minimum and maximum output values, respectively resulting from the varying the input over its entire range.

For each of the variables we get a sensitivity index more than 50%, indicating that all the aforementioned variables can have a significant effect in our output. In table 7.6 the results of the sensitivity index calculation are presented.

Table 7.6: Sensitivity index of model parameter values

Parameter - description	Range of input values	Range of simulation values [Bq/kg(d.m.)]	Sensitivity index (%)
Distribution coefficients in river water column and sediment K_{pw}, K_{pb}	$(4\times10^{-6} – 4)$ m^3/kg	4.00E-05 – 3.58E+03	100
S_w – solids concentration in the water column	(0.038 – 0.851) kg/m^3	10.30 – 213.72	95
C_{WWTP} - ^{131}I activity concentration of the WWTP outflow	(56 – 603) mBq/kg	2.72 – 29.26	91
Mass transfer coefficient between water column and pore water of bed sediment k_L	$(10^{-8} - 10^{-5})$ m/s	10.30 – 26.01	67
S_b – solids concentration in the sediment	(140 - 560) kg/m^3	7.68 – 21.13	64

The sensitivity index provides a good indication of parameter and model variability, however since the variables have different range (for example, the ^{131}I activity concentration of the WWTP outflow has 1 order of magnitude range while the distribution coefficients in river water column and sediment have 6), in order to get a better understanding of the influence of each parameter in our model we create a sensitivity plot (figure 7.22).

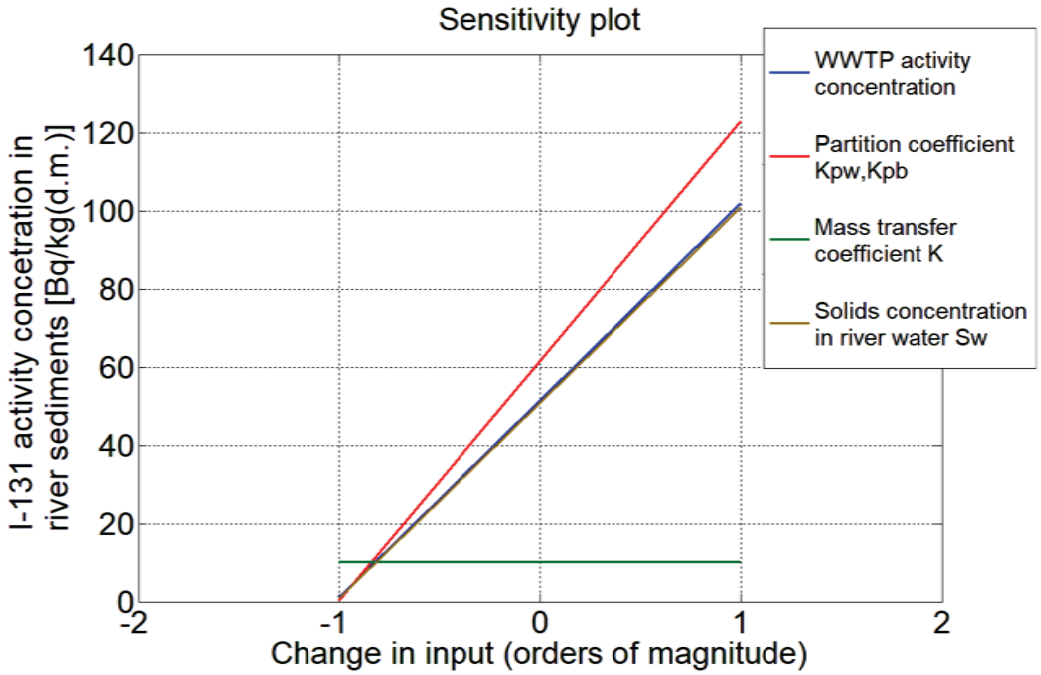

Figure 7.22 Sensitivity plot for different parameters of our model.

For understanding the influence of each parameter in our model, independent of the range its value may cover, we change the value of each of the parameter by one order of magnitude. In the case of solids concentration in the sediment, this approximation was not physically meaningful so it was not performed. From figure 7.22 one can observe that the model is more sensitive to changes in the partition coefficient value than to other parameters. The changes in the ^{131}I activity concentration of the WWTP outflow and in the solids concentration in the river water appear to have a similar influence on our model results while the changes in the mass transfer coefficient produce insignificant changes to our simulation results.

The overall performance of our model is good, since the majority of our experimental values fall within the uncertainty bands created from the variation of the parameters used. One should not forget that a model is an approximation and several factors can contribute to the overall error (estimate calculated as standard error equal to 31.27). The possibility of faulty parameter approximation and assumptions should not be excluded. As mentioned before, the water residence time can significantly vary depending on the discharge conditions and strong flood and ebb currents could make the assumption of slow kinetics of sorption compared to kinetics of transformation reactions or the time of transport (advection, dispersion, sedimentation, resuspension) no longer valid. Furthermore the assumption of a steady state condition during the simulation period for the solids concentrations may not hold, since the suspended particulate matter concentration is correlated with the river discharge, although with relatively low average concentration (Schuchardt et. al, 1993). The simplification when considering two particle sizes for the sediments could be wrong (see also footnote 3). Moreover, processes, such as biological uptake of ^{131}I by aquatic biota, may not be negligible. Last but not least, errors due to the numerical methods (see §3.4) applied can produce significant differences in our simulations, a matter not treated under the scope of this work.

7.5 General comment on ^{131}I dispersion-sedimentation model in Weser River

This chapter presented a 3 compartment model which computes the ^{131}I behaviour in a tidal river for routine releases with hourly time steps. The complexity of the physical and chemical processes involved rule out completely simplistic approaches and analytical solutions for the problem, however despite the simplifications considered, the comparison between simulated and experimental data confirms that the simulations provide realistic results and indicates the model capability of predicting the dispersion of medically derived iodine, originating from the WWTP, in the water body and banks of Weser River. With minor adjustments, one could possibly use the model for the prediction of dispersion for different radionuclides (adjustments in boundary/initial conditions, half-lives and partition coefficients, etc.), different area (adjustments in grid, boundary/initial conditions, WWTP effluent concentration, solid concentration in water/sediment and sediment distribution, tidal parameters, etc.) and in emergency situations (adjustments in time scale of the simulation, approximations of steady state, etc.).

7.6 References for Chapter 7

Cushman-Roisin B., 2014, *Environmental fluid mechanics*.John Wiley & Sons, Inc.

Deutsches Gewässerkundliches Jahrbuch Weser- und Emsgebiet, 2014. Retrieved from https://www.nlwkn.niedersachsen.de/wasserwirtschaft/publikationen/gewaesserkundliche_monatsberichte/deutsches_gewaesserkundliches_jahrbuch/deutsches-gewaesserkundliches-jahrbuch-weser--und-emsgebiet-43607.html

Dougherty C., 2002. *Introduction to Econometrics.* Second Edition, Oxford University Press, Oxford.

Elman H., Silvester D., Wathen A., 2014, *Finite Elements and Fast Iterative Solvers with Applications in Incompressible Fluid Dynamics,* Second Edition, Oxford Science Publications.

Fischer H. B., List E.J., Koh R. C.Y., Imberger J., Brooks N.H., 1979, *Mixing in Inland and Coastal Waters.* Academic Press Inc.

Fischer, H.W., Ulbrich, S., Pittauerová, D., Hettwig, B., 2009. *Medical radioisotopes in the environment-following the pathway from patient to river sediment.* Journal of Environmental Radioactivity 200**,** 1079-1085.

Grabemann I., Kuehle H., Kunze B., Mueller A., 1996. *Studies on Transport Times and Water Quality in the Weser Estuary (Germany)*, in Mixing in estuaries and Coastal Seas, American Geophysical Union, Washington, D.C..

Grabemann I., Krause G., 2001, *On Different Time Scales of Suspended Matter Dynamics in the Weser Estuary*. Estuaries, 24, 5, 688-698.

Hamby D.M., 1994. *A review of techniques for parameter sensitivity analysis on environmental models.* Environmental Monitoring and Assessment, 32, 2, 135-154.

Herrling G. and Niemeyer H.D., 2008. *Hydro- and Morphological Pressures and Impacts*, HARBASINS Report. Retrieved from: http://www.nlwkn.niedersachsen.de/download/70702.

Kappenberg J., Grabemann I., 2001, *Variability of the Mixing Zones and Estuarine Turbidity Maxima in the Elbe and Weser Estuaries,* Estuaries, 24, 5, 699-706.

Mount J.F., 1995. *California Rivers and Streams: The Conflict Between Fluvial Process and Land Use*. University of California Press.

Mueller A., 1992, *Lower Weser Monitoring and Modelling*, Coastal and Estuarine Studies, 36, 285-294.

Parker G. and Garcia M.H., 2006. *River, Coastal and Estuarine Morphodynamics: RCEM 2005.* Taylor and Francis.

Pineiro G., Perelman S., Guerschman J.P., Paruelo J.M., 2008. *How to evaluate models: Observed vs. predicted or predicted vs. observed?* Ecological Modelling, 216, 3-4, 316-322.

Schnoor J.L., 1996. Environmental Modeling: Fate and Transport of Pollutants in Water, Air and Soil. John Wiley & Sons

Schuchartdt B., Haesloop U., Schirmer M., 1993, *The tidal freshwater reach of the Weser estuary: Riverine or Estuarine?* Netherlands Journal of Aquatic Ecology, 27(2-4), 215-226.

Semizhon T., Röllin S., Spasova Y., Klemt E., 2010. *Transport and distribution of artificial gamma-emitting radionuclides in the River Yenisei and its sediment.* Journal of Environmental Radioactivity, 101 (5), 385 - 402.

Sheppard S., Long J., Sanipelli B., 2009. *Solid/liquid partition coefficients (Kd) for selected soils and sediments at Forsmark and Laxemar-Simpevarp*. Swedish Nuclear Fuel and Waste Management Co. SKB Rapport R-09-27. Retrieved from: http://www.skb.com/publication/1951648/R-09-27.pdf

Stoschek O. and Matheja A., 2001, *Simulation von Sedimenttransportprozessen in TidebeeinflusstenHafengebieten*. Franzius Inst. F. Wasserbau u. KüsteningenieurwesenUni Hannover, Heft 86/01, 18-56

Thibodeaux L.J., 1996. *Movement of chemicals in air, water, and soil.* Second Edition. John Wiley & Sons, INC.

Till J.E. and Meyer H.R., 1983. *Radiological Assessment. A Textbook on Environmental Dose Analysis.* NUREG/CR-3332 ORNL-5968. Retrieved from: https://www.nrc.gov/docs/ML0917/ML091770419.pdf

Trento A.E. and Alvarez A.M., 2011. *A Numerical Model for the Transportation of Chromium and Fine Sediments.* Environmental Modeling and Assessment, 16, 6, 551-564.

Vandenbruwaene W., PlanckeY.,Verwaest T., Mostaert F., 2013, *Interestuarine comparison: hydro-geomorphology. Hydro- and geomorphodynamics of the TIDE estuaries Scheldt, Elbe, Weser and Humber.*Version 4. WL Rapporten, 770_62b. Flanders Hydraulics Research: Antwep, Belgium. Retrieved from: http://www.tide-project.eu/downloads/WL2013R770_62b_rev4_20130220_TIDE_IC_HGM.pdf

Wilhelm R.G., 2004. *Understanding the variation in partition coefficient, kd, values. Volume III: Review of Geochemistry and Available Kd values for Americium, Arsenic, Curium, Iodine, Neptunium, Radium and Technetium.* Environmental Protection Agency, Office of Air and Radiation EPA 402-R-04-002C. Retrieved from: https://www.epa.gov/sites/production/files/2015-05/documents/402-r-04-002c.pdf

WSV, *Wasserstraßen- und Schifffahrtsverwaltung des Bundes*, http://www.wsv.de/, 2017.

Zhang Y., 2008. *Geochemical Kinetics*. Princeton University Press

Zheleznyak M., Donchytz G., Hygynyak V., Marinetz A., Lyashenko G., Tkalich P., 2003, *RIVTOX-one dimensional model for the simulation of the transport o radionuclides in a network of river channels.*RODOS-WG4-TN(97)05. Retrieved from: https://resy5.iket.kit.edu/RODOS/Documents/Public/HandbookV6/Volume3/RIVTOX.pdf

Chapter 8

Summary and Outlook

In this chapter the most important findings of this study are summarized and suggestions for future improvements and investigations are given.

8.1 Summary

Within this work medical ^{131}I was successfully used as an environmental tracer for hydrological and sedimentological processes of the tidally influenced Weser River. The quantification of its distribution in the water-sediment system allowed the study of advection, dispersion and sedimentation processes.

^{131}I was measured through gamma spectroscopy. Genie automatic peak fit function in cases of low activities proved unsatisfactory and a manual fit, by setting the FWHM and the low tail of the peak as fixed parameters, provided better accuracy to our experimental results.

In addition, requirement of low detection limits to be met for the successful detection of ^{131}I in river water samples a chemical extraction method was developed and tested with both WWTP effluent and river water samples. The method which targets both inorganic and organically bound iodine creates one combined precipitate and has a high chemical yield of (86 ± 15) %. It is applicable to large volumes of samples, independent of natural pH, salinity and conductivity and provides reliable and reproducible results. For a 4 day measurement in the lab detectors in a precipitate formed from a 50 L river water sample ^{131}I can be detected with values as low as 0.5 mBq/kg.

Under the scope of this project, 17 campaigns in the Weser River were performed for obtaining 85 river water and 14 sediment samples, resulting in a large collection of ^{131}I activity concentration values in these media. Quantification of ^{131}I in the suspended matter of the river water was not possible due to low activity concentration values. The complexity of the hydrological system challenged the interpretation of the results, especially for ^{131}I activity concentration in the river water, which is strongly dependent on the tidal cycle. The local WWTP was identified as the source of ^{131}I (finding additionally supported when comparing with the rather steady sediment profiles of ^{40}K, ^{7}Be and ^{137}Cs) with concentrations varying between 0.8 to 207 mBq/kg for the river water samples and 0.9 to 36 Bq/kg(d.m.) for the bank sediment samples. The longitudinal profiles of ^{131}I in both media were analogous, with a sharp peak at the discharge point and the formation of a background value in the vicinity of the WWTP.

Additionally the results in both media are in agreement with previous measurements done in the area.

Furthermore, a model developed with the aim of computing ^{131}I behavior in Weser River water and sediments was developed during this work. The model is solves numerically basic equations of physics (Navier Stokes equations, advection dispersion equations) in a specified domain with preselected boundary and initial conditions. Extensive literature research provided not only values for numerous parameters of these equations but also a basic validation of our simulations. Assessment of the model was done by comparing ^{131}I activity concentration values in river water and bank sediments for experimental and simulated results under the same hydrological conditions. Despite the simplifications and assumptions considered, the comparison confirms that the model provides realistic results and indicated the models capability of predicting the dispersion of medially derived ^{131}I, originating from the WWTP in the water body and banks of Weser River. It could be further applied in different river systems and with the interest of additional radionuclides, leading to a better understanding of environmental and man-made radioactivity.

8.2 Study in numbers

In the course of this study 3083 kg of WWTP effluent and 3846 kg of river water were sampled. For the development and testing of a suitable chemical extraction method for ^{131}I in river water samples, 12 methods were tested and a total of 97 extractions were performed. 268 samples were measured in the gamma detectors (producing the same amount of spectra which required analysis) and with an average measuring time of 20 h, occupied our detectors for more than 220 days. Our experimental data from the Weser River, were collected during 17 sampling campaigns with an average sampling time of 6 hours, leading to more than 100 h sampling time outdoors. In total 122 gamma spectra were produced, 83 of which were water samples treated with the chemical extraction method. Longer measuring times, with an average of 54 h per sample, were required for the detection ^{131}I, bringing our detectors to full capacity for more than 275 days. Last, more than 10000 simulations were performed (average simulation time of 10 min) running for more than 70 days in the computer system.

8.3 Outlook

Time limitations as well as the nature of this study (multidisciplinary; incorporating physics, chemistry, mathematics and computer science) restricted the depth on which each topic of this work was covered, allowing future work and improvements on the subject.

The developed chemical extraction method, could be improved (eg. precipitating ^{131}I bound to colloid particles) reaching higher yield values. It could also be tested on effluent from other WWTPs with different water treatment and water samples (eg. river water, lake water, drinking water, groundwater) with different iodine chemistry.

River water sampling on routine basis and on a greater extent (more sampling locations, sampling in both directions from the WWTP during the tidal cycle in order to better quantify the background ^{131}I activity concentration) could create a more comprehensive dataset. In addition sampling larger volume of samples would lead to better accuracy in the measurements and possibly to detection of ^{131}I in locations where it has not been detected. In situ measurements of physical and chemical parameters of the river water (temperature, salinity, pH, conductivity, metals, etc) along with precise hydrological data for each sampling location would facilitate better understanding of the underlying distribution processes.

An extensive testing of the model for both other regions and for different inputs is necessary. A current student of the group working on his master thesis “Medical Iodine-131 in the River Hunte” will use this model for simulating the distribution of iodine in a different system. Especially for the sedimentation sub-model, collection of daily WWTP effluent samples could lead to more realistic simulation results. Last but not least, an important aspect of modeling not treated in this work is an in depth error estimation of the simulations (due to numerical methods, assumptions, parameterization, etc) which has to be addressed.

Publications

2013

Ulbrich S., Hormann V., Souti M.E., Toma E., Igbinosa A., Hettwig B., Fischer H.W.,2013. Verfahren zur Bestimmung von ^{131}I in Fliessgewässern. Oral Presentation at 15. Fachgespräch zur Überwachung der Umweltradioaktivität, 5-7 March 2013, Bremen, Germany.

Fischer H.W., Souti M.E., Ulbrich S.,Hormann V., 2013. Freshwater sediments and sludges: two important terrestrial sinks for emissions from damages NPPs. Poster Presentation at European Geosciences Union General Assembly, 7-12 April 2013, Vienna, Austria.

2014

Souti M.E., Hormann V., Toma E., Fischer H.W., 2014.^{131}I extraction from fresh water and sewage plant effluent. Oral Poster Presentation at 3rd International Conference on Radioecology & Environmental Radioactivity, 7-12 September 2014, Barcelona, Spain.

Fischer H.W., Ulbrich S., Souti M.E., Gellermann R., 2013. Medical ^{131}I in German Rivers. Poster Presentation at 3rd International Conference on Radioecology & Environmental Radioactivity, 7-12 September 2014, Barcelona, Spain.

Fischer H.W., Igbinosa A., Souti M.E., 2013. Beryllium-7 in rainwater, river sediment and sewage sludge. Poster Presentation at 3rd International Conference on Radioecology & Environmental Radioactivity, 7-12 September 2014, Barcelona, Spain.

2015

Souti M.E., Fischer H.W.,2015.Medical ^{131}I in River Water and Sediments–Case study of Weser River in NW Germany. Poster presentation at ENVIRA 2015, International Conference Environmental Radioactivity, 21-25 September 2015, Thessaloniki, Greece.

Souti M.E., Amoo P.B., Anesiadou A., Fischer H.W.,2015. Be-7 in various environmental media in the Bremen Region. Oral presentation at ENVIRA 2015, International Conference Environmental Radioactivity, 21-25 September 2015, Thessaloniki, Greece.

2016

Souti M.E., Fischer H.W.,2016. Modeling^{131}I distribution in a tidal river.Poster presentation at II International Conference on Radioecological Concentration Processes, 06.-09 November 2016, Seville, Spain.

Anesiadou A., Kirchner G., Souti M.E., Fischer H.W., 2016. Re-examination of ^{137}Cs profiles in Northern Germany.Poster presentation at II International Conference on Radioecological Concentration Processes, 06.-09 November 2016, Seville, Spain.

2017

Anesiadou A., Kaiser P., Kirchner G., Souti M.E., Fischer H.W., 2017. Re-examination of Cs-137 depth profiles in undisturbed soilsin northern Germany. Deutsche Physikalische Gesellschaft Tangungen 13-17 March 2017, Bremen, Germany.

Souti M.E., Fischer H.W.,2017. Quantification of medical 131I path from patient to river sediments.Poster Presentation at 4th International Conference on Radioecology & Environmental Radioactivity, 3-8 September 2017, Berlin, Germany.

Papers to be published

Geibert W., Pittauer D., Souti M.E., Fischer H.W., Puigcorbe V., Garcia-Orellana J., Casacuberta N., Lück A., Brennwald M., Kadko D., LeRoy E., vanBeek P., An interlaboratory comparison of beryllium-7 measurements in water. For submission to Limnology and Oceanography: Methods

Souti M.E. and Fischer H.W..Medical ^{131}I in River Water and Sediments. Case study of Weser River in NW Germany. For submission to Journal of Environmental Radioactivity.

Appendix

Appendix 1- Chemical extraction methods

Unless stated otherwise, all methods produced two different precipitates which were measured in gamma detectors and the overall chemical yield was calculated as

$$y = \frac{P_1 + P_2}{O} \cdot 100 \text{ and its error } \quad e = y \cdot \left(\frac{e_{P1}}{P_1} + \frac{e_{P2}}{P_2} \right),$$

where

y: the chemical yield of the method, given in (%)

P_1*:* the ^{131}I activity concentration in the first precipitate, given in (mBq/kg)

P_2*:* the ^{131}I activity concentration in the second precipitate, given in (mBq/kg)

O: the ^{131}I activity concentration in the WWTP effluent, given in (mBq/kg)

e_{P1}*:* the error of the ^{131}I activity concentration in the first precipitate, given in (mBq/kg)

e_{P2}: the error of the ^{131}I activity concentration in the second precipitate, given in (mBq/kg)

Method I

#	spectrum	Mass (kg)	Measuring time (s)	Efficiency for ^{131}I (364.5 keV)	WWTP ^{131}I effluent activity (mBq/kg)	Bentonite ^{131}I precipitate activity (mBq/kg)	Fe ^{131}I precipitate activity (mBq/kg)	Combined chemical yield (%)
MS1	30923	4.00	73572	0.01323	240.55 ±15.35			
MS13	40721	20.10	17175	0.02888		98.60± 7.29		78 ±12
MS15	51212	20.10	12294	0.01928			90.26 ±10.40	
MS2	40716	4.00	72719	0.01293	236.50 ± 25.34			
MS14	61497	20.02	13668	0.02631		94.24 ±7.57		86 ± 15
MS16	30931	20.02	63823	0.02629			108.88 ± 5.20	
MS36	40769	4.00	60127	0.01293	302.79 ± 28.77			
MS38	40772	19.80	10757	0.02888		204.43 ±9.60		85 ±13
MS50	61560	19.80	151172	0.01838			54.80 ±3.61	
MS93	31006	4.00	23536	0.01323	167.65 ±26.38			
MS106	51471	19.92	19771	0.02509		130.90 ±8.06		89 ±20
MS113	31017	19.92	64892	0.01919			18.86 ±3.19	
MS97	51465	4.05	23529	0.01329	169.51 ±28.55			
MS107	51475	19.48	74834	0.02509		147.85 ±5.33		95 ±22
MS109	51477	19.48	75597	0.01928			14.49 ±4.27	
MS101	61637	4.00	23437	0.01188	191.59 ±32.92			
MS112	31016	18.76	10052	0.02929		125.75 ±10.45		78 ±21
MS115	31019	18.76	62943	0.01919			24.49 ±3.96	
MS94	31007	4.00	70027	0.01323	193.03 ±15.64			
MS108	51476	19.23	13002	0.02509		160.25 ±11.59		94 ±17
MS117	61649	19.23	92185	0.01838			21.28 ±4.66	
MS102	61638	4.00	62192	0.01188	208.16 ± 23.24			
MS114	31018	19.78	12033	0.02929		138.69 ±10.35		75 ±15
MS118	51478	19.78	92154	0.01928			18.13 ±4.02	
MS128	51485	4.00	75800	0.01329	85.89 ±17.97			
MS137	61659	19.90	16789	0.02631		60.59 ±6.26		76 ±25
MS132	51586	19.90	89032	0.01928			3.69 ±2.39	

MS148	40870	4.00	75029	0.01293	192.70 ±24.46			
MS150	40873	20.04	20676	0.02888		159.98 ±8.94		92 ± 18
MS151	40874	20.04	86462	0.01997			18.05 ±4.14	
MS96	51464	4.00	57978	0.01329	152.81 ± 18.39			
MS99	51467	20.80	12074	0.02509		151.41 ± 7.87		110 ± 20
MS105	51469	20.80	151551	0.01928			18.21 ± 1.90	
MS98	51466	4.00	69914	0.01329	113.92 ± 16.70			
MS111	61648	19.88	8575	0.02631		137.78 ±21.51		144 ±46
MS119	40846	19.88	145800	0.01997			25.55 ± 5.59	
MS135	61656	4.00	97817	0.01188	55.90 ± 13.47			
MS125	40861	19.38	20044	0.02888		66.21 ± 6.74		118 ± 40
MS127	40859	19.38	83833	0.01997			< DL	

Method II

#	spectrum	Mass (kg)	Measuring time (s)	Efficiency for ^{131}I (364.5 keV)	WWTP ^{131}I effluent activity (mBq/kg)	Bentonite ^{131}I precipitate activity (mBq/kg)	Fe ^{131}I precipitate activity (mBq/kg)	Combined chemical yield (%)
MS3	61493	4.00	69269	0.01188	244.23 ± 18.51			
MS19	30932	19.84	74551	0.01919		80.81 ±5.14		39 ± 6
MS17	61498	19.84	78501	0.03438			15.43 ± 2.20	
MS4	30924	4.00	63195	0.01323	239.30 ± 17.71			
MS20	61499	19.40	61499	0.01838		84.14 ± 10.98		44 ± 9
MS18	40722	19.40	40722	0.03593			21.22 ± 2.62	
MS43	51314	4.00	80273	0.01329	220.21 ± 18.69			
MS49	51321	20.08	15178	0.01620		105.43 ± 12.52		61 ± 12
MS48	51320	20.08	77775	0.03319			29.66 ± 2.34	

Method III

#	spectrum	Mass (kg)	Measuring time (s)	Efficiency for ^{131}I (364.5 keV)	WWTP ^{131}I effluent activity (mBq/kg)	Bentonite ^{131}I precipitate activity (mBq/kg)	Fe ^{131}I precipitate activity (mBq/kg)	Combined chemical yield (%)
MS5	40717	4.02	61901	0.01293	265.39 ± 26.84			
MS21	40723	19.46	15669	0.03593		111.34 ± 8.00		78 ± 13
MS23	30933	19.46	65761	0.02432			96.42 ±4.95	
MS6	61494	4.00	62590	0.01188	240.93 ± 23.14			
MS22	40724	21.30	64677	0.03593		139.99± 5.17		89 ±13
MS25	61500	21.30	65434	0.01838			73.66 ± 5.48	
MS42	51313	4.00	60165	0.01329	248.57 ± 21.23			
MS44	51315	20.02	10608	0.02509		195.18 ± 10.03		96 ±13
MS46	51317	20.02	151271	0.01928			43.73 ± 2.89	

Method IV

#	spectrum	Mass (kg)	Measuring time (s)	Efficiency for ^{131}I (364.5 keV)	WWTP^{131}I effluent activity (mBq/kg)	Combined Bentonite and Fe^{131}I precipitate activity (mBq/kg)	Combined chemical yield (%)
MS7	61495	4.00	101242	0.01188	277.07±24.57		
MS27	30934	19.88	170225	0.01919		98.88 ± 4.59	36 ± 5
MS8	51201	4.00	102388	0.01329	215.69 ±17.46		
MS26	61501	20.20	170433	0.01838		78.08±4.40	36 ± 5
MS45	51316	4.00	87198	0.01329	231.01 ± 20.36		
MS51	40781	19.84	67544	0.01997		162.94 ± 8.88	71 ± 10

Method V

#	spectrum	Mass (kg)	Measuring time (s)	Efficiency for ^{131}I (364.5 keV)	WWTP ^{131}I effluent activity (mBq/kg)	Bentonite ^{131}I precipitate activity (mBq/kg)	Fe ^{131}I precipitate activity (mBq/kg)	Combined chemical yield (%)
MS9	40718	4.01	101994	0.01293	251.35 ± 24.72			
MS28	40726	19.40	75375	0.02888		95.97 ± 7.30		77 ± 14
MS30	61503	19.40	82974	0.01838			96.89 ± 8.14	
MS11	40719	4.00	68969	0.01293	281.17 ± 32.69			
MS33	30935	18.92	72404	0.02929		76.61 ± 5.22		62 ± 12
MS35	51229	18.92	81484	0.01928			97.78 ± 9.01	
MS37	40770	4.00	21054	0.01293	252.7 ± 42.81			
MS47	51319	20.22	8803	0.02509		187.20 ±13.02		100 ± 24
MS41	40780	20.22	98847	0.01997			67.41 ± 5.22	

Method VI

#	spectrum	Mass (kg)	Measuring time (s)	Efficiency for ^{131}I (364.5 keV)	WWTP ^{131}I effluent activity (mBq/kg)	Bentonite ^{131}I precipitate activity (mBq/kg)	Fe ^{131}I precipitate activity (mBq/kg)	Combined chemical yield (%)
MS66	40791	4.00	74572	0.01293	213.8 ± 22.68			
MS69	40798	20.06	56891	0.02888		155.88 ± 5.92		94 ± 15
MS64	51356	20.06	85478	0.01929			44.64 ± 4.20	
MS79	51441	4.00	66351	0.01329	247.48 ± 22.25			
MS87	51445	19.74	7382	0.02509		186.17 ± 12.23		100 ± 16
MS90	61627	19.74	71702	0.01838			59.95 ± 4.78	
MS80	51442	4.01	23179	0.01329	287.50 ± 33.06			
MS88	51446	20.04	9912	0.02509		190.04 ± 10.60		
MS85	40834	20.04	68297	0.01997			62.91±5.99	88 ± 16
MS145	40866	4.00	59820	0.01293	217.70 ± 23.04			
MS154	51595	19.80	9202	0.02509		16460 ± 9.67		89 ± 15
MS149	40871	19.80	353375	0.01997			30.09 ± 2.37	

MS176	61731	4.00	235300	0.01188	535.81 ± 19.77			
MS178	61735	19.44	8157	0.02631		371.26 ± 19.63		85 ± 9
MS182	40894	19.44	22096	0.01997			87.40 ± 10.80	
MS175	61730	4.00	23962	0.01188	602.67 ± 53.32			
MS181	31075	19.46	8170	0.02929		338.11 ± 20.61		75 ± 12
MS186	51626	19.46	22427	0.01928			113.91 ± 9.40	
MS167	40888	4.01	71484	0.01293	564.20 ± 34.99			
MS180	31074	19.04	7955	0.02929		383.84 ± 22.89		83 ± 11
MS179	51624	19.04	17683	0.01928			85.86 ± 9.99	
MS203	61792	4.00	57256	0.01188	202.93 ± 29.70			
MS206	51647	19.32	17317	0.02509		133.77 ± 9.71		83 ± 19
MS208	51650	19.32	63485	0.01928			34.23 ± 3.08	
MS201	51641	4.01	57656	0.01329	192.64 ± 28.51			
MS207	51649	20.04	16310	0.02509		131.85 ±10.59		90 ± 22
MS205	40914	20.04	63089	0.01997			40.94 ± 6.47	
MS59	51336	4.00	72235	0.01329	162.52 ± 17.36			
MS62	51349	20.04	56931	0.02509		153.73 ±15.94		132 ±33
MS63	51352	20.04	62042	0.01928			61.26 ±15.15	
MS152	51592	4.00	59516	0.01329	160.80 ± 9.04			
MS147	40869	19.68	9417	0.02888		138.27 ± 16.04		106±13
MS156	51597	19.68	353511	0.01928			32.49 ± 1.77	
MS170	51614	4.00	59893	0.01329	430.42 ± 27.13			
MS172	51619	19.46	12131	0.02509		409.52 ± 13.89		115 ± 11
MS174	51621	19.46	234711	0.01928			84.92 ± 3.06	
MS164	40885	4.00	60015	0.01293	534.08 ± 34.11			
MS166	40887	19.58	10201	0.02888		468.97 ± 15.44		108 ± 10
MS169	40890	19.58	234943	0.01997			108.48 ± 4.33	
MS195	51636	4.01	68845	0.01329	153.53 ± 20.36			
MS209	61795	19.60	9544	0.02631		125.91 ± 12.03		112 ± 26
MS210	61799	19.60	61549	0.01838			47.14 ± 5.75	

Method VII

#	spectrum	Mass (kg)	Measuring time (s)	Efficiency for ^{131}I (364.5 keV)	WWTP ^{131}I effluent activity (mBq/kg)	Bentonite ^{131}I precipitate activity (mBq/kg)	Fe^{131}I precipitate activity (mBq/kg)	Combined chemical yield (%)
MS61	51340	3.99	150183	0.01329	215.07 ± 17.71			
MS71	40805	20.02	85321	0.02888		122.44 ± 5.34		82 ± 12
MS58	61582	20.02	156309	0.01838			54.63 ± 5.11	
MS81	51443	4.01	226570	0.01329	232.89 ± 14.41			
MS84	40832	19.82	6962	0.02888		159.58 ± 13.67		95 ± 13
MS82	30993	19.82	64279	0.01919			62.33 ± 4.44	
MS78	61616	4.00	227015	0.01188	276.47 ± 13.36			
MS89	61625	19.62	6614	0.02631		183.72 ± 14.03		91 ± 12
MS91	61628	19.62	28498	0.01838			65.94 ± 8.49	
MS60	51339	4.00	81368	0.01329	160.44 ± 19.20			
MS72	40806	20.12	156252	0.02888		150.56 ± 4.87		121 ± 20
MS65	51357	20.12	156293	0.01928			42.32 ± 3.52	

Method VIII

#	spectrum	Mass (kg)	Measuring time (s)	Efficiency for ^{131}I (364.5 keV)	WWTP ^{131}I effluent activity (mBq/kg)	Resin ^{131}I activity (mBq/kg)	Fe ^{131}I precipitate activity (mBq/kg)	Combined chemical yield (%)
MS56	61573	4.01	81212	0.01188	223.17 ± 20.31			
MS75	40818	20.06	86041	0.04577		48.74 ± 6.94		29 ± 11
MS76	40819	20.06	149274	0.01997			16.23 ± 11.80	
MS68	40793	4.00	150283	0.01293	249.71 ± 24.47			
MS73	51431	19.60	86272	0.02509		50.43 ± 4.80		30 ± 9
MS74	51432	19.60	149298	0.01620			25.90 ± 10.72	
MS77	61615	4.00	23163	0.01188	297.13 ± 36.73			
MS83	30994	19.54	17627	0.06111		62.41 ± 4.07		27 ± 5
MS86	40835	19.54	240770	0.02888			18.68 ± 2.27	

Method IX

#	spectrum	Mass (kg)	Measuring time (s)	Efficiency for ^{131}I (364.5 keV)	WWTP ^{131}I effluent activity (mBq/kg)	Resin ^{131}I activity (mBq/kg)	Fe ^{131}I precipitate activity (mBq/kg)	Combined chemical yield (%)
MS67	40792	4.02	93499	0.01293	251.80 ± 25.81			
MS70	40801	20.08	61953	0.02888		121.31 ± 5.67		60 ± 10
MS57	61581	20.08	85495	0.02631			29.43 ± 3.23	

Method X

#	spectrum	Mass (kg)	Measuring time (s)	Efficiency for ^{131}I (364.5 keV)	WWTP ^{131}I effluent activity (mBq/kg)	Bentonite ^{131}I precipitate activity (mBq/kg)	Fe ^{131}I precipitate activity (mBq/kg)	Combined chemical yield (%)
MS92	31005	4.01	57598	0.01323	163.68 ± 16.26			
MS103	61642	20.66	19303	0.02631		104.56 ± 7.09		96 ± 17
MS110	61646	20.66	65027	0.01838			51.93 ± 5.10	
MS120	40853	4.01	81849	0.01293	92.61 ± 20.27			
MS124	40857	19.56	16978	0.02888		42.95 ± 6.52		59 ± 25
MS139	61662	19.56	70182	0.01838			11.92 ± 3.87	
MS123	40856	4.01	155528	0.01293	75.38 ± 14.42			
MS138	61661	18.64	19723	0.02631		47.97 ± 6.50		71 ± 27
MS133	51587	18.64	83402	0.01928			4.65 ± 3.66	
MS100	61636	4.00	58350	0.01188	158.71 ± 18.12			
MS95	31008	20.06	12104	0.02929		109.91 ± 7.44		103 ± 18
MS104	31010	20.06	152394	0.01919			54.25 ± 2.60	

Method XI

#	spectrum	Mass (kg)	Measuring time (s)	Efficiency for ^{131}I (364.5 keV)	WWTP ^{131}I effluent activity (mBq/kg)	Bentonite ^{131}I precipitate activity (mBq/kg)	$Ca^{131}I$ precipitate activity (mBq/kg)	Combined chemical yield (%)
MS158	61718	4.00	352492	0.01188	197.40 ± 13.82			
MS159	61722	18.80	14249	0.02631		154.31 ± 11.66		78 ± 12
MS160	61723	18.80	185830	0.01838			< DL	
MS146	40868	4.00	73946	0.01293	205.25 ± 24.10			
MS143	31060	19.26	19978	0.02929		159.40 ± 10.05		83 ± 17
MS144	31061	19.26	86470	0.01919			10.86 ± 3.52	
MS173	51620	4.00	23850	0.01329	456.52 ± 41.20			
MS177	61734	19.10	7933	0.02631		420.01 ± 20.79		98 ± 15
MS185	51625	19.10	64638	0.01928			29.13 ± 5.13	

Method XII

#	spectrum	Mass (kg)	Measuring time (s)	Efficiency for ^{131}I (364.5 keV)	WWTP ^{131}I effluent activity (mBq/kg)	Combined Bentonite and $Ca^{131}I$ precipitate activity (mBq/kg)	Combined chemical yield (%)	WWTP effluent properties		
								Conductivity (µS/cm)	Salinity (ppt)	pH
MS153	51594	4.00	73514	0.01329	167.96 ± 18.41			1120	0.3	7.35
MS162	31063	19.60	236918	0.02929		143.27 ± 6.63	85 ± 13			
MS171	51618	4.00	66464	0.01329	453.96 ± 27.65			1114	0.3	7.34
MS168	40889	19.78	10453	0.02888		418.72 ± 15.08	92 ± 9			
MS165	40886	4.01	69881	0.01293	501.38 ± 31.63			1108	0.3	7.36
MS163	31070	19.74	5913	0.02929		439.83 ± 24.35	88 ± 10			
MS188	61782	4.00	59882	0.01188	199.26 ± 22.23			n.a.	n.a.	n.a.
MS190	61786	20.38	11207	0.02631		165.40 ± 8.38	83 ± 13			

MS197	40904	4.01	59920	0.01293	238.27 ± 24.36			n.a.	n.a.	n.a.
MS194	51635	19.96	10955	0.02509		163.57 ± 9.14	69 ± 11			
MS189	61784	4.01	72929	0.01188	194.43 ± 19.50			1158	0.4	7.54
MS200	31085	20.03	8125	0.02929		160.60 ± 11.04	83 ± 14			
MS192	51633	4.01	59983	0.01329	190.50 ± 19.56			n.a.	n.a.	n.a.
MS199	31084	20.42	10664	0.02929		141.78 ± 8.90	74 ± 12			
MS193	51634	4.03	72607	0.01329	170.69 ± 21.29			1152	0.4	7.3
MS196	51638	19.92	7804	0.02509		153.16 ± 10.86	89 ± 17			
MS198	40906	4.01	63562	0.01293	249.60 ± 26.74			1150	0.4	7.15
MS204	61794	20.04	10885	0.02631		158.20 ± 9.83	63 ± 11			
MS191	61787	4.00	68827	0.01188	216.82 ± 22.62			1145	0.3	7.14
MS202	51643	21.80	10285	0.02509		146.29 ± 9.72	67 ± 12			
MS222	40921	4.01	65189	0.01293	207.40 ± 25.19			1193	0.4	7.36
MS229	31098	20.38	8895	0.02929		166.48 ± 10.31	80 ± 15			
MS211	61809	4.01	64757	0.01188	169.83 ± 19.38			1190	0.4	7.32
MS224	40923	19.82	9957	0.02888		158.18 ± 9.45	93 ± 16			
MS216	51657	4.00	65142	0.01329	166.99 ± 19.88			1195	0.4	7.37
MS218	51659	20.06	10129	0.02509		173.96 ± 9.99	104 ± 18			
MS217	51658	4.00	73421	0.01329	191.41 ± 20.60			1193	0.4	7.35
MS220	51661	19.98	22628	0.02631		171.54 ± 7.61	90 ± 14			
MS223	40922	4.00	73672	0.01293	215.40 ± 21.29			1178	0.4	7.3
MS226	40925	19.22	22219	0.02888		167.57 ± 7.04	78 ± 11			
MS212	61810	4.05	66793	0.01188	201.24 ± 21.07			1181	0.4	7.3
MS213	61812	19.80	22164	0.02631		165.99 ± 7.18	83 ± 12			
MS227	40926	4.00	235168	0.01293	213.94 ± 21.01			1178	0.4	7.3
MS221	51665	19.46	9586	0.02509		157.89 ± 11.96	74 ± 13			
MS214	61813	4.01	233998	0.01188	214.26 ± 16.88			1176	0.4	7.28
MS230	31101	20.06	7630	0.02929		153.33 ± 12.75	71 ± 12			
MS225	40924	4.01	67516	0.01293	217.18 ± 23.87			1178	0.4	7.26
MS228	40930	19.86	9073	0.02888		136.44 ± 11.09	63 ± 12			
MS219	61816	4.00	67226	0.01188	161.54 ± 20.64			1177	0.4	7.22
MS215	51660	20.46	7504	0.02631		160.20 ± 13.04	99 ± 21			
MS231	61820	4.00	58458	0.01188	115.14 ± 19.76			1016	0.3	7.47

MS234	61825	19.52	4721	0.06774		104.42 ± 7.31	90 ± 22			
MS242	40932	4.01	59752	0.01293	118.60 ± 21.06			1014	0.3	7.44
MS240	51672	19.98	12989	0.06144		110.14 ± 5.12	92 ± 21			
MS248	31102	4.00	59185	0.01323	110.58 ± 13.54			1011	0.3	7.4
MS245	40936	19.96	13057	0.05977		99.43 ± 5.08	89 ± 16			
MS232	61822	4.02	70037	0.01188	106.03 ± 20.67			1007	0.3	7.39
MS251	31108	19.24	11677	0.02929		103.44 ± 8.04	97 ± 27			
MS233	61824	4.00	240285	0.01188	120.25 ± 12.18			1007	0.3	7.36
MS235	61827	19.30	11124	0.02631		99.58 ± 8.42	83 ± 15			
MS249	31104	4.00	70586	0.01323	138.17 ± 20.12			1006	0.3	7.37
MS246	40938	19.70	11550	0.02888		95.72 ± 8.87	70 ± 17			
MS243	40934	4.00	70414	0.01293	146.49 ± 20.96			1005	0.3	7.38
MS236	61830	19.16	10930	0.02631		96.88 ± 9.65	66 ± 16			
MS244	40935	4.00	240477	0.01293	100.24 ± 13.81			1004	0.3	7.32
MS247	40941	20.08	10898	0.02888		99.20 ± 9.35	99 ± 23			
MS238	51669	4.00	61147	0.01329	121.67 ± 20.16			1005	0.3	7.31
MS252	31109	19.46	7618	0.02929		97.67 ± 9.90	80 ± 21			
MS255	51697	4.00	65901	0.01329	171.61 ± 19.49			1179	0.4	7.34
MS261	40954	19.38	14643	0.02888		153.52 ± 7.85	90 ± 15			
MS257	61849	4.00	66088	0.01188	164.70 ± 21.30			1176	0.4	7.3
MS264	61853	19.58	13587	0.02631		155.87 ± 10.01	95 ± 18			
MS259	40951	4.01	65684	0.01293	197.80 ± 21.49			1178	0.4	7.28
MS265	51700	19.80	14019	0.02509		169.68 ± 8.45	86 ± 13			
MS253	31124	4.00	60237	0.01323	187.68 ± 18.73			1179	0.4	7.29
MS263	31129	19.66	14870	0.02929		157.99 ± 8.95	84 ± 13			
MS260	40953	4.00	69181	0.01293	168.80 ± 24.52			1172	0.4	7.33
MS262	40955	18.88	10994	0.02888		159.53 ± 9.54	95 ± 20			
MS237	51668	4.02	75355	0.01329	79.86 ± 15.55			1013	0.3	7.4
MS250	31106	20.16	13113	0.02929		104.88 ± 4.76	131 ± 31			
MS239	51671	4.00	240379	0.01329	83.34 ± 12.80			1003	0.3	7.35
MS241	51674	19.81	11401	0.02509		101.78 ± 9.85	123 ± 31			

Appendix 2- Sampling location coordinates

#	spectrum	Sampling location	Downstream distance from the WWTP [km]	Latitude	Longitude
Sampling campaign 1 – 23.09.14					
MS269	51799	WWTP	0	+53.1151779	+8.7146639
MS270	41051	1.1	0	+53.1166548	+8.7157120
MS271	51800	1.2	0	+53.1174488	+8.7162216
MS272	31220	1.3	0	+53.1181561	+8.7168989
MS273	61949	1.4	0	+53.1189610	+8.7169919
MS274	61948	1.5	0	+53.1193786	+8.7173866
Sampling campaign 2 – 06.10.14					
MS275	51806	WWTP	0	+53.1151779	+8.7146639
MS276	31228	1.1	0	+53.1166548	+8.7157120
MS277	41057	1.2	0	+53.1174488	+8.7162216
MS278	61955	1.3	0	+53.1181561	+8.7168989
MS279	41058	1.4	0	+53.1189610	+8.7169919
MS280	51810	1.5	0	+53.1193786	+8.7173866
Sampling campaign 3 – 12.11.14					
MS281	41079	WWTP	0	+53.1151779	+8.7146639
MS282	41080	1.1	0	+53.1166656	+8.7155936
MS283	31255	2.1	0.5	+53.1178541	+8.7081783
MS284	41082	3.1	1	+53.1178335	+8.7007193
MS285	51831	1.1	0	+53.1166656	+8.7155936
MS286	61980	1.1	0	+53.1166656	+8.7155936
Sampling campaign 4 – 12.03.15					
MS287	62061	WWTP	0	+53.1151779	+8.7146639

MS288	51940	1.1	0	+53.1166656	+8.7155936
MS289	51941	2.1	0.5	+53.117833	+8.707267
MS290	41150	2.1	0.5	+53.117833	+8.707267
MS291	62062	1.1	0	+53.1166656	+8.7155936
Sampling campaign 5 – 18.03.15					
MS292	41151	WWTP	0	+53.1151779	+8.7146639
MS293	62067	0	0	+53.1161440	+8.7153498
MS294	51948	0	0	+53.1161440	+8.7153498
MS295	51946	0	0	+53.1161440	+8.7153498
MS296	51947	1.1	0	+53.1166656	+8.7155936
MS297	62068	1.1	0	+53.1166656	+8.7155936
MS298	41153	3.1	1	+53.1178335	+8.7007193
MS299	62069	3.1	1	+53.1178335	+8.7007193
MS300	41152	3.1	1	+53.1178335	+8.7007193
MS301	41154	3.2	1	+53.1183848	+8.7007046
MS302	51949	3.2	1	+53.1183848	+8.7007046
Sampling campaign 6 – 26.03.15					
MS303	62073	Left bank	0	+5311638087	+8.71588647
MS304	51954	Left bank	0	+531167405	+8.715108181
MS305	51953	Left bank	0.5	+53.11745623	+8.70832801
MS306	62072	Left bank	1	+53.11764941	+8.70058179
MS307	62074	Left bank	2	+53.1204816	+8.68330836
MS308	51955	Left bank	5	+53.12607101	+8.64997387
MS309	41155	Left bank	-0.5	+53.1144941	+8.72223794
MS310	41156	Left bank	-1	+53.11184733	+8.72753799

Sampling campaign 7 – 08.04.15					
MS311	51963	Right bank	0	+53.11945234	+8.71709883
MS312	41160	Right bank	5	+53.12858172	+8.65123987
MS313	62081	Right bank	-2	+53.1141584	+8.7424451
Sampling campaign 8 – 04.05.15					
MS315	41177	WWTP	0	+53.1151779	+8.7146639
MS316	31413	6.1	-0.5	+53.1147894	+8.7226590
MS317	62098	6.1	-0.5	+53.1147894	+8.7226590
MS318	41179	6.2	-0.5	+53.1156316	+8.7233077
MS319	31414	6.3	-0.5	+53.1162508	+8.7234730
MS320	62099	6.4	-0.5	+53.1164682	+8.7236604
MS321	51979	6.5	-0.5	+53.1182094	+8.7248223
Sampling campaign 9 – 26.05.15					
MS322	51994	WWTP	0	+53.1151779	+8.7146639
MS323	31431	5.1	5	+53.126717	+8.648797
MS324	62114	5.1	5	+53.126717	+8.648797
MS325	41196	5.2	5	+53.127425	+8.648408
MS326	51996	5.3	5	+53.1278	+8.64865
MS327	31432	5.4	5	+53.128325	+8.648731
MS328	62115	5.5	5	+53.128742	+8.649111
Sampling campaign 10 – 09.06.15					
MS329	52001	WWTP	0	+53.1151779	+8.7146639
MS330	52003	4.1	2	+53.120610	+8.683405
MS331	62121	4.1	2	+53.120610	+8.683405
MS332	31438	4.2	2	+53.121412	+8.684057
MS333	41201	4.3	2	+53.122146	+8.684743

MS334	62122	4.4	2	+53.122738	+8.685226
MS335	31440	4.5	2	+53.123440	+8.685551
Sampling campaign 11 – 23.06.15					
MS336	52012	WWTP	0	+53.1151779	+8.7146639
MS337	31457	3.1	1	+53.11805	+8.699633
MS338	41210	3.1	1	+53.11805	+8.699633
MS339	31458	3.2	1	+53.118917	+8.699717
MS340	52013	3.3	1	+53.119767	+8.700033
MS341	62131	3.4	1	+53.12045	+8.7006
MS342	31459	3.5	1	+53.1211	+8.701083
Sampling campaign 12 – 07.07.15					
MS343	62137	WWTP	0	+53.1151779	+8.7146639
MS344	41217	WWTP	0	+53.1151779	+8.7146639
MS345	62138	2.1	0.5	+53.117833	+8.707267
MS346	31475	2.1	0.5	+53.117833	+8.707267
MS347	31476	2.2	0.5	+53.118217	+8.707483
MS348	62139	2.3	0.5	+53.1187	+8.707483
MS349	52054	2.4	0.5	+53.119167	+8.70755
MS350	41220	2.5	0.5	+53.1194	+8.708
Sampling campaign 13 – 20.07.15					
MS351	41225	WWTP	0	+53.1151779	+8.7146639
MS352	62147	WWTP	0	+53.1151779	+8.7146639
MS353	62148	1.1	0	+53.1166656	+8.7155936
MS354	41227	1.1	0	+53.1166656	+8.7155936
MS355	31489	1.2	0	+53.117453,	+8.716161
MS356	41229	1.3	0	+53.118017	+8.716267
MS357	62150	1.4	0	+53.118683	+8.716617

MS358	52034	1.5	0	+53.119267	+8.716717
Sampling campaign 14 – 25.08.15					
MS359	52058	WWTP	0	+53.1151779	+8.7146639
MS360	62181	WWTP	0	+53.1151779	+8.7146639
MS361	31527	1.1	0	+53.1166656	+8.7155936
MS362	62182	2.1	0.5	+53.117833	+8.707267
MS363	41256	3.1	1	+53.11805	+8.699633
MS364	52059	4.1	2	+53.120610	+8.683405
MS365	62183	5.1	5	+53.126717	+8.649111
Sampling campaign 15 – 02.09.15					
MS366	62184	WWTP	0	+53.1151779	+8.7146639
MS367	52063	WWTP	0	+53.1151779	+8.7146639
MS368	31535	1.1	0	+53.1166656	+8.7155936
MS369	62185	2.1	0.5	+53.117833	+8.707267
MS370	41259	3.1	1	+53.11805	+8.699633
MS371	52064	4.1	2	+53.120610	+8.683405
MS372	31536	5.1	5	+53.126717	+8.649111
Sampling campaign 16 – 05.10.15					
MS373	52076	WWTP	0	+53.1151779	+8.7146639
MS374	62198	WWTP	0	+53.1151779	+8.7146639
MS375	52078	1.1	0	+53.1166656	+8.7155936
MS376	41273	1.1	0	+53.1166656	+8.7155936
MS377	31559	1.1	0	+53.1166656	+8.7155936
MS378	62200	2.1	0.5	+53.117833	+8.707267
MS379	31560	3.1	1	+53.11805	+8.699633
MS380	41274	4.1	2	+53.120610	+8.683405
MS382	52079	5.1	5	+53.126717	+8.649111

Sampling campaign 17 – 14.10.15					
MS383	31563	WWTP	0	+53.1151779	+8.7146639
MS384	52083	WWTP	0	+53.1151779	+8.7146639
MS385	52084	7.1	-1	+53.111772	+8.727923
MS386	31564	7.1	-1	+53.111772	+8.727923
MS387	41279	7.2	-1	+53.112612	+8.729378
MS388	62208	7.3	-1	+53.113223	+8.730955
MS389	62209	7.4	-1	+53.114124	+8.732288
MS390	31565	7.5	-1	+53.115705	+8.733776

Appendix 3- Water measurement results

Measurements for the 1st and 2nd sampling campaigns

#	spectrum	Sampling location	Down-stream distance from the WWTP [km]	Sample mass (kg)	Mass of preci-pitate (g)	Efficiency for ^{131}I (364.5 keV)	Measuring time (s)	Conductivity (µS/cm)	Salinity (ppt)	Ph	Measured ^{131}I activity concentration [mBq/kg]	Calculated ^{131}I activity concentration [mBq/kg] (chemical yield used)
Sampling campaign 1- 23.09.14												
MS269	51799	WWTP	0	4.11	-	0.01329	140893	n.a.	n.a.	n.a.	67.16 ± 11.65	-
MS270	41051	1.1	0	49.68	216.0	0.02791	320675	1753	0.7	7.86	< 0.98	< 1.14
MS271	51800	1.2	0	48.42	220.2	0.02971	320282	1756	0.7	7.99	< 0.84	< 0.98
MS272	31220	1.3	0	49.80	163.5	0.04090	237732	1773	0.7	7.95	< 0.61	< 0.71
MS273	61949	1.4	0	48.12	156.0	0.03727	260926	1796	0.7	7.97	< 0.92	< 1.07
MS274	61948	1.5	0	48.86	180.7	0.03826	237048	1921	0.8	7.84	< 0.89	< 1.03
Sampling campaign 2- 06.10.14												
MS275	51806	WWTP	0	4.00	-	0.01329	75663	n.a.	n.a.	n.a.	90.24 ± 17.16	-
MS276	31228	1.1	0	50.56	266.1	0.02960	407496	1539	0.6	7.93	0.97 ± 0.30	1.13 ±0.40
MS277	41057	1.2	0	41.64	221.5	0.02792	167946	1528	0.6	8.01	< 1.55	< 1.80
MS278	61955	1.3	0	50.34	266.9	0.02961	239774	1525	0.6	7.93	< 0.97	< 1.13
MS279	41058	1.4	0	51.80	224.4	0.02643	238988	1509	0.6	7.96	< 1.23	< 1.50
MS280	51810	1.5	0	50.96	274.0	0.02651	239407	1534	0.6	7.92	< 1.20	< 1.40

Measurements during different times on the tidal cycle

The normalized ^{131}I activity is calculated as

$$C = \frac{C_x}{C_{WWTP}} \text{ and its error } \sigma_C = C \cdot \left(\frac{\sigma_{C_x}}{C_x} + \frac{\sigma_{C_{WWTP}}}{C_{WWTP}} \right)$$

where

C_x: the calculated ^{131}I activity concentration (chemical yield used) in mBq/kg

C_{WWTP}: the effluent measured ^{131}I activity concentration in mBq/kg

σ_{Cx}: the error of the calculated ^{131}I activity concentration in mBq/kg

σ_{CWWTP}: the error of the effluent measured ^{131}I activity concentration in mBq/kg

#	spectrum	Sampling location	Down-stream distance from the WWTP [km]	Sample mass (kg)	Mass of preci-pitate (g)	Efficiency for ^{131}I (364.5 keV)	Measuring time (s)	Conductivity (µS/cm)	Salinity (ppt)	Ph	Measured ^{131}I activity concentration [mBq/kg]	Calculated ^{131}I activity concentration [mBq/kg] (chemical yield used)	Normalized ^{131}I Activity (to WWTP concentration)
Sampling campaign 5 - 18.03.15 Mean daily river discharge: 274 m^3/s 0.5-1 h after HW Chemical yield: (86 ± 15) %													
MS292	41151	WWTP	0	4.00	-	0.01293	57137	n.a.	n.a.	n.a.	358.36 ± 18.53	-	1.000 ± 0.103
MS293	62067	0	0	20.36	91.6	0.05093	20049	1228	0.4	8.20	160.99 ± 6.01	187.20 ± 33.39	0.522 ± 0.120
MS296	51947	1.1	0	20.26	101.3	0.04571	20131	1244	0.4	8.21	146.80 ± 5.90	170.70 ± 30.55	0.476 ± 0.110
MS298	41153	3.1	1	49.70	236.6	0.02533	232560	1316	0.5	8.34	1.92 ± 0.23	2.23 ± 0.47	0.006 ± 0.002
Sampling campaign 16 - 05.10.15 Mean daily river discharge: 101 m^3/s Chemical yield: (86 ± 15) %													3-3.5 h after HW
MS373	52076	WWTP	0	4.00	-	0.01329	69555	1205	0.4	8.18	141.41 ± 10.31	-	1.000 ± 0.125
MS375	52078	1.1	0	18.64	119.2	0.03951	91956	1192	0.4	8.24	86.39 ± 3.23	100.45 ± 17.92	0.710 ± 0.179

MS378	62200	2.1	0.5	50.10	1989.1	0.01912	511017	1290	0.4	8.34	0.80 ± 0.18	0.93 ± 0.26	0.007 ± 0.002
MS379	31560	3.1	1	50.76	2081.0	0.01993	314105	1283	0.4	8.31	< 1.08	< 1.26	-
MS380	41274	4.1	2	51.20	2199.6	0.01841	419231	1266	0.4	8.28	< 1.82	< 2.12	-
MS382	52079	5.1	5	51.02	2216.8	0.01859	313143	1247	0.4	8.30	< 1.39	< 1.62	-
Sampling campaign 15 - 02.09.15 Mean daily river discharge: 147 m^3/s Chemical yield: (86 ± 15) %													4-4.5 h after HW
MS366	62184	WWTP	0	4.00	-	0.01189	98137	962	0.2	8.29	102.96 ± 7.78	-	1.000 ± 0.151
MS368	31535	1.1	0	20.32	134.4	0.04545	74452	1040	0.3	8.32	63.72 ± 5.14	74.09 ± 14.24	0.720 ± 0.193
MS369	62185	2.1	0.5	50.14	335.8	0.02544	320363	1231	0.4	8.34	2.74 ± 0.19	3.19 ± 0.60	0.031 ± 0.008
MS370	41259	3.1	1	50.38	356.3	0.01901	3200583	1248	0.4	8.33	1.79 ± 0.27	2.08 ± 0.48	0.020 ± 0.006
MS371	52064	4.1	2	50.70	296.4	0.02418	243983	1216	0.4	8.27	0.62 ± 0.19	0.72 ± 0.25	0.010 ± 0.005
MS372	31536	5.1	5	50.32	310.8	0.02499	243829	1209	0.4	8.27	< 0.88	< 1.02	-

Sampling campaign 4 - 12.03.15 Mean daily river discharge: 293 m^3/s Chemical yield: (86 ± 15) %													4-4.5 h after HW
MS287	62061	WWTP	0	4.00	-	0.01188	63548	n.a.	n.a.	n.a.	427.55 ± 25.27	-	1.000 ± 0.118
MS288	51940	1.1	0	19.92	136.5	0.03707	10315	1203	0.4	8.3	177.95 ± 7.71	206.92± 37.19	0.484 ± 0.116
MS289	51941	2.1	0.5	48.72	253.3	0.02738	190203	1200	0.4	8.24	16.36 ± 0.72	19.02 ± 3.42	0.044 ± 0.011
Sampling campaign 3 - 12.11.14 Mean daily river discharge: 182 m^3/s Chemical yield: (86 ± 15) %													5-5.5 h after HW
MS281	41079	WWTP	0	4.00	-	0.01293	72742	n.a.	n.a	n.a.	326.94 ± 24.48	-	1.000 ± 0.150
MS282	41080	1.1	0	48.66	238.9	0.02580	65817	1380	0.5	8.25	72.47 ± 2.56	84.27 ± 15.00	0.258 ± 0.065
MS283	31255	2.1	0.5	47.84	276.5	0.03819	65829	1460	0.5	8.27	2.35 ± 0.34	2.73 ± 0.62	0.008 ± 0.003
MS284	41082	3.1	1	47.74	164.1	0.03209	320489	1456	0.5	7.96	< 1.15	< 1.34	-

Measurements for each river section on -1,-0.5,0,0.5,1,2 and 5 km distance from the WWTP, 3-4 hours after HW (downstream sampling) and LW (upstream sampling). Bottom water samples are indicated by the symbol b. followed by the depth of the water column in m.

#	spectrum	Sampling location	Down-stream distance from the WWTP [km]	Sample mass (kg)	Mass of preci-pitate (g)	Efficiency for ^{131}I (364.5 keV)	Measuring time (s)	Conductivity (µS/cm)	Salinity	Ph	Measured ^{131}I activity concentration [mBq/kg]	Calculated ^{131}I activity concentration [mBq/kg] (chemical yield used)	Normalized ^{131}I Activity (to WWTP concentration)
Sampling campaign 8 - 04.05.15 Mean daily river discharge: 233 m^3/s Chemical yield: (86 ± 15) %													
MS315	41177	WWTP	0	4.00	-	0.01292	81892	n.a.	n.a.	n.a.	182.54 ± 11.26	-	-
MS316	31413	6.1	- 0.5	49.24	181.8	0.03878	170975	1234	0.4	8.42	1.26 ± 0.17	1.47 ± 0.32	8.05E-03 ± 2.25E-03
MS317	62098	6.1 b.4	- 0.5	47.82	185.7	0.03614	170976	1240	0.4	8.42	1.04 ± 0.16	1.21 ± 0.28	6.63E-03 ± 1.94E-03
MS318	41179	6.2	- 0.5	51.76	186.4	0.03136	419296	1239	0.4	8.42	1.00 ± 0.14	1.16 ± 0.26	6.35E-03 ± 1.82E-03
MS319	31414	6.3	- 0.5	50.48	161.1	0.04091	237619	1217	0.4	8.42	1.12 ± 0.15	1.30 ± 0.29	7.12E-03 ± 2.03E-03
MS320	62099	6.4	- 0.5	49.42	166.0	0.04128	319855	1218	0.4	8.41	< 0.67	< 0.78	-
MS321	51979	6.5	- 0.5	49.88	175.6	0.03379	409163	1226	0.4	8.46	0.74 ± 0.12	0.86 ± 0.20	4.71E-03 ± 1.39E-03
Sampling campaign 9 - 26.05.15 Mean daily river discharge: 152 m^3/s Chemical yield: (86 ± 15) %													
MS322	51994	WWTP	0	4.01	-	0.01329	66115	n.a.	n.a.	n.a.	307.13 ± 15.76	-	-
MS323	31431	5.1	5	49.49	207.8	0.02999	85134	1471	0.5	8.36	1.69 ± 0.27	1.97 ± 0.46	6.41E-03 ± 1.83E-03
MS324	62114	5.1 b.5	5	47.04	220.1	0.03200	85118	1479	0.5	8.33	2.24 ± 0.27	2.60 ± 0.55	8.47E-03 ± 2.23E-03
MS325	41196	5.2	5	50.22	206.5	0.02976	339632	1440	0.5	8.38	0.99 ± 0.16	1.15 ± 0.27	3.74E-03 ± 1.07E-03
MS326	51996	5.3	5	47.44	212.0	0.02952	340133	1455	0.5	8.36	1.61 ± 0.16	1.87 ± 0.38	6.09E-03 ± 1.55E-03

MS327	31432	5.4	5	50.36	216.4	0.03218	324678	1443	0.5	8.33	1.24 ± 0.16	1.44 ± 0.31	4.69E-03 ± 1.25E-03
MS328	62115	5.5	5	47.14	198.1	0.03260	325232	1453	0.5	8.34	0.65 ± 0.15	0.76 ± 0.22	2.47E-03 ± 8.43E-04
Sampling campaign 10 - 09.06.15 Mean daily river discharge: 126 m^3/s Chemical yield: (86 ± 15) %													
MS329	52001	WWTP	0	4.02	-	0.01329	64382	n.a.	n.a.	n.a.	172.93 ± 11.49	-	-
MS330	52003	4.1	2	49.56	212.2	0.02952	342867	1412	0.5	8.46	1.34 ± 0.15	1.56 ± 0.32	9.02E-03 ± 2.45E-03
MS331	62121	4.1 b.3	2	48.22	208.9	0.03203	186058	1454	0.5	8.47	1.18± 0.18	1.37 ± 0.32	7.92E-03 ± 2.38E-03
MS332	31438	4.2	2	50.52	209.9	0.03365	177682	1397	0.5	8.49	1.24 ± 0.17	1.44 ± 0.32	8.33E-03 ± 2.40E-03
MS333	41201	4.3	2	50.60	191.6	0.02953	340424	1397	0.5	8.45	0.79 ± 0.16	0.91 ± 0.24	5.26E-03 ± 1.74E-03
MS334	62122	4.4	2	49.14	263.6	0.03116	238845	1380	0.5	8.41	< 1.09	< 1.27	-
MS335	31440	4.5	2	49.96	263.1	0.02960	220852	1374	0.5	8.42	1.03 ± 0.18	1.20 ± 0.30	6.94E-03 ± 2.20E-03
Sampling campaign 11 - 23.06.15 Mean daily river discharge: 134 m^3/s Chemical yield: (86 ± 15) %													
MS336	52012	WWTP	0	4.00	-	0.01329	89880	n.a.	n.a.	n.a.	211.86 ± 18.35	-	-
MS337	31457	3.1	1	50.32	448.0	0.01955	93025	1412	0.5	8.38	2.63 ± 0.39	3.06 ± 0.70	1.44E-02 ± 4.560E-03
MS338	41210	3.1 b.4	1	50.40	302.5	0.01725	503165	1400	0.5	8.37	2.61 ± 0.23	3.03 ± 0.59	1.43E-02 ± 4.02E-03
MS339	31458	3.2	1	50.64	304.0	0.02704	76219	1379	0.5	8.31	1.49 ± 0.27	1.73 ± 0.44	8.17E-03 ± 2.78E-03
MS340	52013	3.3	1	49.90	423.5	0.02320	409651	1401	0.5	8.40	< 1.34	< 1.56	-
MS341	62131	3.4	1	51.60	318.9	0.02876	409092	1396	0.5	8.38	< 0.71	< 0.83	-
MS342	31459	3.5	1	49.24	293.9	0.02636	333971	1391	0.5	8.43	0.66± 0.29	0.77 ± 0.36	3.63E-03 ± 2.01E-03
Sampling campaign 12 - 07.07.15 Mean daily river discharge: 131 m^3/s Chemical yield: (86 ± 15) %													
MS343	62137	WWTP	0	4.00	-	0.01188	64827	n.a.	n.a.	n.a.	216.54 ± 20.72	-	-

MS345	62138	2.1	0.5	50.60	297.7	0.02593	166161	1488	0.5	8.46	2.12 ± 0.22	2.47 ± 0.50	1.14E-02 ± 3.40E-03
MS346	31475	2.1 b.4	0.5	52.06	300.8	0.02543	166420	1463	0.5	8.47	1.48 ± 0.22	1.72 ± 0.39	7.94E-03 ± 2.56E-03
MS347	31476	2.2	0.5	50.38	296.5	0.02544	239167	1431	0.5	8.40	0.78 ± 0.17	0.91 ± 0.25	4.20E-03 ± 1.56E-03
MS348	62139	2.3	0.5	50.18	290.4	0.02686	239592	1456	0.5	8.41	< 1.00	< 1.16	-
MS349	52054	2.4	0.5	50.54	283.4	0.07981	319523	1454	0.5	8.41	< 0.94	< 1.09	-
MS350	41220	2.5	0.5	46.58	310.1	0.02108	319665	1453	0.5	8.42	< 1.36	< 1.58	-
Sampling campaign 13 - 20.07.15 Mean daily river discharge: 146 m^3/s Chemical yield: (86 ± 15) %													
MS351	41225	WWTP	0	4.00	-	0.01293	83755	n.a.	n.a.	n.a.	92.56 ± 9.49	-	-
MS353	62148	1.1	0	21.36	112.5	0.04416	77247	1066	0.3	8.27	21.61 ± 1.24	25.13 ± 4.61	2.71E-01 ± 7.76E-02
MS354	41227	1.1 b.2.5	0	50.90	272.0	0.02495	84561	957	0.2	8.19	21.43 ± 9.27	24.92 ± 4.48	2.69E-01 ± 7.60E-02
MS355	31489	1.2	0	45.98	215.1	0.03218	83480	1312	0.4	8.32	1.29 ± 0.19	1.50 ± 0.34	1.62E-02 ± 5.33E-03
MS356	41229	1.3	0	48.96	265.8	0.02426	246656	1336	0.5	8.28	< 1.73	< 2.01	-
MS357	62150	1.4	0	49.24	265.1	0.02732	248102	1339	0.5	8.34	< 1.07	<1.24	-
MS358	52034	1.5	0	47.84	277.8	0.02460	241153	1335	0.5	8.29	< 1.38	< 1.60	-
Sampling campaign 17 - 14.10.15 Mean daily river discharge: 126 Chemical yield: (86 ± 15) %													
MS383	31563	WWTP	0	3.62	-	0.01485	77063	1229	0.4	8.10	209.83 ± 23.21	-	-
MS385	52084	7.1	- 1	49.32	2204.4	0.01886	336226	1384	0.5	8.30	< 1.28	< 1.49	-
MS386	31564	7.1 b.4	- 1	50.82	2306.7	0.01930	187254	1382	0.5	8.30	< 1.20	< 1.40	-
MS387	41279	7.2	- 1	50.46	2112.7	0.01839	328237	1387	0.5	8.29	2.55 ± 0.31	2.97 ± 0.63	1.42E-02 ± 4.57E-03
MS388	62208	7.3	- 1	50.36	2040.2	0.01910	183192	1395	0.5	8.29	1.46 ± 0.27	1.70 ± 0.43	8.10E-03 ± 2.95E-03
MS389	62209	7.4	- 1	49.98	2301.0	0.01850	226961	1391	0.5	8.25	1.30 ± 0.30	1.51 ± 0.44	7.20E-03 ± 2.89E-03
MS390	31565	7.5	- 1	47.66	2240.0	0.01930	235630	1408	0.5	8.29	< 1.41	< 1.64	-

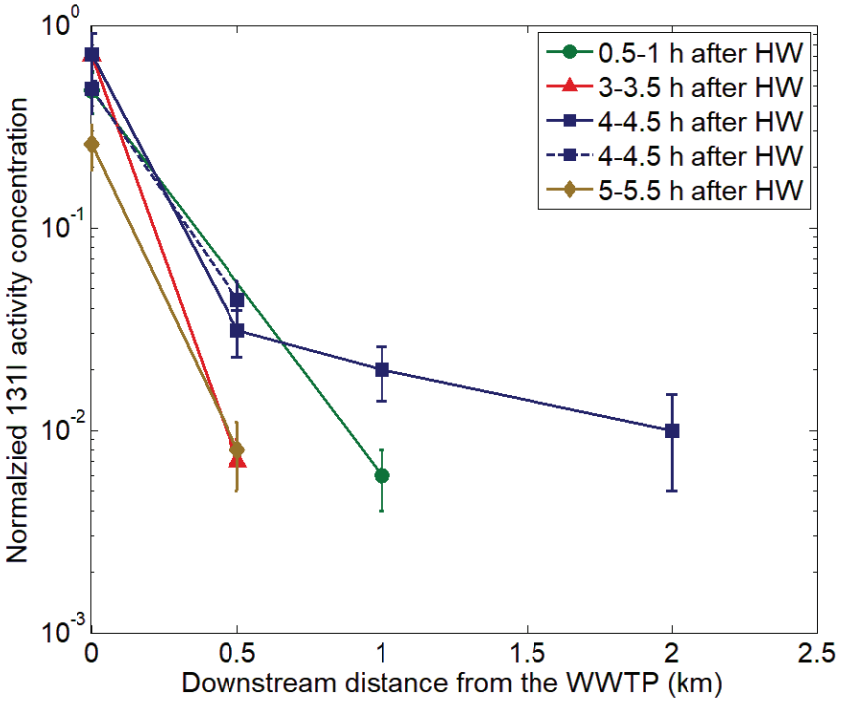

Figure A1: Normalized ^{131}I concentration over downstream distance close to the left bank (corresponding locations illustrated in figure 6.14) during different times in the tidal cycle. Values below detection limit not included.

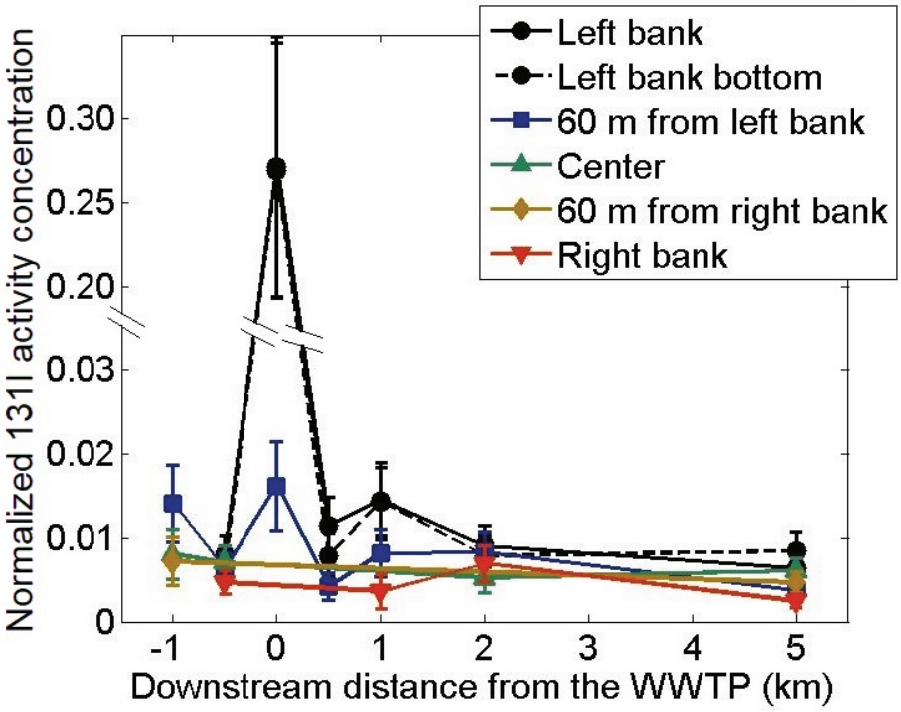

Figure A2: Normalized ^{131}I activity of surface samples, 3 to 4 hours after high and low water, on 5 equidistance points across the river in locations -1, -0.5, 0, 0.5, 1, 2 and 5 km distance from the WWTP. Negative values indicate upstream locations. On the left bank additionally bottom samples were analyzed. Values below detection limit not included.

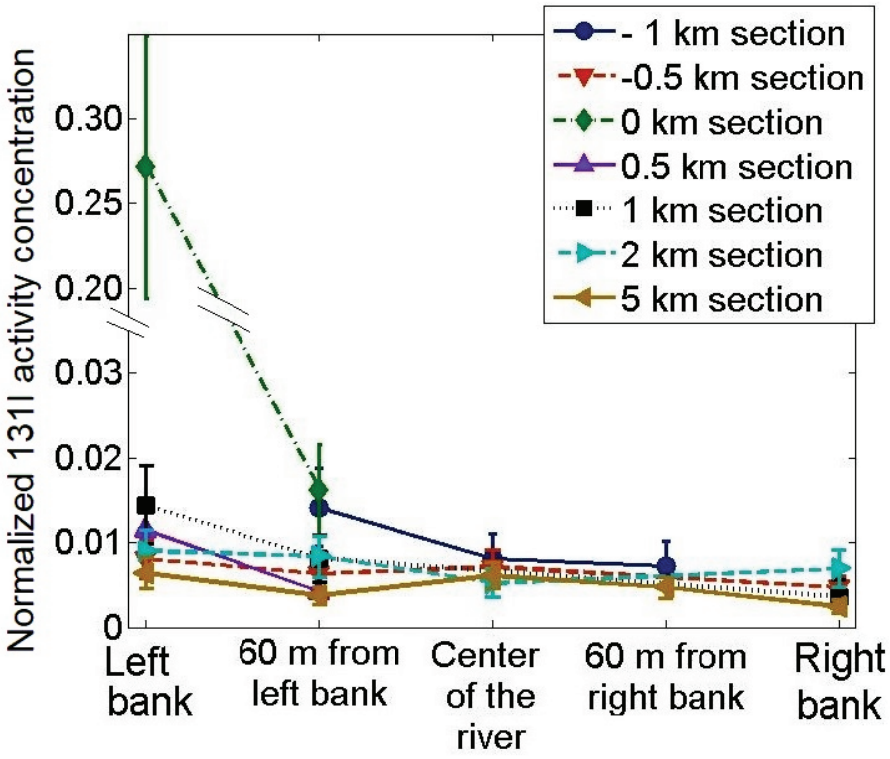

Figure A3: Normalized ^{131}I activity of surface samples, 3 to 4 hours after high and low water, on 5 equidistance points across the river in sections -1, -0.5, 0, 0.5, 1, 2 and 5 km distance from the WWTP. Values below detection limit not included.

Appendix 4- ^{131}I in WWTP effluent

Table A1: ^{131}I activity concentration in the WWTP effluent before and after river water sampling

#	spectrum	Time before/after sampling campaign	Date/time of sampling	Mass of sample (kg)	Measuring time (s)	Measured ^{131}I activity concentration (mBq/kg)
MS269	51799	Before	23.9.14/12:00	4.11	140893	67.16 ± 11.62
MS275	51806	Before	06.10.14/14:30	4.00	75663	90.24 ± 17.16
MS281	41079	Before	12.11.14/10:00	4.00	72742	326.94 ± 24.48
MS287	62061	Before	12.03.15/09:30	4.00	63548	427.55 ± 25.27
MS292	41151	Before	18.03.15/12:30	4.00	57137	371.77 ± 27.91
MS315	41177	Before	04.05.15/13:00	4.00	81892	187.25 ± 19.88
MS322	51994	Before	26.05.15/10:50	4.01	66115	315.39 ± 21.68
MS329	52001	Before	09.06.15/10:30	4.02	64382	185.70 ± 22.02
MS336	52012	Before	23.06.15/10:40	4.00	89880	211.86 ± 18.35
MS343	62137	Before	07.07.15/10:10	4.00	64827	216.54 ± 20.72
MS344	41217	After	07.07.15/13:00	4.00	59375	240.86 ± 27.01
MS351	41225	Before	20.7.15/09:15	4.00	83755	92.46 ± 17.70
MS352	62147	After	20.7.15/12:20	4.00	77247	72.55 ± 15.92
MS359	52058	Before	25.8.15/11:20	4.00	60368	203.09 ± 19.02
MS360	62181	After	25.8.15/14:20	4.01	60721	266.76 ± 21.59
MS366	62184	Before	2.9.15/09:20	4.00	98137	111.98 ± 15.30
MS367	52063	After	2.9.15/11:40	4.00	105406	81.75 ± 19.45
MS373	52076	Before	5.10.15/09:50	4.01	69555	139.46 ± 19.04
MS374	62198	After	5.10.15/13:15	4.00	69874	130.69 ± 17.36
MS383	31563	Before	14.10.15/13:50	3.62	77063	209.83 ± 23.21
MS384	52083	After	14.10.15/17:10	4.01	92792	212.73 ± 20.68

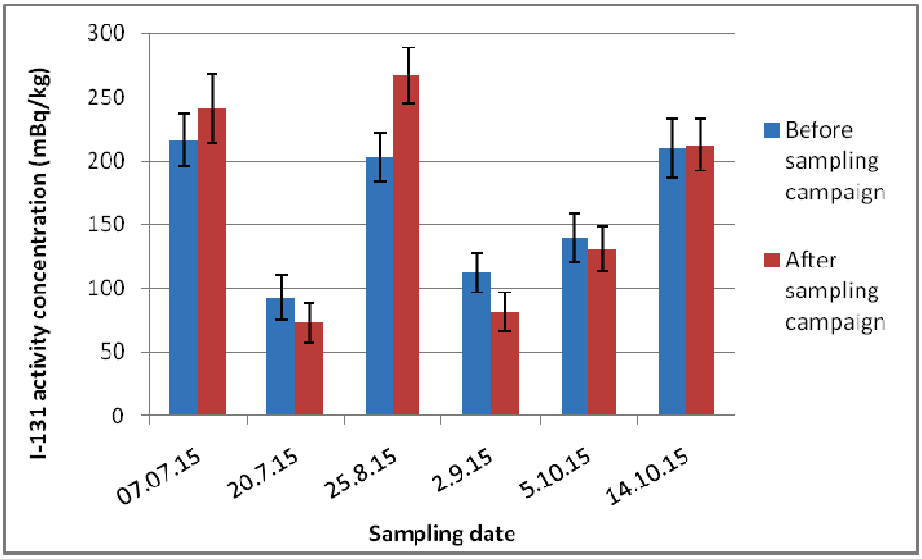

Figure A3: Graphical representation of the ^{131}I activity concentration of WWTP effluent before and after each sampling campaign.

Appendix 5 – River discharge

Mean daily discharge at station Intschede (river km 331.28). Data are available from Weserdatenbank (fgg-weser.de), in the table results are given for the sampling dates of our river water sampling campaigns.

Date	Mean daily discharge (m^3/s)
12.11.14	182
12.03.15	293
18.03.15	274
04.05.15	233
26.05.15	152
09.06.15	126
23.06.15	134
07.07.15	131
20.07.15	146
02.09.15	147
05.10.15	101
14.10.15	126

Appendix 6- Sediment measurement results

#	spectrum	Sampling location (depth- m)	Distance from WWTP (km)	Sample mass Wet /dry (g)	Measuring time (s)	Efficiency for ^{131}I (365.4 keV)	^{131}I Bq/kg (d.m.)	Efficiency for ^{7}Be (477.6 keV)	^{7}Be Bq/kg (d.m.)	Efficiency for ^{40}K (1460.8 keV)	^{40}K Bq/kg (d.m.)	Efficiency for ^{137}Cs (661.7 keV)	^{137}Cs Bq/kg (d.m.)
Sampling campaign 4 - 12.03.15													
MS291	62062	1.1 (4)	0	532.5 /69.6	254795	0.02574	6.45± 0.62	0.02167	18.69 ± 0.80	0.01040	386.48 ± 15.44	0.01751	5.13 ± 0.16
Sampling campaign 5- 18.03.15													
MS295	51946	0 (4)	0	1400.9 /564.2	91602	0.03179	0.47 ± 0.03	0.02697	40.88 ± 4.05	0.01335	317.67 ± 14.15	0.02214	5.93 ± 0.49
MS300	41152	3.1 (3.5)	1	517.2 /209.6	111531	0.02923	< 0.40	0.02414	46.32 ± 2.42	0.01132	527.89 ± 21.47	0.01942	12.44 ± 0.35
Sampling campaign 6- 26.03.15													
MS310	41156	Left bank	1 km up	639.0 /233.2	236320	0.03366	1.64 ± 0.08	0.02813	44.02 ± 1.82	0.01313	426.32 ± 17.17	0.02265	9.30 ± 0.25
MS309	41155	Left bank	0.5 km up	583.2 /153.9	62270	0.03430	9.64 ± 0.53	0.02862	85.86 ± 4.46	0.01326	537.7 ± 22.51	0.02299	12.50 ± 0.56
MS303	62073	Left bank	0 km up	607.5 /192.9	19101	0.03257	19.39 ± 1.01	0.02770	66.64 ± 4.95	0.01383	514.19 ± 22.95	0.02271	11.39 ± 0.66
MS304	51954	Left bank	0 km down	568.3 /175.3	19365	0.03179	35.75 ± 1.44	0.02697	68.48 ± 5.52	0.01335	503.92 ± 22.85	0.02214	10.66 ± 0.52
MS305	51953	Left bank	0.5 km down	572.5 /185.1	61758	0.03179	11.64 ± 0.53	0.02697	74.96 ± 3.88	0.01335	514.56 ± 21.31	0.02215	10.62 ± 0.48
MS306	62072	Left bank	1 km down	607.1 /253.0	61835	0.03257	4.39 ± 0.25	0.02770	51.18 ± 2.23	0.01383	346.54 ± 14.38	0.02271	7.31 ± 0.32
MS307	62074	Left bank	2 km down	511.8 /167.3	92266	0.03319	5.59 ± 0.34	0.02817	88.09 ± 3.30	0.01397	531.96 ± 21.77	0.02305	10.92 ± 0.41
MS308	51955	Left bank	5 km down	602.7 /197.6	89780	0.03148	2.89 ± 0.27	0.02674	61.93 ± 3.20	0.01328	451.84 ± 19.32	0.02199	7.84 ± 0.26

Sampling campaign 7- 08.04.15													
MS313	62081	Right bank	2 km up	567.3 /186.9	152201	0.03320	0.85 ± 0.08	0.02818	76.61 ± 2.68	0.01397	521.78 ± 21.08	0.02305	9.78 ± 0.32
MS311	51963	Right bank	0 km	630.0 /230.0	152045	0.03120	1.00 ± 0.08	0.02652	65.05 ± 1.95	0.01321	490.06 ± 19.77	0.02182	8.75 ± 0.25
MS312	41160	Right bank	5 km down	517.2 /209.6	78349	0.03463	2.44 ± 0.26	0.02886	150.54 ± 4.84	0.01336	495.97 ± 20.41	0.02316	11.48 ± 0.46

*Measuring container 0.5 L Marinelli (exception sample MS295 with 1 L Marinelli).

Appendix 7- Suspended matter results

#	spectrum	Sample mass (kg)	Measuring time (s)	Efficiency for ^{131}I (364.5 keV)	WWTP ^{131}I effluent activity(mBq/kg)	Total ^{131}I activity in suspended matter (mBq)	Radioactive analysis (%)
MS256	51699	4.00	56399	0.01329	148.67 ± 23.57		
MS266	51702	19.24	171940	0.09517		71.99 ± 10.81	2.51
MS258	61852	4.00	69779	0.01188	197.06 ± 21.27		
MS267	31132	17.94	252803	0.01285		38.64 ± 6.26	1.10
MS254	31128	4.00	56674	0.01323	197.92 ± 19.38		
MS268	61856	18.92	243498	0.01170		46.98 ± 8.78	1.25
MS269	61862	4.00	62319	0.08375	314.92 ± 24.79		
MS274	31139	48.16	103317	0.09410		128.12 ± 16.07	0.84
MS271	51708	4.00	62055	0.01329	272.36 ± 23.56		
MS273	61869	48.52	103085	0.08375		158.10 ± 19.24	1.20
MS270	40963	4.01	61820	0.01293	305.53 ± 27.70		
MS272	51714	47.44	103115	0.07762		118.77 ± 18.07	0.82

#	spectrum	Sample mass (kg)	Measuring time (s)	Efficiency for ^{131}I (364.5 keV)	River water^{131}I effluent activity(mBq/kg)	Total ^{131}I activity in suspended matter (mBq)	Radioactive analysis (%)
MS277	61887	4.02	154286	0.01188	62.72 ± 14.24	< 19.93	-
MS279	61889			0.08565			
MS276	51730	4.04	81826	0.01329	136.27 ± 19.20	< 15.45	-
MS278	61888		264208	0.08567			
MS275	40987	4.06	153305	0.01293	< 28.08	-	-
MS285	51831	4.05	73716	0.01329	175.10 ± 19.88		
MS286	61980	51.20	82261	0.04311		20.16 ± 0.79	11.51

Appendix 8 – Water level data

Date	Time	Water level (m)
10-Jan-16	0:01:00	6.04
10-Jan-16	0:02:00	6.05
10-Jan-16	0:03:00	6.05
10-Jan-16	0:04:00	6.08
10-Jan-16	0:05:00	6.1
10-Jan-16	0:06:00	6.1
10-Jan-16	0:07:00	6.12
10-Jan-16	0:08:00	6.14
10-Jan-16	0:09:00	6.16
10-Jan-16	0:10:00	6.14
10-Jan-16	0:11:00	6.18
10-Jan-16	0:12:00	6.2
10-Jan-16	0:13:00	6.18
10-Jan-16	0:14:00	6.24
10-Jan-16	0:15:00	6.22
10-Jan-16	0:16:00	6.24
10-Jan-16	0:17:00	6.26
10-Jan-16	0:18:00	6.28
10-Jan-16	0:19:00	6.3
10-Jan-16	0:20:00	6.3
10-Jan-16	0:21:00	6.33
10-Jan-16	0:22:00	6.34
10-Jan-16	0:23:00	6.36
10-Jan-16	0:24:00	6.37
10-Jan-16	0:25:00	6.38
10-Jan-16	0:26:00	6.4
10-Jan-16	0:27:00	6.42
10-Jan-16	0:28:00	6.42
10-Jan-16	0:29:00	6.44
10-Jan-16	0:30:00	6.46
10-Jan-16	0:31:00	6.46
10-Jan-16	0:32:00	6.5
10-Jan-16	0:33:00	6.5
10-Jan-16	0:34:00	6.5
10-Jan-16	0:35:00	6.52
10-Jan-16	0:36:00	6.53
10-Jan-16	0:37:00	6.53
10-Jan-16	0:38:00	6.56
10-Jan-16	0:39:00	6.56
10-Jan-16	0:40:00	6.56
10-Jan-16	0:41:00	6.57
10-Jan-16	0:42:00	6.6
10-Jan-16	0:43:00	6.61
10-Jan-16	0:44:00	6.61
10-Jan-16	0:45:00	6.63
10-Jan-16	0:46:00	6.63
10-Jan-16	0:47:00	6.64
10-Jan-16	0:48:00	6.66
10-Jan-16	0:49:00	6.66
10-Jan-16	0:50:00	6.68
10-Jan-16	0:51:00	6.68
10-Jan-16	0:52:00	6.69
10-Jan-16	0:53:00	6.7
10-Jan-16	0:54:00	6.72
10-Jan-16	0:55:00	6.74
10-Jan-16	0:56:00	6.74
10-Jan-16	0:57:00	6.76
10-Jan-16	0:58:00	6.76
10-Jan-16	0:59:00	6.77
10-Jan-16	1:00:00	6.78
10-Jan-16	1:01:00	6.79
10-Jan-16	1:02:00	6.8
10-Jan-16	1:03:00	6.8
10-Jan-16	1:04:00	6.82
10-Jan-16	1:05:00	6.84
10-Jan-16	1:06:00	6.86
10-Jan-16	1:07:00	6.86
10-Jan-16	1:08:00	6.87
10-Jan-16	1:09:00	6.88
10-Jan-16	1:10:00	6.88
10-Jan-16	1:11:00	6.89
10-Jan-16	1:12:00	6.91
10-Jan-16	1:13:00	6.92
10-Jan-16	1:14:00	6.93
10-Jan-16	1:15:00	6.94
10-Jan-16	1:16:00	6.94
10-Jan-16	1:17:00	6.96
10-Jan-16	1:18:00	6.96
10-Jan-16	1:19:00	6.98
10-Jan-16	1:20:00	7
10-Jan-16	1:21:00	7
10-Jan-16	1:22:00	7.01
10-Jan-16	1:23:00	7.02
10-Jan-16	1:24:00	7.02
10-Jan-16	1:25:00	7.04
10-Jan-16	1:26:00	7.06
10-Jan-16	1:27:00	7.06
10-Jan-16	1:28:00	7.06
10-Jan-16	1:29:00	7.08
10-Jan-16	1:30:00	7.09
10-Jan-16	1:31:00	7.1
10-Jan-16	1:32:00	7.11
10-Jan-16	1:33:00	7.12
10-Jan-16	1:34:00	7.12
10-Jan-16	1:35:00	7.13
10-Jan-16	1:36:00	7.14
10-Jan-16	1:37:00	7.16
10-Jan-16	1:38:00	7.16
10-Jan-16	1:39:00	7.16
10-Jan-16	1:40:00	7.16
10-Jan-16	1:41:00	7.19
10-Jan-16	1:42:00	7.2
10-Jan-16	1:43:00	7.2
10-Jan-16	1:44:00	7.2
10-Jan-16	1:45:00	7.21
10-Jan-16	1:46:00	7.22
10-Jan-16	1:47:00	7.22
10-Jan-16	1:48:00	7.22
10-Jan-16	1:49:00	7.22
10-Jan-16	1:50:00	7.24
10-Jan-16	1:51:00	7.24
10-Jan-16	1:52:00	7.26
10-Jan-16	1:53:00	7.27
10-Jan-16	1:54:00	7.28
10-Jan-16	1:55:00	7.28
10-Jan-16	1:56:00	7.29
10-Jan-16	1:57:00	7.29
10-Jan-16	1:58:00	7.3
10-Jan-16	1:59:00	7.31
10-Jan-16	2:00:00	7.31

10-Jan-16	2:01:00	7.32
10-Jan-16	2:02:00	7.32
10-Jan-16	2:03:00	7.33
10-Jan-16	2:04:00	7.34
10-Jan-16	2:05:00	7.34
10-Jan-16	2:06:00	7.35
10-Jan-16	2:07:00	7.36
10-Jan-16	2:08:00	7.36
10-Jan-16	2:09:00	7.36
10-Jan-16	2:10:00	7.37
10-Jan-16	2:11:00	7.37
10-Jan-16	2:12:00	7.37
10-Jan-16	2:13:00	7.38
10-Jan-16	2:14:00	7.38
10-Jan-16	2:15:00	7.39
10-Jan-16	2:16:00	7.39
10-Jan-16	2:17:00	7.4
10-Jan-16	2:18:00	7.4
10-Jan-16	2:19:00	7.4
10-Jan-16	2:20:00	7.41
10-Jan-16	2:21:00	7.41
10-Jan-16	2:22:00	7.42
10-Jan-16	2:23:00	7.42
10-Jan-16	2:24:00	7.42
10-Jan-16	2:25:00	7.43
10-Jan-16	2:26:00	7.42
10-Jan-16	2:27:00	7.43
10-Jan-16	2:28:00	7.43
10-Jan-16	2:29:00	7.44
10-Jan-16	2:30:00	7.44
10-Jan-16	2:31:00	7.44
10-Jan-16	2:32:00	7.44
10-Jan-16	2:33:00	7.44
10-Jan-16	2:34:00	7.44
10-Jan-16	2:35:00	7.44
10-Jan-16	2:36:00	7.44
10-Jan-16	2:37:00	7.44
10-Jan-16	2:38:00	7.44
10-Jan-16	2:39:00	7.44
10-Jan-16	2:40:00	7.44
10-Jan-16	2:41:00	7.44
10-Jan-16	2:42:00	7.44
10-Jan-16	2:43:00	7.44
10-Jan-16	2:44:00	7.44
10-Jan-16	2:45:00	7.44
10-Jan-16	2:46:00	7.42
10-Jan-16	2:47:00	7.42
10-Jan-16	2:48:00	7.42
10-Jan-16	2:49:00	7.42
10-Jan-16	2:50:00	7.42
10-Jan-16	2:51:00	7.41
10-Jan-16	2:52:00	7.4
10-Jan-16	2:53:00	7.4
10-Jan-16	2:54:00	7.4
10-Jan-16	2:55:00	7.39
10-Jan-16	2:56:00	7.39
10-Jan-16	2:57:00	7.38
10-Jan-16	2:58:00	7.38
10-Jan-16	2:59:00	7.37
10-Jan-16	3:00:00	7.37
10-Jan-16	3:01:00	7.36
10-Jan-16	3:02:00	7.36
10-Jan-16	3:03:00	7.34
10-Jan-16	3:04:00	7.34
10-Jan-16	3:05:00	7.33
10-Jan-16	3:06:00	7.32
10-Jan-16	3:07:00	7.32
10-Jan-16	3:08:00	7.31
10-Jan-16	3:09:00	7.3
10-Jan-16	3:10:00	7.29
10-Jan-16	3:11:00	7.28
10-Jan-16	3:12:00	7.27
10-Jan-16	3:13:00	7.26
10-Jan-16	3:14:00	7.26
10-Jan-16	3:15:00	7.24
10-Jan-16	3:16:00	7.23
10-Jan-16	3:17:00	7.22
10-Jan-16	3:18:00	7.21
10-Jan-16	3:19:00	7.2
10-Jan-16	3:20:00	7.19
10-Jan-16	3:27:00	7.12
10-Jan-16	3:28:00	7.1
10-Jan-16	3:29:00	7.09
10-Jan-16	3:30:00	7.08
10-Jan-16	3:31:00	7.07
10-Jan-16	3:32:00	7.06
10-Jan-16	3:33:00	7.04
10-Jan-16	3:34:00	7.03
10-Jan-16	3:35:00	7.02
10-Jan-16	3:36:00	7
10-Jan-16	3:37:00	7
10-Jan-16	3:38:00	6.98
10-Jan-16	3:39:00	6.96
10-Jan-16	3:40:00	6.96
10-Jan-16	3:41:00	6.94
10-Jan-16	3:42:00	6.93
10-Jan-16	3:43:00	6.92
10-Jan-16	3:44:00	6.9
10-Jan-16	3:45:00	6.89
10-Jan-16	3:46:00	6.88
10-Jan-16	3:47:00	6.86
10-Jan-16	3:48:00	6.84
10-Jan-16	3:49:00	6.84
10-Jan-16	3:50:00	6.82
10-Jan-16	3:51:00	6.81
10-Jan-16	3:52:00	6.8
10-Jan-16	3:53:00	6.78
10-Jan-16	3:54:00	6.76
10-Jan-16	3:55:00	6.76
10-Jan-16	3:56:00	6.74
10-Jan-16	3:57:00	6.73
10-Jan-16	3:58:00	6.72
10-Jan-16	3:59:00	6.7
10-Jan-16	4:00:00	6.68
10-Jan-16	4:01:00	6.68
10-Jan-16	4:02:00	6.66
10-Jan-16	4:03:00	6.65
10-Jan-16	4:04:00	6.64
10-Jan-16	4:05:00	6.62

*Only 2 out of 105 pages with water level data available are provided here.

Appendix 9 – Poiseulle flow

Under the assumption of an incompressible Newtonian fluid in laminar flow, moving through a pipe (or between two parallel plates) of constant cross section, considerable smaller than its length, the Navier- Stokes equations are reduced to the Poiseuille equation which describes the proportionality of the volume flow rate to the pressure drop per unit distance.

In order to calculate the flow profile (both velocity and streamfunction) in the inflow boundary, we consider the pressure equal to P=P(x)=-2avx+b (reducing with increasing distance from the inflow boundary), with v being the fluid viscosity and a, b constants and an one-dimensional flow (u_y=0). In the following calculation x and y are given as normalized lengths.

The continuity equation then becomes:

$$\frac{\partial u_x}{\partial x} = 0\,,\ u_x = u_x(y)$$

and the Navier-Stokes equation takes the form:

$$-\frac{\partial P}{\partial x} + v\frac{\partial^2 u_x}{\partial y^2} = 0\ ,\ \frac{\partial P}{\partial y} = 0$$

By solving for $u_x(y)$ we get

$$u_x(y) = \frac{1}{v}\frac{\partial P}{\partial x}\frac{y^2}{2} + C_1 y + C_2\text{, with } C_1, C_2 \text{ constants}$$

$$u_x(y) = \frac{1}{v}(-2\ v\ a)\frac{y^2}{2} + C_1 y + C_2 \rightarrow u_x(y) = -a\ y^2 + C_1 y + C_2\ ,\ \text{a parabolic flow profile.}$$

By applying the following conditions for the inflow boundary

$u_x(0.25)=0$, $u_x(1)=0$ and $u_x(0.625)=0.75$ we obtain

$$\boxed{u_x(y) = -5.3y^2 + 6.667y - 1.333}\ \text{(A)}$$

Accordingly we define a streamfunction Ψ, such that

$$u_x = \frac{\partial \Psi}{\partial y}\ (1)\ \text{and}\ u_y = \frac{\partial \Psi}{\partial x}\ (2).$$

By definition, since we have a non divergent field:

$$\frac{\partial u_x}{\partial x}+\frac{\partial u_y}{\partial y}=0 \quad (3)$$

Solving for Ψ we get:

$$(1)\rightarrow u_x=\frac{\partial \Psi}{\partial y} \rightarrow \Psi=\int_{y_0}^{y} u_x dy + a(x) \rightarrow \frac{\partial \Psi}{\partial x}=\int_{y_0}^{y}\frac{\partial u_x}{\partial x}dy+\frac{da}{dx}$$

$$\overset{(2)}{(3)}\rightarrow \frac{\partial \Psi}{\partial x}=\int_{y_0}^{y}\left(-\frac{\partial u_y}{\partial y}\right)dy+\frac{da}{dx}\ ^{2}\rightarrow -u_y(x,y)=-u_y(x,y)+u_y(x,y_0)+\frac{da}{dx}$$

So,

$$\Psi=\int_{y_0}^{y} u_x(x,y)dy-\int_{x_0}^{x} u_y(x,y_0)dx$$

By assuming $u_y(x,y_0)=0$ (no lateral component of velocity in the inflow boundary), we get

$\Psi=\int_{y_0}^{y} u_x(x,y)dy$ and by using (A) it yields:

$$\Psi=\int_{1}^{y}\left(-5.3y^2+6.667y-1.333\right)dy$$

$$\rightarrow \boxed{\Psi=-\frac{5.3}{3}y^3+\frac{6.667}{2}y^2-1.333y-0.234}$$

Appendix 10 – Past sediment measurement results

The following tables provides ^{131}I activity concentration values on sediment (table 1) and water (table 2) samples collected during the diploma work of S. Ulbrich at 2008 and the master thesis of M.E. Souti at 2012.

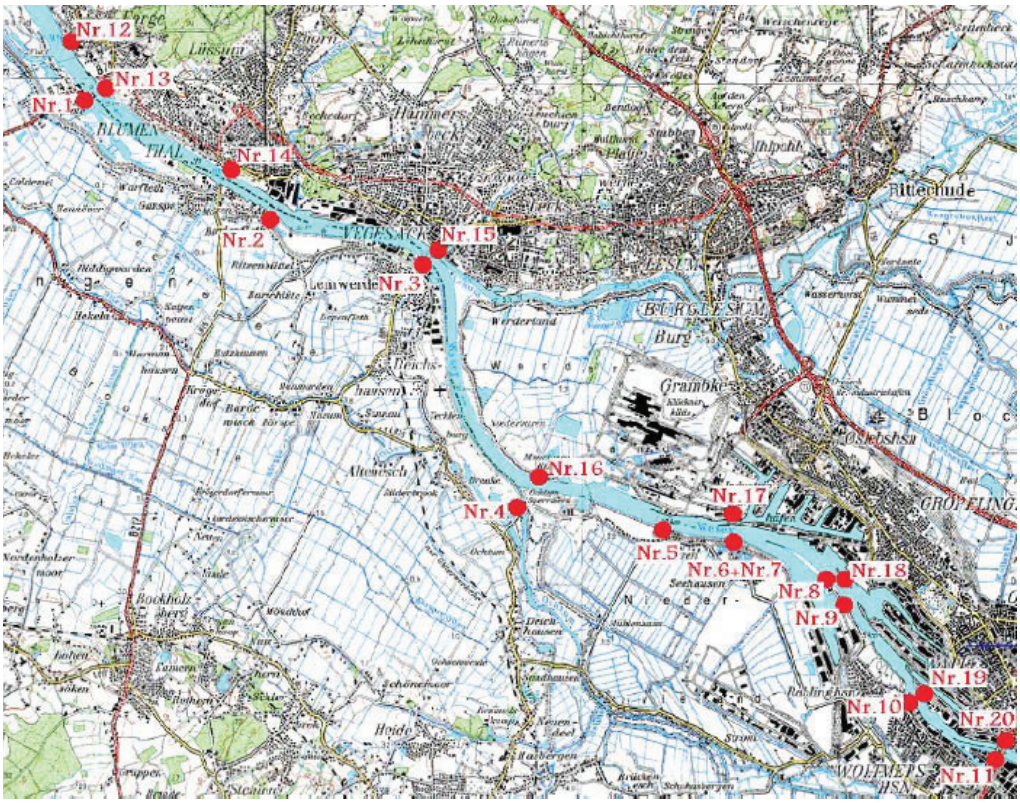

Figure A4: Overview of the sampling locations.

Table A2: ^{131}I activity concentration in sediment during 2008 sampling campaigns

Nr.	Date	Distance from the WWTP (km)	Bank	Geographical Coordinates	Measuring geometry	^{131}I activity concentration (Bq/kg[d.m.])
1	23.04.2008	+17.5	left	N 53°11'44.9'' E 8°30'59''	1 L Marinelli	< 0.09
2	23.04.2008	+12.75	left	N 53°10'25.8'' E 8°34'23.58''	1 L Marinelli	0.65 ± 0.08
3	23.04.2008	+9.75	left	N 53°9'58.34'' E 8°37'7.98''	1 L Marinelli	0.63 ± 0.10
4	23.04.2008	+5	left	N 53°7'21.47'' E 8°38'56.51''	1 L Marinelli	0.46 ± 0.19
5	23.04.2008	+1.75	left	N 53°7'7.74'' E 8°41'28.38''	1 L Marinelli	3.74 ± 0.18
6	23.04.2008	0	left	N 53°6'58.6'' E 8°42'56''	PMMA dish (70×20 mm)	98.71 ± 2.28

Nr.	Date	Distance from the WWTP (km)	Bank	Geographical Coordinates	Measuring geometry	^{131}I activity concentration (Bq/kg[d.m.])
7	04.05.2008	0	left	N 53°6'58.6'' E 8°42'56''	PMMA dish (70×20 mm)	122.30 ± 3.11
8	04.05.2008	-2	left	N 53°6'32'' E 8°44'20''	PMMA dish (70×20 mm)	2.51 ± 0.87
9	04.05.2008	-2.5	left	N 53°6'22'' E 8°44'37''	PMMA dish (70×20 mm)	1.80 ± 0.27
10	04.05.2008	-4.5	left	N 53°5'30'' E 8°45'45''	PMMA dish (70×20 mm)	2.34 ± 0.38
11	04.05.2008	-6.5	right	N 53°4'45'' E 8°47'18''	1 L Marinelli	1.89 ± 0.16
12	04.06.2008	+20	right	N 53°13'03'' E 8°29'55''	1 L Marinelli	0.45 ± 0.05
13	04.06.2008	+17.5	right	N 53°11'52'' E 8°31'8''	1 L Marinelli	0.84 ± 0.11
14	04.06.2008	+14	right	N 53°10'53'' E 8°33'44''	1 L Marinelli	0.75 ± 0.07
15	04.06.2008	+9.75	right	N 53°10'7'' E 8°37'22''	1 L Marinelli	0.73 ± 0.07
16	04.06.2008	+4.5	right	N 53°7'42'' E 8°39'14''	PMMA dish (70×20 mm)	2.73 ± 0.28
17	08.06.2008	+0.5	right	N 53°7'11'' E 8°42'48''	PMMA dish (70×20 mm)	1.75 ± 0.47
18	08.06.2008	-2.25	right	N 53°6'32'' E 8°44'44''	PMMA dish (70×20 mm)	1.50 ± 0.39
19	08.06.2008	-3.75	right	N 53°5'31.3'' E 8°45'54.2''	PMMA dish (70×20 mm)	0
20	08.06.2008	-6.5	right	N 53°4'52.4'' E 8°47'21.4''	PMMA dish (70×20 mm)	1.60 ± 0.26

Figure A5: Water sampling locations at 2012 with corresponding sediment sampling locations from 2008 campaigns (Souti, 2012. Image adapted from Google Maps, 2012).

Table A3: ^{131}I activity concentration in river water during 2012 sampling campaigns. All river water samples were measured in 1 L Marinelli geometry while the WWTP effluent samples were measured in 2 L Marinelli filled to a volume of sample of 4 L.

Nr.	Date	Latitude	Longitude	WWTP effluent activity concentration (mBq/kg)	^{131}I activity concentration (mBq/kg)
11	03.07.2012	53.11641	8.71525	121.1 ± 12.3	9.6 ± 1.4
12	03.07.2012	53.11635	8.71559	121.1 ± 12.3	9.5 ± 1.3
13	05.07.2012	53.116086	8.717206	219.5 ± 18.0	21.9 ± 1.8
14	05.07.2012	53.1145	8.722436	219.5 ± 18.0	< 3.4
15	05.07.2012	53.111506	8.727997	219.5 ± 18.0	< 3.7
16	05.07.2012	53.108719	8.731219	219.5 ± 18.0	< 4.2
17	09.07.2012	53.116572	8.7148	239.0 ± 16.0	50.3 ± 7.6
18	09.07.2012	53.117481	8.707653	239.0 ± 16.0	7.9 ± 2.5
19	09.07.2012	53.117533	8.701722	239.0 ± 16.0	5.7 ± 2.6
20	09.07.2012	53.117567	8.695825	239.0 ± 16.0	<4.1

Appendix 11 – Comparison experimental and simulated data

The square of residuals between experimental (A_{exp}) and simulated (A_{sim}) is calculated as:

$$SR = \left(A_{\exp} - A_{sim}\right)^2.$$

The difference between experimental (A_{exp}) and simulated (A_{sim}), including the experimental error (*err*), is calculated as:

$$D = \frac{\left|\left(A_{\exp} \pm err\right) - A_{sim}\right|}{\left[\left(A_{\exp} \pm err\right) + A_{sim}\right]/2} \cdot 100 \quad (\%)$$

A. Tidal influenced data

Time during the tidal cycle (hours after HW)	Location	Normalized experimental result	Error	Simulation result with ε=0.01 m^2/s	Squares of residuals (ε= 0.01 m^2/s)	Difference D (%)	Simulation result with ε=0.0025m^2/s	Squares of residuals (ε= 0.0025 m^2/s)	Simulation result with ε=0.005m^2/s	Squares of residuals (ε= 0.005 m^2/s)
0.5 – 1	1.1	4.76E-01	1.10E-01	2.94E-01	3.31E-02	22	2.15E-01	6.81E-02	2.61E-01	4.65E-02
0.5 – 1	3.1	6.22E-03	1.63E-03	5.39E-04	3.23E-05	158	7.42E-04	3.00E-05	6.19E-04	3.14E-05
3 – 3.5	1.1	7.10E-01	1.79E-01	2.69E-01	1.95E-01	66	1.74E-01	2.88E-01	2.26E-01	2.34E-01
3 – 3.5	2.1	6.58E-03	2.32E-03	5.20E-03	1.90E-06	20	8.10E-02	5.54E-03	6.50E-03	5.87E-09
3 – 3.5	3.1	<8.91E-03		6.26E-04			7.67E-04		6.97E-04	
3 – 3.5	4.1	<1.50E-02		3.78E-04			5.36E-04		4.43E-04	
3 – 3.5	5.1	<1.15E-02		1.24E-04			2.56E-04		2.07E-04	

4 – 4.5	1.1	7.20E-01	1.93E-01	2.78E-01	1.95E-01	62	1.88E-01	2.82E-01	2.38E-01	2.32E-01
4 – 4.5	2.1	3.10E-02	8.17E-03	4.80E-03	6.86E-04	130	7.60E-03	5.47E-04	6.10E-03	6.19E-04
4 – 4.5	3.1	2.02E-02	6.19E-03	6.01E-04	3.84E-04	184	7.72E-04	3.78E-04	6.78E-04	3.81E-04
4 – 4.5	4.1	9.72E-03	5.24E-03	3.60E-04	8.76E-05	170	5.38E-04	8.43E-05	4.32E-04	8.62E-05
4 – 4.5	5.1	<9.91E-03		9.41E-05			2.51E-04		1.94E-04	
4 – 4.5	1.1	4.84E-01	1.16E-01	2.78E-01	4.23E-02	28	1.88E-01	8.74E-02	2.38E-01	6.04E-02
4 – 4.5	2.1	4.45E-02	1.06E-02	4.80E-03	1.57E-03	150	7.60E-03	1.36E-03	6.10E-03	1.47E-03
5 – 5.5	1.1	2.58E-01	6.52E-02	2.95E-01	1.41E-03	9	2.17E-01	1.64E-03	2.62E-01	1.98E-05
5 – 5.5	2.1	8.35E-03	2.52E-03	4.10E-03	1.81E-05	35	6.50E-03	3.42E-06	5.10E-03	1.06E-05
5 – 5.5	3.1	<4.10E-03		2.92E-04			5.15E-04		3.97E-04	

B. ^{131}I activity concentration in Weser water – 3-4 hours after HW

Distance from river banks	Location	Distance from the WWTP (km)	Normalized experimental result	Error	Simulation result with ε=0.01 m^2/s	Squares of residuals (ε= 0.01 m^2/s)	Difference D (%)	Simulation result with ε=0.0025 m^2/s	Squares of residuals (ε= 0.0025 m^2/s)	Simulation result with ε=0.005 m^2/s	Squares of residuals (ε= 0.005 m^2/s)
Left bank	7.1	-1	<7.10E-03		2.18E-06			3.33E-08		4.47E-07	
Left bank	6.1	-0.5	8.05E-03	2.25E-03	1.50E-03	4.29E-05	118	1.30E-03	4.56E-05	1.60E-03	4.16E-05
Left bank	1.1	0	2.71E-01	7.76E-02	2.69E-01	5.76E-06	26	1.74E-01	9.49E-03	2.26E-01	2.06E-03

Left bank	2.1	0.5	1.14E-02	3.40E-03	5.20E-03	3.85E-05	42	8.10E-03	1.09E-05	6.50E-03	2.41E-05
Left bank	3.1	1	1.44E-02	4.56E-03	6.26E-04	1.91E-04	176	7.67E-04	1.87E-04	6.97E-04	1.89E-04
Left bank	4.1	2	9.02E-03	2.45E-03	3.78E-04	7.47E-05	178	5.36E-04	7.20E-05	4.43E-04	7.36E-05
Left bank	5.1	5	6.41E-03	1.83E-03	1.24E-04	3.96E-05	189	2.56E-04	3.79E-05	2.07E-04	3.85E-05
60 m from left bank	7.2	-1	1.42E-02	4.57E-03	5.82E-05	1.99E-04	198	1.09E-06	2.00E-04	1.36E-05	2.00E-04
60 m from left bank	6.2	-0.5	6.35E-03	1.82E-03	9.70E-03	1.12E-05	17	1.14E-02	2.55E-05	1.06E-02	1.80E-05
60 m from left bank	1.2	0	1.62E-02	5.33E-03	4.60E-03	1.35E-04	81	1.96E-05	2.62E-04	4.13E-04	2.49E-04
60 m from left bank	2.2	0.5	4.20E-03	1.56E-03	1.04E-02	3.84E-05	57	6.10E-03	3.60E-06	9.50E-03	2.81E-05
60 m from left bank	3.2	1	8.17E-03	2.78E-03	4.00E-03	1.74E-05	29	4.60E-03	1.27E-05	4.30E-03	1.49E-05
60 m from left bank	4.2	2	8.33E-03	2.40E-03	2.30E-03	3.63E-05	88	2.90E-03	2.95E-05	2.60E-03	3.28E-05
60 m from left bank	5.2	5	3.74E-03	1.07E-03	6.38E-04	9.65E-06	123	1.20E-03	6.47E-06	1.10E-03	6.99E-06
Center of the river	7.3	-1	8.10E-03	2.95E-03	7.69E-04	5.38E-05	148	2.40E-03	3.25E-05	1.30E-03	4.63E-05
Center of the river	6.3	-0.5	7.12E-03	2.03E-03	5.60E-03	2.32E-06	9	1.79E-04	4.82E-05	1.80E-03	2.83E-05
Center of the river	1.3	0	<2.17E-02		1.55E-05			1.03E-10		8.89E-08	
Center of the river	2.3	0.5	<5.36E-03		6.30E-03			1.56E-04		1.90E-03	
Center of the river	3.3	1	<7.36E-03		5.00E-03			1.20E-03		3.30E-03	
Center of the river	4.3	2	5.26E-03	1.74E-03	3.20E-03	4.25E-06	10	1.80E-03	1.20E-05	2.80E-03	6.06E-06
Center of the river	5.3	5	6.09E-03	1.55E-03	8.70E-04	2.72E-05	136	1.30E-03	2.29E-05	1.40E-03	2.20E-05

60 m from the right bank	7.4	-1	7.20E-03	2.89E-03	2.15E-04	4.87E-05	181	2.30E-06	5.18E-05	1.57E-05	5.16E-05
60 m from the right bank	6.4	-0.5	<8.43E-03		3.10E-04			7.52E-10		3.60E-06	
60 m from the right bank	1.4	0	<1.34E-03		2.67E-08			9.81E-17		7.48E-12	
60 m from the right bank	2.4	0.5	<5.03E-03		1.40E-03			2.51E-07		7.88E-05	
60 m from the right bank	3.4	1	<3.92E-03		2.10E-03			7.20E-06		3.50E-04	
60 m from the right bank	4.4	2	<7.34E-03		2.30E-03			2.52E-04		1.30E-03	
60 m from the right bank	5.4	5	4.69E-03	1.25E-03	6.42E-04	1.64E-05	137	1.60E-03	9.54E-06	9.95E-04	1.36E-05
Right bank	7.5	-1	<7.82E-03		5.38E-09			3.81E-20		3.41E-13	
Right bank	6.5	-0.5	4.71E-03	1.39E-03	2.17E-05	2.20E-05	197	1.77E-12	2.22E-05	7.88E-08	2.22E-05
Right bank	1.5	0	<1.73E-02		2.90E-10			3.02E-25		7.43E-15	
Right bank	2.5	0.5	<7.30E-03		1.75E-04			4.27E-10		2.35E-06	
Right bank	3.5	1	3.63E-03	2.01E-03	3.07E-04	1.11E-05	136	2.44E-07	1.32E-05	3.56E-05	1.30E-05
Right bank	4.5	2	6.94E-03	2.20E-03	3.71E-04	4.31E-05	171	1.83E-05	4.79E-05	1.81E-04	4.57E-05
Right bank	5.5	5	2.47E-03	8.43E-04	1.25E-04	5.52E-06	171	1.21E-04	5.54E-06	1.92E-04	5.21E-06

C. ^{131}I activity concentration in Weser sediments

Left bank

Distance from the WWTP (km)	-1	-0.5	0	0.5	1	2	5
Experimental Bq/kg(d.m.)	1.70	9.64	35.72	11.64	4.39	5.59	2.89
Error Bq/kg(d.m.)	0.08	0.53	2.55	0.53	0.25	0.34	0.27
Input: Simulated ^{131}I activity concentration in river water							
Simulation-no background Bq/kg(d.m.)	2.95E-04	0.01	127.61	0.99	0.18	1.63	1.63
Simulation-with background Bq/kg(d.m.)	0.97	1.15	128.47	1.10	2.48	2.47	2.47
Input: Measured ^{131}I activity concentration in river water							
Simulation-no background Bq/kg(d.m.)	0.00	1.54	135.86	0.74	0.79	4.41	3.14
Simulation-with background Bq/kg(d.m.)	0.97	2.69	136.72	0.85	0.88	5.25	3.98

Right bank

Distance from the WWTP (km)	-1.00	-0.50	0.00	0.50	1.00	2.00	5.00
Experimental Bq/kg(d.m.)	-	-	1.03	-	-	-	-
Error Bq/kg(d.m.)			0.08				0.26
Input: Simulated ^{131}I activity concentration in river water							
Simulation-no background Bq/kg(d.m.)	2.96E-05	6.22E-0.4	12.82	0.10	0.02	0.16	0.16
Simulation-with background Bq/kg(d.m.)	0.97	1.15	0.89	0.12	0.10	0.93	0.91
Input: Measured ^{131}I activity concentration in river water							
Simulation-no background Bq/kg(d.m.)	0.00	0.90	0.00	0.00	0.20	3.40	1.21
Simulation-with background Bq/kg(d.m.)	0.97	2.05	0.86	0.11	0.29	4.24	2.05

D. Sensitivity analysis

Left bank

Distance from the WWTP (km)	-1	-0.5	0	0.5	1	2	5
C_{WWTP} - ^{131}I activity concentration of the WWTP outflow							
Simulation-min value Bq/kg(d.m.)	0.26	0.31	34.42	0.30	0.07	0.66	0.66
Simulation-max value Bq/kg(d.m.)	2.80	3.33	370.67	3.18	0.80	7.13	7.13
Simulation- 1 order of magnitude lower from case D Bq/kg(d.m.)	0.01	0.12	12.91	0.11	0.03	0.25	0.25
Simulation-1 order of magnitude higher from case D Bq/kg(d.m.)	9.74	11.60	1290.90	11.08	2.78	24.84	24.84
Distribution coefficients in river water column and sediment K_{pw}, K_{pb}							
Simulation-min value Bq/kg(d.m.)	4.51E-06	4.69E-06	4.66E-04	2.43E-05	8.25E-06	9.44E-06	9.44E-06
Simulation-max value Bq/kg(d.m.)	417.02	469.49	5.53E+04	470.13	117.35	1063.5	1063.5
Simulation- 1 order of magnitude lower from case D Bq/kg(d.m.)	0.04	0.04	4.47	0.04	0.01	0.09	0.09
Simulation-1 order of magnitude higher from case D Bq/kg(d.m.)	11.76	14.00	1559.10	13.27	3.31	29.99	29.99
Mass transfer coefficient between water column and pore water of bed sediment k_L							
Simulation-min value Bq/kg(d.m.)	0.97	1.15	128.47	1.10	2.48	2.47	2.47
Simulation-max value Bq/kg(d.m.)	2.84	3.04	310.29	12.83	4.29	6.21	6.21
Simulation- 1 order of magnitude lower from case D Bq/kg(d.m.)	0.97	1.15	128.31	1.09	0.27	2.47	2.47
Simulation-1 order of magnitude higher from case D Bq/kg(d.m.)	0.99	1.17	130.11	1.21	0.31	2.51	2.51
S_b – solids concentration in the sediment							
Simulation-min value Bq/kg(d.m.)	2.02	2.40	267.65	2.30	0.58	5.15	5.15
Simulation-max value Bq/kg(d.m.)	0.73	0.87	97.33	0.84	0.21	1.87	1.87
S_w – solids concentration in the water column							
Simulation-min value Bq/kg(d.m.)	0.97	1.15	128.47	1.10	2.48	2.47	2.47
Simulation-max value Bq/kg(d.m.)	20.42	24.32	2707.60	23.03	5.75	52.09	52.09
Simulation- 1 order of	0.10	0.12	13.02	0.12	0.03	0.25	0.26

magnitude lower from case D Bq/kg(d.m.)							
Simulation-1 order of magnitude higher from case D Bq/kg(d.m.)	9.64	11.48	1278.50	10.88	2.72	24.59	24.59

Right bank

Distance from the WWTP (km)	-1	-0.5	0	0.5	1	2	5
C_{WWTP} - ^{131}I activity concentration of the WWTP outflow							
Simulation-min value Bq/kg(d.m.)	0.26	0.31	0.24	0.03	0.03	0.25	0.24
Simulation-max value Bq/kg(d.m.)	2.80	3.33	2.56	0.34	0.30	2.70	2.62
Simulation- 1 order of magnitude lower from case D Bq/kg(d.m.)	0.10	0.12	0.89	0.01	0.01	0.09	0.09
Simulation-1 order of magnitude higher from case D Bq/kg(d.m.)	9.74	11.59	8.91	1.19	1.05	9.39	9.11
Distribution coefficients in river water column and sediment K_{pw}, K_{pb}							
Simulation-min value Bq/kg(d.m.)	4.51E-06	4.69E-06	4.62E-06	4.07E-06	4.13E-06	4.47E-06	4.36E-06
Simulation-max value Bq/kg(d.m.)	416.97	496.04	3.81E+02	50.32	440.26	401.91	390.02
Simulation- 1 order of magnitude lower from case D Bq/kg(d.m.)	0.04	0.04	0.03	0.05	0.04	0.03	0.03
Simulation-1 order of magnitude higher from case D Bq/kg(d.m.)	11.76	13.99	10.75	1.42	1.25	11.34	11.00
Mass transfer coefficient between water column and pore water of bed sediment k_L							
Simulation-min value Bq/kg(d.m.)	0.97	1.15	0.89	0.12	0.10	0.93	0.91
Simulation-max value Bq/kg(d.m.)	2.84	3.04	2.84	2.11	2.13	2.80	2.72
Simulation- 1 order of magnitude lower from case D Bq/kg(d.m.)	0.97	1.15	0.88	0.12	0.10	0.93	0.91
Simulation-1 order of magnitude higher from case D Bq/kg(d.m.)	0.99	1.17	0.90	0.14	0.12	0.95	0.92
S_b – solids concentration in the sediment							
Simulation-min value Bq/kg(d.m.)	2.02	2.40	1.85	0.25	0.22	1.95	1.89
Simulation-max value Bq/kg(d.m.)	0.73	0.87	0.67	0.09	0.08	0.71	0.69

S_w – solids concentration in the water column							
Simulation-min value Bq/kg(d.m.)	0.97	1.15	0.89	0.12	0.10	0.93	0.91
Simulation-max value Bq/kg(d.m.)	20.42	24.29	18.67	2.47	2.17	19.68	19.10
Simulation- 1 order of magnitude lower from case D Bq/kg(d.m.)	0.10	0.12	0.09	0.01	0.01	0.10	0.09
Simulation-1 order of magnitude higher from case D Bq/kg(d.m.)	9.64	11.47	8.82	1.17	1.03	9.29	9.02

Appendix 12 – Analytical solution of 1D advection dispersion equation

The activity concentration in the bank sediments (r[Bq/kg(d.m.)]) is calculated through an unsteady state one-dimensional equation (eq. 1) which includes first order processes of radioactive decay (λ radioactive decay constant), sedimentation (k_s sedimentation rate constant) and resuspension (α scour rate constant). The diffusion between the pore water and the overlying water is based on concentration differences (k_L mass transfer coefficient between water column and pore water of bed sediment).

$$\frac{\partial r}{\partial t} = \left(-\lambda \frac{r}{1 + k_{\mathrm{pb}} S_b}\right) + \frac{k_s k_{\mathrm{pw}} S_w \gamma}{\left(S_b + \frac{1}{k_{\mathrm{pb}}}\right)} \frac{1}{\left(1 + k_{pw} S_w\right)} C + \left(-a \frac{S_b}{\left(S_b + \frac{1}{k_{\mathrm{pb}}}\right)} r\right) +$$

$$+ \left(\frac{-k_L}{\left(S_b + \frac{1}{k_{\mathrm{pb}}}\right) d} \frac{r}{k_{\mathrm{pb}}}\right) + \left(\frac{k_L}{\left(S_b + \frac{1}{k_{\mathrm{pb}}}\right)} \frac{C}{\left(1 + k_{\mathrm{pw}} S_w\right)}\right) \qquad \textit{eq. 1}$$

With the sedimentation rate described as $k_s = \frac{v_w}{h(t)}$, where v_w the sedimentation velocity and h(t) the tidally influenced water depth and the resupension rate as $\alpha = \frac{k_s S_w \gamma}{S_b}$.

By rearranging the equation we get:

$$\frac{\partial r}{\partial t} = \left[-\left(\frac{\lambda}{1 + k_{pb} S_b}\right) - \left(\frac{\alpha S_b}{S_b + \frac{1}{k_{pb}}}\right) - \left(\frac{k_L}{d\left(S_b + \frac{1}{k_{pb}}\right)} \frac{1}{k_{pb}}\right) \right] r +$$

$$+ \left[\left(\frac{k_s k_{pw} S_w \gamma}{S_b + \frac{1}{k_{pb}}} \frac{1}{\left(1 + k_{pw} S_w\right)}\right) + \frac{k_L}{d\left(S_b + \frac{1}{k_{pb}}\right)} \left(\frac{1}{1 + k_{pw} S_w}\right) \right] C \qquad \textit{eq.2}$$

Or simpler:

$$\frac{dr(t)}{dt} = -a(t)\, r(t) + b(t)\, C(t) \qquad \textit{eq.3}$$

$$\frac{dr(t)}{dt} = -\left[a_1 + a_2(t) + a_3\right] r(t) + \left[b_1(t) b_2 + b_3\right] C(t), \text{ where}$$

$$a_1 = \frac{\lambda}{1 + k_{pb} S_b},\ a_2(t) = \frac{\alpha\ S_b}{S_b + \frac{1}{k_{pb}}},\ a_3 = \frac{k_L}{d\left(S_b + \frac{1}{k_{pb}}\right)} \frac{1}{k_{pb}}$$

and

$$b_1(t) = \frac{k_s k_{pw} S_w}{S_b + \frac{1}{k_{pb}}} \frac{1}{\left(1 + k_{pw} S_w\right)},\ b_2 = \gamma\ ,\ b_3 = \frac{k_L}{d\left(S_b + \frac{1}{k_{pb}}\right)} \frac{1}{1 + k_{pw} S_w}$$

Equation 3 is a first order linear ordinary differential equation with the alternate form:

$$-r(t)\left(a_1 + a_2(t) + a_3\right) + C(t)\left(b_1(t)\, b_2 + b_3\right) = r'(t)$$

and solution:

$$r(t) = e^{-\int_0^t (a_1 + a_2(t) + a_3)\, dt} \cdot$$

$$\cdot \int_0^t e^{\int_1^{t'} \left(a_1 + a_2(t') + a_3\right) dt'} \left(b_1(t)\, b_2 C(t) + b_3\ C(t)\right) dt +$$

$$+ c_1 e^{-\int_0^t (a_1 + a_2(t) + a_3)\, dt} \qquad \textit{eq. 4}$$

With c_1 an integration constant. When applying the initial condition r(0)=0, then c_1=0 and the solution is:

$$r(t) = e^{-\int_0^t (a_1 + a_2(t) + a_3)\, dt} \cdot$$

$$\cdot \int_0^t e^{\int_0^{t'} \left(a_1 + a_2(t') + a_3\right) dt'} \left(b_1(t)\, b_2 C(t) + b_3\ C(t)\right) dt \qquad \textit{eq. 5}$$

<u>The calculation of the solution is as follows:</u>

$$-r(t)\left(a_1 + a_2(t) + a_3\right) + C(t)\left(b_1(t)\, b_2 + b_3\right) = r'(t) \qquad (*)$$

> We assume the existence of the integration factor $\mu(t)$ and multiply (*):

$$\mu(t)\frac{dr(t)}{dt} = -\mu(t)\, r(t)\left(a_1 + a_2(t) + a_3\right) + \mu(t)\, C(t)\left(b_1(t)\, b_2 + b_3\right)$$

> We assume $\mu(t)$ satisfies $\mu(t)\left(a_1 + a_2(t) + a_3\right) = \mu'(t)$ (**)

$$\underbrace{\mu(t)\frac{dr(t)}{dt} + \mu'(t)\, r(t)} = \mu(t)\, C(t)\left(b_1(t)\, b_2 + b_3\right)$$

By using the product rule for $\mu(t)\frac{dr(t)}{dt}+\mu'(t)r(t)$ we get: $\left(\mu(t)r(t)\right)'=\mu(t)C(t)\left(b_1(t)b_2+b_3\right)$

and when integrating both sides it becomes $\int_0^t\left(\mu(t)r(t)\right)'dt=\int_0^t\mu(t)C(t)\left(b_1(t)b_2+b_3\right)dt$ or

$\mu(t)r(t)+c_1=\int_0^t\mu(t)C(t)\left(b_1(t)b_2+b_3\right)dt$.

> Solving for r(t) the equation takes the following form $\mu(t)r(t)=c_2\int_0^t\mu(t)C(t)\left(b_1(t)b_2+b_3\right)dt$

Or $r(t)=\dfrac{c_2+\int_0^t\mu(t)C(t)\left(b_1(t)b_2+b_3\right)}{\mu(t)}$ (A)

>We determine the function $\mu(t)$ from (**) as: $\mu(t)\left(a_1+a_2(t)+a_3\right)=\mu'(t)$. By rearranging we get $\frac{\mu'(t)}{\mu(t)}=\left(a_1+a_2(t)+a_3\right)$ which is $\left(\ln\mu(t)\right)'=\left(a_1+a_2(t)+a_3\right)$. The integration over time gives: $\ln\mu(t)+k_2=\int_0^t\left(a_1+a_2(t)+a_3\right)dt$ or $\ln\mu(t)=\int_0^t\left(a_1+a_2(t)+a_3\right)dt+k_1$ which is equal to

$\mu(t)=e^{\int_0^t(a_1+a_2(t)+a_3)\,dt+k_1}$ or $\mu(t)=e^{k_1}\,e^{\int_0^t(a_1+a_2(t)+a_3)\,dt}$. Since e^{k_1} is a constant it can be written as k and $\mu(t)$ then becomes: $\mu(t)=k\,e^{\int_0^t(a_1+a_2(t)+a_3)\,dt}$

By substituting it in equation (A) one gets:

$$r(t)=\frac{c_2+\int_0^t k\,e^{\int_0^{t'}\left(a_1+a_2(t')+a_3\right)dt'}C(t)\left(b_1(t)b_2+b_3\right)dt}{k\,e^{\int_0^t(a_1+a_2(t)+a_3)\,dt}}$$ and rearranging we get:

$$r(t)=\frac{\frac{c_2}{k}+\int_0^t e^{\int_0^{t'}\left(a_1+a_2(t')+a_3\right)dt'}C(t)\left(b_1(t)b_2+b_3\right)dt}{e^{\int_1^t(a_1+a_2(t)+a_3)\,dt}}$$ or

$$r(t)=\frac{\frac{c_2}{k}}{e^{\int_0^t (a_1+a_2(t)+a_3)\,dt}}+\frac{\int_0^t e^{\int_0^{t'} (a_1+a_2(t')+a_3)\,dt'} C(t)\left(b_1(t)\,b_2+b_3\right)dt}{e^{\int_0^t (a_1+a_2(t)+a_3)\,dt}}$$ and

$$r(t)=c\,e^{-\int_0^t (a_1+a_2(t)+a_3)\,dt}+$$

$$+e^{-\int_0^t (a_1+a_2(t)+a_3)\,dt}\int_0^t e^{\int_{10}^{t'} (a_1+a_2(t')+a_3)\,dt'} C(t)\left(b_1(t)\,b_2+b_3\right)dt \qquad \textit{eq. 6}$$

By setting the initial conditions of r(0)=0 and C(0)=0, we get the final form of the equation as:

$$r(t)=e^{-\int_0^t (a_1+a_2(t)+a_3)\,dt}\cdot\int_0^t e^{\int_0^{t'} (a_1+a_2(t')+a_3)\,dt'} C(t)\left(b_1(t)\,b_2+b_3\right)dt$$

Appendix 13 – ^{131}I in WWTP effluent – IMIS values for Bremen 1993-2014

Sampling date	^{131}I activity concentration (mBq/l)	Error (%)
11-08-94	3.00E-01	10
31-10-94	1.78E-01	9.9
22-03-95	9.38E-02	25.7
14-08-95	1.04E-01	18.3
14-11-96	1.01E-01	7.1
10-04-97	3.70E-02	19.5
09-07-97	4.81E-02	19.8
27-02-98	1.24E-01	17.4
14-04-98	5.14E-02	30.1
09-07-98	1.26E-01	17.3
25-03-99	1.05E-01	10.1
17-05-99	8.89E-02	19.6
09-07-99	1.13E-01	11
05-11-99	7.18E-02	26
07-01-00	4.11E-02	20.8
06-04-00	8.64E-02	13.4
07-12-00	1.64E-01	6.3
16-02-01	2.47E-01	4.7
06-09-01	9.89E-02	28.9
06-02-02	1.59E-01	11
08-05-02	9.87E-02	9.8
10-09-02	1.30E-01	10.8
08-11-02	1.42E-01	11.1
05-03-03	1.61E-01	10.1
18-06-03	1.61E-01	15.4
08-09-03	6.03E-02	29.8
16-10-03	1.29E-01	12
28-01-04	4.66E-01	4.4
09-06-04	1.92E-01	13.2
22-07-04	1.14E-01	14.2
04-11-04	1.84E-01	9.2
16-02-05	4.95E-01	5.5
26-05-05	1.03E-01	13.4
23-08-05	2.37E-01	12.7

Sampling date	^{131}I activity concentration (mBq/l)	Error (%)
08-12-05	2.46E-01	9.3
25-01-06	2.94E-01	13.1
31-05-06	1.28E-01	21.8
01-09-06	1.37E-01	23.2
12-12-06	3.19E-01	14.6
08-02-07	9.77E-01	4.8
20-04-07	3.24E-01	7.4
21-09-07	2.20E-01	18.3
11-12-07	3.00E-01	10.4
23-01-08	2.25E-01	16.5
24-04-08	3.99E-01	7.3
03-12-08	4.55E-01	8.1
10-02-09	2.79E-01	10.7
16-04-09	1.56E-01	17.5
24-09-09	2.35E-01	13
28-10-09	2.54E-01	14.1
13-01-10	2.53E-01	15.4
04-05-10	2.12E-01	14.6
16-08-10	1.40E-01	23
17-12-10	2.59E-01	8.2
23-02-11	2.68E-01	11.9
23-06-11	2.33E-01	13.1
07-09-11	2.39E-01	13
08-11-11	3.12E-01	10.4
03-02-12	1.85E-01	4.8
11-05-12	2.52E-01	16.9
19-08-12	2.26E-01	35.1
02-11-12	2.95E-01	6.2
27-02-13	3.22E-01	11.3
29-05-13	2.25E-01	11.4
08-08-13	5.36E-01	10.1
27-11-13	3.50E-01	10.8

Appendix 14-Corrections in the activity and its uncertainty for the 364.5 keVpeak using the interactive peak fit function

	^{131}I activity concentration before fitting(mBq/kg)	Error (%)	^{131}I activity concentration after fitting(mBq/kg)	Error (%)	Change in uncertainty after fitting(%)
MS283	2.00	28.53	2.35	14.36	49.67
MS291	484.24	15.46	473.03	7.13	53.88
MS297	3.85	15.07	3.43	7.78	48.37
MS299	4.48	17.84	4.12	8.71	51.18
MS302	2.04	22.58	1.87	9.50	57.93
MS311	1029.33	15.85	1001.82	7.53	52.49
MS313	947.95	24.42	848.40	8.86	63.72
MS316	1.19	21.57	1.26	13.21	38.76
MS317	0.79	42.42	1.04	15.19	64.19
MS319	1.19	25.45	1.12	13.41	47.31
MS321	1.26	24.07	0.74	15.89	33.98
MS322	315.39	6.88	307.13	5.13	25.44
MS323	1.50	31.32	1.69	16.23	48.18
MS324	2.56	27.70	2.24	12.26	55.74
MS326	1.79	20.11	1.61	10.18	49.38
MS327	1.38	18.68	1.24	12.73	31.85
MS328	0.54	44.25	0.65	22.39	49.40
MS329	185.70	11.86	172.93	6.65	43.93
MS330	1.41	29.24	1.34	11.55	60.50
MS331	1.21	32.52	1.18	14.80	54.49
MS332	1.35	26.63	1.24	13.81	48.14
MS335	0.99	35.32	1.03	17.82	49.55
MS337	2.25	22.78	2.63	14.64	35.73
MS339	1.62	33.58	1.49	18.42	45.15
MS340	0.66	43.26	0.79	19.40	55.15
MS345	2.36	17.93	2.12	10.19	43.17
MS346	1.05	32.66	1.48	14.69	55.02
MS347	0.58	52.42	0.78	22.29	57.48
MS352	72.55	21.95	66.76	11.41	48.02
MS355	1.22	27.91	1.29	15.03	46.15
MS360	266.76	8.09	261.22	5.34	33.99
MS361	1.01	42.53	1.05	17.22	59.51
MS362	3.16	20.90	3.56	10.10	51.67
MS366	111.98	13.66	102.96	7.55	44.73
MS367	81.75	18.28	75.06	9.63	47.32
MS369	3.03	14.63	2.74	6.83	53.32
MS370	1.83	15.13	1.79	15.09	0.26
MS378	0.74	47.71	0.80	22.48	52.88

Appendix 15 - MatLab m-files

All m-files mentioned in this section unless stated otherwise are included in the IFISS package (available for download from http://www.maths.manchester.ac.uk/~djs/ifiss/). The m-files provided here have several discrepancies with the aforementioned package files, as to be suitable in our case. The changed m-files can be easily distinguished since on the filename the word weser and/or tide is included.

A. Grid formation

The function final_weser_grid creates and plots the Weser grid as shown in figures 5.3-5.5. It calls the IFISS functions: rec_domain_q2 (calls: meshgrid, reshape), findboundary, macrogridplot (calls: gplot) and saves the relative information at final_weser_grid.mat file.

```
function final_weser_grid
%WESER DOMAIN obstacle domain Q2 grid generator
obs = [];xy = [];mv = []; sbnde = [];
% bndxy: vertices that define the domain and obstacle(s)
%        (x-coordinate y-coordinate)
% bnde: boundary edges
%      (node1 node2 1(for dirichlet)/0(for neumann))
% obs: obstacles
%      (node1 node2 node3 node4)
% sbnde: boundary edges near which stretching is needed
%       (edge1 edge2 ...)
% 'obs' and/or 'sbnde' can be absent if there is no obstacle in the problem
% and/or only uniform grid is needed
bndxy = ...
    [0 0.25
     0 1
     3.75 1
     3.75 0.4375
     5 0.4375
     5 0.3125
     6 0.3125
     6 0.25
     7 0.25
     7 0.375
     12 0.375
     12 0.3125
     15 0.3125
     15 -0.3125
     12 -0.3125
     12 -0.375
     7 -0.375
     7 -0.25
     6 -0.25
     6 -0.3125
     5 -0.3125
```

```
     5 -0.4375
     3.75 -0.4375
     3.75 -1
     1 -1
     1 0.25
    1.25 -0.0625
    3.5 -0.0625
    3.5 0.125
    1.25 0.125];

bnde = ...
    [1 2 1
    2 3 1
    3 4 1
    4 5 1
    5 6 1
    6 7 1
    7 8 1
    8 9 1
    9 10 1
    10 11 1
    11 12 1
    12 13 1
    13 14 0
    14 15 1
    15 16 1
    16 17 1
    17 18 1
    18 19 1
    19 20 1
    20 21 1
    21 22 1
    22 23 1
    23 24 1
    24 25 1
    25 26 1
    26 1 1
    27 28 1
    28 29 1
    29 30 1
    30 27 1];

obs = ...
    [27 28 29 30];
sbnde = [27 28 29 30];
%% compute mesh size h and uniform x, y coordinate
hx = 0.125/2; hy=0.03125;
x = [0:hx:15]';
y = [-1:hy:1]';
%% generate xy coordinates and element mapping matrix
%%%%domain I%%%%%
[xyI,mvI]= rec_domain_q2(0,1,0.25,1,hx,hy,xy);
xy = [xy;xyI];
mv = [mv;mvI];
%%%%%object domain II%%%%%%
[xyII1,mvII1] = rec_domain_q2(1,1.25,-1,1,hx,hy,xy);
```

```
xy = [xy;xyII1];
mv = [mv;mvII1];
[xyII2,mvII2] = rec_domain_q2(1.25,3.5,-1,-0.0625,hx,hy,xy);
xy = [xy;xyII2];
mv = [mv;mvII2];
[xyII3,mvII3] = rec_domain_q2(1.25,3.5,0.125,1,hx,hy,xy);
xy = [xy;xyII3];
mv = [mv;mvII3];

[xyII4,mvII4] = rec_domain_q2(3.5,3.75,-1,1,hx,hy,xy);
xy = [xy;xyII4];
mv = [mv;mvII4];
%%%%domain III%%%%%
[xyIII,mvIII]= rec_domain_q2(3.75,5,-0.4375,0.4375,hx,hy,xy);
xy = [xy;xyIII];
mv = [mv;mvIII];
%%%%domain IV%%%%%
[xyIV,mvIV]= rec_domain_q2(5,6,-0.3125,0.3125,hx,hy,xy);
xy = [xy;xyIV];
mv = [mv;mvIV];
%%%%domain V%%%%%
[xyV,mvV]= rec_domain_q2(6,7,-0.25,0.25,hx,hy,xy);
xy = [xy;xyV];
mv = [mv;mvV];
%%%%domain VI%%%%%
[xyVI,mvVI]= rec_domain_q2(7,12,-0.375,0.375,hx,hy,xy);
xy = [xy;xyVI];
mv = [mv;mvVI];
%%%%domain VII%%%%%
[xyVII,mvVII]= rec_domain_q2(12,15,-0.3125,0.3125,hx,hy,xy);
xy = [xy;xyVII];
mv = [mv;mvVII];
%% compute boundary vertices and edges
[bound,mbound] = findboundary(bndxy,bnde,xy,mv);
macrogridplot(xy, mv, bound, mbound)
fprintf('  All done.\n\n')
gohome
cd datafiles
save final_weser_grid.mat mv xy bound mbound x y bndxy bnde obs sbnde
return
```

B. Hydrodynamics » Steady State Navier- Stokes

For solving the Navier-Stokes equation on our domain first one has to set up the inflow/outflow problem by calling the final_weser_grid_stokes m-file (calls: q1p0grid, stokes_q1p0 for the Q_1-P_0 element and matrix grid generation respectively) followed by xsolve_navier m-file (calls: specific_flow_weser, navier_q1, newton_q1, newton_bc, flowplot_p_weser) which solves the NS equations and saves the a vector under the name flowsol containing the velocity and pressure values.

```
%WESER_CHANNEL_STOKES set up inflow/outflow problem in weser domain
%   IFISS scriptfile: DJS; 27 July 2015.
% Copyright (c) 2005 D.J. Silvester, H.C. Elman, A. Ramage
%clear variables
%% define geometry
pde=3; domain=1; enclosed=0;
outbnd=15;
load final_weser_grid.mat
%
%% set up matrices
q_in=2;
qmethod=q_in-1;

   [ev,ee,ebound,xyp] = q1p0grid(x,y,xy,mv,bound,mbound);
   [A,B,Q,C,G,Bx,By,f,g] = stokes_q1p0(xy,xyp,mv,ev);

gohome
cd datafiles
save final_weser_grid_stokes_nobc.mat  outbnd  domain  pde A B Q f g xy xyp
mbound bound x y qmethod
save final_weser_grid_stokes_nobc.mat Bx By bndxy bnde obs -append
   save final_weser_grid_stokes_nobc.mat C G ev ee ebound -append

   fprintf('system matrices saved in final_weser_grid_stokes_nobc.mat ...\n')
```

```
%XSOLVE_NAVIER solve Navier-Stokes problem in weser asap domain
%   IFISS scriptfile: DJS; 27 July 2015.
% Copyright (c) 2005 D.J. Silvester, H.C. Elman, A. Ramage
%clear variables
fprintf('(incompressible flow problem in final_weser_grid ...\n')
viscosity=1/100;
%'Picard-Newton hybrid linearization
%number of Picard iterations
   maxit_p=6;
%number of Newton iterations
   maxit_n=5;
%nonlinear tolerance
```

```
tol_nl=1.e-8;
%% initialize for nonlinear iteration: compute Stokes solution
%% load assembled matrices
gohome
cd datafiles
load final_weser_grid_stokes_nobc.mat
fprintf('weser asap system ...\n')
qmethod=1;
%% boundary conditions
[Ast,Bst,fst,gst] = flowbc_weser(A,B,f,g,xy,bound);
nlres0_norm = norm([fst;gst]);
nv=length(fst)/2; np=length(gst);
      beta=1/4;     % default parameter
   xst=[Ast,Bst';Bst,-beta*C]\[fst;gst];

[msgstr,msgid] = lastwarn;
if length(msgid)==27,
   if sum(msgid=='MATLAB:nearlySingularMatrix')==27,
      fprintf('This should not cause difficulty for enclosed flow
problems.\n\n');
   end
end
lastwarn('');
% compute residual of Stokes solution

   nubeta=beta/viscosity;
   N = navier_q1(xy,ev,xst);

Anst = viscosity*A + [N, sparse(nv,nv); sparse(nv,nv), N];
[Anst,Bst,fst,gst] = flowbc_weser(Anst,B,f,g,xy,bound);
 nlres = [Anst,Bst';Bst,-nubeta*C]*xst-[fst;gst];

nlres_norm  = norm(nlres);

contourn = 50;
fprintf('\n\ninitial nonlinear residual is %e ',nlres0_norm)
fprintf('\nStokes solution residual is %e\n', nlres_norm)
flowsol = xst;
pde=4;
it_p = 0;
% nonlinear iteration
%% Picard startup step
while nlres_norm>nlres0_norm*tol_nl && it_p<maxit_p,
   it_p = it_p+1;
   fprintf('\nPicard iteration number %g \n',it_p),
% compute Picard correction and update solution

   dxns = -[Anst,Bst';Bst,-nubeta*C]\nlres;

   [msgstr,msgid] = lastwarn;
   if length(msgid)==27,
      if sum(msgid=='MATLAB:nearlySingularMatrix')==27,
         fprintf('This should not cause difficulty for enclosed flow
problems.\n\n');
      end
```

```
   end
   lastwarn('');
   xns = flowsol + dxns;
% compute residual of new solution
   N = navier_q1(xy,ev,xns);
      Anst = viscosity*A + [N, sparse(nv,nv); sparse(nv,nv), N];
   [Anst,Bst,fst,gst] =flowbc_weser(Anst,B,f,g,xy,bound);

   nlres = [Anst,Bst';Bst,-nubeta*C]*xns-[fst;gst];

   nlres_norm = norm(nlres);
   nnv=length(fst); soldiff=norm(xns(1:nnv)-flowsol(1:nnv));
   fprintf('nonlinear residual is %e',nlres_norm)
   fprintf('\n   velocity change is %e\n',soldiff)
   flowsol = xns;
%% end of Picard iteration loop
end
%%
%
it_nl = it_p;
it_n = 0;
%% Newton iteration loop
while (nlres_norm > nlres0_norm*tol_nl) && (it_nl < maxit_p + maxit_n),

   it_n = it_n+1;
   it_nl = it_nl+1;
   fprintf('\nNewton iteration number %g \n',it_n),
% compute Jacobian of current solution
    [Nxx,Nxy,Nyx,Nyy] = newton_q1(xy,ev,flowsol);
      J = viscosity*A + [N + Nxx, Nxy; Nyx, N + Nyy];
   Jnst = newtonbc(J,xy,bound);
% compute Newton correction and update solution
dxns = -[Jnst,Bst';Bst,-nubeta*C]\nlres;
[msgstr,msgid] = lastwarn;
   if length(msgid)==27,
      if sum(msgid=='MATLAB:nearlySingularMatrix')==27,
         fprintf('This should not cause difficulty for enclosed flow
problems.\n\n');
      end
   end
   lastwarn('');
   xns = flowsol + dxns;
% compute residual of new solution
    N = navier_q1(xy,ev,xns);
     Anst = viscosity*A + [N, sparse(nv,nv); sparse(nv,nv), N];
   [Anst,Bst,fst,gst] = flowbc_weser(Anst,B,f,g,xy,bound);
      nlres = [Anst,Bst';Bst,-nubeta*C]*xns-[fst;gst];
    nlres_norm = norm(nlres);
   nnv=length(fst); soldiff=norm(xns(1:nnv)-flowsol(1:nnv));
   fprintf('nonlinear residual is %e',nlres_norm)
   fprintf('\n   velocity change is %e\n',soldiff)
end
%%%%%%%%%%plot solution%%%%%%%%%%%
   pause(1)
```

```
flowplotp_weser(qmethod,xns,By,Bx,A,xy,xyp,x,y,bound,bndxy,bnde,obs,contourn,
168)
   flowsol = xns;
%% end of Newton iteration loop
 if nlres_norm <= nlres0_norm * tol_nl,
   fprintf('\nfinished, nonlinear convergence test satisfied\n\n');
% explicitly reorthogonalize to remove hydrostatic pressure component
   nlres = nlres -
[zeros(2*nv,1);(sum(nlres(2*nv+1:2*nv+np))/np)*ones(np,1)];
else
   fprintf('\nfinished, stopped on iteration counts\n\n');
end
%
gohome
cd datafiles
save final_weser_grid.mat flowsol mv xy bound mbound x y bndxy bnde obs sbnde
N
```

The flowbc_weser file imposed inflow boundary conditions by calling the specific_flow_weser file:

```
function [bcx,bcy] = specific_flow_weser(xbd,ybd)
%
%   [bcx,bcy] = specific_flow(xbd,ybd);
%   input
%          xbd          x coordinate vector
%          ybd          y coordinate vector
%
%   specifies Poiseuille flow boundary condition
%   IFISS function: DJS; 6 March 2005.
% Copyright (c) 2005 D.J. Silvester, H.C. Elman, A. Ramage
bcx=0*xbd; bcy=0*xbd;
k=find(xbd==0 & ybd>0.25 & ybd<1); bcx(k)=(-7.1*ybd(k).*ybd(k)+8.875*ybd(k)-
1.775);
return
```

The flowplot_p_weser file plots the flow data on our domain by calling additionally the streambc_weser, which imposes the Dirichlet boundary conditions on the streamfunction (calls the stream_bc_weser which specifies the streamfunction associated with this specific flow).

```
function
flowplotp_weser(qmethod,sol,By,Bx,A,xy,xyp,x,y,bound,bndxy,bnde,obs,contourn,
fig);
%FLOWPLOTP_weser plots flow data on weser domain
%   flowplotp(qmethod,sol,By,Bx,A,xy,xyp,x,y,bound,fig);
%   input
%          qmethod    mixed method
%          sol        flow solution vector
%          By         velocity  y-derivative matrix
%          Bx         velocity x-derivative matrix
%          A          vector diffusion matrix
```

```
%          xy         velocity nodal coordinate vector
%          xyp        pressure nodal coordinate vector
%          x          vector of x-axis interpolation points
%          y          vector of y-axis interpolation points
%          bound      boundary vertex vector
%          fig        figure number
%
% calls function streambc.m to set boundary values
%   IFISS function: DJS; 30 April 2012.
% Copyright (c) 2005 D.J. Silvester, H.C. Elman, A. Ramage
k1=figure(fig); k2=figure(fig+1); k3=figure(fig+2); k4=figure(fig+3);
k5=figure(fig+4);
nvtx=length(xy); nu=2*nvtx; np=length(xyp);
Asv=A(1:nvtx,1:nvtx);
% compute auxilliary quantites
u=sol(1:nu);p=sol(nu+1:end);
f=[By,-Bx]*u;
[Asv,fsv] = streambc_weser(Asv,f,xy,bound);
phi=Asv\fsv;
%
%%%%---------plot horizontal velocity-----------%%%%%
[X,Y]=meshgrid(x,y);
xysol = griddata(xy(:,1),xy(:,2),phi,X,Y);
maxphi=max(max(xysol)); minphi=min(min(xysol));
vneg=[minphi:-minphi/12:0];vpos=[maxphi/12:maxphi/12:maxphi];
xysol = griddata(xy(:,1),xy(:,2),u(1:nvtx),X,Y);
if size(obs,1)~=0
   [II,JJ] = findobsXY(obs,X,Y,bndxy); xysol(II,JJ)=nan;
end
[II,JJ]=find(X<1 & Y<0.25); xysol(II,JJ)=nan;
[II,JJ]=find(X>3.75 & Y>0.4375); xysol(II,JJ)=nan;
[II,JJ]=find(X>3.75 & Y<-0.4375); xysol(II,JJ)=nan;
[II,JJ]=find(X>5 & X<6 & Y>0.3125); xysol(II,JJ)=nan;
[II,JJ]=find(X>5 & X<6 & Y<-0.3125); xysol(II,JJ)=nan;
[II,JJ]=find(X>6 & X<7 & Y>0.25); xysol(II,JJ)=nan;
[II,JJ]=find(X>6 & X<7 & Y<-0.25); xysol(II,JJ)=nan;
[II,JJ]=find(X>7 & X<12 & Y>0.375); xysol(II,JJ)=nan;
[II,JJ]=find(X>7 & X<12 & Y<-0.375); xysol(II,JJ)=nan;
[II,JJ]=find(X>12 & Y>0.3125); xysol(II,JJ)=nan;
[II,JJ]=find(X>12 & Y<-0.3125); xysol(II,JJ)=nan;

figure(k1)

%subplot(122),
 contour(X,Y,xysol,contourn),axis('tight'), colorbar('EastOutside')
   title('Horizontal velocity contours','FontSize',12);
   axis('off')
%
% plot the boundary
hold on
for i = 1:size(bnde,1)
   plot([bndxy(bnde(i,1),1),
bndxy(bnde(i,2),1)],[bndxy(bnde(i,1),2),bndxy(bnde(i,2),2)],'-k')
end
hold off;
%
```

```
figure(k2)
mesh(X,Y,xysol),axis('tight'),colorbar('EastOutside')
title('Horizontal velocity','FontSize',12);

fprintf('done\n')
axis('off')
% plot the boundary
hold on
for i = 1:size(bnde,1)
   plot([bndxy(bnde(i,1),1),
bndxy(bnde(i,2),1)],[bndxy(bnde(i,1),2),bndxy(bnde(i,2),2)],'-k')
end
hold off;


%%%%---------plot lateral/vertical velocity----------%%%%
[X,Y]=meshgrid(x,y);
xysol = griddata(xy(:,1),xy(:,2),phi,X,Y);
maxphi=max(max(xysol)); minphi=min(min(xysol));
vneg=[minphi:-minphi/12:0];vpos=[maxphi/12:maxphi/12:maxphi];
xysol = griddata(xy(:,1),xy(:,2),u(nvtx+1:2*nvtx),X,Y);
if size(obs,1)~=0
   [II,JJ] = findobsXY(obs,X,Y,bndxy); xysol(II,JJ)=nan;
end
[II,JJ]=find(X<1 & Y<0.25); xysol(II,JJ)=nan;
[II,JJ]=find(X>3.75 & Y>0.4375); xysol(II,JJ)=nan;
[II,JJ]=find(X>3.75 & Y<-0.4375); xysol(II,JJ)=nan;
[II,JJ]=find(X>5 & X<6 & Y>0.3125); xysol(II,JJ)=nan;
[II,JJ]=find(X>5 & X<6 & Y<-0.3125); xysol(II,JJ)=nan;
[II,JJ]=find(X>6 & X<7 & Y>0.25); xysol(II,JJ)=nan;
[II,JJ]=find(X>6 & X<7 & Y<-0.25); xysol(II,JJ)=nan;
[II,JJ]=find(X>7 & X<12 & Y>0.375); xysol(II,JJ)=nan;
[II,JJ]=find(X>7 & X<12 & Y<-0.375); xysol(II,JJ)=nan;
[II,JJ]=find(X>12 & Y>0.3125); xysol(II,JJ)=nan;
[II,JJ]=find(X>12 & Y<-0.3125); xysol(II,JJ)=nan;

figure(k3)

%subplot(122),
 contour(X,Y,xysol,contourn),axis('tight'), colorbar('EastOutside')
   title('Lateral velocity contours','FontSize',12);

%
% plot the boundary
hold on
for i = 1:size(bnde,1)
   plot([bndxy(bnde(i,1),1),
bndxy(bnde(i,2),1)],[bndxy(bnde(i,1),2),bndxy(bnde(i,2),2)],'-k')
end
 axis('off')
hold off;
%
figure(k4)
mesh(X,Y,xysol),axis('tight'),colorbar('EastOutside')
title('Lateral velocity','FontSize',12);
```

```
fprintf('done\n')
axis('off')
% plot the boundary
hold on
for i = 1:size(bnde,1)
   plot([bndxy(bnde(i,1),1),
bndxy(bnde(i,2),1)],[bndxy(bnde(i,1),2),bndxy(bnde(i,2),2)],'-k')
end
hold off;

%%%%---------plot pressure----------%%%%

if qmethod==2
   xx=x(1:2:end); yy=y(1:2:end);
elseif qmethod==3
   p=p(1:3:end); xx=x(1:end); yy=y(1:end);
else
   xx=x(1:end); yy=y(1:end);
end
% interpolate to a cartesian product mesh
[X,Y]=meshgrid(xx,yy);
xysol = griddata(xyp(:,1),xyp(:,2),p,X,Y);
if size(obs,1)~=0
   [II,JJ] = findobsXY(obs,X,Y,bndxy); xysol(II,JJ)=nan;
end
[II,JJ]=find(X<1 & Y<0.25); xysol(II,JJ)=nan;
[II,JJ]=find(X>3.75 & Y>0.4375); xysol(II,JJ)=nan;
[II,JJ]=find(X>3.75 & Y<-0.4375); xysol(II,JJ)=nan;
[II,JJ]=find(X>5 & X<6 & Y>0.3125); xysol(II,JJ)=nan;
[II,JJ]=find(X>5 & X<6 & Y<-0.3125); xysol(II,JJ)=nan;
[II,JJ]=find(X>6 & X<7 & Y>0.25); xysol(II,JJ)=nan;
[II,JJ]=find(X>6 & X<7 & Y<-0.25); xysol(II,JJ)=nan;
[II,JJ]=find(X>7 & X<12 & Y>0.375); xysol(II,JJ)=nan;
[II,JJ]=find(X>7 & X<12 & Y<-0.375); xysol(II,JJ)=nan;
[II,JJ]=find(X>12 & Y>0.3125); xysol(II,JJ)=nan;
[II,JJ]=find(X>12 & Y<-0.3125); xysol(II,JJ)=nan;
figure(k5)

 contour(X,Y,xysol,contourn),  axis('tight'), colorbar('EastOutside')
title('Pressure field','FontSize',12)
  axis('off')
% plot the boundary
hold on
for i = 1:size(bnde,1)
   plot([bndxy(bnde(i,1),1),
bndxy(bnde(i,2),1)],[bndxy(bnde(i,1),2),bndxy(bnde(i,2),2)],'-k')
end
hold off;

return
```

```
function bc = stream_bc_weser(xbd,ybd)
%
%   bc = specific_bc(xbd,ybd);
%   input
%          xbd          x boundary coordinate vector
%          ybd          y boundary coordinate vector
%
%   specifies streamfunction associated with specific flow
%   IFISS function: DJS; 6 March 2005.
% Copyright (c) 2005 D.J. Silvester, H.C. Elman, A. Ramage
bc=0*xbd;
k=find(xbd==0);
bc(k)=-
(7.1*ybd(k).*ybd(k).*ybd(k))/3+(8.875*ybd(k).*ybd(k))/2+1.775*ybd(k)+8.875/3;
k=find(ybd==1); bc(k)=-2.6625;
return
```

C. Convection-Diffusion » Steady State CD

For solving the convection diffusion equation for steady state one must provide as input the domain, the solution for the velocity vector and the tidal factor controlling the maximum value of the horizontal velocity depending on the time of the tidal cycle. This is done by running the solve_cd_tide function which calls the following files: q1grid (creates the element grid), femq1_cd_tide and femq1_cd_supg_tide which both call the gauss_transprt_tide function in order to evaluate the convection field at Gauss point, nonzerobc which calls the specific_bc_weser function for setting the problem boundary conditions and plot_cd_weser which plots the solution.

```
%SOLVE_CD_tide solve convection-diffusion problem in weser domain
%   IFISS scriptfile: DJS; 27 May 2012.
% Copyright (c) 2005 D.J. Silvester, H.C. Elman, A. Ramage
function concentration=solve_cd_tide(tidal_factor);
global viscosity;
pde=2; domain=1;
gohome
cd datafiles
load final_weser_grid.mat flowsol mv xy bound mbound x y bndxy bnde obs sbnde
tic
%% set up matrices
qmethod=1;
[ev,ebound] = q1grid(xy,mv,bound,mbound);
[A,N,Q,epe,eph,epw] = femq1_cd_tide(xy,ev,tidal_factor);

viscosity=0.01;
%% update cofficient matrix
supg=0;
A = viscosity*A + N; f = zeros(size(xy(:,1)));
%% compute element peclet numbers
epe = epe/viscosity;
```

```
fprintf('maximum element Peclet number is %10.6e\n',max(epe))
%
%% include streamline diffusion matrix (if necessary)
esupg=find(epe<=1); expe=epe;   %expe(esupg)=0;
if any(expe),
   supg=inf;%default('SUPG parameter (default is optimal)',inf);
   if isinf(supg)
      expe=0.5*(1-1./expe);
      expe(esupg)=inf;
   else
      expe=ones(size(expe)); expe=supg*expe; expe(esupg)=inf;
   end
   epp=expe; epp(esupg)=0; epp=epp.*eph./epw;

   supg=1;
   S = femq1_cd_supg_tide(xy,ev,expe,eph,epw,tidal_factor); A= A+S;
end
%

%% boundary conditions
[Asupg,fsupg] = nonzerobc(A,f,xy,bound);
%

%% compute solution

fprintf('solving linear system ...  ')
xsupg=Asupg\fsupg;
conc=xsupg;

 % compute residual of solution
   nlres = A*xsupg-fsupg;
   nlres_norm = norm(nlres);
%%%%update solution due to preconditioning with iteration loops%%%
%%%%linear iteration, update convection matrix%%%%
it_nb=0;
while it_nb<9
     it_nb = it_nb+1;

%% end of iteration loop
end
conc = xsupg;
concentration=conc;
fprintf('done\n')
etoc=toc; fprintf('linear system solved in  %8.3e seconds\n\n',etoc)
plot_cd_weser(concentration,ev,xy,x,y,bound,bndxy,bnde,obs,22);
 return
```

```
function [flowx,flowy] = gauss_transprt_tide(s,t,xl,yl,xy,tidal_factor)
%GAUSS_TRANSPRT evaluates convection field at Gauss point
%   [flowx,flowy] = gauss_transprt(s,t,xl,yl);
%   input
%          s         reference element x coordinate
%          t         reference element y coordinate
%          xl        physical element x vertex coordinates
```

```
%          yl        physical element y vertex coordinates
%
%   calls simulation results from navier-stokes
%   IFISS function: DJS; 4 March 2005.
% Copyright (c) 2005 D.J. Silvester, H.C. Elman, A. Ramage
load final_weser_grid.mat flowsol
nvtx=length(xy); nu=2*nvtx;
%u=sol(1:nu);v=u(nvtx+1:2*nvtx);
      nel=length(xl(:,1));
      zero_v = zeros(nel,1);
xx=zero_v;
      yy=xx;
xy_gauss=zeros(nel,2);

      [phi_e,dphids,dphidt] = shape(s,t);
      for ivtx=1:4
xx = xx + phi_e(ivtx) * xl(:,ivtx);
      yy = yy + phi_e(ivtx) * yl(:,ivtx);
end
       for i=1:nel
      [distance_x,index_x]= min(abs(xx(i)-xy(:,1)));
      xy_gauss(i,1)=xy(index_x,1);
       [distance_y,index_y]= min(abs(yy(i)-xy(:,2)));
      xy_gauss(i,2)=xy(index_y,2);
       end
       for j=1:nel
           [Lia,Locb]=ismember(xy_gauss(j,:),xy,'rows');
           row=nonzeros(Locb);
           flowx(j)=flowsol(row)*12.5;
           flowy(j)=flowsol(row+nvtx);
       end
       %%%%normalization
       %flowx=flowx*12.5;
       %%%%%include tidal effect
       flowx=flowx*tidal_factor;
            source_yy=find(xy(:,1)==5.5 & xy(:,2)==-0.3125);
flowy(source_yy)=0.009;
            source_yy1=find(xy(:,1)==5.5625 & xy(:,2)==-0.3125);
flowy(source_yy1)=0.009;

      return
```

```
function bc = specific_bc_weser(xbd,ybd)
%solution1_bc   Reference problem 3.1  boundary condition
%   bc = specific_bc(xbd,ybd);
%   input
%          xbd          x boundary coordinate vector
%          ybd          y boundary coordinate vector
%   requires viscosity to be a globally declared variable
%   IFISS function: DJS; 5 March 2005.
% Copyright (c) 2005 D.J. Silvester, H.C. Elman, A. Ramage
%global viscosity


nobd=length(xbd);
```

```
bc=zeros(size(xbd));
source=find(xbd==5.5 & ybd==-0.3125);
bc(source)=1;
source1=find(xbd==5.5625 & ybd==-0.3125);
bc(source1)=1;

return
```

```
function plot_cd_weser(sol,ev,xy,x,y,bound,bndxy,bnde,obs,fig)
%ERRPLOT plots solution and error on weser domain
%   errplot(sol,eldata,ev,xy,x,y,fig);
%   input
%          sol        nodal solution vector
%          eldata     element error vector
%          ev         element mapping matrix
%          xy         vertex coordinate vector
%          x          vector of x-axis interpolation points
%          y          vector of y-axis interpolation points
%          fig        figure number
%
%   IFISS function: DJS; 30 April 2012.
% Copyright (c) 2005 D.J. Silvester, H.C. Elman, A. Ramage
fprintf('plotting solution and estimated errors... ')
% interpolate to a cartesian product mesh
k1=figure(fig); k2=figure(fig+1); k3=figure(fig+2); k4=figure(fig+3);
k5=figure(fig+4);
%x=0.5*(x(1:end-1)+x(2:end));
%y=0.5*(y(1:end-1)+y(2:end));
[X,Y]=meshgrid(x,y);
xysol = griddata(xy(:,1),xy(:,2),sol,X,Y);
if size(obs,1)~=0
   [II,JJ] = findobsXY(obs,X,Y,bndxy); xysol(II,JJ)=nan;
end
[II,JJ]=find(X<1 & Y<0.25); xysol(II,JJ)=nan;
[II,JJ]=find(X>3.75 & Y>0.4375); xysol(II,JJ)=nan;
[II,JJ]=find(X>3.75 & Y<-0.4375); xysol(II,JJ)=nan;
[II,JJ]=find(X>5 & X<6 & Y>0.3125); xysol(II,JJ)=nan;
[II,JJ]=find(X>5 & X<6 & Y<-0.3125); xysol(II,JJ)=nan;
[II,JJ]=find(X>6 & X<7 & Y>0.25); xysol(II,JJ)=nan;
[II,JJ]=find(X>6 & X<7 & Y<-0.25); xysol(II,JJ)=nan;
[II,JJ]=find(X>7 & X<12 & Y>0.375); xysol(II,JJ)=nan;
[II,JJ]=find(X>7 & X<12 & Y<-0.375); xysol(II,JJ)=nan;
[II,JJ]=find(X>12 & Y>0.3125); xysol(II,JJ)=nan;
[II,JJ]=find(X>12 & Y<-0.3125); xysol(II,JJ)=nan;

figure(k1)
hold on
for i = 1:size(bnde,1)
   plot([bndxy(bnde(i,1),1),
bndxy(bnde(i,2),1)],[bndxy(bnde(i,1),2),bndxy(bnde(i,2),2)],'-k');
end
[C,h] =contour(X,Y,xysol,500),axis('tight'),colorbar('EastOutside');
clabel(C,h);
title('Finite Element Solution','FontSize',12)
```

```
%%%%for labeling the contours manualy%%%
%C=contour(X,Y,xysol,500),axis('tight'),colorbar('EastOutside')
%title('Finite Element Solution','FontSize',12)
%clabel(C,'manual') ;


hold off;
axis('off')


figure(k2)
mesh(X,Y,xysol),axis('tight'),colorbar('EastOutside')
title('Finite Element Solution','FontSize',12)
axis('off')
hold on
for i = 1:size(bnde,1)
   plot([bndxy(bnde(i,1),1),
bndxy(bnde(i,2),1)],[bndxy(bnde(i,1),2),bndxy(bnde(i,2),2)],'-k')
end
hold off;
%%

return
```

One can disable the plotting command, especially when the solve_cd_tide function is called successively during the modeling of the 1D equation on activity concentration in bank sediments.

D. 1D equation on activity concentration in bank sediments

For the calculation of the activity concentration in the bank sediments one must first provide the activity concentration in the water as an input. Thus can be done by calling the solve_cd_tide function for each different tidal factor, i.e. for every hour of a simulating time of a month, total of 720 times. This simulation requires approximately 2.5 days by MatLab version R2012b and a processor Intel Core i5-3330 CPU @ 3.00GHz with a RAM of 4.00GB.

```
%This is a script file to calculate the activity concentration in sediments
%The calculation is done by integrating the first order time dependent
%linear ordinary differential equation, taking into account the tidal
%fluctuations and the convection-diffusion sub-model.

%load appropriate matrices
```

```
tic
t=[];
time=719;
g=9.81;
H=12; %mean depth without tide ~12m

Cback=0.006;
%%%%%%%%%%%%%%%%%%%%simulation of tide%%%%%%%%%%%%%%%%%%%%
%%%%%%%%%%%%%%%%%%%%%%%%%%%%%%%%%%%%%%%%%%%%%%%%%%%%%%%%
%%%%%%General equation: h(t)=M2+S2+N2+K1+O1+M4+M6+S4+MS4 %%%%%%%%%
%%%%%%%%%%%%%%%%%%%%%%%%%%%%%%%%%%%%%%%%%%%%%%%%%%%%%%%%
% with M2: principal lunar semidiurnal constituent
%      S2: principal solar semidiurnal constituent
%      N2: larger lunar elliptic semidiurnal constituent
%      K1: luni-solar declinational diurnal constituent
%      O1: lunar declinational diurnal constituent
%      M4: first overtide of M2 constituent
%      M6: second overtide of M2 constituent
%      S4: first overtide of S2 constituent
%      MS4: a compound tide of M2 and S2

%initialize parameters
%amplitude      %period                          %phase
M2_amp=0.6937;  M2_period=0.5175;     M2_phase=-2.387;
S2_amp=0.0757;  S2_period=0.5;        S2_phase=1.2876;
N2_amp=0.3134;  N2_period=0.5274;     N2_phase=2.5796;
K1_amp=0.0268;  K1_period=0.9973;     K1_phase=-2.0964;
O1_amp=0.1116;  O1_period=1.0758;     O1_phase=1.4722;
M4_amp=0.2568;  M4_period=0.2588;     M4_phase=-0.2164;
M6_amp=0.1494;  M6_period=0.1725;     M6_phase=0.00038278;
S4_amp=0.0085;  S4_period=0.25;       S4_phase=0.7284;
MS4_amp=0.0775; MS4_period=0.2543;    MS4_phase=-1.7686;


vw_sand=0.007;               %mean particle settling velocity for sand m/s
vw_silt=0.00015;               %mean particle settling velocity for silt m/s
h=[]; h1=[];
M2=[];
S2=[];
N2=[];
K1=[];
O1=[];
M4=[];
M6=[];
S4=[];
MS4=[];
for i=0:1:time
t(i+1)=i;
```

```
M2h(i+1)=2*M2_amp*cos(360/M2_phase)*cos(M2_period*t(i+1));
S2h(i+1)=2*S2_amp*cos(360/S2_phase)*cos(S2_period*t(i+1));
N2h(i+1)=2*N2_amp*cos(360/N2_phase)*cos(N2_period*t(i+1));
K1h(i+1)=2*K1_amp*cos(360/K1_phase)*cos(K1_period*t(i+1));
O1h(i+1)=2*O1_amp*cos(360/O1_phase)*cos(O1_period*t(i+1));
M4h(i+1)=2*M4_amp*cos(360/M4_phase)*cos(M4_period*t(i+1));
M6h(i+1)=2*M6_amp*cos(360/M6_phase)*cos(M6_period*t(i+1));
S4h(i+1)=2*S4_amp*cos(360/S4_phase)*cos(S4_period*t(i+1));
MS4h(i+1)=2*MS4_amp*cos(360/MS4_phase)*cos(MS4_period*t(i+1));

h(i+1)=M2h(i+1)+S2h(i+1)+N2h(i+1)+K1h(i+1)+O1h(i+1)+M4h(i+1)+M6h(i+1)+S4h(i+1
)+MS4h(i+1);

M2v2(i+1)=-2*sqrt(g/H)*M2_amp*cos(360/M2_phase)*cos(M2_period*t(i+1)+pi/2);
S2v2(i+1)=-2*sqrt(g/H)*S2_amp*cos(360/S2_phase)*cos(S2_period*t(i+1)+pi/2);
N2v2(i+1)=-2*sqrt(g/H)*N2_amp*cos(360/N2_phase)*cos(N2_period*t(i+1)+pi/2);
K1v2(i+1)=-2*sqrt(g/H)*K1_amp*cos(360/K1_phase)*cos(K1_period*t(i+1)+pi/2);
O1v2(i+1)=-2*sqrt(g/H)*O1_amp*cos(360/O1_phase)*cos(O1_period*t(i+1)+pi/2);
M4v2(i+1)=-2*sqrt(g/H)*M4_amp*cos(360/M4_phase)*cos(M4_period*t(i+1)+pi/2);
M6v2(i+1)=-2*sqrt(g/H)*M6_amp*cos(360/M6_phase)*cos(M6_period*t(i+1)+pi/2);
S4v2(i+1)=-2*sqrt(g/H)*S4_amp*cos(360/S4_phase)*cos(S4_period*t(i+1)+pi/2);
MS4v2(i+1)=-
2*sqrt(g/H)*MS4_amp*cos(360/MS4_phase)*cos(MS4_period*t(i+1)+pi/2);

v(i+1)=M2v2(i+1)+S2v2(i+1)+N2v2(i+1)+K1v2(i+1)+O1v2(i+1)+M4v2(i+1)+M6v2(i+1)+
S4v2(i+1)+MS4v2(i+1);

end
tidal_factor=v;

figure
plot(t,h,t,v);
title('Simulated tidal cycle for a month as a standing wave');
legend('Water level (m)','Flow velocity (m/s)')
xlabel('Time in hours');


%Sampling locations
%find the correspondingy value for each location
xl=[-1,-0.5,0,0.5,1,2,5];                %distance from WWTP in km left bank
xr=[-1,-0.5,0,0.5,1,2,5];               %distance from WWTP in km right bank

%Activity concentration in water
%%%Call solve_cd_tide for each tidal_factor (i.e. 720 for a month)
%%%and retrieve the activity in river water for the above locations (use
%%%find)
%%%%locations%%%%
xl_cd=[3.5,4.5,5.5,6.5,7.5,9.5,15];
xr_cd=[3.5,4.5,5.5,6.5,7.5,9.5,15];
```

```
yl_cd=[-0.9688,-0.40625,-0.28125,-0.21875,-0.34375,-0.34375,-0.28125];
yr_cd=[0.9688,0.40625,0.28125,0.21875,0.34375,0.34375,0.28125];
bankl1=find(xy(:,1)==xl_cd(1) &xy(:,2)==yl_cd(1));
bankl2=find(xy(:,1)==xl_cd(2) &xy(:,2)==yl_cd(2));
bankl3=find(xy(:,1)==xl_cd(3) &xy(:,2)==yl_cd(3));
bankl4=find(xy(:,1)==xl_cd(4) &xy(:,2)==yl_cd(4));
bankl5=find(xy(:,1)==xl_cd(5) &xy(:,2)==yl_cd(5));
bankl6=find(xy(:,1)==xl_cd(6) &xy(:,2)==yl_cd(6));
bankl7=find(xy(:,1)==xl_cd(7) &xy(:,2)==yl_cd(7));
bankr1=find(xy(:,1)==xr_cd(1) &xy(:,2)==yr_cd(1));
bankr2=find(xy(:,1)==xr_cd(2) &xy(:,2)==yr_cd(2));
bankr3=find(xy(:,1)==xr_cd(3) &xy(:,2)==yr_cd(3));
bankr4=find(xy(:,1)==xr_cd(4) &xy(:,2)==yr_cd(4));
bankr5=find(xy(:,1)==xr_cd(5) &xy(:,2)==yr_cd(5));
bankr6=find(xy(:,1)==xr_cd(6) &xy(:,2)==yr_cd(6));
bankr7=find(xy(:,1)==xr_cd(7) &xy(:,2)==yr_cd(7));

 %%%%%%For either running concentration in river water for each time in
 %%%%%%tidal cycle or for using the measured values of concentration
 %%%when loading the simulated concentrations no need for this
Cl=zeros(time,7);
Cr=zeros(time,7);
for i=1:1:time
%%%%%call weser_cd_tide and solve_cd_tide to calculate the concentration in
%%%%%the river water at a specific tide time
[concentration]=solve_cd_tide(tidal_factor(i));
concentration(concentration<0)=0;
  % Non-dimensionalized activity concentration in water left bank
Cl(i,1)=concentration(bankl1);
Cl(i,2)=concentration(bankl2);
Cl(i,3)=concentration(bankl3);
Cl(i,4)=concentration(bankl4);
Cl(i,5)=concentration(bankl5);
Cl(i,6)=concentration(bankl6);
Cl(i,7)=concentration(bankl7);
%Non-dimensionalized activity concentration in water right bank
Cr(i,1)=concentration(bankr1);
Cr(i,2)=concentration(bankr2);
Cr(i,3)=concentration(bankr3);
Cr(i,4)=concentration(bankr4);
Cr(i,5)=concentration(bankr5);
Cr(i,6)=concentration(bankr6);
Cr(i,7)=concentration(bankr7);

end
%%%%including background concentration%%%%%

for i=1:time
```

```
if tidal_factor(i)<=0

Cl(i,1)=Cl(i,1)Cback;
Cl(i,2)=Cl(i,2)+Cback;
Cl(i,3)=Cl(i,3)+Cback;
Cl(i,4)=Cl(i,4)+Cback;
Cl(i,5)=Cl(i,5)+Cback;
Cl(i,6)=Cl(i,6)+Cback;
Cl(i,7)=Cl(i,7)+Cback;
Cr(i,1)=Cr(i,1)+Cback;
Cr(i,2)=Cr(i,2)+Cback;
Cr(i,3)=Cr(i,3)+Cback;
Cr(i,4)=Cr(i,4)+Cback;
Cr(i,5)=Cr(i,5)+Cback;
Cr(i,6)=Cr(i,6)+Cback;
Cr(i,7)=Cr(i,7)+Cback;

end


%measured data
%if tidal_factor(i)>0

    %Cl(i,1)=0;
    %Cl(i,2)=0;
    %Cl(i,3)=2.71E-01;
    %Cl(i,4)=1.14E-02;
    %Cl(i,5)=1.44E-02;
    %Cl(i,6)=9.02E-03;
    %Cl(i,7)=6.41E-03;
    %Cr(i,1)=0;
    %Cr(i,2)=0;
    %Cr(i,3)=0;
    %Cr(i,4)=0;
    %Cr(i,5)=3.63E-03;
    %Cr(i,6)=6.94E-03;
    %Cr(i,7)=2.47E-03;

%end
%if tidal_factor(i)<=0

    %Cl(i,1)=0+Cback;
    %Cl(i,2)=8.05E-03+Cback;
    %Cl(i,3)=0+Cback;
    %Cl(i,4)=0+Cback;
    %Cl(i,5)=0+Cback;
    %Cl(i,6)=0+Cback;
    %Cl(i,7)=0+Cback;
    %Cr(i,1)=0+Cback;
```

```
    %Cr(i,2)=4.71E-03+Cback;
    %Cr(i,3)=0+Cback;
    %Cr(i,4)=0+Cback;
    %Cr(i,5)=0+Cback;
    %Cr(i,6)=0+Cback;
    %Cr(i,7)=0+Cback;
   %end
end


%%%%multiply with wwtp data%%%
wwtp_factor_mean=209;
wwtp_factor_min=56;
wwtp_factor_max=603;
for i=1:time
Cl_mean(i,:)=Cl(i,:)*wwtp_factor_mean;
Cr_mean(i,:)=Cr(i,:)*wwtp_factor_mean;
Cl_max(i,:)=Cl(i,:)*wwtp_factor_max;
Cr_max(i,:)=Cr(i,:)*wwtp_factor_max;
Cl_min(i,:)=Cl(i,:)*wwtp_factor_min;
Cr_min(i,:)=Cr(i,:)*wwtp_factor_min;
end

%%%%%%%experimental data for comparison%%%%%
Sl=[1.7,9.64,35.72,11.64,4.39,5.59,2.89];%measured activity concentration in
sediment left bank
eSl=[0.2,0.53,1.44,0.53,0.25,0.34,0.27];
%corresponding error
Sr=[0,0,1.03,0,0,0,2.44];               %measured activity concentration in
sediment right bank
eSr=[0,0,0.16,0,0,0,0.26];                                  %corresponding
error
rl_mean=[]; rr_mean=[];


%%%%%%%%%%%%%%%%%%%%%%%%%%%%%%%%%%%%%%%%%%%%%%%%%%%%%%%%%%%%%%%%%%%%%%%%
%%%%%   EQUATION:  dr/dt=-[a1+a2+a3]r+[b1*b2+b3]C   %%%%%
%%%%%%%%%%%%%%%%%%%%%%%%%%%%%%%%%%%%%%%%%%%%%%%%%%%%%%%%%%%%%%%%%%%%%%%%
for j=1:7
%Parameter definition
lamda=10^-6;        %radioactive decay constant for I-131 in s-1
kpw=0.01;              %distribution(partition) coefficient in water column
kpb=0.01;              %distribution (partition) coefficient in sediment
Sw=0.04;               %solids concentration in the water column
d=1.5*10^-3;                %depth of active bed sediment (sedimentation
growth rate*time)
Sb=400;               %solids concentration in bed
kl=10^-8;              %mass transfer coefficient between water column and
pore water in m/s
```

```
gamma=2300; %3.5m/1.5mm
%Term definition
a1=lamda/(1+kpb*Sb);                    %radioactive decay
b2=gamma;
step=500;
xmin=1;

a3=(kl/(d*(Sb+(1/kpb))))*(1/kpb);          %pore water diffusion
b3=(kl/(d*(Sb+(1/kpb))))*(1/(1+kpw*Sw));  %pore water diffusion

%%%%%%%%%%%%%%%%%%%%%%%%%%%%%%%%%%%%%%%%%%%%%%%%%%%%%%%%%%%%%%%%%%%%%%%%%%%%%%%%
%%%%%   SOLUTION:  r(t)=exp(-int[a1+a2(t)+a3]dt)*int(exp(-
int[a1+a2(t)+a3]dt)*[b1(t)*b2C(t)+b3C(t)]dt)    %%%%%
%%%%%%%%%%%%%%%%%%%%%%%%%%%%%%%%%%%%%%%%%%%%%%%%%%%%%%%%%%%%%%%%%%%%%%%%%%%%%%%%
%%%%%%%%%%%%%%%%%%%%%%
min_h=-0.5;
h0=0.5;
xmin=0;
for i=1:1:time
xmax=i*step;

if (h(i)>min_h)  && (h(i+1)>min_h)
        int1_sand_total=0;
        int1_silt_total=0;
        int2l_sand_total_mean=0;
        int2l_silt_total_mean=0;
        int2r_sand_total_mean=0;
        int2r_silt_total_mean=0;
        int2l_sand_total_min=0;
        int2l_silt_total_min=0;
        int2r_sand_total_min=0;
        int2r_silt_total_min=0;
        int2l_sand_total_max=0;
        int2l_silt_total_max=0;
        int2r_sand_total_max=0;
        int2r_silt_total_max=0;
t_S=xmin:1:xmax;
       M2_S=2*M2_amp*cos(360/M2_phase)*cos(M2_period*t_S/step);
       S2_S=2*S2_amp*cos(360/S2_phase)*cos(S2_period*t_S/step);
       N2_S=2*N2_amp*cos(360/N2_phase)*cos(N2_period*t_S/step);
       K1_S=2*K1_amp*cos(360/K1_phase)*cos(K1_period*t_S/step);
       O1_S=2*O1_amp*cos(360/O1_phase)*cos(O1_period*t_S/step);
       M4_S=2*M4_amp*cos(360/M4_phase)*cos(M4_period*t_S/step);
       M6_S=2*M6_amp*cos(360/M6_phase)*cos(M6_period*t_S/step);
       S4_S=2*S4_amp*cos(360/S4_phase)*cos(S4_period*t_S/step);
       MS4_S=2*MS4_amp*cos(360/MS4_phase)*cos(MS4_period*t_S/step);
        h1=h0+M2_S+S2_S+N2_S+K1_S+O1_S+M4_S+M6_S+S4_S+MS4_S;
ks_sand=vw_sand*(h1.^-1);
ks_silt=vw_silt*(h1.^-1);
```

```
a_sand=ks_sand*Sw*gamma/Sb;
a_silt=ks_silt*Sw*gamma/Sb;
        a2_sand=a_sand*Sb/(Sb+(1/kpb));                    %resuspension sand
        a2_silt=a_silt*Sb/(Sb+(1/kpb));                    %resuspension silt

        fun1_sand=a1+a2_sand+a3;
        fun1_silt=a1+a2_silt+a3;
        int1_sand=simps(fun1_sand);
        int1_silt=simps(fun1_silt);

end
xmin=xmax;
    int1_sand_total=int1_sand_total+int1_sand;
    int1_silt_total=int1_silt_total+int1_silt;
end
xmin=0;
funl_sand_min=[]; b1_sand=[]; b1_silt=[];
int2l_sand_mean=0;
int2l_sand_min=0;
int2l_sand_max=0;
funl_silt_mean=[];
funl_silt_min=[];
funl_silt_max=[];
int2l_silt_mean=0;
int2l_silt_min=0;
int2l_silt_max=0;
funr_sand_mean=[];
funr_sand_min=[];
funr_sand_max=[];
int2r_sand_mean=0;
int2r_sand_min=0;
int2r_sand_max=0;
funr_silt_mean=[];
funr_silt_min=[];
funr_silt_max=[];
int2r_silt_mean=0;
int2r_silt_min=0;
int2r_silt_max=0;
rl_sand_mean=0;
rl_silt_mean=0;
rr_sand_mean=0;
rr_silt_mean=0;
rl_sand_min=0;
rl_silt_min=0;
rr_sand_min=0;
rr_silt_min=0;
rl_sand_max=0;
rl_silt_max=0;
rr_sand_max=0;
rr_silt_max=0;
```

```
xmin=0;
for i=1:1:time
Ccl_mean=Cl_mean(i,j);
Ccr_mean=Cr_mean(i,j);
Ccl_min=Cl_min(i,j);
Ccr_min=Cr_min(i,j);
Ccl_max=Cl_max(i,j);
Ccr_max=Cr_max(i,j);
xmax=i*step;
        int2l_sand_total_mean=0;
        int2l_silt_total_mean=0;
        int2r_sand_total_mean=0;
        int2r_silt_total_mean=0;
        int2l_sand_total_min=0;
        int2l_silt_total_min=0;
        int2r_sand_total_min=0;
        int2r_silt_total_min=0;
        int2l_sand_total_max=0;
        int2l_silt_total_max=0;
        int2r_sand_total_max=0;
        int2r_silt_total_max=0;
if (h(i)>min_h) && (h(i+1)>min_h)
t_S=xmin:1:xmax;
       M2_S=2*M2_amp*cos(360/M2_phase)*cos(M2_period*t_S/step);
       S2_S=2*S2_amp*cos(360/S2_phase)*cos(S2_period*t_S/step);
       N2_S=2*N2_amp*cos(360/N2_phase)*cos(N2_period*t_S/step);
       K1_S=2*K1_amp*cos(360/K1_phase)*cos(K1_period*t_S/step);
       O1_S=2*O1_amp*cos(360/O1_phase)*cos(O1_period*t_S/step);
       M4_S=2*M4_amp*cos(360/M4_phase)*cos(M4_period*t_S/step);
       M6_S=2*M6_amp*cos(360/M6_phase)*cos(M6_period*t_S/step);
       S4_S=2*S4_amp*cos(360/S4_phase)*cos(S4_period*t_S/step);
       MS4_S=2*MS4_amp*cos(360/MS4_phase)*cos(MS4_period*t_S/step);
        h1=h0+M2_S+S2_S+N2_S+K1_S+O1_S+M4_S+M6_S+S4_S+MS4_S;
ks_sand=vw_sand*(h1.^-1);
ks_silt=vw_silt*(h1.^-1);
        b1_sand=ks_sand*kpw*(Sw/(Sb+(1/kpb)))*(1/(1+kpw*Sw));
%sedimentation_sand
b1_silt=ks_silt*kpw*(Sw/(Sb+(1/kpb)))*(1/(1+kpw*Sw));
%sedimentation_silt


funl_sand_mean=Ccl_mean*(b1_sand*b2+b3)*exp(int1_sand_total);
funl_silt_mean=Ccl_mean*(b1_silt*b2+b3)*exp(int1_silt_total);
funr_sand_mean=Ccr_mean*(b1_sand*b2+b3)*exp(int1_sand_total);
funr_silt_mean=Ccr_mean*(b1_silt*b2+b3)*exp(int1_silt_total);
funl_sand_min=Ccl_min*(b1_sand*b2+b3)*exp(int1_sand_total);
funl_silt_min=Ccl_min*(b1_silt*b2+b3)*exp(int1_silt_total);
funr_sand_min=Ccr_min*(b1_sand*b2+b3)*exp(int1_sand_total);
funr_silt_min=Ccr_min*(b1_silt*b2+b3)*exp(int1_silt_total);
```

```
funl_sand_max=Ccl_max*(b1_sand*b2+b3)*exp(int1_sand_total);
funl_silt_max=Ccl_max*(b1_silt*b2+b3)*exp(int1_silt_total);
funr_sand_max=Ccr_max*(b1_sand*b2+b3)*exp(int1_sand_total);
funr_silt_max=Ccr_max*(b1_silt*b2+b3)*exp(int1_silt_total);

        int2l_sand_mean=simps(funl_sand_mean);
        int2l_silt_mean=simps(funl_silt_mean);
        int2r_sand_mean=simps(funr_sand_mean);
        int2r_silt_mean=simps(funr_silt_mean);
        int2l_sand_min=simps(funl_sand_min);
        int2l_silt_min=simps(funl_silt_min);
        int2r_sand_min=simps(funr_sand_min);
        int2r_silt_min=simps(funr_silt_min);
        int2l_sand_max=simps(funl_sand_max);
        int2l_silt_max=simps(funl_silt_max);
        int2r_sand_max=simps(funr_sand_max);
        int2r_silt_max=simps(funr_silt_max);

end
        int2l_sand_total_mean=int2l_sand_total_mean+int2l_sand_mean;
        int2l_silt_total_mean= int2l_silt_total_mean+int2l_silt_mean;
        int2r_sand_total_mean= int2r_sand_total_mean+int2r_sand_mean;
        int2r_silt_total_mean=int2r_silt_total_mean+int2r_silt_mean;

        int2l_sand_total_min=int2l_sand_total_min+int2l_sand_min;
        int2l_silt_total_min= int2l_silt_total_min+int2l_silt_min;
        int2r_sand_total_min= int2r_sand_total_min+int2r_sand_min;
        int2r_silt_total_min=int2r_silt_total_min+int2r_silt_min;
        int2l_sand_total_max=int2l_sand_total_max+int2l_sand_max;
        int2l_silt_total_max= int2l_silt_total_max+int2l_silt_max;
        int2r_sand_total_max= int2r_sand_total_max+int2r_sand_max;
        int2r_silt_total_max=int2r_silt_total_max+int2r_silt_max;


xmin=xmax;


rl_sand_mean=rl_sand_mean+(exp(-int1_sand)*int2l_sand_mean);
rl_silt_mean=rl_silt_mean+(exp(-int1_silt)*int2l_silt_mean);
rr_sand_mean=rr_sand_mean+(exp(-int1_sand)*int2r_sand_mean);
rr_silt_mean=rr_silt_mean+(exp(-int1_silt)*int2r_silt_mean);

rl_sand_min=rl_sand_min+(exp(-int1_sand)*int2l_sand_min);
  rl_silt_min=rl_silt_min+(exp(-int1_silt)*int2l_silt_min);
  rr_sand_min=rr_sand_min+(exp(-int1_sand)*int2r_sand_min);
  rr_silt_min=rr_silt_min+(exp(-int1_silt)*int2r_silt_min);
  rl_sand_max=rl_sand_max+(exp(-int1_sand)*int2l_sand_max);
  rl_silt_max=rl_silt_max+(exp(-int1_silt)*int2l_silt_max);
  rr_sand_max=rr_sand_max+(exp(-int1_sand)*int2r_sand_max);
  rr_silt_max=rr_silt_max+(exp(-int1_silt)*int2r_silt_max);
```

```
end
percent_sand=0;
percent_silt=0;
if j==1
percent_sand=0.52;
percent_silt=0.48;
else if j==2
percent_sand=0.62;
percent_silt=0.38;
else if j==3
percent_sand=0.46;
percent_silt=0.54;
else if j==4
percent_sand=0.04;
percent_silt=0.96;
else if j==5
percent_sand=0.03;
percent_silt=0.97;
else if j==6
percent_sand=0.45;
percent_silt=0.48;
else if j==7
percent_sand=0.45;
percent_silt=0.48;
else
fprintf('Error');
end
end
end
end
end
end
end


rl_mean(j)= percent_sand*rl_sand_mean+percent_silt*rl_silt_mean;
rr_mean(j)= percent_sand*rr_sand_mean+percent_silt*rr_silt_mean;

rl_min(j)= percent_sand*rl_sand_min+percent_silt*rl_silt_min;
rr_min(j)= percent_sand*rr_sand_min+percent_silt*rr_silt_min;
rl_max(j)= percent_sand*rl_sand_max+percent_silt*rl_silt_max;
rr_max(j)= percent_sand*rr_sand_max+percent_silt*rr_silt_max;

end

Rl_mean=[rl_mean(1),rl_mean(2),rl_mean(3),rl_mean(4),rl_mean(5),rl_mean(6),rl
_mean(7)];                    %simulated activity concentration in sediment
left bank
```

```
Rr_mean=[rr_mean(1),rr_mean(2),rr_mean(3),rr_mean(4),rr_mean(5),rr_mean(6),rr
_mean(7)];                        %simulated activity concentration in sediment
right bank

Rl_min=[rl_min(1),rl_min(2),rl_min(3),rl_min(4),rl_min(5),rl_min(6),rl_min(7)
];                     %simulated activity concentration in sediment left
bank
Rr_min=[rr_min(1),rr_min(2),rr_min(3),rr_min(4),rr_min(5),rr_min(6),rr_min(7)
];
Rl_max=[rl_max(1),rl_max(2),rl_max(3),rl_max(4),rl_max(5),rl_max(6),rl_max(7)
];                     %simulated activity concentration in sediment left
bank
Rr_max=[rr_max(1),rr_max(2),rr_max(3),rr_max(4),rr_max(5),rr_max(6),rr_max(7)
];


Ql=[0,0,110.55,0,0,3.74,0];%measured activity concentration in sediment left
bank
eQl=[0,0,5.36,0,0,0.18,0];                                %corresponding error
Qr=[0,0,0,1.75,0,0,2.73];               %measured activity concentration in
sediment right bank
eQr=[0,0,0,0.47,0,0,0.28];
fig=figure;
p1=errorbar(xl,Sl,eSl,'b');
hold on;
p2=plot(xl,Rl_mean,'--b');
hold on;
p3=errorbar(xr,Sr,eSr,'r');
hold on;
p4=plot(xr,Rr_mean,'--r');
hold on
p5=plot(xl,Rl_min,':b');
hold on;
p6=plot(xl,Rl_max,':b');
hold on;
p7=plot(xr,Rr_min,':r');
hold on
p8=plot(xr,Rr_max,':r');
hold on
p9=errorbar(xl,Ql,eQl,'c');
hold on
p10=errorbar(xr,Qr,eQr,'m');

title('Measured and simulated I-131 activity concentration in sediments');
%title('Simulated I-131 activity concentration in sediments');
xlabel('Distance from WWTP in km');
ylabel('Activity concentration in Bq/kg(d.m.)');
%legend([p2 p4],{'Simulated activity left bank (mean)','Simulated activity
right bank (mean)'});
```

```
legend([p1 p9 p2 p3 p10 p4],{'Measured activity left bank -2015','Measured
activity left bank -2008','Simulated activity left bank (mean)','Measured
activity right bank - 2015','Measured activity right bank - 2008','Simulated
activity right bank (mean)'});
fprintf('done\n')
etoc=toc; fprintf('total simulation time  %8.3e seconds\n\n',etoc)
print(fig,'Sediment simulation','-dpng')
```

Appendix 16 - Simplification of the 2D advection dispersion equation

The 2D advection dispersion equation in river water has the following form:

$$\frac{\partial C_T}{\partial t} = -u_x \frac{\partial C_T}{\partial x} + E\frac{\partial^2 C_T}{\partial x^2} - u_y \frac{\partial C_T}{\partial y} + E\frac{\partial^2 C_T}{\partial y^2}$$
$$-\lambda\left(\frac{C_T}{1+K_{P,W}S_W}\right) - k_S\left(\frac{K_{P,W}S_W}{1+K_{P,W}S_W}\right)C_T + \frac{k_L}{h}\left(\frac{r}{K_{P,b}} - \frac{C_T}{1+K_{P,W}S_W}\right) + \alpha\frac{S_b r}{\gamma} \qquad \text{eq. 3.14}$$

With the aid of table 7.3, where the model parameter values used in this study are given, it is easy to calculate the time scale for each reaction term.

- Radioactive decay term

$$\lambda\left(\frac{1}{1+K_{P,W}S_W}\right) = 10^{-6}s^{-1}\left(\frac{1}{1+0.01m^3/kg\cdot 0.04kg/m^3}\right) \approx 10^{-6}s^{-1}$$

- Sedimentation term

$$k_S\left(\frac{K_{P,W}S_W}{1+K_{P,W}S_W}\right) = \frac{v_W}{h}\left(\frac{K_{P,W}S_W}{1+K_{P,W}S_W}\right) = \frac{\left[7\times10^{-3} - 1.5\times10^{-4}\right]m/s}{12m}\left(\frac{0.01m^3/kg\cdot 0.04kg/m^3}{1+0.01m^3/kg\cdot 0.04kg/m^3}\right)$$
$$\approx \left[10^{-8} - 10^{-6}\right]s^{-1}$$

- Resuspension term

$$\alpha\frac{S_b r}{\gamma} = \frac{k_S S_W \gamma}{S_b}\frac{S_b}{\gamma} = k_s S_W = \frac{v_W}{h}S_W = \frac{\left[7\times10^{-3} - 1.5\times10^{-4}\right]m/s}{12m}0.04kg/m^3 \approx \left[10^{-5} - 10^{-7}\right]s^{-1}kg/m^3$$

- Pore water diffusion to sediments term

$$\frac{k_L}{h}\left(\frac{1}{1+K_{P,W}S_W}\right) = \frac{10^{-8}m/s}{12m}\left(\frac{1}{1+0.01m^3/kg\cdot 0.04kg/m^3}\right) \approx 10^{-10}s^{-1}$$

- Pore water diffusion from sediments term

$$\frac{k_L}{h}\left(\frac{1}{K_{P,b}}\right) = \frac{10^{-8}m/s}{12m}\left(\frac{1}{0.01m^3/kg}\right) \approx 10^{-8}s^{-1}kg/m^3$$

In a time scale of 1 hour (time of the simulation) these terms can be neglected cause their effect in the activity concentration on the river water would be less than 1%.